A DISSERTATION

submitted in partial fulfillment of the requirements

for the degree of Doctor of Science

学位申請論文

Study on layered transition metal oxides for positive electrodes of Li- and Na-ion batteries

（リチウムおよびナトリウムイオン電池正極用層状遷移金属酸化物の研究）

March 2017

平成 29 年 3 月

Department of Applied Chemistry, Tokyo University of Science

東京理科大学大学院　総合化学研究科　博士後期課程

Shinichi Kumakura

熊倉　真一

Contents

Chapter 1. Introduction

1.1 Rechargeable batteries

Rechargeable (secondary) batteries are capable to store electrical energy as chemical energy and offer multiple usage in contrast with primary cells. Among several types of rechargeable batteries, lithium ion batteries (LIBs) are widely used all over the world. Fig. 1-1 shows gravimetric power and energy densities for different rechargeable batteries.[1] Compared to conventional aqueous secondary batteries, such as lead acid, nickel-cadmium (Ni-Cd) and nickel-metal hydride (Ni-MH) batteries, LIBs have the higher energy and power density. LIBs are capable to operate high voltage ~ 4 V while other batteries are operating around 1.5 V. Operating such a high voltage for LIBs requires using non-aqueous electrolyte since voltage window based on aqueous electrolyte severely limits operating voltage of the batteries.

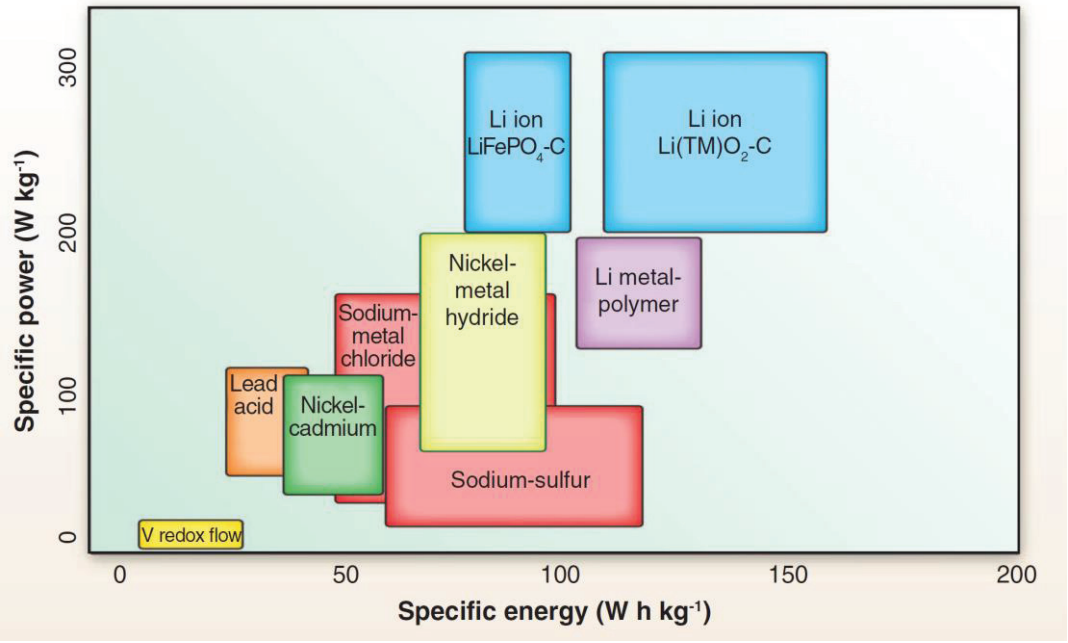

Fig. 1-1. Gravimetric power and energy densities for different rechargeable batteries.[1]

Research and development related with electrical energy storage (EES) system are one of the most important topic for modern society and fit 3 megatrends in the world, (1) rapid evolution of mobile electronic devices, (2) electrification of automotive, and (3) utilization of renewable energy as overviewed below,

(1) Recently, product development of mobile electric products is getting very fast. Appearance of smart phones, tablets etc. makes "Ubiquitous society" nearly feasible. Moreover, power tool is possible to be codeless such as vacuum and industrial tools etc. LIBs are playing a critical role for all these products because of high energy and power density. Future technology like "wearable device" probably further demands small, safe and long-lasting rechargeable batteries.

(2) Electrification of automotive such as electric vehicle (EV), hybrid electric vehicle (HEV), and plug-in hybrid electric vehicle (PHEV) etc. is also a recent big movement to reduce gaseous emissions from the burning of fossil fuels and to realize low- or zero-CO_2 emission society.

(3) Utilization of renewable energy such as solar, wind, and geothermal power etc. is expected as alternative energy sources to replace fossil fuels and nuclear power. As well as development of effective alternative energy generation system, the energy storage system is necessary to provide stable power supply and to achieve "Smart grid" in future.

To meet a variety of requirement for rechargeable batteries, there are so many chances to suggest advanced and/or post LIBs. In the following section, current system of LIBs and emerging technology is briefly overviewed.

1.1.1 Li-ion batteries

Lithium-ion batteries (LIBs) have achieved a worldwide commercial success and are leading above mentioned mega-trend all over the world. Compared to conventional aqueous secondary batteries, LIBs have some advantages, such as the higher energy density, the higher operating voltage, and the lower self-discharge. There are solid reasons of the merits by using lithium, (1) lithium is the lightest and smallest (Li^+ ion radius: 0.68 Å) metal, (2) its oxidation-reduction is of single electron reaction and the electrochemical equivalent (0.26 g Ah^{-1}) is the smallest of all metal elements. Consequently, lithium allows the production of batteries having higher operating voltage or high energy density as contributed by the lowest oxidation-reduction potential about ~3.03 V vs. SHE. Fig. 1-2 shows a schematic illustration of conventional LIBs. Currently, LIB cells consisting of $LiCoO_2$//graphite are regarded as most conventional ones.

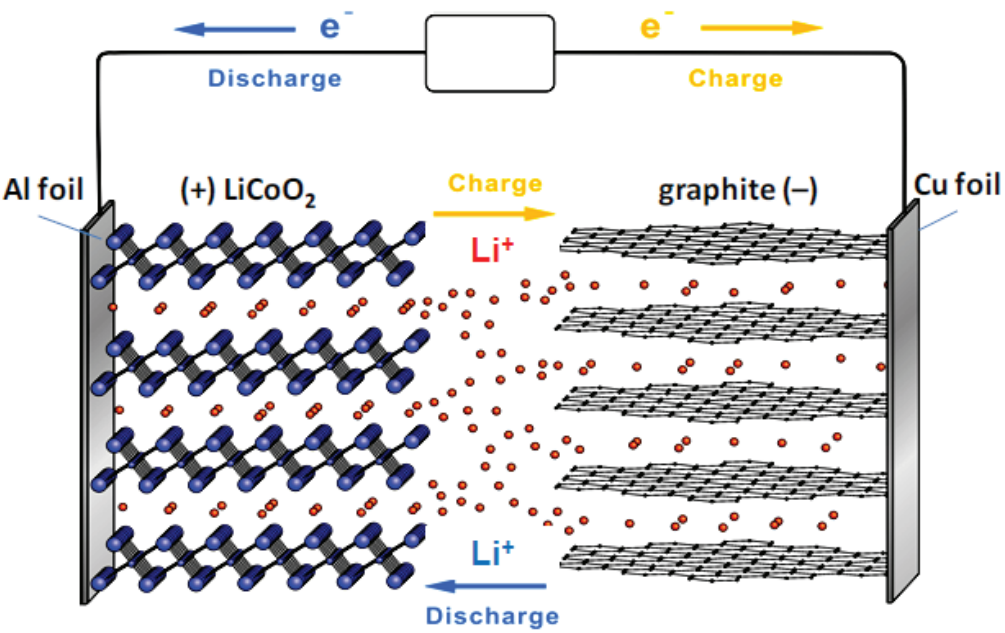

Fig. 1-2. A schematic illustration of conventional LIB system. In the commercial LIBs, $LiCoO_2$ and graphite carbon are usually used as positive and negative electrode materials, respectively, with non-aqueous electrolyte containing lithium salts.

In this section, each component of LIB system is shortly overviewed and in the next section, the detailed introduction of positive electrode materials will be described.

Negative electrode materials

In principle, Li metal is the best choice as negative electrode materials because of the lowest potential and nearly unlimited theoretical capacity. In practice use, however, the cycle stability of the battery is limited due to the dendritic growth of lithium metal, which causes short-circuit of the cells. Consequently, the most widely used negative electrode for LIBs is made of carbon, especially graphite, because its working potential is very low and close to that of metallic lithium, flat discharge performance, high-power availability and safety compared to lithium metal electrode with the specific capacity of 372 mAh g^{-1}.[2-5] Interestingly, a passivation layer, so-called solid electrolyte interphase (SEI), forming during initial charge plays an important role in reversible lithium intercalation into graphite. Therefore, combination with electrolyte and electrolyte additive is very important for development of negative electrode materials.

Electrolyte

Using non-aqueous electrolyte was a key of LIBs operating high voltage and thus, LIBs are also called non-aqueous rechargeable batteries. Most of the commercial LIBs are using the non-aqueous solutions, in which roughly 1.0 molar of lithium hexafluoro-phosphate ($LiPF_6$) salt is dissolved in the mixture of carbonate ester solvents selected from cyclic carbonates, *i.e.*, ethylene carbonate (EC) and propylene carbonate (PC), and linear carbonates, *i.e.*, dimethyl carbonate (DMC), ethyl methyl carbonate (EMC) and diethyl carbonate (DEC). Recent researches in the liquid electrolytes are mainly focused on the electrolyte additives, such as vinylene carbonate (VC),[6-8], ethylene sulfite (ES),[9, 10] fluoroethylene carbonate (FEC),[11] *etc*. These additives provide extra functions to the

liquid electrolytes in addition to a fundamental function as an ionic conductor, such as SEI formation and suppression of undesirable surface reaction at both positive and negative electrodes.

Binder

In general, an electrode binder for LIBs is being used to bind active material layers, bind together active material layers and current collectors and provide the slurry of electros with certain viscosity. Since the commercialization of LIBs in 1991, poly(vinylidene fluoride) (PVdF) has been widely used as a binder to bind together the graphite and $LiCoO_2$ powder for electrodes of LIBs. Additionally, an aqueous dispersion of sodium carboxymethyl cellulose (CMCNa) as thicker and styrene-butadiene rubber (SBR) latex is usually used as a binder for negative electrodes in the current LIBs.[12-18] Recently, some reports suggested that a choice of binder is also important to form SEI layer and design a longer-life cells.[19, 20]

Current collector

Both aluminum and copper foils have been widely used as a current collector for LIB. Al forms alloy with Li by electrochemical reaction at lower potential than ca. 1 V vs. Li. Therefore, it is impossible to use inexpensive and lighter Al foil than Cu foil in a negative electrode. In addition, the Cu foil is easily oxidized at the potential above 2 V vs. Li, making it impractically to use Cu foil in the positive electrode. From these reasons, an Al foil[21, 22] is used as a current collector in the positive electrode, while a Cu foil is used in the negative electrode[23] of commercial LIBs. Using Cu foil is an un-negligible factor for the total cost of large cells for LIBs and no need to use Cu foil is one of the advantage for Na-ion batteries which will be shown in next section.

Separator

A separator is a porous membrane placed between positive and negative electrodes and capable to pass ionic career but prevent electric contact of the electrodes. A variety of separators have been used in batteries so far. The liquid LIBs usually use microporous polyolefin separators.[24] Separators play a key role in the battery performance such as rate, cycle-life and safety properties and also, occupy un-negligible cost in the components of LIBs.

As above itemized, each component of the LIB cells has a very important role. For the further improvement of LIBs, it is necessary to develop not only the components themselves but also the combination among them because the components are interacting each other in the cells during electrochemical reactions. Such an integration of these technologies requires the researchers to have wide knowledge and the attitude of open mind for the different field.

1.1.2 Advanced and post LIBs; Na ion batteries and others

After the success of LIBs, the demand of EES is continuously increased and the application field will be expected to be dramatically expanding. For future society, the development of next generation battery having superior feature to LIBs is highly required. Note that the new battery needs not to totally exceed the current LIB system and one significant advantage such as cost, power, and safety may provide a chance to appear the commercial market. There are a lot of research topics expected as advanced or post LIB technology, such as rapid development of solid electrolyte for all-solid-state LIBs, [25-27] aqueous 3 V-class LIBs stimulated by finding of hydrate-melt electrolyte,[28] K-ion batteries[29, 30] and so on.

Among them, Na-ion battery (NIB) is one of the most promising candidates as post LIBs since Na is cheaper and more abundant than Li. In addition, NIBs have a potential to show superior feature of safety and rate properties. Fig. 1-3 shows a schematic illustration of current idea of NIBs. Typically, NIB cells consisting of layered oxides and disordered carbon as positive and negative electrode materials, respectively, are the most promising system. Other components of NIBs are in general very similar to

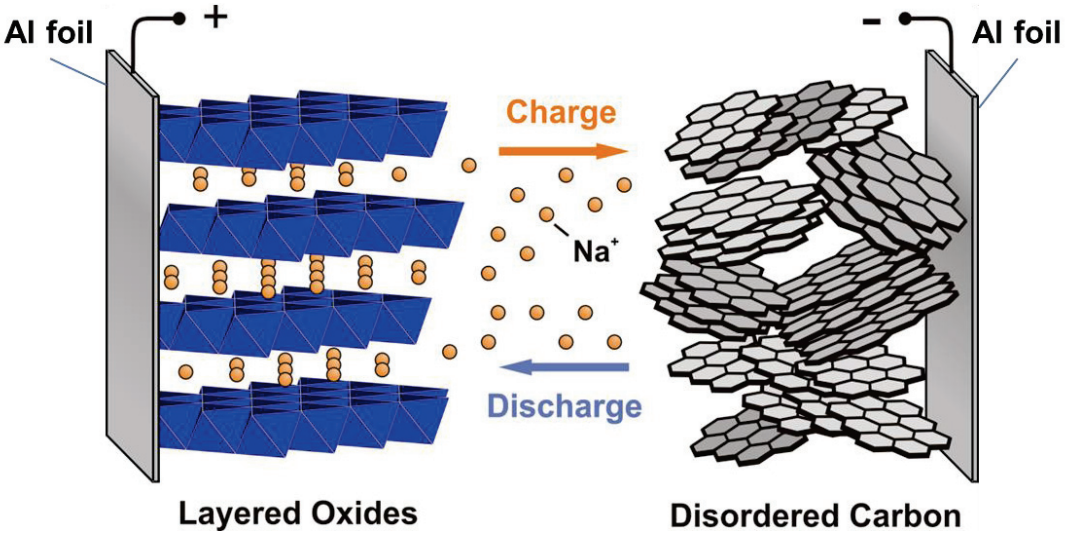

Fig. 1-3. A schematic illustration of current idea of NIBs.

those of LIBs such as cell configuration, electrolyte, separator and so on. Therefore, we can import a lot of know-how of LIB technology. In addition to great potential to practical application of NIBs, we believe that the knowledge obtained from NIB system will be very useful for further improvement of LIB system. The advantage of NIBs in view of positive electrode materials will be summarized in the next section. One of the obvious advantage of NIBs is using Al foil for the current collector of negative electrode instead of Cu foil which is not a trivial cost in the large LIB cells. As described in the last section, Al foil is not possible to use negative electrode because of alloying with Li, however, Na doesn't form alloy with Al foil.[31] In fact, the number of publications on NIBs has drastically increased in recent years after 2010, as shown in Fig. 1-4.

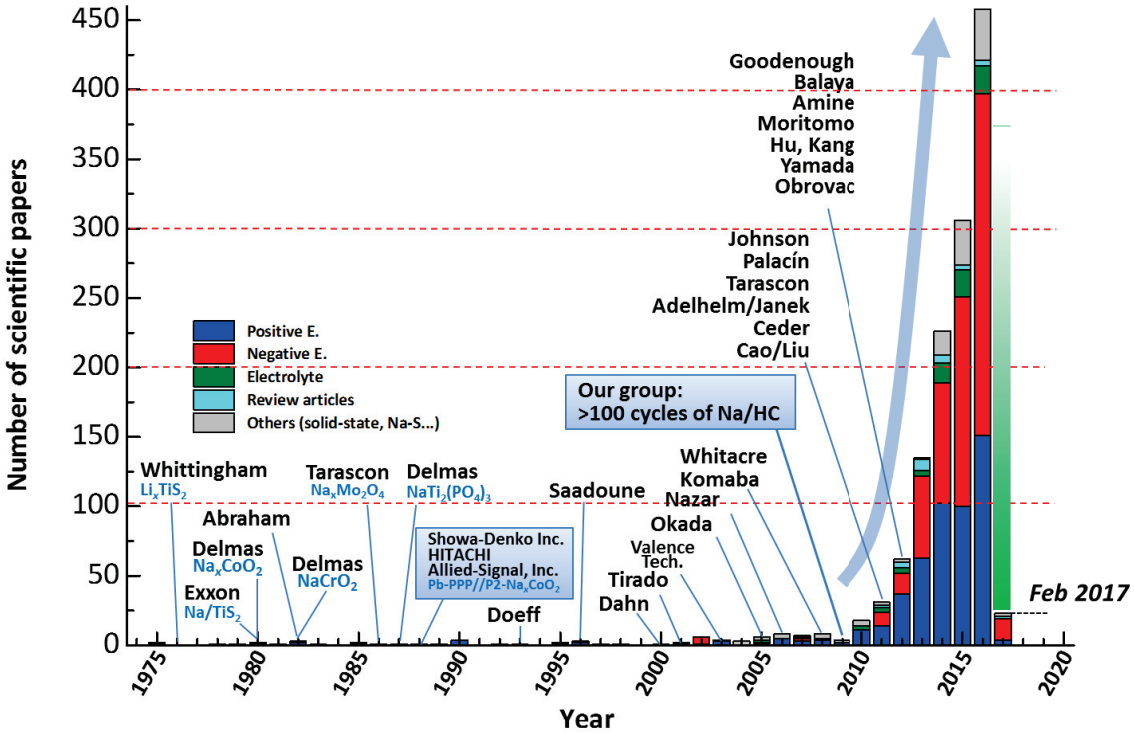

Fig. 1-4. A number of original papers related to NIBs, published in the past three decades. Data are based upon Web of Knowledge and updated on Feb 7, 2017.

1.2 Positive electrode materials for rechargeable batteries

A variety of materials are reported for the positive electrode materials of LIBs and NIBs, so far. The brief summary of the reported materials and the current research topics are shown in this section.

1.2.1 Positive electrode materials for LIBs

In material development for positive electrode of LIB cells, layered transition metal oxides have always been in the leading role since 1970s. Whittingham et al. reported reversible Li insertion into TiS_2 which has a hexagonal close-packed lattice, so called the CdI_2 structure.[32-34] Afterwards, Mizushima and Goodenough et al. reported $LiCoO_2$ which has a cubic close-packed lattice, so called α-$NaFeO_2$ structure.[35] Compared to TiS_2, $LiCoO_2$ has several merits, originally containing Li, high redox voltage ~ 4V, and so on. By combining developments of negative electrode and electrolyte, LIB cells was commercialized by Sony in 1991. Started from a success of $LiCoO_2$, layered mixed transition metal oxides, LiMO$_2$ (M = Ni, Mn, Co *etc.*) are intensively studied. A schematic illustration of the crystal structure of LiMO$_2$ is shown in Fig. 1-5a. This structure is classified as O3-type layered structure by Delmas et al.[36] and this classification will be further discussed in the next section since Na system has richer layered phases. In comparison with $LiCoO_2$, $LiNiO_2$ is capable to show higher capacity in the same voltage range, however, several drawbacks are known, cation mixing with Li and Ni, thermodynamic instability and so on.[37] Ohzuku et al. reported electrochemical performance of solid solution with $LiCoO_2$ - $LiNiO_2$ and its end members as shown in Fig. 1-5b.[38] There is a clear trend observed that larger

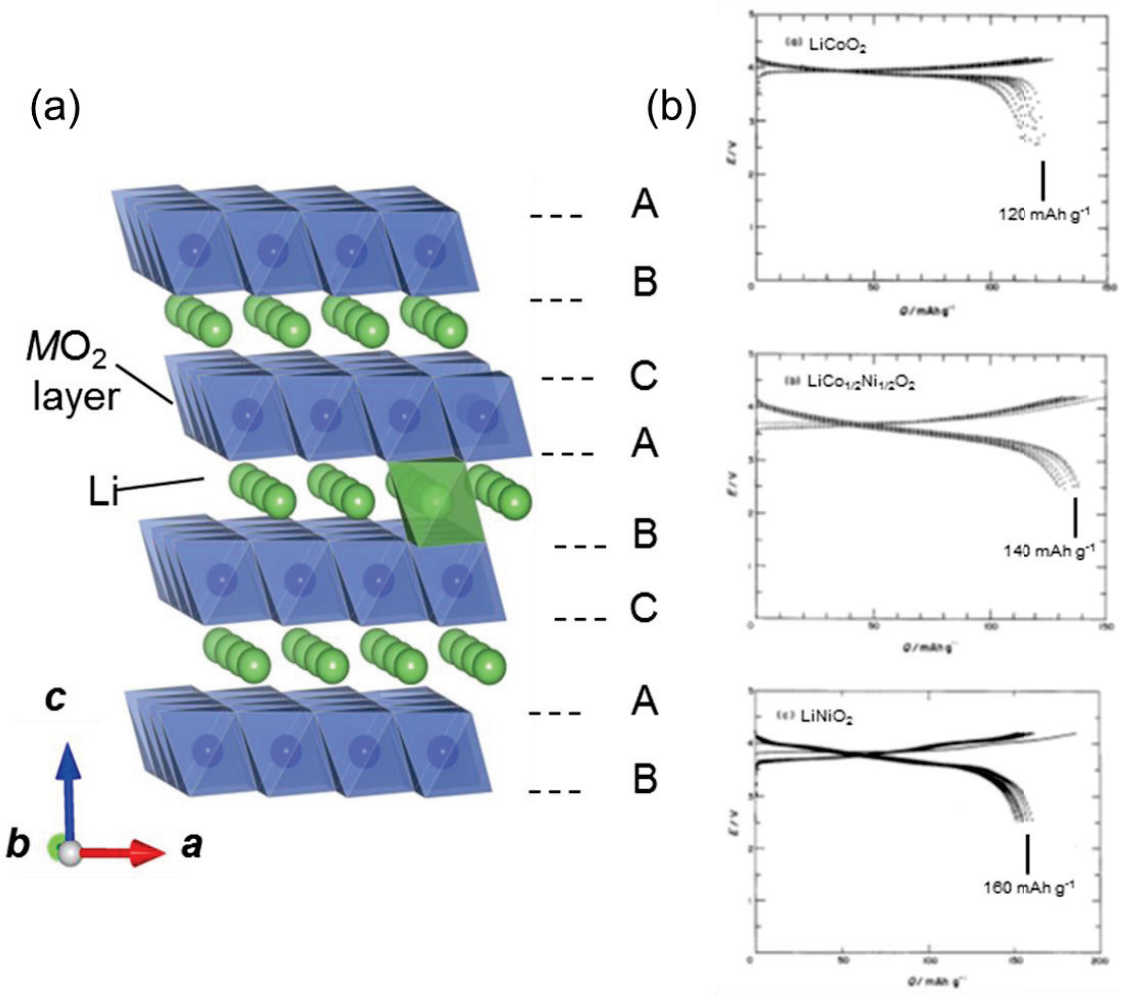

Fig. 1-5. (a) A schematic illustration of LiMO$_2$ structure and (b) charge/discharge curves of LiCoO$_2$-LiNiO$_2$ solid solution.[38]

reversible capacity is obtained with a little sacrifice of operating voltage as x increases in LiCo$_{1-x}$Ni$_x$O$_2$. Though α-NaFeO$_2$ type LiMnO$_2$ has never been obtained by conventional solid-state reaction, manganese is also possible to be combined in LiMO$_2$. Basically manganese in LiMO$_2$ is thought to be tetravalent and electrochemically inactive and provides structural stability and cost advantage as well studied for LiNi$_{0.5}$Mn$_{0.5}$O$_2$.[39-41] .Based on these knowledge, mixed transition metal oxides with cobalt nickel and manganese, Li(Ni,Mn,Co,)O$_2$ has

been widely examined to optimize their electrode performances, such as $LiNi_{1/3}Mn_{1/3}Co_{1/3}O_2$,[42-44] $LiNi_{0.5}Mn_{0.3}Co_{0.2}O_2$, and $LiNi_{0.4}Mn_{0.2}Co_{0.2}O_2$.[45] These compounds can be expressed the ternary system of $LiCoO_2$-$LiNiO_2$-$LiMnO_2$ shown as the triangle phase (Fig. 1-6). In view of practical application, the direction toward right–bottom area in the triangle phase, in other words toward high Ni concentration, is one of current research trend to realize high-mileage vehicles. $LiNi_{1/3}Mn_{1/3}Co_{1/3}O_2$ is relatively conventional but still being used in a lot of products such as power tools, EV, and HEV. $LiNi_{0.5}Mn_{0.3}Co_{0.2}O_2$ would be one of the main positive electrode materials of LIBs for EV application in a coming few years. $LiNi_{0.4}Mn_{0.2}Co_{0.2}O_2$ will come to the EV market in 5 years after overcoming safety and cycle life issues.

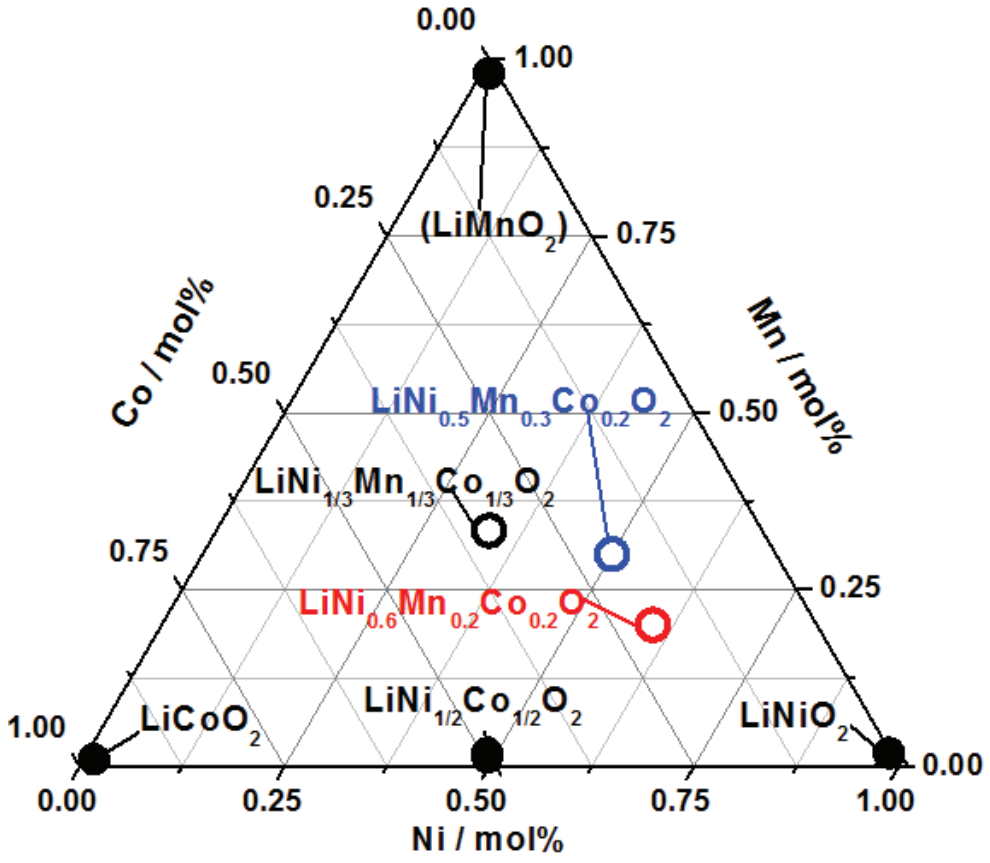

Fig. 1-6. A triangle phase of the ternary system of $LiCoO_2$-$LiNiO_2$-$LiMnO_2$.

In general, there are 2 important parameters, specific capacity and operating potential for positive electrode materials to achieve advanced performance of LIBs. The comparison of potential vs. capacity between several positive electrodes materials reported so far is summarized in Fig. 1-7.[46] While right-top area is ideal to achieve both higher potential and larger capacity for the energy performance, left-top area will be useful for power application and right-bottom area will be useful for long-lasting product in the triangle phase. In addition to these 2 main parameters, material cost, volumetric, gravimetric, and pressed density, safety, and compatibility with other cell components, especially electrolyte are necessary to be considered for design of positive electrode materials. As discussed in Section 1-1, advanced LIBs will be used in a variety of application field and thus, studying a variety of materials having different feature is very important to grab a chance of future application.

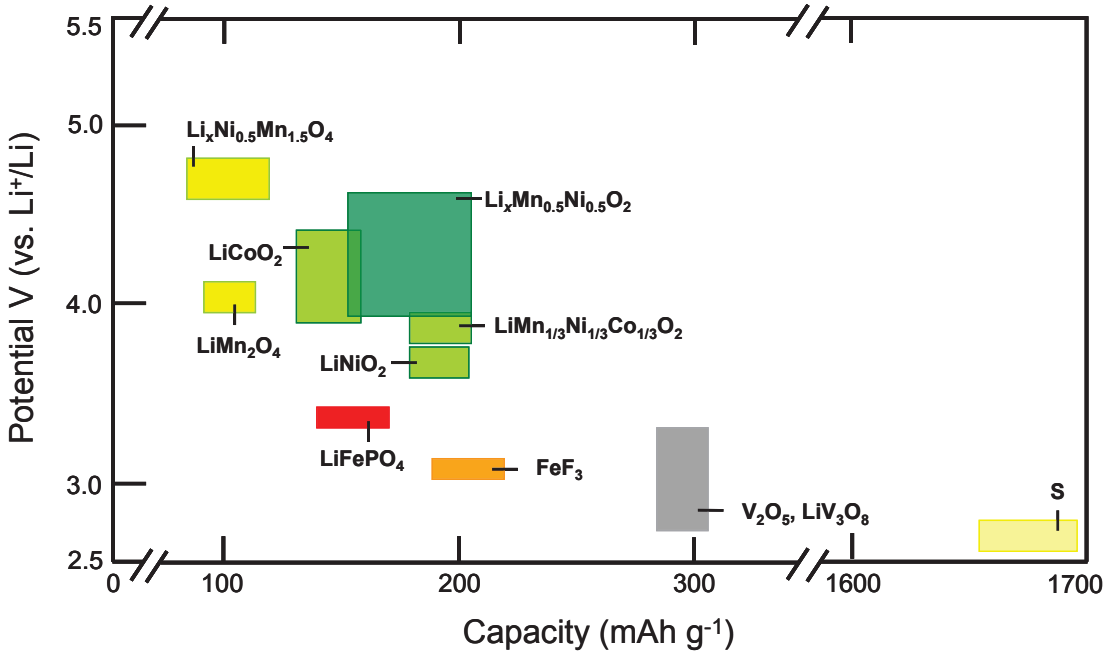

Fig. 1-7. Potential versus capacity of several positive electrode materials that have been reported and studied actively.[46]

1.2.2 Positive electrode materials for NIBs

In addition to a great potential of NIBs for practical application as introduced in Section 1.1.2, there are 2 obvious importance to study on positive electrode materials for NIBs, 1) because of the similarity of electrode materials and their working mechanism to LIB system, the knowledge accumulation of NIB technologies are also useful for further improvement of positive electrodes for LIBs, 2) since studies on electrode materials for LIBs have been attracted much attention since 1980s and those for NIBs have just launched, there are so many rooms remained un-studied and thus, it's a great chance to have new findings in the structural and physical field as well as electrochemistry.

To describe positive electrode materials for NIBs, it may be best to start from layered sodium cobaltite, $NaCoO_2$. O3-$NaCoO_2$ has the same crystal structure as O3-$LiCoO_2$ and is known as the Na insertion host since 1981.[47] In Fig.1-8, comparison of initial charge/discharge curves of Li//$LiCoO_2$ and Na//$NaCoO_2$ cells are shown.[31] At the charged state >100 mAh g^{-1} for both cells, the difference in voltage is about 0.4 V, which is quite similar to the difference in the standard electrochemical potential for Li (3.04 V) and Na (2.71 V). In all other region, however, the operating voltage of $LiCoO_2$ is higher than that of $NaCoO_2$ more than 1.0 V. As a result, the available energy density is much lower for the Na system when the same chemistry (redox species and host crystal structures) with the Li system is used as the comparison between $LiCoO_2$ and $NaCoO_2$. This fact also implies the different mechanism from the Li system and thus studying materials for positive electrodes of NIBs are important to find a new strategy to maximize their electrode performance.

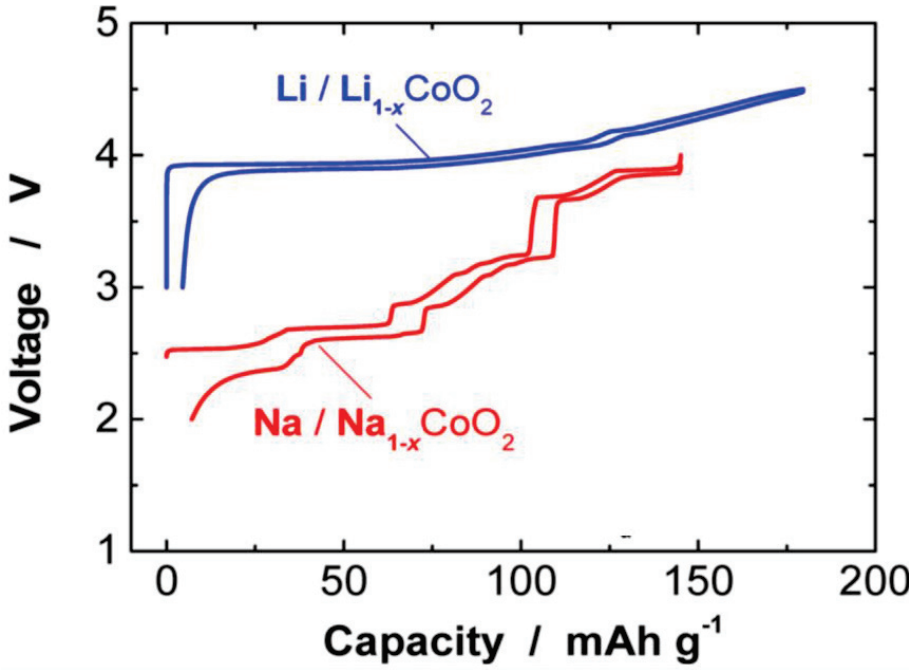

Fig. 1-8. Comparison of initial charge/discharge curves of Li//$LiCoO_2$ and Na//$NaCoO_2$ cells.[31]

In view of crystal structure, layered sodium transition metal oxides are interesting because of its rich structural diversity in the as-prepared state and structural changes during Na extraction. In particular, the existence of P-type layered structure, in which the sodium ions are accommodated at prismatic sites, is the significant difference from layered lithium transition metal oxides whose Li ions are in principle accommodated at octahedral sites. Classification of Na−Me−O layered materials is shown in Fig. 1-9.[31] In addition to O3-type structure which is explained in the last section for LiMO_2, P2-type structure is stabilized basically at a sodium off-stoichiometry condition such as $0.6 < x < 0.7$ of Na_xMO_2 because Na^+ ions have larger ionic radius (1.02 Å) than Li^+ ions (0.76 Å). While O3 and P2 type structure is common at the as-prepared state, P3-type and O2-type layered structure typically appears during electrochemical Na extraction/insertion. P3-

type structure is formed by the gliding of MeO_2 stabs without breaking Me-O bonds when Na^+ ions are partly extracted from O3-strcuture.[36, 47] O2-type structure is also explained by the gliding of MeO_2 caused by Na extraction from prismatic sites of P2-type structure. P2-O2 phase transition often causes severe stacking fault due to 2 glide vector.[48]

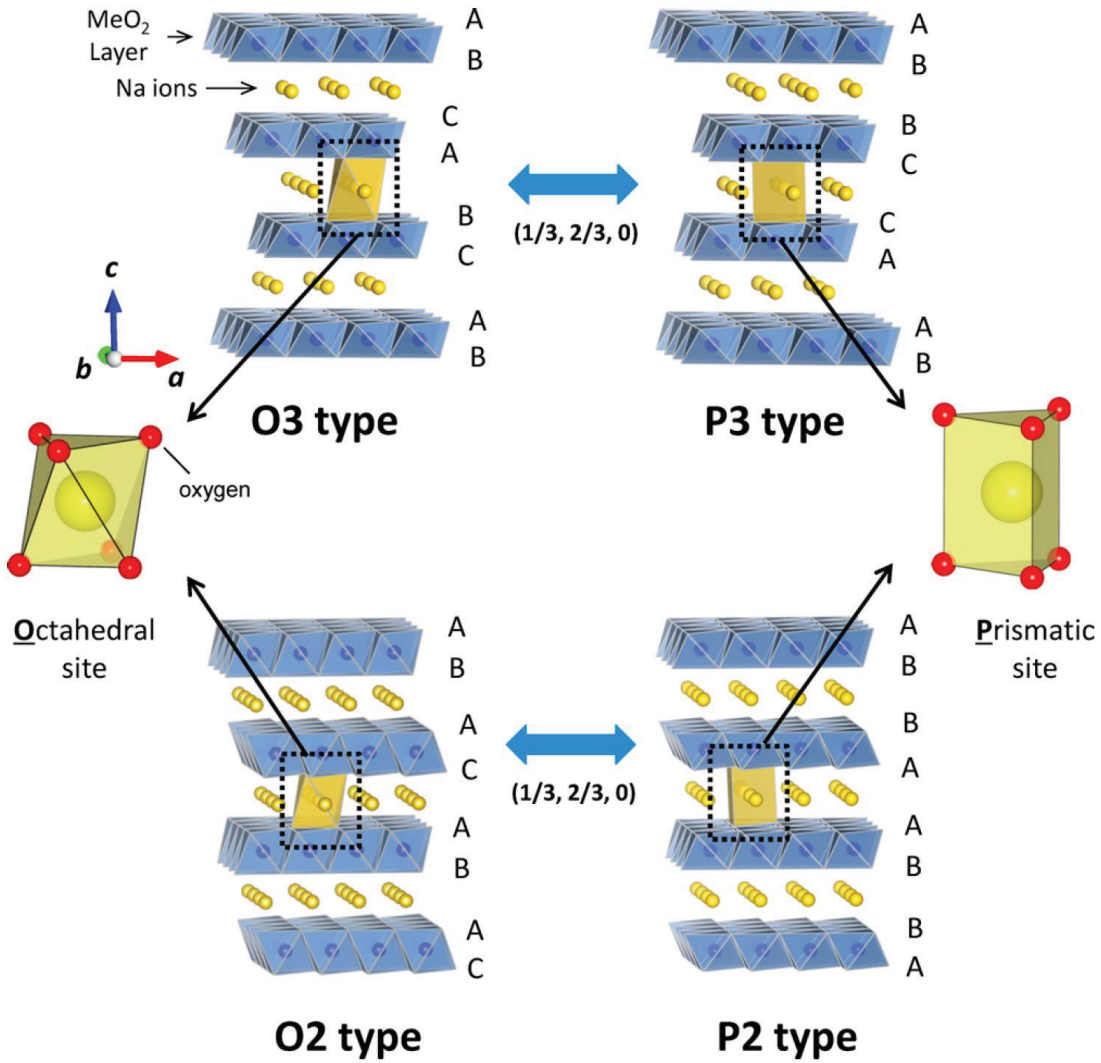

Fig. 1-9. Classification of Na−Me−O layered materials with sheets of edge-sharing MeO_6 octahedra and phase transition processes induced by sodium extraction.[31]

In 2012, our group reported that P2-type $Na_{2/3}Fe_{1/2}Mn_{1/2}O_2$ consists only on the cheap and earth-abundant metals and shows promising electrode performance, such as > 190 mAh g^{-1} of reversible capacity in the sodium cells. In addition to high reversible capacity, P2-type structure is expected to show high rate capability because Na^+ ions are diffused in a prismatic layer more easily than an octahedral layer.[31] Therefore, NIB cells may have a chance to be applied to large low-cost battery for EES and high rate application.

Manganese is attracting much attention due to potential use as low cost, low toxicity, safe, and high capacity positive electrodes in NIBs. Na-Mn-O system shows a variety of polymorphs such as tunnel-type and layeredtype structures highly depending on Na/Mn ratio and calcination temperature as shown the crystal structure and phase variations in Fig. 1-10. While O3-type layered $LiMnO_2$ can't be obtained by conventional solid-state reaction, O'3- (distorted O3) and P2-type layered structure is known since 1971.[49] O'3-$NaMnO_2$ shows reversible capacity of 185 mAh g^{-1} in the voltage range between 3.8 and 2.0 V[50] and also Caballero *et al.* reported 150 mAh g^{-1} of initial reversible capacity for P2-$Na_{2/3}MnO_2$.[51] However, both materials show insufficient cycle stability and further improvement is required. In addition to forming layer structure, Na-Mn-O system has an advantage that spinel structure is not stable[52] while spinel formation is one of the drawback of Mn containing layered lithium oxides.[53]

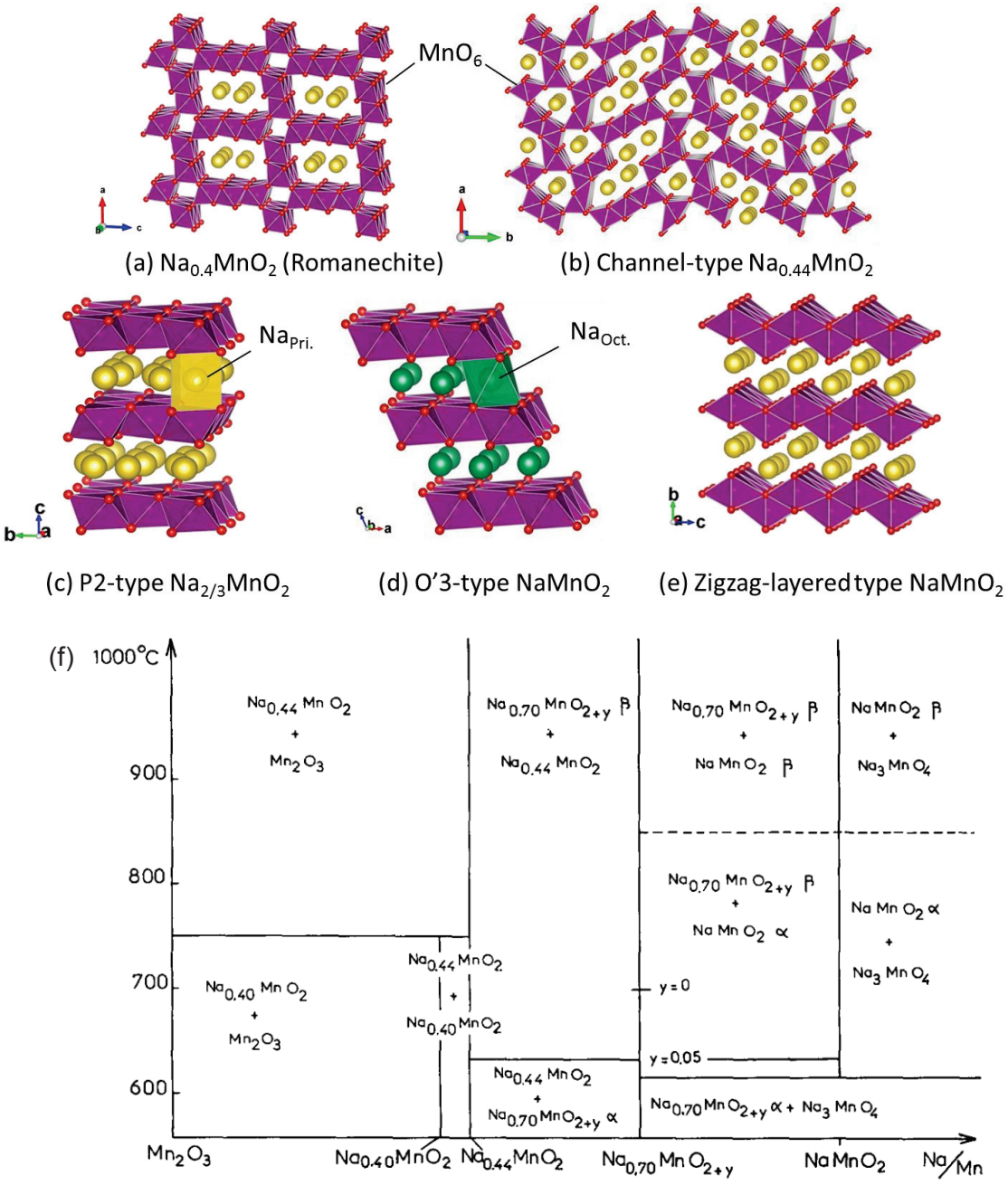

Fig. 1-10. A schematic illustration of crystal polymorphs in Na-Mn-O system (a)-(e) and structural phase of Na/Mn ratio vs. calcination temperature (f).[49]

1.3 Reaction mechanism of positive electrode materials

Understanding reaction mechanism of electrode materials is necessary for material design of advanced materials. It is one of the goal of this study to provide a new insight of reaction mechanism of electrode materials for further material development. In this section, to explain our strategy of finding advanced positive electrode materials, the reaction mechanism and electronic state of layered transition metal oxides will be briefly discussed and a new mechanism, which is recently suggested, will be introduced.

1.3.1 Reaction mechanism of conventional layered transition oxides

Basic description of the working mechanism of LIBs is shown in Fig. 1-11.[54, 55] The open-circuit voltage of a cell, V_{oc}, is basically determined by the electrochemical potential of anode and cathode, μ_A and μ_C, respectively. However, the operating voltage is limited by the top of the anion-*p* bands of the cathode or the voltage window of electrolyte, namely energy gap (E_g) between HOMO and LUMO of the electrolyte.[54, 55] A μ_A above the electrolyte LUMO / a μ_C located below the HOMO reduces / oxidizes the electrolyte unless the anode- / cathode- electrolyte reaction becomes blocked by the formation of a passivating SEI layer. A basic principle of operating voltage in LIBs is based on the most basic feature of materials, electronic structure.

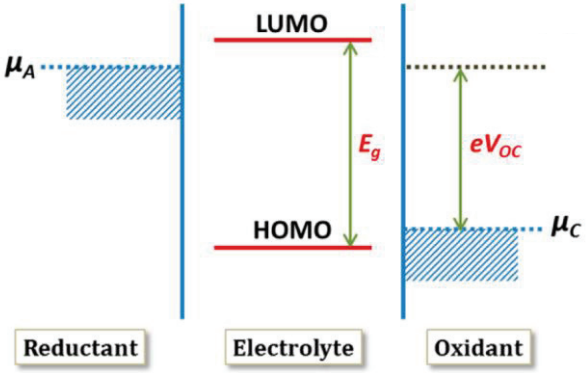

Fig. 1-11. Relative energies of the electrolyte window Eg and the electrode electrochemical potentials μ_A and μ_C.[54]

The energy of a given μ_A and μ_C basically correspond to the Fermi energy in an itinerant-electron band for carbon, or the energy of a redox couple of a transition-metals. The initial discharge curve and the band structure of electrode materials are shown in in Fig. 1-12.[55] The energy level of a redox couple depends not only on the formal valence state of the cation, but also on the covalent component of its nearest-neighbor bonding, which is influenced by the placement and character of any counter cations and by the Madelung energy of the ionic component of the bonding, which is influenced by the structure. In addition, the position of a redox couple relative to the bottom of a broad conduction band or to the top of an anion-*p* band may determine the intrinsic voltage limit versus Li^+/Li^0 of a given electrode. The upper voltage limits in the sulfides are much lower than those in the oxides. The top of the sulfide S-3*p* bands of the layered sulfides, $LiMS_2$ is ~2.5 eV below the μ_A of a Li anode, $\mu_A(Li^+/Li^0)$, whereas the top of the O-2*p* bands of the layered oxides, $LiMO_2$ is ~4.0 eV below $\mu_A(Li^+/Li^0)$, which is why oxides are used as positive electrodes in current LIBs.[55] Energy gap between Li and Fermi level of transition metals reflects the operating voltage of LIB half cells.

Empirically, operating voltage of transition metal oxides can be roughly estimated by the number of d electrons. Fig. 1-13 shows approximate operating voltages of transition metal (di)oxides in non-aqueous cells.[56] It is reasonable to assume the trend of operating voltage is 3*d*- > 4*d*- > 5*d*-transition metal oxides. Comparison among 3*d*-transition metal oxides suggests that the operating voltage is proportional to orbital binding energy between 2*s* orbital of lithium and 3*d* orbitals of transition metals, which is discussed in Fig. 1-12. Note that this is the ideal case and too simple to depict actual situation. Many other factors, microscopic factors such as electronic conductivity, Jahn-

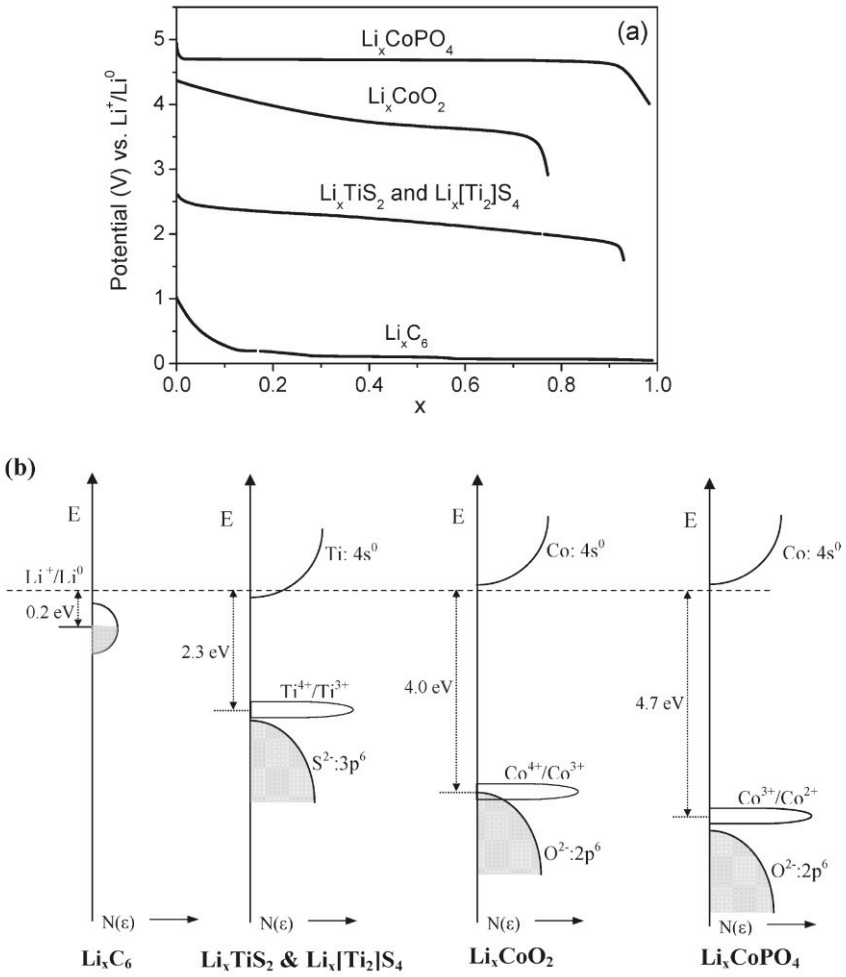

Fig. 1-12. (a) Voltage profiles of the discharge curves of Li_xC_6, Li_xTiS_2 and $Li_xTi_2S_4$, Li_xCoO_2, and Li_xCoPO_4. (b) schematic drawing of their corresponding energy vs. density of states showing the relative positions of the Fermi energy in an itinerant electron band.[55]

Teller effect, one-phase vs. two-phase reaction, Li conduction path etc. and macroscopic factors such as crystallinity, morphology, interface resistance and so on are necessary to be considered.

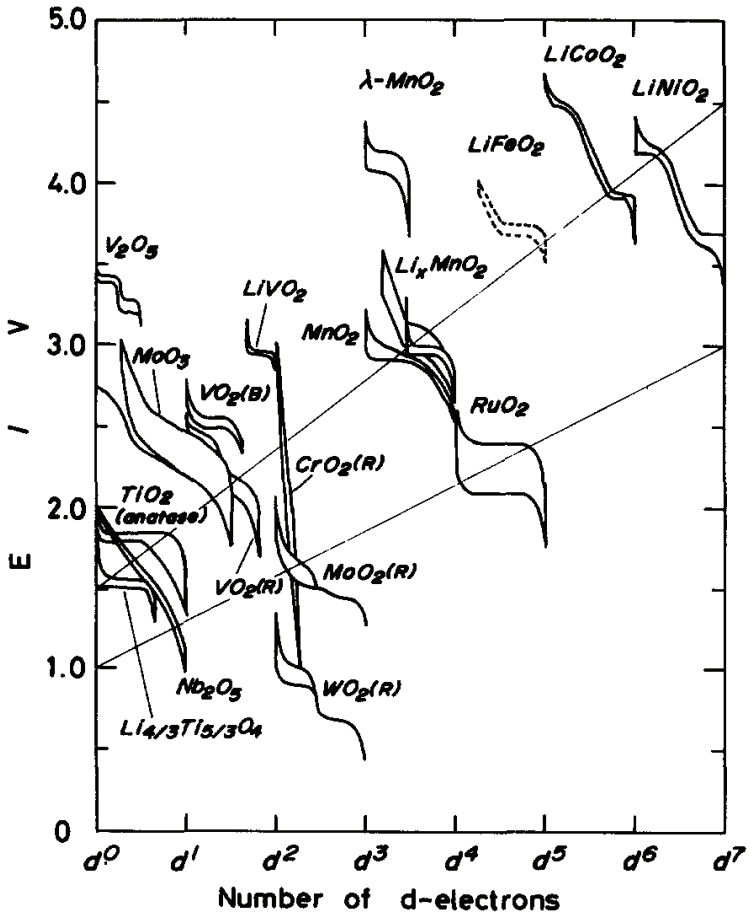

Fig. 1-13. The trend of operating voltages for transition metal (di)oxides in non-aqueous LIB cells.[56]

1.3.2 New working mechanism of redox reaction

In the last section, basic understanding of redox reaction of transition metals is shown. For material design of next generation battery materials, it is important to find new working mechanism as positive electrode materials. Here, a few recent findings of the reaction mechanism beyond redox couple of transition metals are introduced.

Lithium excess layered transition metals, $Li(Li_xM_{1-x})O_2$ (*M*: Transition metals), where excess Li^+ ions are accommodated at the sites of transition metals, are one of the promising candidates for next generation positive electrodes of LIBs because of

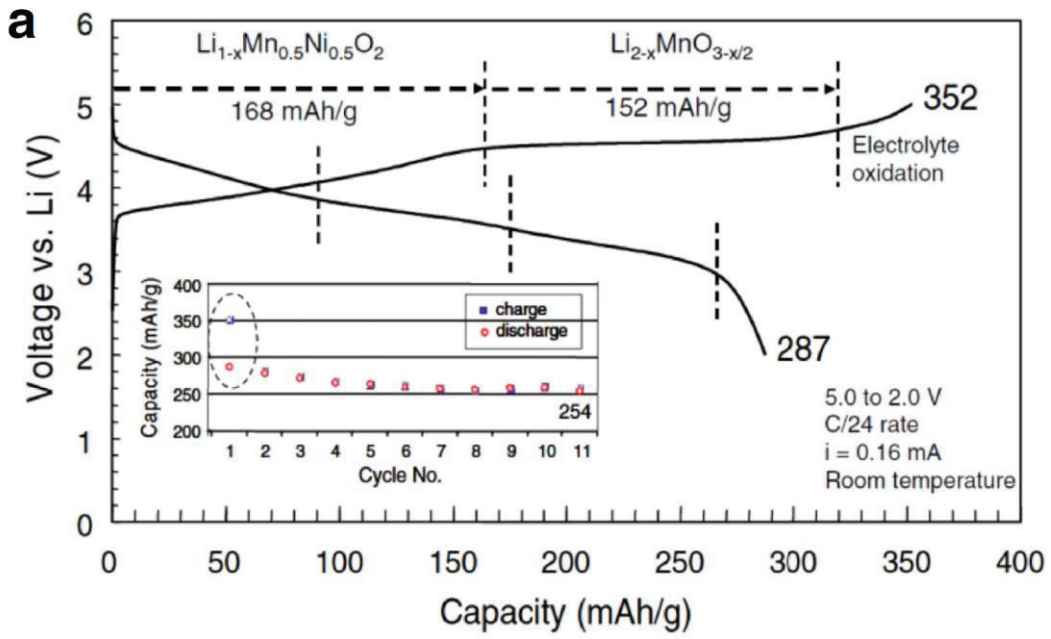

Fig. 1-14. Charge/discharge profiles of layered lithium excess materials, $0.3 \cdot Li_2MnO_3$ - $0.7 \cdot LiNi_{0.5}Mn_{0.5}O_2$.[57]

their high theoretical capacity. Many compounds of Li excess layered materials are designed as a basis of solid solution with $LiMO_2$ - Li_2MnO_3.[57] The end member, Li_2MnO_3, which can be described as $Li(Li_{1/3}Mn_{2/3})O_2$ by layered notation, has 2 kinds of layer, Li layer and ($Li_{1/3}Mn_{2/3}$) layer with honeycomb-type ordering of Li/Mn ions[58] and doesn't show reversible electrochemical activity since Mn(IV) is not able to be further oxidized and instead of oxidation of manganese, oxygen is released.[59] In contrast to Li_2MnO_3, a solid solution of $0.3 \cdot Li_2MnO_3$ - $0.7 \cdot LiNi_{0.5}Mn_{0.5}O_2$ delivers 287 mAh g^{-1} of reversible capacity as shown in Fig. 1-14.[57] While the microscopic mechanism is still under debate, the significantly large reversible capacity is thought to be derived from reversible redox reaction of oxide ions after the activation via oxygen release during initial charge.[60-62] Moreover, this participation of oxide ions into electrochemical reaction is reported in NIB system, such as P2-$Na_{2/3}$(Mg, Mn)O_2[63] and Na_2RuO_3.[64]

In addition, while disordered structure is thought to be not suitable for positive electrode materials because there is no Li^+ conduction path in the past, a percolation-type Li diffusion was recently suggested in the Li-excess system.[65, 66] This result illustrates disordered materials to be promising candidates for high capacity positive electrode materials. In fact, several disordered materials delivering high reversible capacity were recently reported such as $Li_{1.3}Nb_{0.3}Mn_{0.4}O_2$,[67] $Li_{1.2}Ti_{0.4}Mn_{0.4}O_2$[68] and $Li_{1.2}Ni_{1/3}Ti_{1/3}Mo_{2/15}O_2$.[69] This design concept toward high-energy density positive electrodes for disordered compounds is also related with redox reaction of oxide ions. Very recently, Ceder et al. suggested microscopic mechanism that Li excess composition is very important regardless of layered or disordered structure to activate redox reaction of oxide ions.[70] As shown in Fig. 1-15, when the Li-O-Li configuration exists in the structure, new electronic state of oxygen appears on the top of transition metal orbitals and thus, redox reaction of oxide ions is found reversibly. And the Li-O-Li configuration is possible for both Li-excess layered or disordered structure. To further understand and realize high energy density positive electrodes, Li-excess and layered/disordered compounds are of great interest.

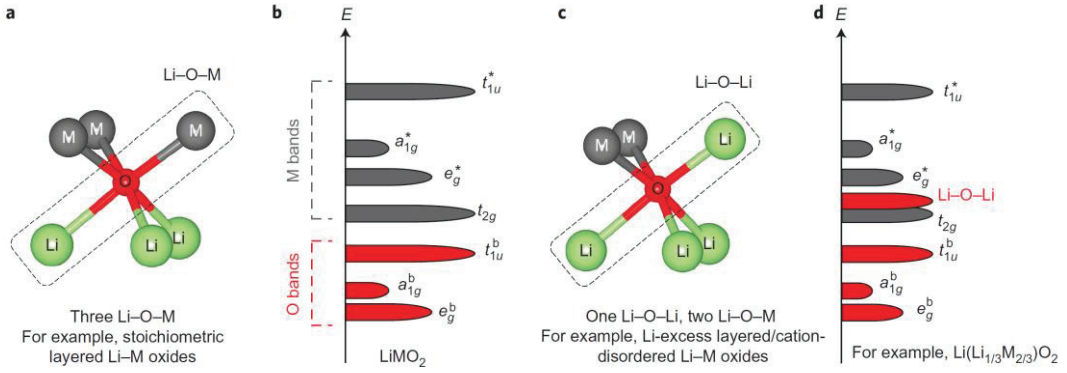

Fig. 1-15. Electronic state of materials with different configuration surrounding oxygen: (a), (b) Li stoichiometric layered and (c), (d) Li excess materials.[70]

1.4 Purpose

In this study, we focus on development of positive electrode materials for both Li- and Na-ion batteries. As already mentioned in this chapter, increasing demand and expanding application field of non-aqueous rechargeable batteries continuously require new battery materials. To meet this rapid increase of demand, as well as finding new and novel materials, understanding reaction mechanism is of great importance for future strategy of material design.

In Chapter 3, 4, 5, and 6, synthesis of new materials, investigation on their electrochemical properties and reaction mechanism will be shown, respectively. In Li system, the positive electrode materials were designed for high capacity and high power materials by using Li-rich molybdate and tungstate in Chapter 3 and 4, respectively. As the closest example to practical application, full cell evaluation of large LIB cells is further conducted at Umicore as the collaborative research with TUS and successfully proves improved power performance of conventional cell system. In Na system, we focused on manganese based oxides because of its potential to have cheap, safe and high capacity feature as described in Chapter 5 and 6. Moreover, we have discussed an influence on reaction mechanism for a percolation-type Li diffusion in disordered rock-salt structure, participation of oxide ions into redox reaction, Mn defect, and cooperative Jahn-Teller distortion.

References

1. B. Dunn, H. Kamath and J. M. Tarascon, *Science*, 2011, **334**, 928-935.
2. J. R. Dahn, T. Zheng, Y. H. Liu and J. S. Xue, *Science*, 1995, **270**, 590-593.
3. J. O. Besenhard, M. Winter, J. Yang and W. Biberacher, *J. Power Sources*, 1995, **54**, 228-231.
4. K. Fukuda, K. Kikuya, K. Isono and M. Yoshio, *J. Power Sources*, 1997, **69**, 165-168.
5. T. Abe, H. Fukuda, Y. Iriyama and Z. Ogumi, *J. Electrochem. Soc.*, 2004, **151**, A1120-A1123.
6. Y. X. Wang, S. Nakamura, K. Tasaki and P. B. Balbuena, *J. Am. Chem. Soc.*, 2002, **124**, 4408-4421.
7. O. Matsuoka, A. Hiwara, T. Omi, M. Toriida, T. Hayashi, C. Tanaka, Y. Saito, T. Ishida, H. Tan, S. S. Ono and S. Yamamoto, *J. Power Sources*, 2002, **108**, 128-138.
8. D. Aurbach, K. Gamolsky, B. Markovsky, Y. Gofer, M. Schmidt and U. Heider, *Electrochim. Acta*, 2002, **47**, 1423-1439.
9. G. H. Wrodnigg, J. O. Besenhard and M. Winter, *J. Electrochem. Soc.*, 1999, **146**, 470-472.
10. H. Ota, T. Sato, H. Suzuki and T. Usami, *J. Power Sources*, 2001, **97-8**, 107-113.
11. R. McMillan, H. Slegr, Z. X. Shu and W. D. Wang, *J. Power Sources*, 1999, **81**, 20-26.
12. S. Pejovnik, R. Dominko, M. Bele, M. Gaberscek and J. Jamnik, *J. Power Sources*, 2008, **184**, 593-597.

13. H. Buqa, M. Holzapfel, F. Krumeich, C. Veit and P. Novak, *J. Power Sources*, 2006, **161**, 617-622.

14. J. Li, R. B. Lewis and J. R. Dahn, *Electrochem. Solid State Lett.*, 2007, **10**, A17-A20.

15. L. B. Chen, X. H. Xie, J. Y. Xie, K. Wang and J. Yang, *Journal of Applied Electrochemistry*, 2006, **36**, 1099-1104.

16. B. Key, R. Bhattacharyya, M. Morcrette, V. Seznéc, J.-M. Tarascon and C. P. Grey, *Journal of the American Chemical Society*, 2009, **131**, 9239-9249.

17. D. Mazouzi, B. Lestriez, L. Roue and D. Guyomard, *Electrochemical and Solid-State Letters*, 2009, **12**, A215-A218.

18. J. Li, R. Klopsch, S. Nowak, M. Kunze, M. Winter and S. Passerini, *J. Power Sources*, 2011, **196**, 7687-7691.

19. S. Komaba, T. Ozeki and K. Okushi, *J. Power Sources*, 2009, **189**, 197-203.

20. S. Komaba, N. Yabuuchi, T. Ozeki, K. Okushi, H. Yui, K. Konno, Y. Katayama and T. Miura, *J. Power Sources*, 2010, **195**, 6069-6074.

21. H. C. Wu, E. Lee and N. L. Wu, *Electrochem. Commun.*, 2010, **12**, 488-491.

22. J. Mun, T. Yim, C. Y. Choi, J. H. Ryu, Y. G. Kim and S. M. Oh, *Electrochem. Solid State Lett.*, 2010, **13**, A109-A111.

23. K. L. Lee, J. Y. Jung, S. W. Lee, H. S. Moon and J. W. Park, *J. Power Sources*, 2004, **129**, 270-274.

24. S. S. Zhang, *J. Power Sources*, 2007, **164**, 351-364.

25. N. Kamaya, K. Homma, Y. Yamakawa, M. Hirayama, R. Kanno, M. Yonemura, T. Kamiyama, Y. Kato, S. Hama, K. Kawamoto and A. Mitsui, *Nat. Mater.*, 2011, **10**, 682.

26. Y. Wang, W. D. Richards, S. P. Ong, L. J. Miara, J. C. Kim, Y. Mo and G. Ceder, *Nat. Mater.*, 2015, **14**, 1026.

27. Y. Kato, S. Hori, T. Saito, K. Suzuki, M. Hirayama, A. Mitsui, M. Yonemura, H. Iba and R. Kanno, *Nat. Energy*, 2016, **1**, 16030.

28. Y. Yamada, K. Usui, K. Sodeyama, S. Ko, Y. Tateyama and A. Yamada, *Nat. Energy*, 2016, **1**, 16129.

29. S. Komaba, T. Hasegawa, M. Dahbi and K. Kubota, *Electrochem. Comm.*, 2016, **60**, 172-175.

30. C. Vaalma, G. A. Giffin, D. Buchholz and S. Passerini, *J. Electrochem. Soc*, 2016, **163**, A1295-A1299.

31. N. Yabuuchi, K. Kubota, M. Dahbi and S. Komaba, *Chemical Reviews*, 2014, **114**, 11636-11682.

32. M. S. Whittingham, *J. Electrochem. Soc*, 1976, **123**, 315.

33. M. S. Whittingham, *Science*, 1976, **192**, 1126.

34. M. S. Whittingham, *Chemical Reviews*, 2004, **104**, 4271-4302.

35. K. Mizushima, P. C. Jones, P. J. Wiseman and J. B. Goodenough, *Mater. Res. Bull*, 1980, **15**, 783-789.

36. C. Delmas, C. Fouassier and P. Hagenmuller, *Physica B*, 1980, **99**, 81-85.

37. T. Ohzuku, A. Ueda and M. Nagayama, *J. Electrochem. Soc.*, 1993, **140**, 1860-1870.

38. T. Ohzuku, A. Ueda, M. Nagayama, Y. Iwakoshi and H. Komori, *Electrochimica Acta*, 1993, **38**, 1159.

39. E. Rossen, C. D. W. Jones and J. R. Dahn, *Solid State Ionics*, 1992, **57**.

40. T. Ohzuku and Y. Makimura, *Chem. Lett.*, 2001, 744.

41. Y. Makimura and T. Ohzuku, *J. Power Sources*, 2003, **119-121**, 156-160.

42. N. Yabuuchi and T. Ohzuku, *J. Power Sources*, 2003, **119**, 171-174.

43. N. Yabuuchi, Y. Koyama, N. Nakayama and T. Ohzuku, *J. Electrochem. Soc.*, 2005, **152**, A1434-A1440.

44. N. Yabuuchi, Y. Makimura and T. Ohzuku, *J. Electrochem. Soc.*, 2007, **154**, A314-A321.

45. J. K. Ngala, N. A. Chernova, M. Ma, M. Mamak, P. Y. Zavalij and M. S. Whittingham, *J. Mater. Chem.*, 2004, **14**, 214.

46. J. B. Goodenough and Y. Kim, *Chem. Mat.*, 2010, **22**, 587-603.

47. C. Delmas, J. J. Braconnier, C. Foassier and P. Hagenmuller, *Solid State Ionics*, 1981, **3-4**, 165.

48. J. Paulsen and J. R. Dahn, *J. Electrochem. Soc*, 2000, **147**, 2478.

49. J.-P. Parant, R. Olazcuaga, M. Devalette, C. Fouassier and P. Hagenmuller, *J. Solid State Chem.*, 1971, **3**, 1-11.

50. X. Ma, H. Chen and G. Ceder, *J. Electrochem. Soc.*, 2011, **158**, A1307.

51. A. Caballero, L. Hernán, J. Morales, L. Sánchez, J. Santos Peña and M. A. G. Aranda, *J. Mater. Chem.*, 2002, **12**, 1142-1147.

52. N. Yabuuchi, M. Yano, S. Kuze and S. Komaba, *Electrochimica Acta*, 2012, **82**, 296-301.

53. A. R. Armstrong, N. Dupre, A. J. Paterson, C. P. Grey and P. G. Bruce, *Chem. Mater.*, 2004, **16**, 3106.

54. J. B. Goodenough and K.-S. Park, *J. Am. Chem. Soc.*, 2013, **135**, 1167.

55. J. B. Goodenough and Y. Kim, *Chem. Mater.*, 2010, **22**, 587-603.

56. T. Ohzuku and A. Ueda, *solid State Ionics*, 1994, **69**, 201.

57. J. Hong, H. Gwon, S.-K. Jung, K. Ku and K. Kang, *J. Electrochem. Soc*, 2015, **162**, A2447-A2467.

58. M. Jansen and R. Hoppe, *Z. Anorg. Allg. Chem.*, 1973, **397**, 279.

59. A. D. Robertson and P. G. Bruce, *Chem Commun (Camb)*, 2002, 2790-2791.

60. N. Yabuuchi, K. Yoshii, S. T. Myung, I. Nakai and S. Komaba, *J. Am. Chem. Soc.*, 2011, **133**, 4404-4419.

61. M. Oishi, C. Yogi, I. Watanabe, T. Ohta, Y. Orikasa, Y. Uchimoto and Z. Ogumi, *J. Power Sources*, 2015, **276**, 89-94.

62. M. Sathiya, A. M. Abakumov, D. Foix, G. Rousse, K. Ramesha, M. Saubanere, M. L. Doublet, H. Vezin, C. P. Laisa, A. S. Prakash, D. Gonbeau, G. VanTendeloo and J. M. Tarascon, *Nat. Mater.*, 2015, **14**, 230-238.

63. N. Yabuuchi, R. Hara, K. Kubota, J. Paulsen, S. Kumakura and S. Komaba, *J. Mater. Chem. A*, 2014, **2**, 16851.

64. B. Mortemard de Boisse, G. Liu, J. Ma, S. Nishimura, S. C. Chung, H. Kiuchi, Y. Harada, J. Kikkawa, Y. Kobayashi, M. Okubo and A. Yamada, *Nat. Commun.*, 2016, **7**, 11397.

65. J. Lee, A. Urban, X. Li, D. Su, G. Hautier and G. Ceder, *Science*, 2014, **343**, 519-522.

66. A. Urban, J. Lee and G. Ceder, *Adv. Energy Mater.*, 2014, **4**, 1400478.

67. N. Yabuuchi, M. Takeuchi, M. Nakayama, H. Shiiba, M. Ogawa, K. Nakayama, T. Ohta, D. Endo, T. Ozaki, T. Inamasu, K. Sato and S. Komaba, *Proc. Natl. Acad. Sci. U. S. A.*, 2015, **112**, 7650.

68. N. Yabuuchi, M. Nakayama, M. Takeuchi, S. Komaba, Y. Hashimoto, T. Mukai, H. Shiiba, K. Sato, Y. Kobayashi, A. Nakao, M. Yonemura, K. Yamanaka, K. Mitsuhara and T. Ohta, *Nat. Commun.*, 2016, **7**, 13814.

69. J. Lee, D.-H. Seo, M. Balasubramanian, N. Twu, X. Li and G. Ceder, *Energy Environ. Sci.*, 2015, **8**, 3255-3265.

70. D.-H. Seo, J. Lee, A. Urban, R. Malik, S. Y. Kang and G. Ceder, *Nat. Chem.*, 2016, **8**, 692.

Chapter 2. Experimental Method

This chapter exhibits the experimental method of material and electrochemical characterization. Preparation of the materials is described in the beginning of each chapter. A variety of materials and electrochemical characterization enable us to discuss the pristine state, the electrochemical activity and reaction mechanism of prepared materials.

2.1 Material characterization

2.1.1 X-ray diffraction

X-ray diffraction (XRD) measurement is one of the most powerful technique to characterize crystalline materials. Incident X-ray is elastically scattered by electrons of the atoms and then, the diffraction patterns are obtained for polycrystalline samples. XRD patterns contain direct information of crystalline phases. The lattice parameters of each sample (or each crystalline phase) can be simply calculated by whole pattern fitting by using TOPAS program.[1] In addition, Rietveld analysis provides further information of the crystalline phase, such as atomic position, site occupancy, the displacement parameter etc by using RIETAN-FP program.[2] The XRD measurement was carried out using a diffractometer equipped with X-ray tube of Cu target with Ni filter (Rigaku, Multiflex). Synchrotron XRD (SXRD) was also measured at the beam line BL02B2, SPring-8 in Japan, equipped with a large Debye–Scherrer camera. The wavelength of incident X-ray beam was set to 0.5 Å using a silicon monochromator which was calibrated with a CeO2 standard.

2.1.2 X-ray absorption spectroscopy

X-ray absorption spectroscopy (XAS) is being used to understand the electronic state and local structure of elements. Incident X-ray is absorbed at certain energy due to excitation of core electrons. X-ray absorption near-edge spectroscopy (XANES) provides the spectra such as K-edge spectrum from 1s orbital and L-edge from 2s or 2p orbitals. For the positive electrode materials, K-/L-edge spectra are known to be very useful to see the oxidation state of transition metals and local structural change during charge and discharge. Charge compensation by the nickel oxidation, resulting in the partial oxidation of divalent nickel ions to the trivalent state was found for $LiNi_{0.5}Mn_{0.5}O_2$. In this study, many samples are analyzed to discuss their reaction mechanism.[3] XAS spectra were collected at beam line BL-12C of Photon Factory in Japan. The spectra were analyzed using Athena software package.[4] Extended X-ray absorption fine-structure spectroscopy (EXAFS) is also useful technique providing local structure such as the bonding distance with the neighbors, however, will not be used in this thesis.

2.1.3 X-ray photoemission spectroscopy

X-ray photoelectron spectroscopy (XPS) is a quantitative spectroscopic technique that measures the element composition, empirical formula, chemical state and electronic state of the element. Contrary to XRD and XAS measurements which provide bulk information of the materials, XPS measurement is a surface-sensitive technique. XPS spectra are obtained by irradiating a material with a beam of X-rays while simultaneously measuring the kinetic energy number of electrons that escape from the top 1 to 10 nm of the material being analyzed. XPS requires ultra-high vacuum conditions.

XPS measurement is often applied to observe the surface and/or interface of active materials. In general, probing depth of the photoelectron increases by hard X-ray excitation; ~ 4 nm by soft X-ray and ~ 10 nm by hard X-ray.[5] X-ray photoelectron spectroscopy (XPS) measurements were carried out with VG ESCALAB 250 spectrometer (Thermo Fisher Scientific K.K.) using monochromatized Al Kα X-ray radiation (1486.6eV). The system was operated at 15 kV and 200 W. The base pressure of the analysis chamber was less than 10−8 Pa. The pass energy was 50.0 eV (wide scan) and 20 eV (individual narrow scan). These characterization were carried our using transfer vessel to avoid moisture /air exposure of the samples.

2.1.4 Scanning/transmission electron microscope

Scanning/transmission electron microscope (SEM/TEM) enable us to directly see the particle and the spatial resolution is nano-meter scale which is much higher than optical microscope. Particle size and morphology of positive electrode materials affect electrode performance a lot.

SEM (JEOL, JSM-7001F/SHL) is measured in the secondary/back scattering electron (SE/BSE) mode at an accelerating voltage of 15 kV. In addition, energy-dispersive spectroscopy (EDS) gives local distribution of the elements. TEM and electron diffraction (TEM, JEM-2100F, JEOL) observation were conducted with an accelerating voltage of 200 keV.

2.1.5 Physical properties

Electrical resistance was measured in direct current (d.c.) two-probe method with inducing high voltage using a resistivity meter (HIOKI, 3453) for insulating samples and

in d.c. four-probe method (Mitsubishi Chemical Analytech, MCP-PD51) for conductive samples. The measurements were carried out on pelletized powdery materials under the pressure of 63.7 MPa, and apparent conductivity of sample was calculated from resistance. Carbon amount contained in the synthesized samples was determined by combustion method (HORIBA, EMIA-920V2). Specific surface area of the samples was measured in Brunauer-Emmett-Teller (BET) method (Bel Japan, BELSORP-miniII). The magnetic susceptibilities were measured in 7T MPMS (Quantum Design).

2.2 Electrochemical characterization

2.2.1 Half cell evaluation

LIB

Electrochemical measurements were carried out at room temperature using R2032-type coin cells. The 80 wt% prepared sample as active material, 10 wt% AB as a conductive agent, and 10 wt% poly(vinylidene fluoride) (PVdF) as a binder were thoroughly mixed in N-methylpyrrolidone (NMP) liquid. Thus obtained slurry was pasted on Al foil with doctor blade and then dried at 80 °C under vacuum overnight prior to cell assembly. The coin cells were assembled in Ar-filled glove box. Lithium metal was used as a negative electrode and electrolyte used was 1.0 mol dm^{-3} $LiPF_4$ dissolved in a mixture of ethylene carbonate (EC) and dimethyl carbonate (DMC) (Kishida Chemical) at a volume ratio of 50:50. In order to observe electrochemical phase evolution and local structure change of the active materials, electrode samples after electrochemical reaction were prepared for *ex-situ* XRD and XAS measurement. All the prepared samples were sealed in

Ar atmosphere with home-made holders to avoid air exposure during measurements.

NIB

R2032-type coin cells were assembled to evaluate the electrode performance of $Na_{2/3}MnO_2$ in Na cell. For electrode preparation, 80 wt% prepared materials, 10 wt% acetylene black, and 10 wt% poly(vinylidene fluoride) binder were thoroughly mixed with N-methylpyrrolidone, and thus obtained black slurry was pasted on Al foil, and then dried at 80 oC in vacuum. Metallic sodium is used as a negative electrode. Electrolyte solution was 1.0 mol dm-3 NaPF6 dissolved in PC : EC : DEC = 1 : 1 : 3 (Kishida Chemical Co., Japan). A glass fiber filter (GB-100R, ADVANTEC Co.) was used as a separator.

Ex-situ and *operando* measurements for electrodes in half cells

Ex-situ electrode measurement was done by taking the electrodes out of the coin cells after charging or discharging to the selected voltage and the voltage was kept for 24 h in order to reach an equivalent state, and then washed with DMC and dried overnight to remove remaining electrolyte. Afterwards, the electrodes were used for XRD, XAS, and XPS measurement.

In contrast to *ex-situ* measurement, *operando* XRD measurement is a way to see the crystal structure directly during change or discharge. Charging/discharging the electrodes and measuring XRD patterns were conducted at the same time by using *operando* XRD cell with Be window (Rigaku, Japan) as shown the schematic illustration and the picture in Fig. 2-1. The electrodes were coated on a thin Al foil (10 um) and sealed in the *operando* cell. X-ray is capable to go through Be window and thin Al foil and reach the electrode materials.

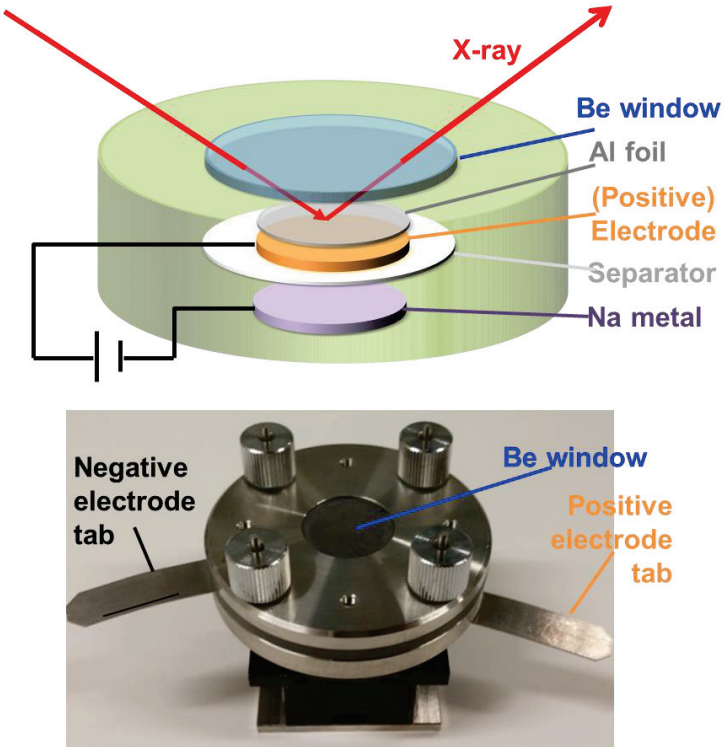

Fig. 2-1. Schematic illustration and the picture of *operando* XRD cell

2.2.2 Full cell evaluation

Full cell making

Full cells are prepared at Umicore Korea and/or Umicore Japan and the results of full cell evaluation are shared as a basis of the collaborative research. 650 mAh pouch-type cells are prepared by the following two steps: I. Slurry making and coating and II. Full cell assembly.

Slurry making and coating

A slurry is prepared by mixing 700g of a mass production $Li_{1.09}[Ni_{0.34}Mn_{0.33}Co_{0.33}]_{0.91}O_2$ (D50=7 um) powder (from Umicore Korea) with NMP, 47.19g of super P® (conductive carbon black of Timcal) and 393.26g of 10wt% PVDF based binder in NMP solution. The mixture is mixed for 2.5 hrs in a planetary mixer. During mixing additional NMP is added, as well as 1wt% of additives according to this

invention. The mixture is transferred to a Disper mixer and mixed for 1.5 hrs under further NMP addition. A typical total amount of NMP used is about 425g. The final solid content in the slurry is about 65wt%. The slurry is transferred to a coating line, where electrodes coated on both sides of the current collector are prepared. The electrode surface is smooth. The electrode loading is 9.6 mg/cm^2. The electrodes are compacted by a roll press to achieve an electrode density of about 3.2 g/cm^3. The electrodes are used to prepare pouch-type full cells as described hereafter.

Full cell assembly

For full cell testing purposes, the prepared positive electrode (cathode) is assembled with a negative electrode (anode) which is typically a graphite type carbon, and a porous electrically insulating membrane (as separator). The full cell is prepared by the following major steps:

a) Electrode slitting: after NMP coating the electrode active material might be slit by a slitting machine. The width and length of the electrode are determined according to the battery application;

b) Attaching the tabs: there are two kinds of tabs. Aluminum tabs are attached to the positive electrode (cathode), and copper tabs are attached to the negative electrode (anode);

c) Electrode drying: the prepared positive electrode (cathode) and negative electrode (anode) are dried at 85°C to 120°C for 8 hrs in a vacuum oven;

d) Jellyroll winding: after drying the electrode a jellyroll is made using a winding machine. A jellyroll consists of at least a negative electrode (anode) a porous electrically insulating membrane (separator) and a positive electrode (cathode);

e) Packaging: the prepared jellyroll is incorporated in a 650 mAh cell with an aluminum laminate film package, resulting in a pouch cell. Further, the non-aqueous electrolyte solution is impregnated for 8hrs at room temperature. The battery is pre-charged at 15% of its theoretical capacity and aged 1 day, also at room temperature. The battery is then degassed using a pressure of -760 mm Hg for 30 seconds, and the aluminum pouch is sealed.

f) Formation: The sealed battery is prepared for use as follows: the battery is charged using a current of 0.25C (with 1C = 650 mA) in CC/CV mode (constant current/constant voltage) up to 4.2V with the end condition of cut-off current of C/20. Then the battery is discharged in CC mode at 0.5C rate down to a cut-off voltage of 2.7V. Finally, the battery is charged for 40 mins under a C-rate of 0.5C in CC/CV mode. After the formation step, the full cell with a SOC (state of charge) of 50% is considered to be a “fresh cell” and ready for use.

The pictures of the positive electrodes and pouch cell are shown in Fig. 2-2.

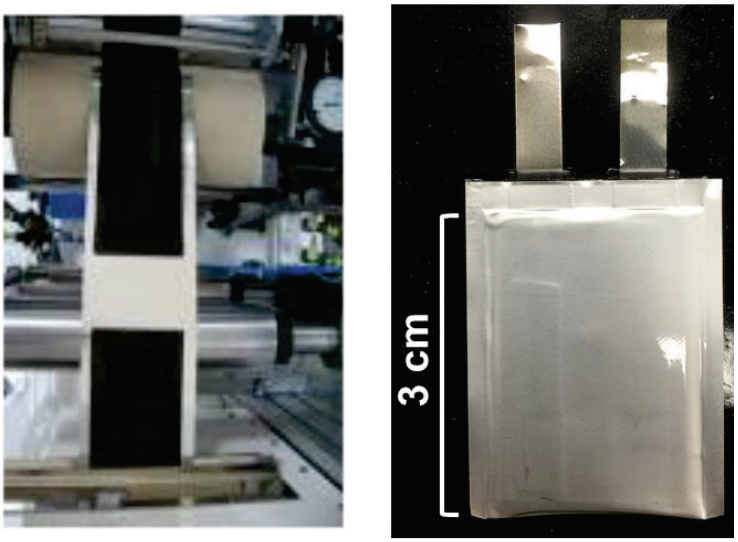

Fig. 2-2. The pictures of the positive electrodes (left) and the assembled pouch-type full cell (right)

Cycle life test

The lithium secondary full cell batteries are charged and discharged several times under the following conditions, both at 25ºC and 45ºC, to determine their charge-discharge cycle performance:

- Charge is performed in CC mode under 1C rate up to 4.2V, then CV mode until C/20 is reached,
- The cell is then set to rest for 10min,
- Discharge is done in CC mode at 1C rate down to 2.7V,
- The cell is then set to rest for 10min,
- The charge-discharge cycles proceed until the battery reaches 80% retained capacity. Every 100 cycles, the discharge is done at 0.2C rate in CC mode down to 2.7 V. The retained capacity at the nth cycle is calculated as the ratio of the discharge capacity obtained at cycle n to cycle 1.

DC resistance (DCR) test

The DC resistance is obtained from the voltage response to current pulses, so called HPPC test. (Hybrid Pulse Power Characterization) The procedure used is according to USABC standard (United States Advanced Battery Consortium LLC). The DC resistance is very relevant for practical application because data can be used to extrapolate fade rates into the future to prognoses battery live, moreover DC resistance is very sensitive to detect damage to the electrodes, because reaction products of the reaction between electrolyte and anode or cathode precipitate as low conductive surface layers. DCR growth is also monitored during cycle life and DCR at SOC 50% is measured at every 100 cycles.

References

1. B. A. T. V. G. P. a. S. Analysis, Software for Powder Diffraction Data. – User's Manual and K. Bruker AXS, Germany, 2008.
2. F. Izumi and K. Momma, *Solid State Phenom.*, 2007, **130**, 15-20.
3. Y. Makimura and T. Ohzuku, *J. Power Sources*, 2003, **119-121**, 156-160.
4. B. Ravel and M. Newville., *J. Synchrotron Rad.*, 2005, **12**, 537-541.
5. N. Yabuuchi, K. Shimomura, Y. Shimbe, T. Ozeki, J. Y. Son, H. Oji, Y. Katayama, T. Miura and S. Komaba, *Advanced Energy Materials*, 2011, **1**, 759-765.

Chapter 3. Lithium-Excess Layered Molybdenum Oxide and Its Carbon Composite

3.1 Introduction

As shortly explained in Section 1-3, Li-excess layered oxides, $Li_2M'O_3$ (*M'* = Ti, Mn, Zr, Mo, Ru, Sn, Ir, Pt *etc.*), have been extensively researched as positive materials for next generation Li-ion batteries due to large theoretical capacity by using excess Li in a metal layer.[1-6] Among them, the materials containing 4*d* transition metal(s), such as Mo and Ru, are expected to deliver high capacity because of multi-electron redox reaction based on their diverse oxidation states up to hexa-valent. Especially, Li_2MoO_3 has large theoretical capacity, achieving 339 mAh g^{-1} without oxygen release. However Li_2MoO_3 presents serious capacity degradation within a few cycles,[4, 7] and hence have been discouraged as a feasible materials for LIBs. Indeed, Li_2MoO_3 has not been actively studied so far, and the capacity degradation had been considered to be caused by the Mo migration in the lattice during 1st cycle, poor electronic conductivity, and/or dissolution of Mo(VI) species into electrolyte.[1, 4, 7, 8]

In 2014, Ceder's group reported a new layered material of solid solution between Li_2MoO_3 and $LiCrO_2$ for positive electrodes and provided a new insight on Mo as a redox center.[9] The Li_2MoO_3-$LiCrO_2$ solid solution achieves not only high reversible capacity but also no obvious capacity decay up to 10 cycles even after an irreversible phase transition from a layered into cation-disordered rock-salt type structure. They have proposed a percolation-type Li diffusion in the disordered structure with the certain amount of excess Li and explained

mechanisms for the unique phenomenon in cycle performance.[10] This result evokes motivation that the irreversible phase transition of layered Li_2MoO_3 into disordered rock-salt type structure may not be direct cause for the poor electrochemical performance and suggests that other factors, such as electronic conductivity and dissolution of Mo(VI) ions (possibly, molybdate anions), lurk behind the severe capacity decay.

Compared to Li_2RuO_3 (~ 10^{-1} S cm^{-1}) and Li_2IrO_3 (~ 10^{-2} S cm^{-1}), Li_2MoO_3 shows lower electronic conductivity which is probably because of localized 4*d* electrons in Mo_3O_{13} clusters.[2, 11] Carbon modifications for the improvement on electron conduction inside electrode has been well developed in transition metal phosphates such as $LiFePO_4$ whose anionic units tend to be isolated from transition elements. The low electronic conductivity of $LiFePO_4$ (10^{-9}~10^{-10} S cm^{-1}) was able to be overcome by additional treatment including simple carbon coating[12] and reducing particle size.[13] As reported by Huang et al.,[14] addition of carbon gel from the first step of synthesis enables to obtain $LiFePO_4$/carbon composites and similar modifications were also reported with graphite, carbon black, and acetylene black.[15] When carbon fine particles are added and dispersed into the starting materials for synthesis, the carbon particles suppress crystal growth of $LiFePO_4$ and improve electronic conduction by existence of carbon coating on $LiFePO_4$ fine particles, providing small-particle size and high electronic conductivity at the same time. Consequently, the rate capability and cycle stability of the $LiFePO_4$/carbon composite have been dramatically improved. Additional benefit of carbon additive from synthesis steps is the effect to avoid over-oxidation state of transition metals during heat treatment in inert gas.

In earlier reports,[1, 4, 7, 8] Li_2MoO_3 is obtained by reducing Li_2MoO_4 in reductive atmosphere by introducing H_2 gas, so that, safety issue has remained. Since several Li-Mo-O phases are stable at different Li/Mo ratios with different oxidation state of molybdenum between +3 and +6,[16, 17] the addition of carbon source from the beginning of synthesis significantly affects resultant Li-Mo-O crystallization, and to the best of our knowledge, any simple synthesis techniques of Li_2MoO_3/C composite have not been reported so far. In addition, this method enables us to synthesize Li_2MoO_3 through a safe route with inert atmosphere free from hazardous hydrogen gas. Carbon addition synthesis would be therefore beneficial as a method to reduce safety risks and access the fundamental problem on low electronic conductivity laid on Li_2MoO_3 to improve the electrochemical property as a positive electrode material for the high-capacity LIBs.

In this study, we demonstrate the new and simple synthesis route of Li_2MoO_3/C composite under Ar atmosphere to increase the electronic conductivity, modify on particle morphology, and control Mo oxidation state of resultant Li_2MoO_3. The electrode performances including reversible capacity, rate performance, and cycle stability are compared between carbon-free Li_2MoO_3 and composite of Li_2MoO_3 with carbon, Li_2MoO_3/C. Furthermore, the mechanism of electrochemical reaction for the Li_2MoO_3/C electrode is discussed using *ex-situ* X-ray diffraction and absorption analyses.

3.2 Synthesis

Li_2MoO_3 composite with carbon was prepared by heating a mixture of Li_2CO_3 (Kanto Chemical), MoO_2 (Sigma-Aldrich), and acetylene black (AB, Strem Chemicals). In the mixture, a weight ratio of Li_2CO_3 and MoO_2 is fixed to be Li:Mo = 2:1 in atomic ratio, and the amount of AB as the carbon additive in the starting materials is calculated on the basis of resultant Li_2MoO_3:AB = 99:1 or 98:2 in weight as summarized in Fig. 3-1. The pelletized mixture was heated at 900 or 1000 °C and kept for 24 h in tube furnace with argon flow. The sample was taken out from the furnace after natural cooling process, and then immediately transferred into an argon-filled glove box to avoid contact with moisture in air.

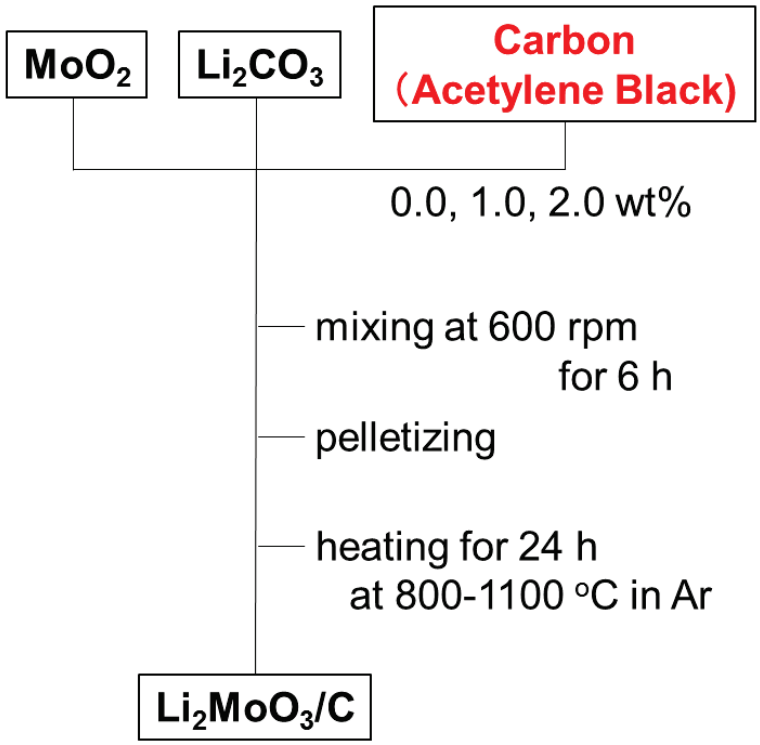

Fig. 3-1. Synthesis condition of Li_2MoO_3 / carbon composite

3.3 Structural and physical characterization

Fig. 3-2 shows XRD patterns for the samples obtained by heat treatment of the starting materials without carbon and with 1 and 2 wt% AB addition at 900 ^{o}C and with 1wt% AB addition at 1000 ^{o}C which are hereinafter denoted by 0-LMO, 1-LMO, 2-LMO, and 1-LMO-1000, respectively. Main diffraction lines in the four patterns can be indexed as Li_2MoO_3 whose crystal structure resembles that of α-$NaFeO_2$ phase with a space group, *R*-3*m*. In Fig. 3-2a for 0-LMO, unindexed diffractions located at $2\theta = 30$, 35.5, and 56° appear, which are probably related to formation of a Li deficient phase of $Li_{2-x}MoO_3$ with higher oxidation of Mo above +4.[18] In general, Mo(IV) tends to be oxidized even in inert gas probably due to trace oxygen contained in starting materials, resulting in the formation of the deficient phase. Indeed, the conventional synthesis for Li_2MoO_3 requires heating in reductive atmosphere to mitigate the increase in valence of molybdenum higher than +4. By heating the starting materials with AB additive, the unindexed diffraction peaks in the 0-LMO pattern disappear, and simultaneously, additional peaks assigned to $LiMo^{III}O_2$ and Mo_2C phases are observed in the case of 1-LMO and 2-LMO. By further raising the synthesis temperature from 900 to 1000 ^{o}C, a single phase of Li_2MoO_3 was obtained without any apparent crystalline impurities as shown in Fig. 3-2d for the XRD pattern of 1-LMO-1000.

From these results, carbon addition can avoid overoxidation of molybdenum above +4 and suppress the formation of impurity phase even without using the explosive gas of H_2. Although the small amounts of carbon additive leads to stabilizing the oxides of both Mo(III) and Mo(IV) and molybdenum carbide at

900 °C, the formation of additional impurity phases was successfully avoided by heat-treatment at 1000 °C.

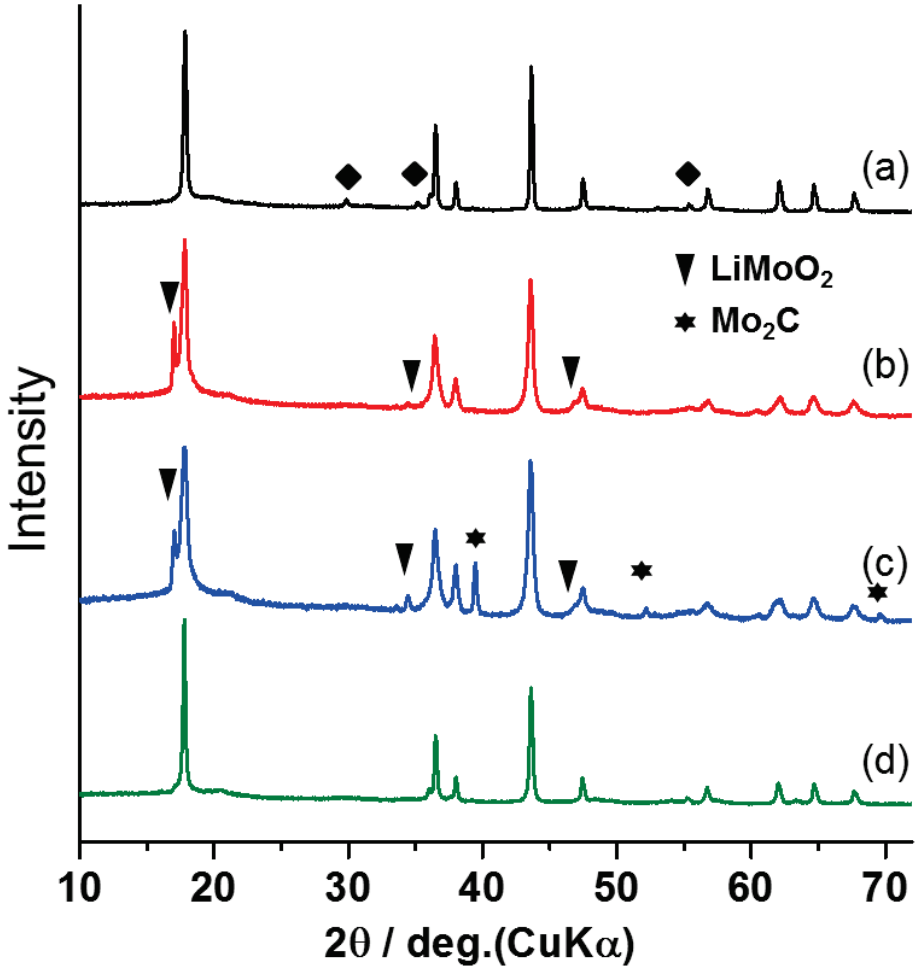

Fig. 3-2. XRD patterns of the synthesized samples; (a) 0-LMO, (b) 1-LMO, (c) 2-LMO, and (d) 1-LMO-1000. The peaks at ♦ are not assigned but probably the Li deficient phase with oxidized Mo state.

In Table 3-1, lattice parameters and crystallite size of Li_2MoO_3 are estimated by computational fitting of whole XRD patterns, BET surface area, carbon content, and conductivity of pelletized samples are summarized and compared for all LMO samples. The obtained lattice parameters, a = 2.8813(3) Å

and c = 14.918(2) Å, for 0-LMO are well consistent with reported values, a = 2.884 Å and c = 14.834 Å, in the literature.[1] Since c-axis of Li_2MoO_3 is elongated by Li extraction,[19] larger lattice parameters of c for carbon composite samples suggest Li deficient state probably because of coexistence with $LiMoO_2$ and Mo_2C. In Fig. 3-2, moreover, diffraction peaks are gradually broadened by increasing the AB additive up to 2 wt%, implying gradual reduction of the crystallite size of Li_2MoO_3. We estimated the crystallite size by Scherrer's equation as shown in Table 3-1. Clearly, the crystallite size is decreased from 61.8 nm to 19.7 nm by carbon addition, which agrees with the increase in BET surface area from 1.28 to 2.03 m^2 g^{-1} in Table 3-1.

Table 3-1. The summary of structural and physical properties.

Sample	Lattice Parameter		Crystallite size (XRD) / nm	Surface area (BET) / m^2 g^{-1}	Remained carbon / wt%	Conductivity of pellet / S cm^{-1}
	a / Å	c / Å				
0-LMO	2.8813(3)	14.918(2)	61.8	1.28	Trace	$1.7x10^{-10}$
1-LMO	2.8812(6)	14.941(4)	34.5	1.65	0.21	$4.1x10^{-7}$
2-LMO	2.8819(3)	14.958(1)	19.7	2.03	0.47	$6.7x10^{-6}$
1-LMO-1000	2.8782(3)	14.946(2)	52.9	1.22	0.12	$7.2x10^{-8}$

In order to elucidate the effect of carbon addition on crystallization and composite condition, particle morphology of 0-LMO, 1-LMO, 2-LMO, and 1-LMO-1000 is examined by microscopy. SEM images of the obtained samples are shown in Fig. 3-3. In the SEM images, it is obvious that even a few percent of carbon strongly influences a morphology of Li_2MoO_3 particles, resulting in the

rougher surface compared to the carbon-free one. No significant change in the size of secondary particles was evidenced by the SEM observation at lower magnification (not shown here). In Table 3-1, the specific surface area linearly increases with increase of added carbon. The larger amount of AB added in the starting materials results in the increase in remaining carbon in the samples up to 0.47 wt%, which was confirmed by combustion method. The finding also implies that carbon remaining in the products modifies the particle surface which suppresses particle growth of Li_2MoO_3.

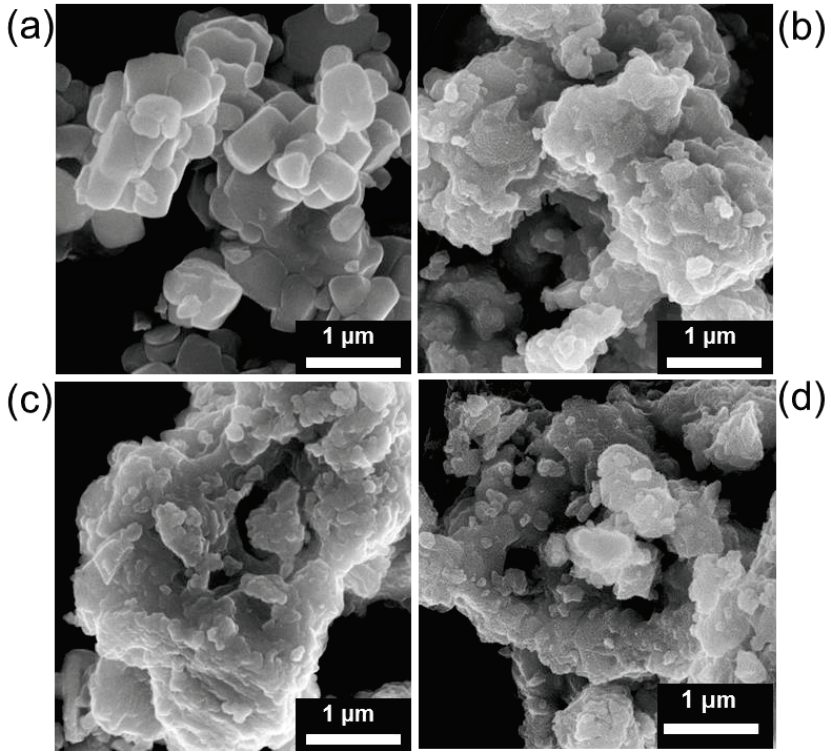

Fig. 3-3. SEM images of the synthesized samples; (a) 0-LMO, (b) 1-LMO, (c) 2-LMO, and (d) 1-LMO-1000.

Electronic conductivity of the pelletized samples without any additional carbon measured by d.c. resistivity meter is compared in Table 3-1. The carbon-

free material shows an apparent insulating feature of ca. 1 x 10^{-10} S cm^{-1}. Considering the fact that Li_2MoO_3 is a family of 4*d*-transition metal oxides, this value is very low and close to that of lithium iron phosphate.[20] According to previous reports showing neutron diffraction, HAADF-STEM and XAS data of Li_2MoO_3,[1, 7, 21, 22] the low conductive characteristic of Li_2MoO_3 originates from Mo_3O_{13} cluster stabilized by strong Mo-Mo bonds. Since 4*d* electrons of molybdenum are localizes in the Mo_3O_{13} cluster inside, random distribution of Mo_3O_{13} cluster over Li and Mo layer disconnects conduction path of electrons. By addition of only carbon 1 wt%, the small but definite amount of 0.21 wt% carbon remains in the Li-Mo-O product, as a result, electronic conductivity is enhanced nearly 1000 times from 1.7 x 10^{-10} to 4.1 x 10^{-7} S cm^{-1}. From the XRD data, the remaining carbon is amorphous, and the nano-sized carbon particles should be highly dispersed on the surface and boundary of the Li-Mo-O particles, resulting in the formation of Li_2MoO_3/C composite. The SEM pictures of Fig. 3-3 also support the formation of such carbon composites for 1-LMO, 2-LMO and 1-LMO-1000. Addition of 2 wt% carbon further increases the conductivity 10-fold higher than that of 1-LMO in Table 3-1. Because the impurity of Mo_2C is highly conductive,[23] the conductivity of 2-LMO is likely increased by Mo_2C. The conductivity of the Li-Mo-oxide and carbon composites is thought to be sufficient to be applied as a positive electrode in non-aqueous Li cell. Accordingly, the Li-Mo-O/carbon composites are synthesized by the heat treatment in Ar atmosphere providing enhanced electronic conductivity and suppression of primary particle growth. Their electrochemical performance is, therefore, examined in Li cells.

3.4 Electrochemical investigation

Fig. 3-4 shows the galvanostatic charge and discharge curves of 0-LMO, 1-LMO, 2-LMO and 1-LMO-1000 in a voltage range of 1.5 – 4.3 V at a current rate of 16 mA g^{-1} corresponding to C/20 rate (a 1C rate is defined as 320 mA g^{-1}). All samples show high electrochemical activity of 100 – 300 mAh g^{-1} in the working voltage between 3.5 and 1.8 V vs. Li. The all electrodes also show ca. 10 % irreversible loss by comparing the initial charge and discharge capacities. In following cycles, highly reversible charge and discharge reaction are exhibited. The reversibility and capacity depend on the synthesis conditions of LMO. Kobayashi et al. also reported the influence of synthesis condition of Li_2MoO_3 on electrochemical properties and comparable initial reversible capacities between 150 and 200 mAh g^{-1}.[4]

As shown in Fig. 3-4, the 0-LMO electrode delivers initial discharge capacity of only 100 mAh g^{-1}, which is probably caused by poor electronic conductivity of Li_2MoO_3. In case of the carbon composite samples of 1-LMO, 2-LMO, and 1-LMO-1000, their initial discharge capacities reach to > 225 mAh g^{-1} corresponding to Li extraction by more than 1.3 mole Li from Li_2MoO_3. The nano-sized and well dispersed carbon particles in the composite is significantly efficient to improve the discharge capacity. Note that $LiMoO_2$, which is detected by XRD in composite samples, is known to show reversible capacity of about 200 mAh g^{-1} corresponding to (de)intercalation of 0.9 mole Li in $LiMoO_2$.[16, 24] In addition to the capacity increase, the capacity retention is greatly improved by carbon composition compared to the Li_2MoO_3 electrodes in previous reports.[4, 7] When the capacity retention during ten cycles is compared in Fig. 3-4, 1-LMO shows the

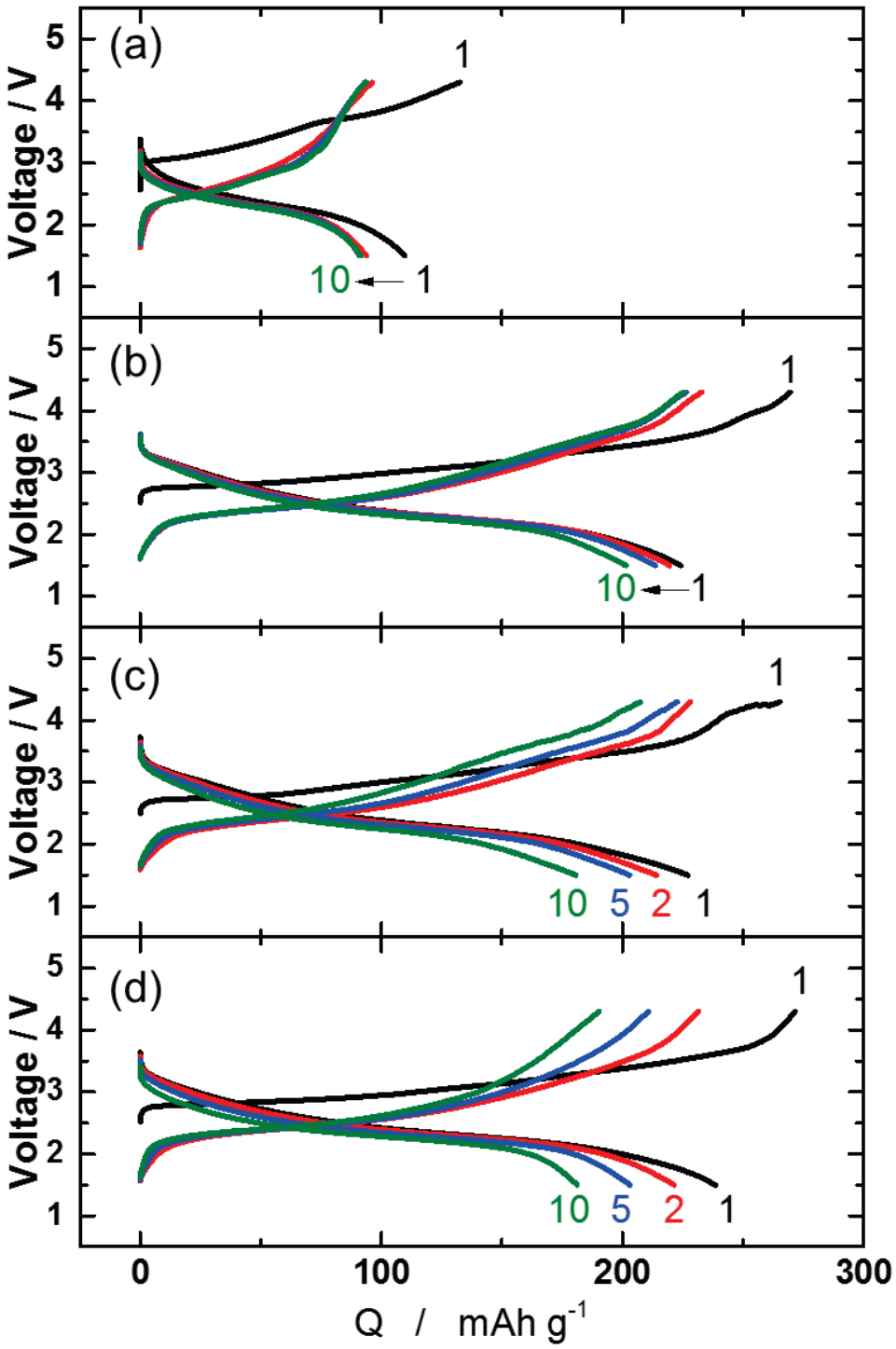

Fig. 3-4. Charge and discharge curves of Li_2MoO_3 electrodes in Li cells; (a) 0-LMO, (b) 1-LMO, (c) 2-LMO, and (d) 1-LMO-1000, in the voltage range of 1.5 – 4.3 V at a current rate of 16 mA g^{-1}.

higher capacity with no significant change of potential variation compared to 2-LMO and 1-LMO-1000. Fig. 3-5 shows the cycle stability plots over 35 cycles. 1-LMO and 1-LMO-1000 demonstrate better cycle performance compared to bare Li_2MoO_3 in the literatures.[4, 7] By increasing the amount of added carbon up to 2 wt%, reversible capacity fades faster during cycles probably due to the impurity phase of MoC_2.

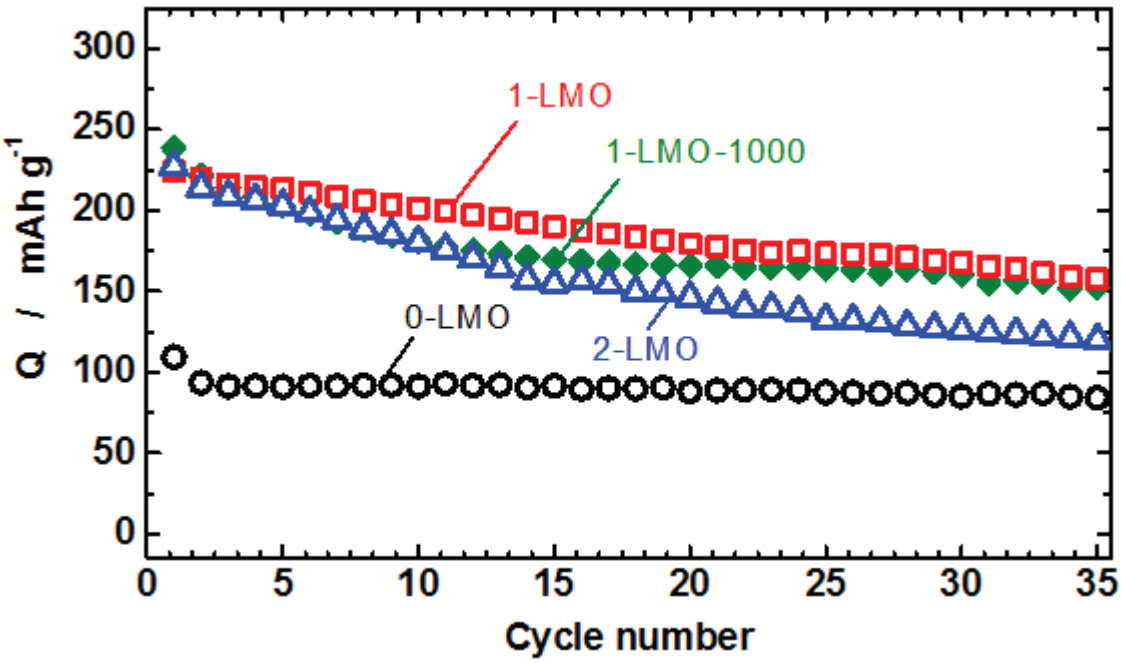

Fig. 3-5. Discharge capacity retention of lithium molybdenum oxide electrodes of 0-LMO, 1-LMO, 2-LMO, and 1-LMO-1000.

To understand difference of cycle stability between 0-LMO and 1-LMO, we have investigated the relationship between charge capacity and Mo dissolution. Pictures of Li metals as negative electrode materials before and after charge are shown in Fig. 3-6. Almost no Mo dissolution is detected at 4.3 V (130 mAh g^{-1}) for 0-LMO and 3.0 V (100 mAh g^{-1}) for 1-LMO. On the other hand, obvious Mo

dissolution is detected at 4.3 V (270 mAh g^{-1}) as many black spots implying accumulation of molybdenum-containing compounds on the surface. Mo dissolution is probably severe above 3.0 V corresponding to 105 mAh g^{-1} for 1-LMO. The anode side of a separator is also investigated to clarify the origin of the black spots by laser microscopy, SEM and EDX measurement as shown in Fig. 3-7. Color map of height gradient of the separator is obtained by laser microscopy and black spots on the separator surface correspond to thick area showing something accumulated on the surface.(Fig. 3-7c) Some surface deposits are also observed in the SEM image. Molybdenum is detected on the separator and relatively strong Mo signal is found from the deposits. Figs. 3-6 and 3-7 prove that Mo dissolution occurs during charge above 3.0 V and Mo containing deposits are accumulated on the separator and Li metal, which are seen as black spots.

These results imply Mo dissolution is related with structural transition caused by Li extraction which will be shown in the next section and further suppression of Mo dissolution is still needed. Figs. 3-4 and 3-5 prove that 1-LMO shows similar or slightly better capacity retention compared to 1-LMO-1000. The 1-LMO and 1-LMO-1000 samples, having the comparable conductivity (see Table 3-1), consist of Li_2MoO_3 with and without $LiMoO_2$, respectively (Fig. 3-1), implying that coexistence of $LiMoO_2$ may suppress forming molybdate anions and dissolution of Mo(VI) species and thus, improve the capacity retention for 1-LMO.

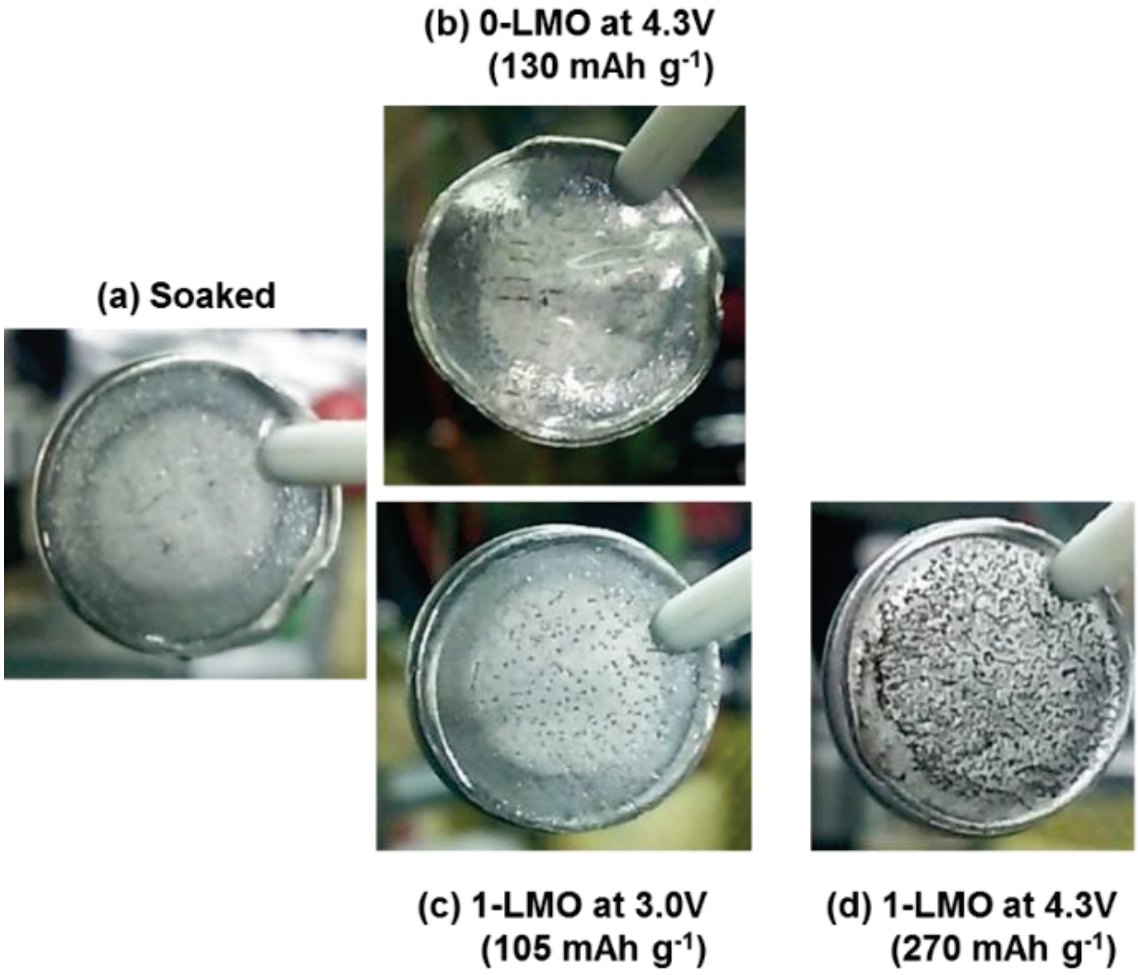

Fig. 3-6. Pictures of Li metals as negative electrode materials for (a) soaked in the electrolyte, (b) 0-LMO charged to 4.3 V (130 mAh g^{-1}), (c) 1-LMO charged to 3.0 V (105 mAh g^{-1}), and (d) 1-LMO charged to 4.3 V (270 mAh g^{-1}) during 1st charging process. (a), (b), and (c) show clean surface and no color change.

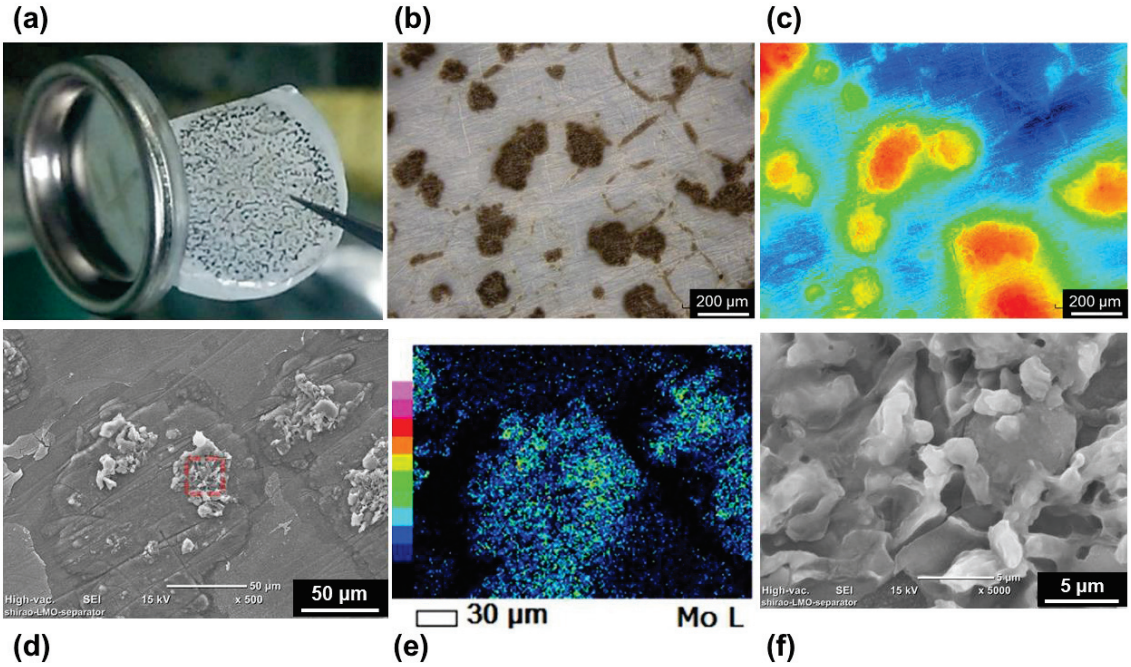

Fig. 3-7. (a) Picture of an anode side of a separator for 1-LMO charged to 4.3 V. Many black spots are observed as well as Li metal in Fig. 3-6. (b) Image of laser microscopy and (c) color map of height gradient of the separator. (d) SEM image and (e) EDX map of Mo L-edge of the separator. The separator is carefully washed by DMC and the anode side is used for the SEM measurement. (f) SEM image with large magnification for the deposits.

The rate performance of 0-LMO, 1-LMO and 2-LMO is presented in Fig. 3-8. Discharge capacity of 2-LMO is only 8 mAh g^{-1} at 2C while that of 0-LMO is 32 mAh g^{-1}. Contrary to increase in electronic conductivity, the carbon composite samples show severe capacity loss at high rate, especially higher than 1C rate. This is not consistent with previous reports on carbon coating for well-known cathode materials such as $LiFePO_4$,[12] $LiNi_{1/3}Mn_{1/3}Co_{1/3}O_2$,[25] and $LiMn_{1.5}Ni_{0.5}O_4$[26] where carbon coating is beneficial for high rate performance. The partially insufficient rate performance of the 1-LMO and 2-LMO can be explained by the Li diffusion in the disordered structure, which will be discussed in the next section based on the results of *ex-situ* XRD.

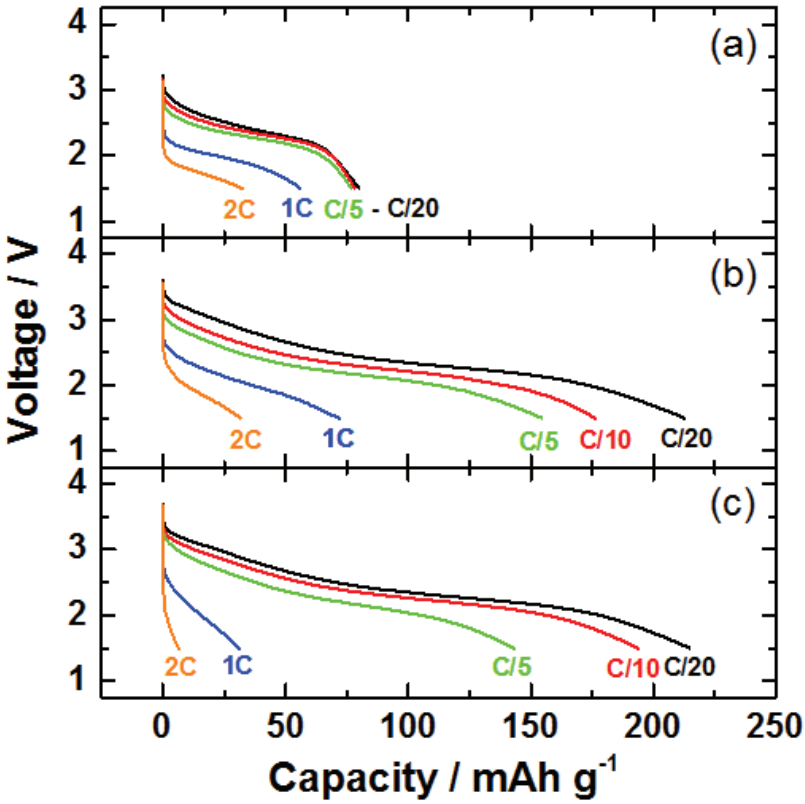

Fig. 3-8. Discharge-rate capability of (a) 0-LMO, (b) 1-LMO and (c) 2-LMO. The cells were charged to 4.3 V at C/20 and then discharged at a different rate (1C = 320 mA g^{-1}).

3.5 Reaction mechanism

The overall result of the electrochemical measurement convinced that the addition of only 1 wt% carbon has a significant impact on performance, resulting in about two time higher reversible capacity obtained in 1-LMO compared to 0-LMO. The reversible capacity of 0-LMO was much lower than that of the composite samples, and possible cause to be considered would be surface morphology which is broadly known to have strong influence to battery performance. XPS and TEM measurements were therefore conducted to compare the Mo oxidation state and surface morphology of 1-LMO and 0-LMO as shown in Fig. 3-9. In the XPS spectra, main peaks at 229.6 and 232.8 eV in 0-/1-LMO are assigned to Mo$3d_{5/2}$ and $3d_{3/2}$ peaks of Mo(IV), respectively. In case of 1-LMO, the peaks of $3d_{5/2}$ of Mo(III) are clearly observed around 228.7 eV, which is consistent with the existence of $LiMoO_2$ phase confirmed by the XRD pattern. In the XPS spectra of both 0-/1-LMO samples, oxidation state of molybdenum is confirmed to be +4 as Mo $3d_{3/2}$ and Mo $3d_{5/2}$ peaks at ca. 232.5 and 229.5 eV, respectively, which are attributed to Mo(IV) of $Li_2Mo^{IV}O_3$. Because the both photoelectron spectra of Mo 3d are almost identical except for a shoulder peak of Mo(III), the 0-LMO and 1-LMO samples have similar molybdenum oxide surface state, excluding $LiMoO_2$ phase. The lower capacity is not caused by different surface and interface condition, and it is probably due to the low electronic conductivity of 0-LMO. We can note that clear difference is recognized in TEM images of their surface morphology as shown in Fig. 3-9b and 9d. Because nano-sized particles are observed on large particles having non-uniform surface in Fig. 3-9d, the particle surface of 1-LMO should be covered with the nano-sized carbon,

while 0-LMO has smooth and uniform surface. This surface difference would influence the electrochemical performance and improving electronic conductivity by adding carbon is effective to obtain better electrochemical performance.

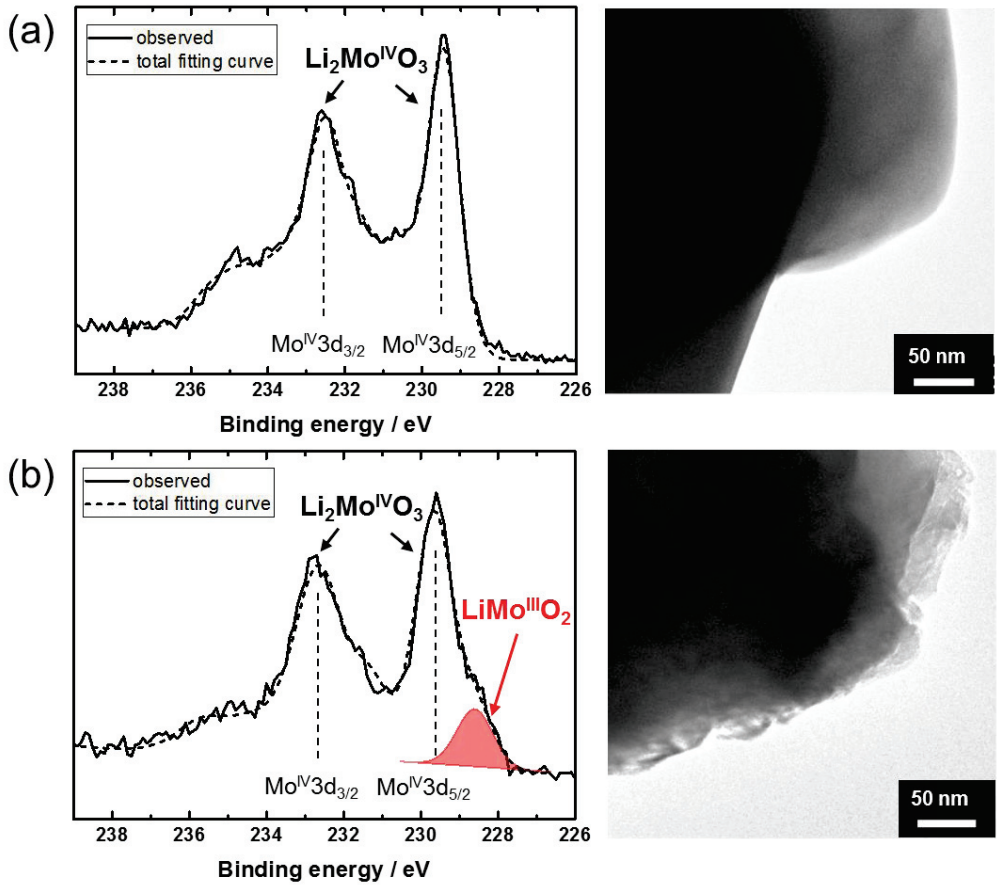

Fig. 3-9. Mo 3d XPS spectra (left) and TEM images (right) of the electrodes of (a) 0-LMO, (b) 1-LMO.

In order to clarify detailed phase evolution during lithiation and delithiation, *ex-situ* XRD measurements of electrodes at selected charged and discharged state were performed as shown in Fig. 3-10. In case of 1-LMO, the layered structure is observed in pristine and charged state at 3.0 V. By further nearly amorphous at 4.3 V because of the decrease and broadening of diffraction

lines in Fig. 3-10b. As reported in the previous literature,[8] fully amorphous feature of $Li_{2-x}MoO_3$ and severe molybdenum dissolution into electrolyte solution were observed by charge to 4.4 V at 60 °C. After discharge to 1.5 V, the 003 peak does not fully recover while the 104 peak returns to the original position, suggesting that the crystal structure after 1st cycle loses the original layered structure and transforms to a dominantly disordered cubic phase. On the other hand, the carbon-free 0-LMO sample keeps the layered structure after charge to 4.3 V and discharge to 1.5V. Generally speaking, many layered oxides such as $LiNi_{0.5}Mn_{0.5}O_2$[27], $LiNi_{0.42}Mn_{0.42}Co_{0.16}O_2$[28] and $x \cdot Li_2MnO_3$-$(1-x) \cdot LiMO_2$[29] present severe capacity loss and poor cycle stability, which is due to antisite disorder caused mainly by the lack of conduction path of Li^+ ions. Ceder's group reported that the cubic disordered rock-salt phase derived from a solid solution between Li_2MoO_3 and $LiCrO_2$ delivered more than 250 mA g^{-1} of reversible capacity.[9] To elucidate the electrochemical activity in the disordered rock-salt phase, they proposed a percolation-type Li diffusion system and pointed out importance of excess Li to make conduction path of Li^+ ions in the structure.[10] As seen in Fig. 3-5, 1-LMO shows relatively stable cycling in 1.5 - 4.3 V and is capable of extraction/insertion of more than 1.3 Li from/into $Li_{2-x}MoO_3$ even after transforming to the cubic disordered rock-salt phase, implying that percolation-type diffusion of Li ions would be possible in this system. Taking account of insufficient rate performance of 1-LMO in Fig. 3-8, the disordered rock-salt phase of Li_2MoO_3 may have higher energy barrier and/or slower kinetics of Li diffusion than those of 2-dimentional diffusion in 0-LMO. In addition, $LiMoO_2$ phase observed in the carbon composite

sample also participates in redox reaction because the peak position of 003 peak assigned to $LiMoO_2$ shifted toward low angle during charge and partly goes back to the original position on discharge, which probably affect electrochemical properties, especially improved cycle stability.

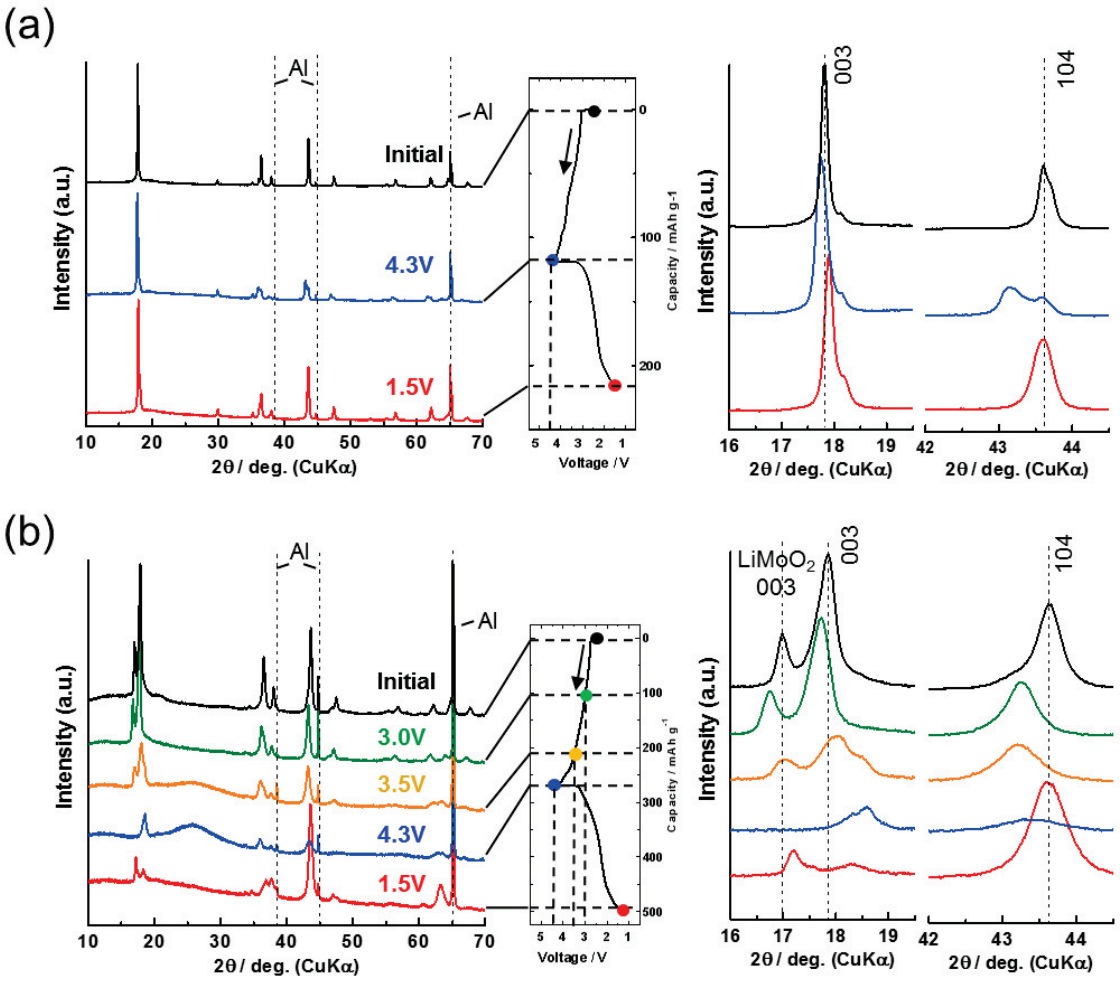

Fig. 3-10. *Ex-situ* XRD patterns of (a) 0-LMO and (b) 1-LMO electrodes during first charge-discharge cycle.

To understand change in electric state of Mo in $Li_{2-x}MoO_3$ accompanied by the structural change during charge/discharge, *ex-situ* XANES spectra at Mo K-edge of Li_2MoO_3/1 wt% C at different charge and discharge states are obtained as

shown in Fig. 3-11. Mo K-edge shifts to high energy by charging, reflecting oxidation of Mo(IV) as shown in Fig. 3-11a. A pre-edge peak at 19995 eV also appears by charge, which is assigned to an electric dipole transition from *s* to *p* orbital in the O 2*p*-Mo 4*d* hybridization state derived from the distortion of the MoO_6 octahedra.[7, 30] Finally, Mo K-edge of fully charged sample to 4.4 V is similar to that of MoO_3, showing that the molybdenum is oxidized from +4 to approximately +6 by Li extraction. On the other hand, Fig. 3-11b reveals that, after first cycle, the absorption of Mo K-edge shifts back to low energy but does not reach the energy of as-prepared sample, and pre-edge peak, which appeared during charge, is somewhat remained. The irreversible change in the energy of Mo K-edge, especially in observation of pre-edge peak, would result not only from irreversible capacity but also from irreversible structural change into the cubic

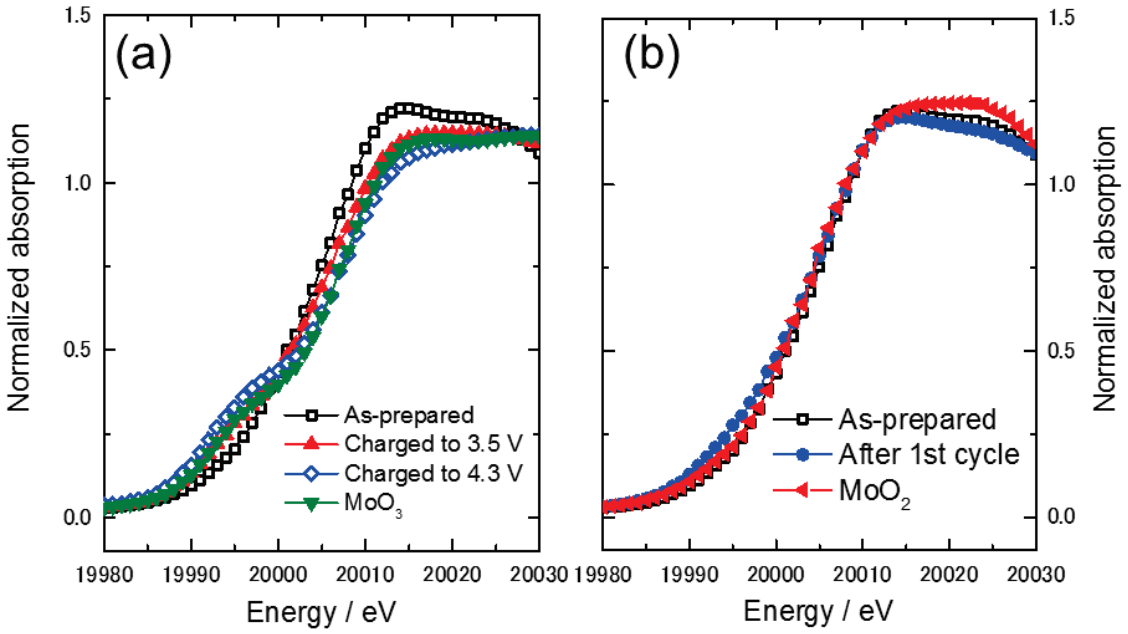

Fig. 3-11. XANES spectra at Mo K-edge for 1-LMO electrodes (a) during charge and MoO_2 and MoO_3 as a reference and (b) as-prepared and after 1st discharge from 4.3 to 1.5 V.

phase after 1st cycle. It is concluded that electrochemical reaction of 1-LMO is dominantly led by redox couple of Mo(IV/VI) with improved electron conduction and smaller particle size by the successful solid-state synthesis of Li-Mo-oxide/C composite by the carbon addition.

3.6 Conclusion

Li_2MoO_3/carbon composite is synthesized with different amount of carbon. Carbon addition in the starting chemicals is effective in avoiding the overoxidation of molybdenum and enhance electronic conductivity 1000 times. In the carbon composite, the surface of Li_2MoO_3 particles is modified with nano-sized carbon, leading to the suppression of crystal growth during the high temperature synthesis. Li_2MoO_3/1C composite delivers approximately 230 mAh g^{-1} of initial discharge capacity in a voltage range of 1.5 – 4.3 V. The structure of Li_2MoO_3 transforms from layered into disordered cubic structure after an initial cycle. The formation of disordered phase does not cause capacity degradation in the following cycles and the disordered phase shows 200 mAh g^{-1} of the retention capacity after 10 cycles while rate performance is sacrificed. Further research on a synthesis of pure Li_2MoO_3 with carbon and analyses of Mo_3O_{13} cluster would clarify mechanism of the insufficient rate capacity and leads to further enhancement of the electrode performance.

References

1. A. C. James and J. B. Goodenough, *J. Solid State Chem.*, 1988, **76**, 87-96.
2. H. Kobayashi, M. Tabuchi, M. Shikano, H. Kageyama and R. Kanno, *J. Mater. Chem.*, 2003, **13**, 957-962.
3. H. Kobayashi, R. Kanno, Y. Kawamoto, M. Tabuchi, O. Nakamura and M. Takano, *Solid State Ionics*, 1995, **85**, 25-31.
4. H. Kobayashi, M. Tabuchi, M. Shikano, Y. Nishimura, H. Kageyama, T. Ishida, H. Nakamura, Y. Kurioka and R. Kanno, *J. Power Sources*, 1999, **81-82**, 524-529.
5. A. D. Robertson and P. G. Bruce, *Chem Commun (Camb)*, 2002, 2790-2791.
6. M. M. Thackeray, S.-H. Kang, C. S. Johnson, J. T. Vaughey, R. Benedek and S. A. Hackney, *J. Mater. Chem.*, 2007, **17**, 3112.
7. J. Ma, Y.-N. Zhou, Y. Gao, X. Yu, Q. Kong, L. Gu, Z. Wang, X.-Q. Yang and L. Chen, *Chem. Mater.*, 2014, **26**, 3256-3262.
8. K.-S. Park, D. Im, A. Benayad, A. Dylla, K. J. Stevenson and J. B. Goodenough, *Chem. Mater.*, 2012, **24**, 2673-2683.
9. J. Lee, A. Urban, X. Li, D. Su, G. Hautier and G. Ceder, *Science*, 2014, **343**, 519-522.
10. A. Urban, J. Lee and G. Ceder, *Adv. Energy Mater.*, 2014, **4**, 1400478.
11. M. J. O'Malley, H. Verweij and P. M. Woodward, *J. Solid State Chem.*, 2008, **181**, 1803-1809.
12. Z. Chen and J. R. Dahn, *J. Electrochem. Soc.*, 2002, **149**, A1184.
13. A. Yamada, S. C. Chung and K. Hinokuma, *J. Electrochem. Soc.*, 2001, **148**, A224.

14. H. Huang, S. C. Yin and L. F. Nazar, *Electrochem. Solid-State Lett.*, 2001, **4**, A170.

15. H. C. Shin, W. I. Cho and H. Jang, *Electrochimica Acta*, 2006, **52**, 1472-1476.

16. D. Mikhailova, N. N. Bramnik, K. G. Bramnik, P. Reichel, S. Oswald, A. Senyshyn, D. M. Trots and H. Ehrenberg, *Chem. Mater.*, 2011, **23**, 3429-3441.

17. C. K. Huang, S. C. Baker and R. A. Huggins, *J. Electrochem. Soc.*, 1988, **135**, 408-412.

18. K. Ben-Kamel, N. Amdouni, H. Groult, A. Mauger, K. Zaghib and C. M. Julien, *J. Power Sources*, 2012, **202**, 314-321.

19. Y. N. Zhou, J. Ma, E. Hu, X. Yu, L. Gu, K. W. Nam, L. Chen, Z. Wang and X. Q. Yang, *Nat. Comm.*, 2014, **5**, 5381.

20. M. Park, X. Zhang, M. Chung, G. B. Less and A. M. Sastry, *J. Power Sources*, 2010, **195**, 7904-7929.

21. S. J. Hibble and I. D. Fawcett, *Inorg Chem*, 1995, **34**, 500-508.

22. S. J. Hibble, I. D. Fawcett and A. C. Hannon, *Acta Cryst. B*, 1997, **53**, 604-612.

23. H.-J. Zhang, K.-X. Wang, X.-Y. Wu, Y.-M. Jiang, Y.-B. Zhai, C. Wang, X. Wei and J.-S. Chen, *Adv. Funct. Mater.*, 2014, **24**, 3399-3404.

24. J. Barker, *Solid State Ionics*, 2003, **158**, 261-267.

25. H.-S. Kim, M. Kong, K. Kim, I.-J. Kim and H.-B. Gu, *J. Power Sources*, 2007, **171**, 917-921.

26. S. Niketic, M. Couillard, D. MacNeil and Y. Abu-Lebdeh, *J. Power Sources*, 2014, **271**, 285-290.

27. J. Bréger, Y. S. Meng, Y. Hinuma, S. Kumar, K. Kang, Y. Shao-Horn, G. Ceder and C. P. Grey, *Chem. Mater.*, 2006, **18**, 4768-4781.

28. H. Yu, Y. Qian, M. Otani, D. Tang, S. Guo, Y. Zhu and H. Zhou, *Energy Environ. Sci.*, 2014, **7**, 1068.

29. J. R. Croy, D. Kim, M. Balasubramanian, K. Gallagher, S.-H. Kang and M. M. Thackeray, *J. Electrochem. Soc.*, 2012, **159**, A781.

30. H. Aritani, T. Tanaka, T. Funabiki, S. Yoshida, M. Kudo and S. Hasegawa, *J. Phys. Chem.*, 1996, **100**, 5440-5446.

Chapter 4. Lithium-Excess Layered Tungsten Oxides for Positive Electrodes and Electrode Additives of LIBs

4.1 Introduction

Material design of Li-excess materials is of interest because of their potential of positive electrode materials for high-capacity LIBs as discussed in the last chapter. One direction of designing Li-excess materials is using relatively heavy metals, compared with conventional 3d transition metals, having high valence state above tetravalent since such metals are likely to accommodate larger amount of Li^+ ions and form Li-rich compounds such as Li_3NbO_4, Li_4MoO_5, Li_4WO_5, Li_5ReO_6 etc.[1] Since the transition metals in these Li-rich compounds have no d-electrons and thus show insulating feature, combination with transition metal oxides has been tried to utilize positive electrode materials such as the binary systems of Li_3NbO_4 – $LiMO_2$ (M = V^{III}, and Mn^{III}) / CoO [2,3] and Li_4MoO_5 – $LiFeO_2$ / NiO.[4,5] While cations in these materials are likely to be disordered, Li_4MoO_5-NiO, namely Li_4NiMoO_6, has a layered structure and similar structure to Li_2MnO_3.

In this chapter, we shed light on the binary system of $0.5 \cdot Li_4WO_5$ – $0.5 \cdot MeO$ (Me = Mn^{II},Ni^{II}, Co^{II}) as positive electrode materials. Tungsten is a heavy metal element so that the use of tungsten could be disadvantageous in view of gravimetric energy density, however, some previous works indicate Li-excess W containing compounds give advantage to fast Li diffusion in the structure.[6-8]

At first we have investigated synthesis of these targeted compounds and investigated their electrochemical properties, then discussed their reaction mechanism. Secondly, solid solution with $LiMO_2$ has been synthesized and finally, applied as the inorganic additives for positive electrodes to improve power performance of the full cells.

4.2 Synthesis

Li_4MeWO_6 (Me =Mg, Ni, Mn, Co) was prepared by heating a mixture of Li_2CO_3 (Kanto Chemical), MgO or Ni, Mn, Co acetates, and ball milled submicron WO_3 or Nb_2O_5 (Wako Chemicals). In the mixture, a weight ratio of each starting material is fixed to be Li:Me:W = 4.1:1:1 in atomic ratio as summarized in Fig. 4-1. The pelletized mixture was heated at 1000 °C in air for Me = Ni and $Ni_{0.6}Mn_{0.2}Co_{0.2}$ and in Ar for Me = Mn after pre-calcination at. 400 °C in air. Pre-ball milling of WO_3 powder is effective to reduce un-reacted WO_3. The materials for inorganic additives into composite electrodes were also prepared by the same way and heated at 600 °C in air for Me = Mg and at 1000 °C in air for Li_3NbO_4. The sample was preserved in a dry room to avoid contact with moisture in air.

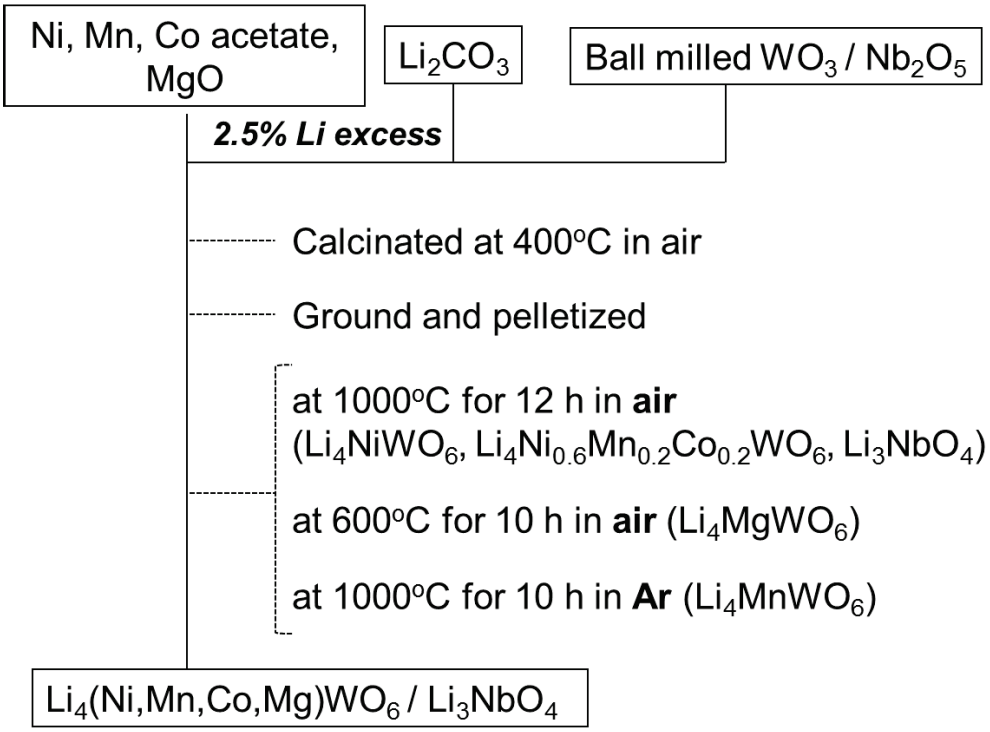

Fig. 4-1. Synthesis condition of Li_4MeWO_6

4.3 Li_4MeWO_6 (Me=Ni, Mn, Co) as positive electrode materials for LIBs

4.3.1 Structural and physical characterization

Fig. 4-2 shows XRD patterns and SEM images for the samples obtained by heat treatment of the starting materials, Li_4NiWO_6, $Li_4Ni_{0.6}Mn_{0.2}Co_{0.2}WO_6$, and Li_4MnWO_6 which are hereinafter denoted by NiW, NMCW and, MnW, respectively. All diffraction peaks can be assigned to a space group, *C2/m*, and their structure is similar to that of Li_2MnO_3.[9] All samples show crystalline micron-scale particles. A schematic illustration of Li_4NiWO_6 crystal structure and in-plane arrangement is shown in Fig. 4-3. Li_4NiWO_6 have 2 types of layer, Li layer and metal layer which contains ordered WO_6 and honeycomb-type sites of $(Ni/Li)O_6$. Thus, Li^+ and Ni^{2+} ions in the $(L_{1/3}Ni_{1/3}W_{1/3})O_2$ layer are randomly distributed in green octahedra.

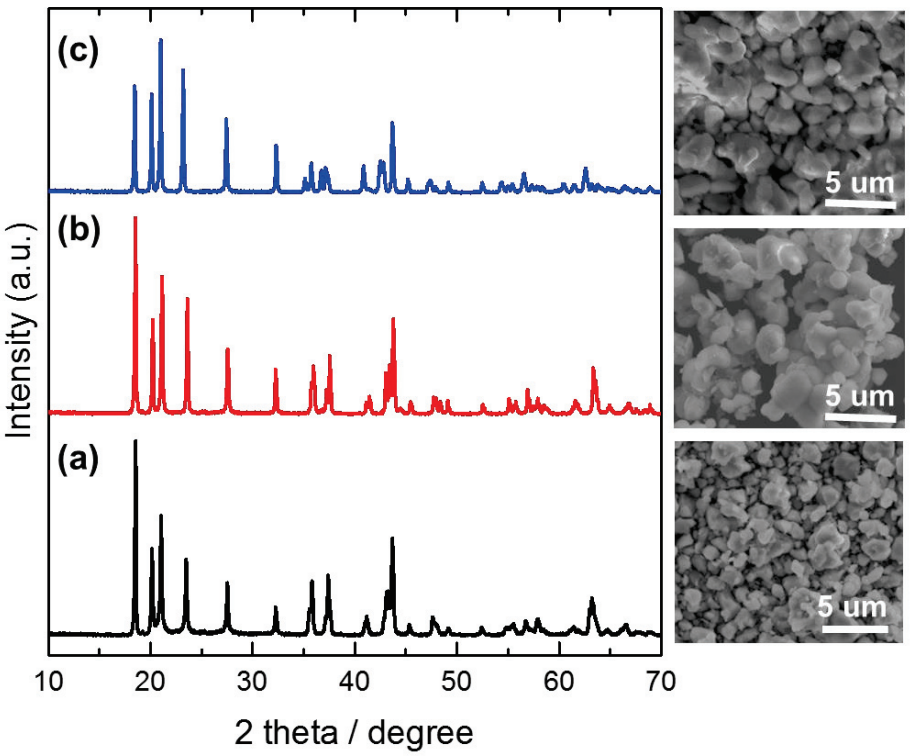

Fig. 4-2. XRD patterns and SEM images of the synthesized samples; (a) NiW, (b) NMCW, and (c) MnW.

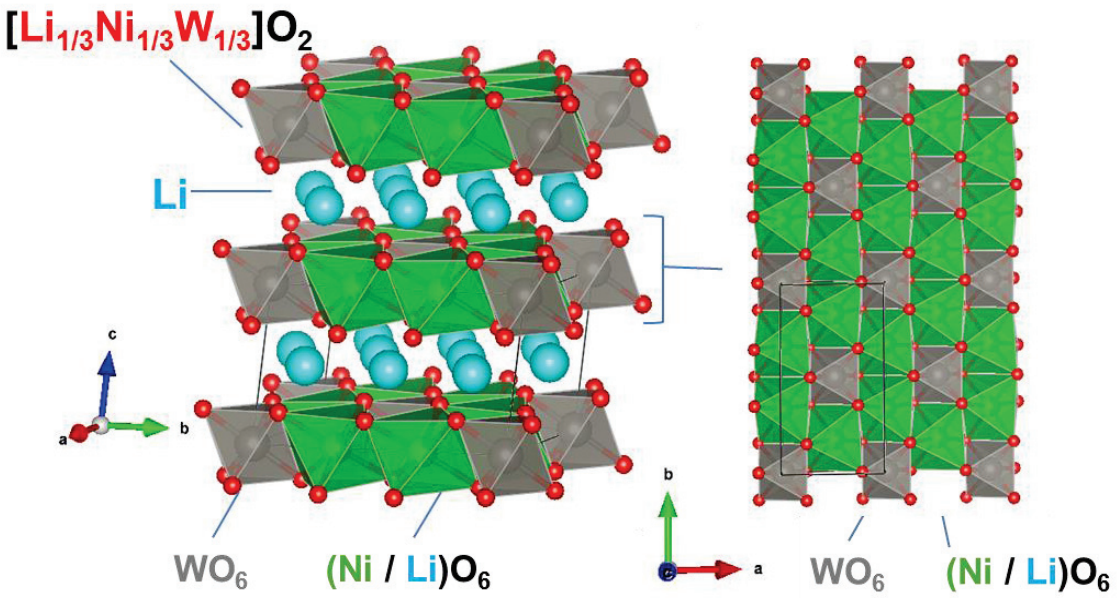

Fig. 4-3. A schematic illustration of NiW crystal structure and in-plane arrangement.

4.3.2 Electrochemical investigation

Fig. 4-4 shows the galvanostatic charge and discharge curves of NiW, NMCW, and MnW in a voltage range of 1.5 – 4.9 V at a current rate of 13 mA g^{-1} corresponding to C/20 rate (a 1C rate is defined as 260 mA g^{-1}). NiW and NMCW show certain electrochemical activity of reversible capacity below 100 mAh g^{-1} in the working voltage between 4.1 and 3.0 V vs. Li with toptactic-like reversible curves with little polariztion and that around 180 mAh g^{-1} in the working voltage between 4.9 and 1.5 V with huge polarization. On the other hand, MnW shows almost no reversible capacity in the both working voltage. Fig. 4-4b shows cycle stability comparing NiW and NMCW. Both samples have stable cycling between 4.1 and 3.0 V and the reversible capacity is about 90 mAh g^{-1} for NiW and 60 mAh

g^{-1} for NMCW. The initial reversible capacity of NiW and NMCW is almost proportional to the Ni amount in each composition since NMCW has 60 atomic% of Ni in whole transition metals. These facts suggest that only Ni can be electrochemically active in Li_4MeWO_6 system. In the following, we will focus more on NiW and its electrochemical properties, structural change during Li extraction/insertion and electronic state of Ni and W.

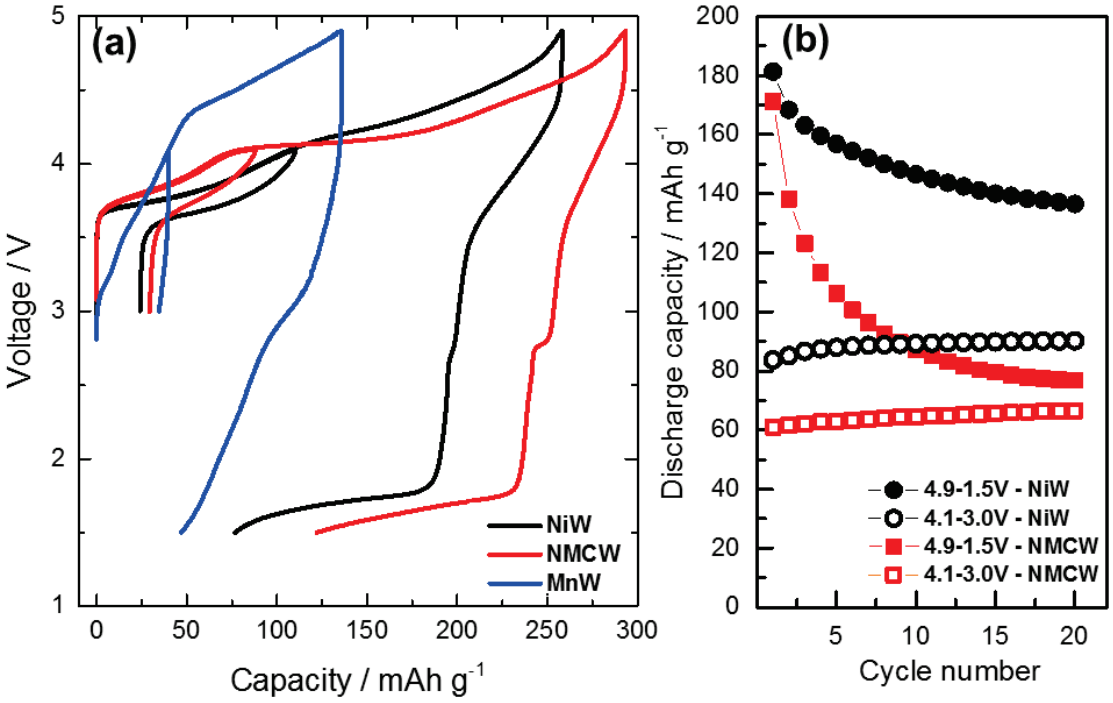

Fig. 4-4. Charge and discharge curves of Li_4MeWO_6 electrodes in Li cells; (a) in the voltage range of 3.0 – 4.1 V and 1.5 – 4.9 V at a current rate of 16 mA g^{-1} for NiW, NMCW, and MnW and (b) cycle stability for NiW and NMCW.

Fig. 4-5 exhibits initial charge/discharge curve in the different voltage window for NiW. As described above, a highly reversible curve in 4.1 – 3.0 V and a largely polarized curve in 4.9 – 1.5 V is found. The polarization is getting large from 4.3 V as seen the curve in 4.3– 3.0 V, which corresponds to exceeding the limit of Ni(II/IV) based

theoretical capacity, 148 mAh g^{-1}. Extra charge capacity beyond Ni(II/IV) would be related with oxidation of O^{2-} anion, resulting in irreversible structural change associated with oxygen release[10] and/or solid-state redox reaction of oxide ions.[11]

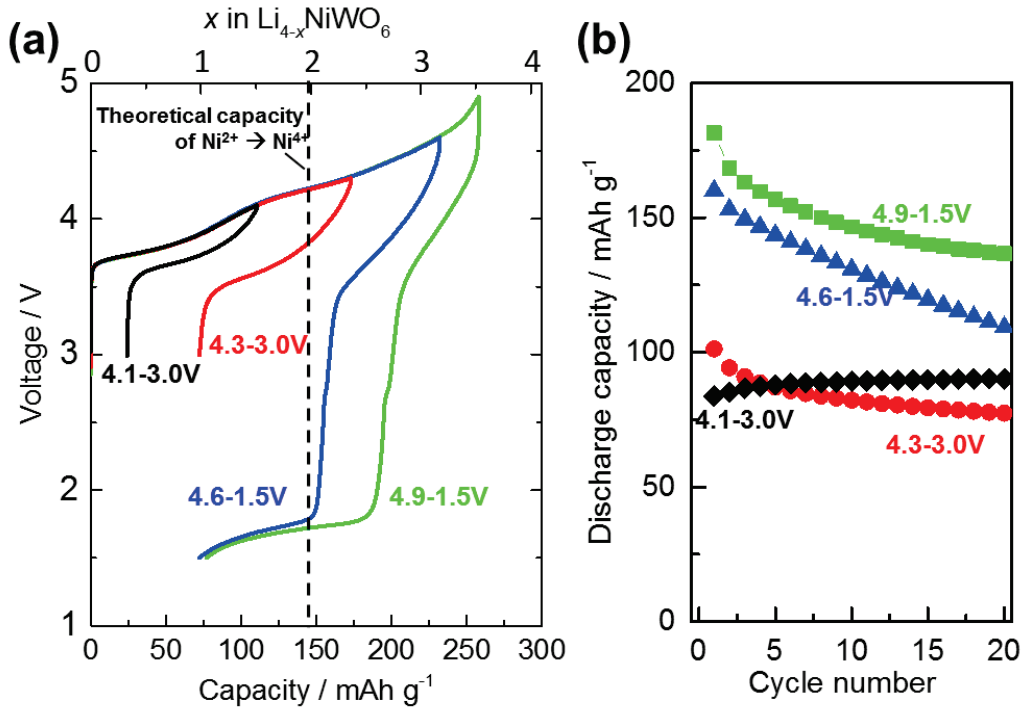

Fig. 4-5. Charge and discharge curves of NiW electrodes in Li cells; (a) in the different voltage range and (b) their cycle stability

Fig. 4-6 shows charge/discharge curves of NiW in 4.1 – 3.0 V and 4.9 – 1.5 V. Even though Tarascon *et al.* reported that Li_4NiTeO_6 shows an increase of redox potential of Ni(II/IV) due to inductive effect of Te(VI) ions,[12, 13] W(VI) ions don't result in such an effect and NiW shows the almost same redox potential of Ni(II/IV) as conventional Li*M*O_2 family. In Fig. 4-6b, the plateau at 1.7 V in discharge is reversibly observed and it is possibly related with the irreversible structural change during initial charge. On the

other hand, continuous voltage decay of discharge curves is found for NiW during cycling between 4.9 and 1.5 V, indicating irreversible structural change in bulk or on the surface.

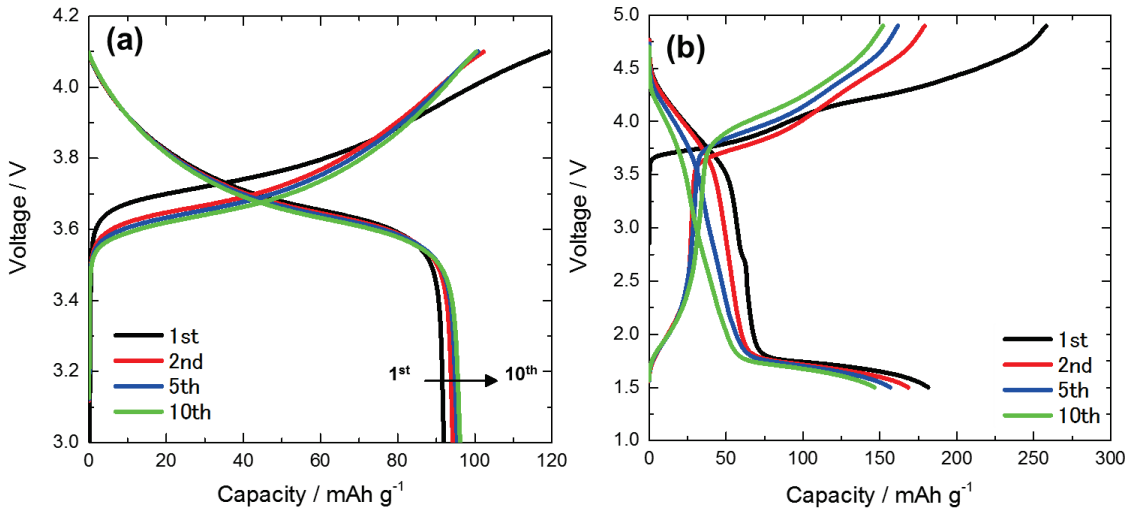

Fig. 4-6. Charge and discharge curves of NiW electrodes in Li cells; (a) in the voltage range of 4.1 – 3.0 V and (b) of 4.9 – 1.5 V

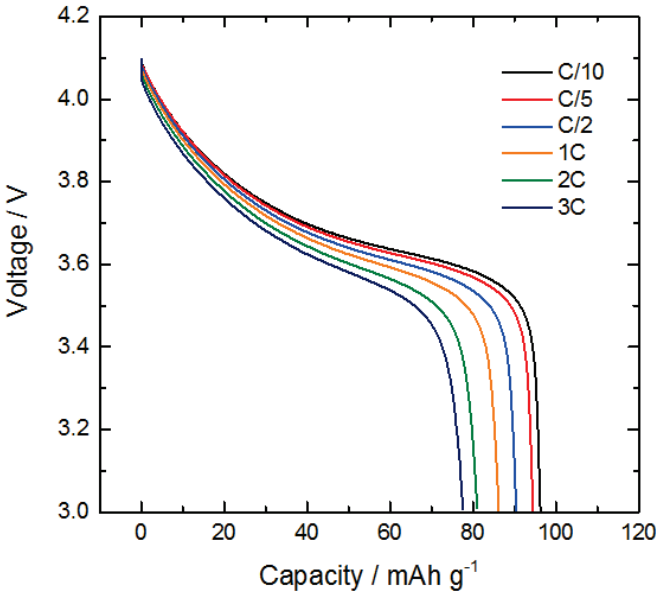

Fig. 4-7. Rate property of NiW in the voltage range of 4.1 – 3.0 V

Rate property of NiW in the voltage range of 4.1 – 3.0 V is shown in Fig. 4-7. In this limited voltage range, NiW shows acceptably good rate performance, 81 %

capacity retention at 3C rate compared with C/10. This also indicates reversible Li intercalation in Li layers in the voltage range of 4.1 – 3.0 V.

4.3.3 Reaction mechanism

Ex-situ XRD measurement is conducted to understand structural change during Li extraction/insertion as shown in Fig. 4-8. In the voltage range of 4.1 – 3.0 V, the structure is maintained throughout the cycle and reversible slight increase of intra-layer distance and decrease of in-plane slab distance is consistent with Li extraction from Li

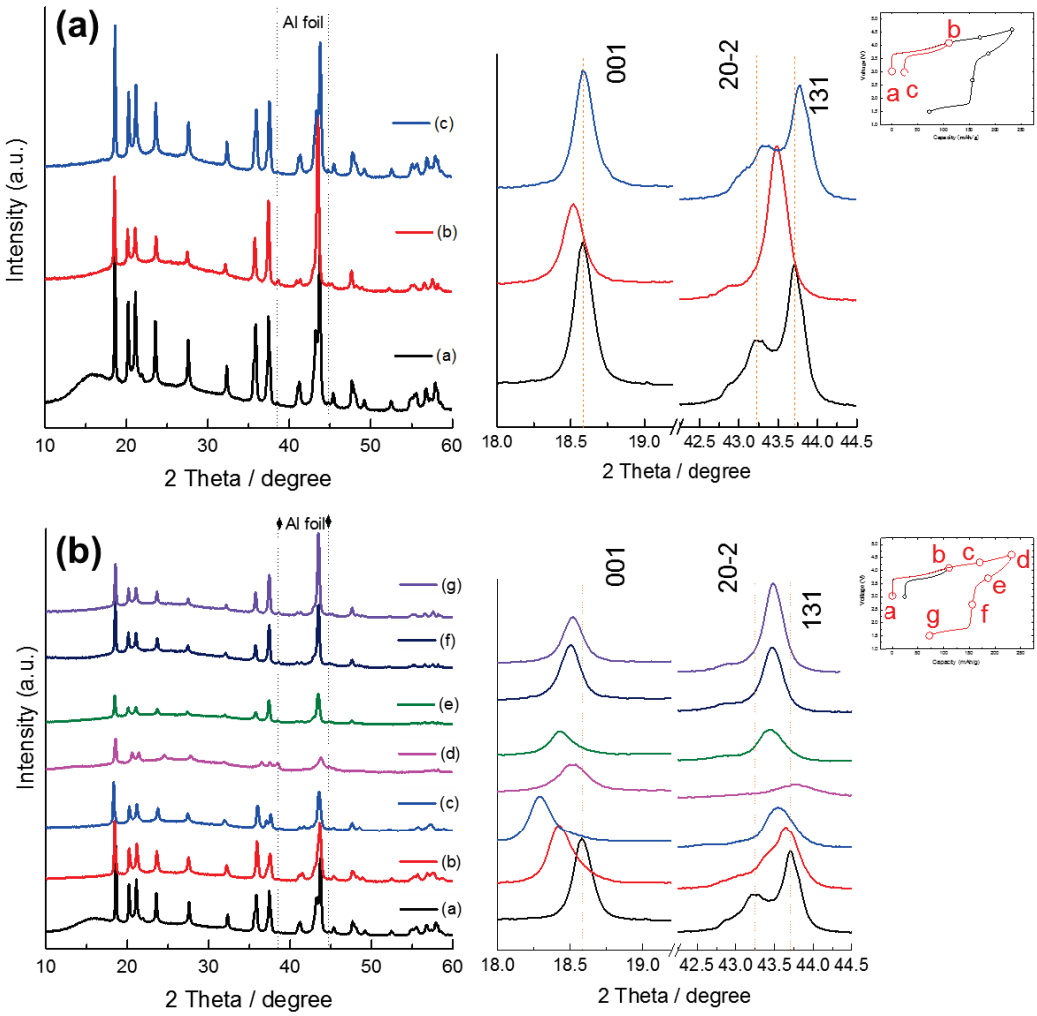

Fig. 4-8. *Ex-situ* XRD patterns in (a) 4.1 – 3.0 V and (b) 4.6 and 1.5 V for NiW

layer and shrink of ionic radius associated with oxidation of nickel from divalent to tetravalent. The change of crystal parameter, interlayer and in-plane slab distances is shown in Fig. 4-9. From the figures, discharge to 1.5 V after charge to 4.6 V results in irreversible change of intra-layer distance and also disappearance of peak splitting between 20-2 and 131. In addition, some new peaks appear at fully charged state at 4.6 V. The intra-layer distance increases at the beginning and then decreases, which is consistent with previous observation of wll known layered positive electrode materials[14-16] due to further Li extraction. In case of Li_4MoO_5-NiO binary system, Mo migration and disappearance of diffraction peaks related with ordering of Mo was observed in charge to 4.6 V.[4, 5] Despite of structural similarity, W is obviously stable in the structure and no migration is seen even after charged to 4.6 V because diffraction peaks originated from W ordering, especially between 20 – 35°, show no change during charge and discharge.

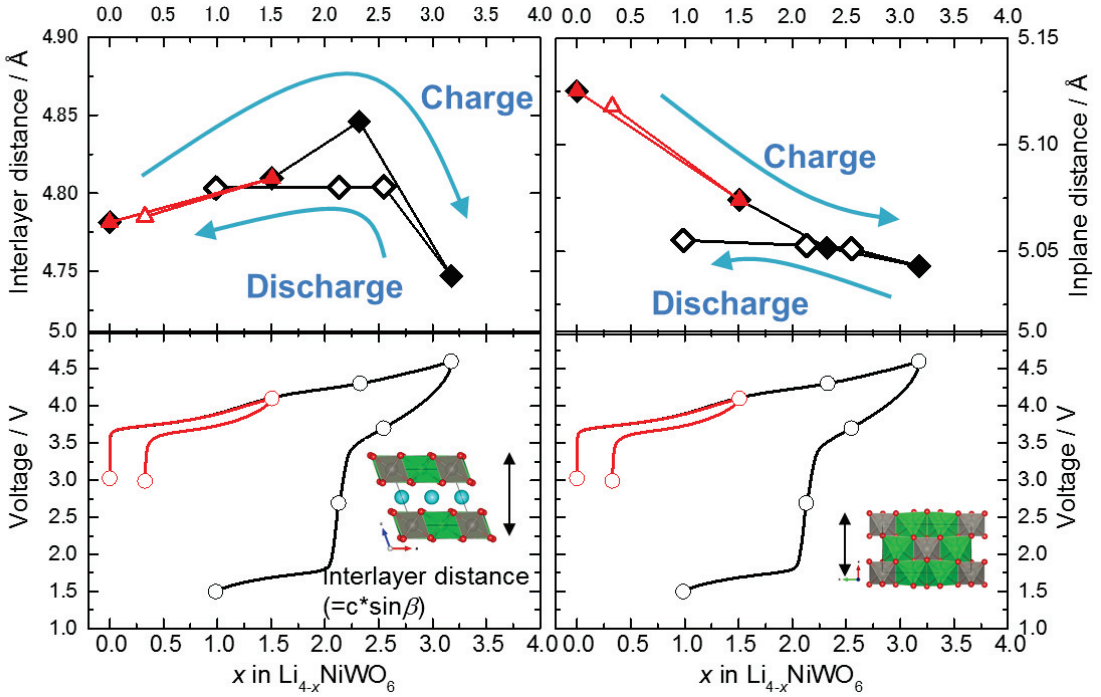

Fig. 4-9. Change of lattice constant during Li extraction/insertion for NiW

Fig. 4-10 shows XANES spectra of Ni *K*-edge, W *L3*-edge, and W *L1*-edge during charge/discharge in the voltage range of 4.6 – 1.5 V. Ni *K*-edge spectra show that Ni oxidation up to 4.3 V as the peak shifts to the higher energy, however, charge from 4.3 to 4.6 V, the peak doesn't shift to higher energy and even shift back to lower energy. This trend is also reported in Li-excess Mn based system and Yabuuchi *et al.* suggested that this shift to lower energy is caused by migration of Ni from octahedral into tetrahedral sites based on the simulation of Ni *K*-edge spectra.[11] As analogous to the Li-excess Mn based system and implication of irreversible structural change by *ex-situ* XRD, Ni migration may occur also for NiW. W *L3* and *L1*-edge spectra also shows reversible and systematic change during charge and discharge. Especially in W *L1*-edge spectra, reversible appearance/disappearance of the pre-edge peak at 12105 eV is observed. In view of electrochemical activity, however, it's not clear whether W participates in redox reaction because such a reversible change can also be explained by the change of surrounding environment, such as Ni's redox reaction and migration into tetragonal sites.[17]

The reaction mechanism suggested from the above results is summarized in Fig. 4-11. At first, topotactic reaction of lithium extraction with Ni redox occurs up to 4.1 V and then, by exceeding theoretical capacity of Ni(II/IV), redox of oxide ion and/or gas generation is anticipated and further supported by the appearance of new diffraction peak in *ex-situ* XRD and Ni migration in XAS spectra. Reversible Li insertion at 1.7 V in discharge is confirmed not from Ni redox reaction but still unclear if it originates from W redox. At least, it is clear that the plateau at 1.7 V is activated by charge above 4.3 V and thus may be related with structural change during initial charge.

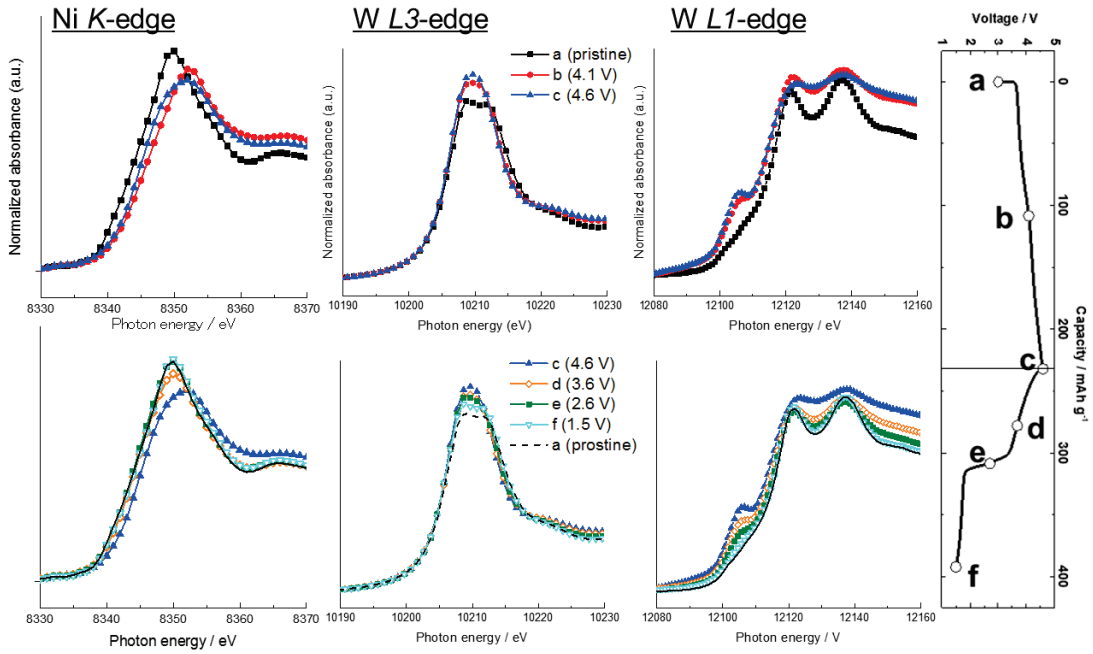

Fig. 4-10. XANES spectra of Ni *K*-edge (left), W *L3*-edge (middle), and W *L1*-edge (right) during initial charge and discharge for NiW.

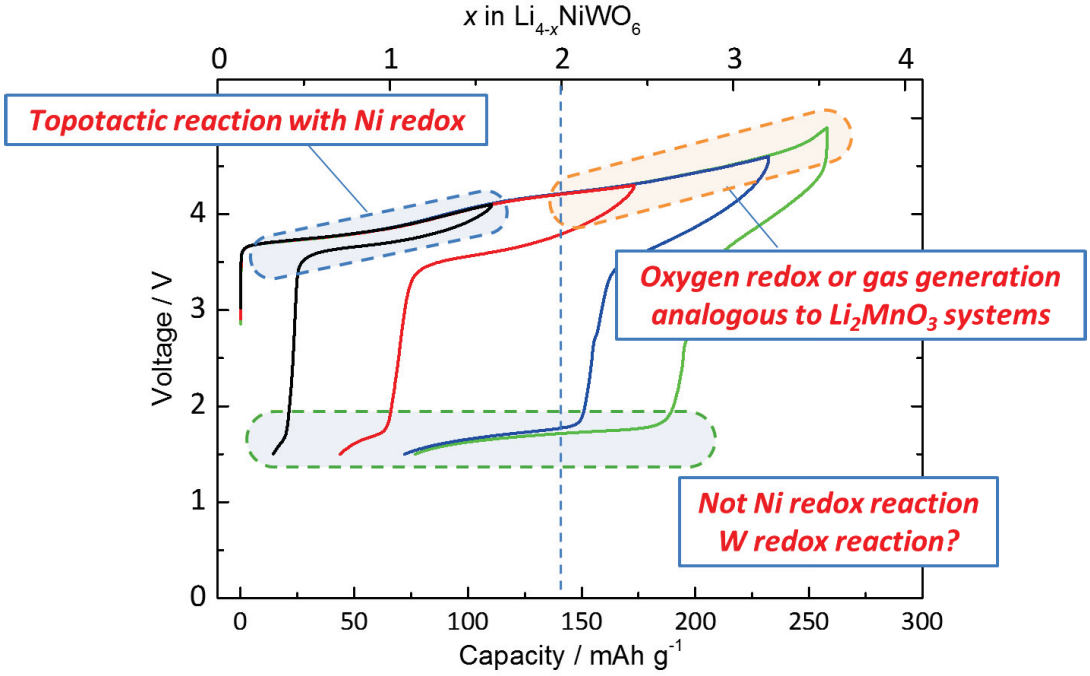

Fig. 4-11. The summary of suggested reaction mechanism of NiW.

4.4 Solid solution of Li_4MeWO_6 - $LiMeO_2$ (Me=Ni, Mn, Co)

We have successfully synthesized new Li-excess layered materials, Li_4MeWO_6 and investigated their electrochemical properties and reaction mechanisms as discussed above. To pursue further material development having superior electrode performance, the analogy to Li_2MnO_3 can be used. Li_2MnO_3 is known to be electrochemically inactive because tetravalent manganese can't be oxidized. Instead of that, electrons are removed from O2*p* band and thus, irreversible reaction occurs during initial charge, and deterioration of reversible capacity is found in the following cycle. Gas generation of O_2 during initial charge is also detected, suggesting irreversible structural change such as oxygen removal.[10] Since 2004, however, the solid solution of Li_2MnO_3 – Li*M*O_2 (*M* = Ni, Mn, Co) has been intensively studied because solid solution with Li*M*O_2 stabilizes the structure and enables high reversible capacity and relatively stable cycling.[11, 18] Because of several similarities between Li_4MeWO_6 and Li_2MnO_3, crystal structure, in terms of in-plane ordering in metal layers, and irreversible structural change in the first cycle, we here synthesize the solid solution of Li_4MeWO_6 – Li*M*O_2 (*M* = Ni, Mn, Co) and evaluate their electrochemical properties.

As shown in Fig. 4-12, 4 different single phases of Li_4MeWO_6 – Li*M*O_2 solid solution, $0.05{\cdot}Li_4MeWO_6$ – $0.95{\cdot}LiMeO_2$, $0.15{\cdot}Li_4MeWO_6$ – $0.85{\cdot}LiMeO_2$ (Me=$Ni_{0.6}Mn_{0.2}Co_{0.2}$), $0.05{\cdot}Li_4NiWO_6$ – $0.95{\cdot}LiCoO_2$, $0.15{\cdot}Li_4NiWO_6$ – $0.85{\cdot}LiCoO_2$ are successfully obtained, which are hereinafter denoted by NMC-1, NMC-2, LCO-1 and, LCO-2, respectively. In other words, these solid solutions can be expressed as co-doping into Li*M*O_2 with tungsten and lithium and actual composition of NMC-1, -2 and LCO-1, -2 are expressed as layered notation of $Li(Me_{0.967}Li_{0.017}W_{0.016})O_2$, $Li(Me_{0.90}Li_{0.05}W_{0.05})O_2$, $Li(Co_{0.95}Li_{0.017}\ Ni_{0.017}W_{0.016})O_2$, $Li(Co_{0.85}Li_{0.05}\ Ni_{0.05}W_{0.05})O_2$, respectively. XRD

patterns in Fig. 4-12 reveal that all diffraction peaks can be assigned to a space group, *R3/m*, and no impurity peaks are found.

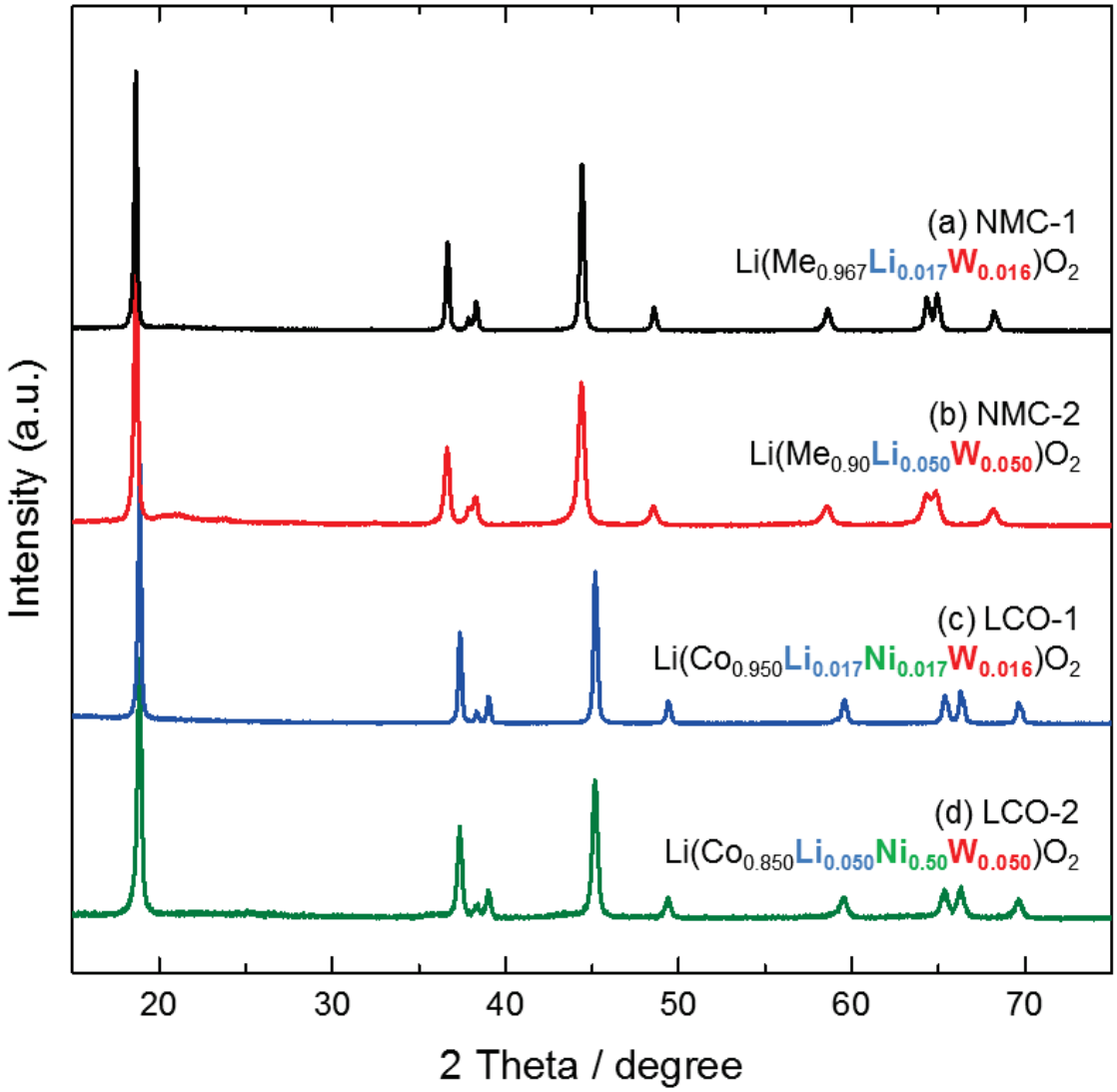

Fig. 4-12. XRD patterns of (a) NMC-1, (b) NMC-2, (c) LCO-1, and (d) LCO-2.

Fig. 4-13 shows step charge/discharge profiles of (a) NMC-1, (b) NMC-2, (c) LCO-1, and (d) LCO-2 from 4.1 V to 4.6V. For NMC-1 and NMC-2, charge/discharge curves show very low polarization and insignificant irreversible capacity is observed by testing up to 4.3 V. By further charge beyond 4.3 V, the polarization is getting large.

LCO-1 and LCO-2 show the same trend but the increase of polarization is more pronounced than that for NMC and the increase of polarization is very serious in charge above 4.3 V. Such a growth of the polarization reminds us the material of end member, Li_4NiWO_6, and the similar irreversible structural change during initial charge is anticipated as described in Section 4-3-3. The interesting point of LCO-1 and LCO-2 is the redox reaction of Ni(II/IV) observed at the beginning of charge curve. It can be described that divalent nickel is induced into LCO by co-doping with Li and W.

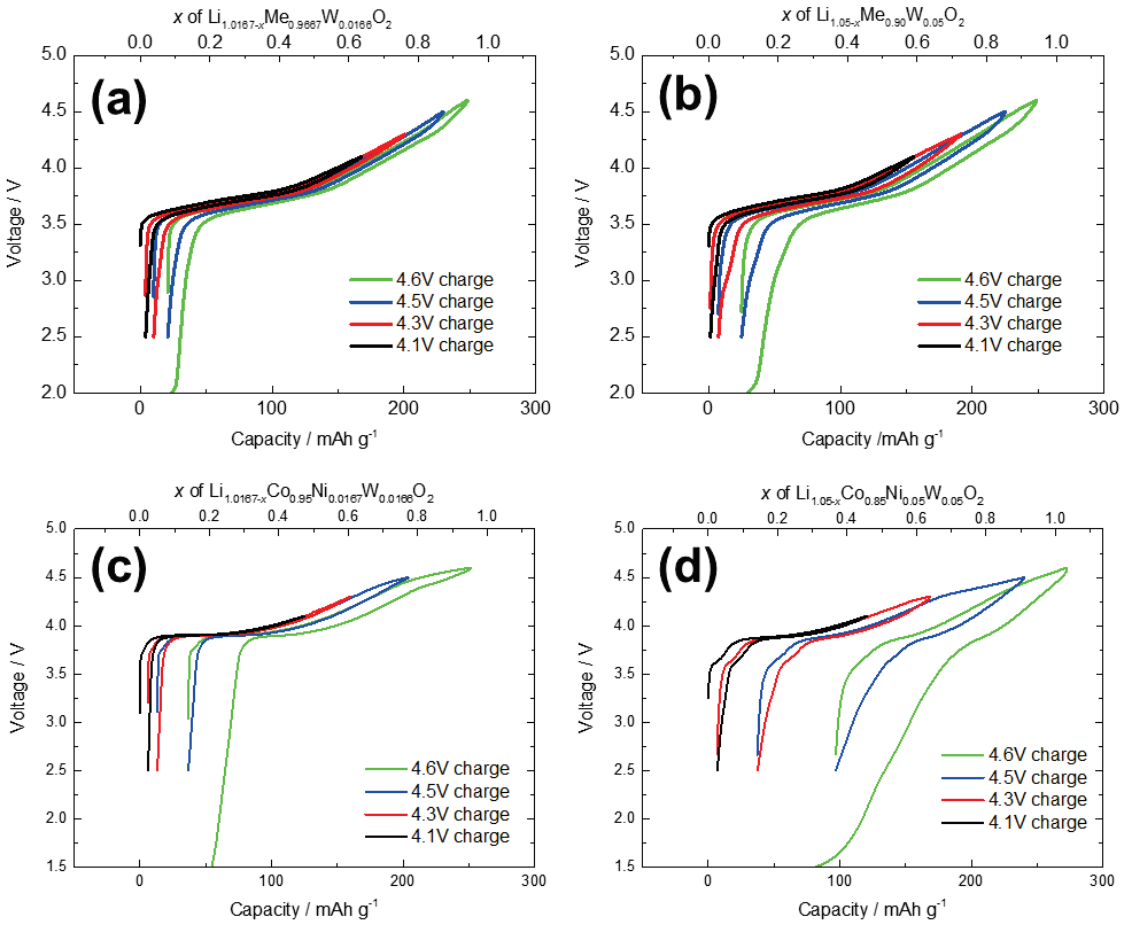

Fig. 4-13. Step charge/discharge profiles of (a) NMC-1, (b) NMC-2, (c) LCO-1, and (d) LCO-2.

Rate performance in the voltage range of 4.3- 3.0 V is evaluated and shown in Fig. 4-14. All samples show good rate performance and especially, LCO-2 shows excellent rate performance, 92% capacity retention at 3C compared with the capacity at C/20. The good rate performance of the solid solution of Li_4MeWO_6 – NMC/LCO samples implies a positive effect on Li diffusion by tungsten.

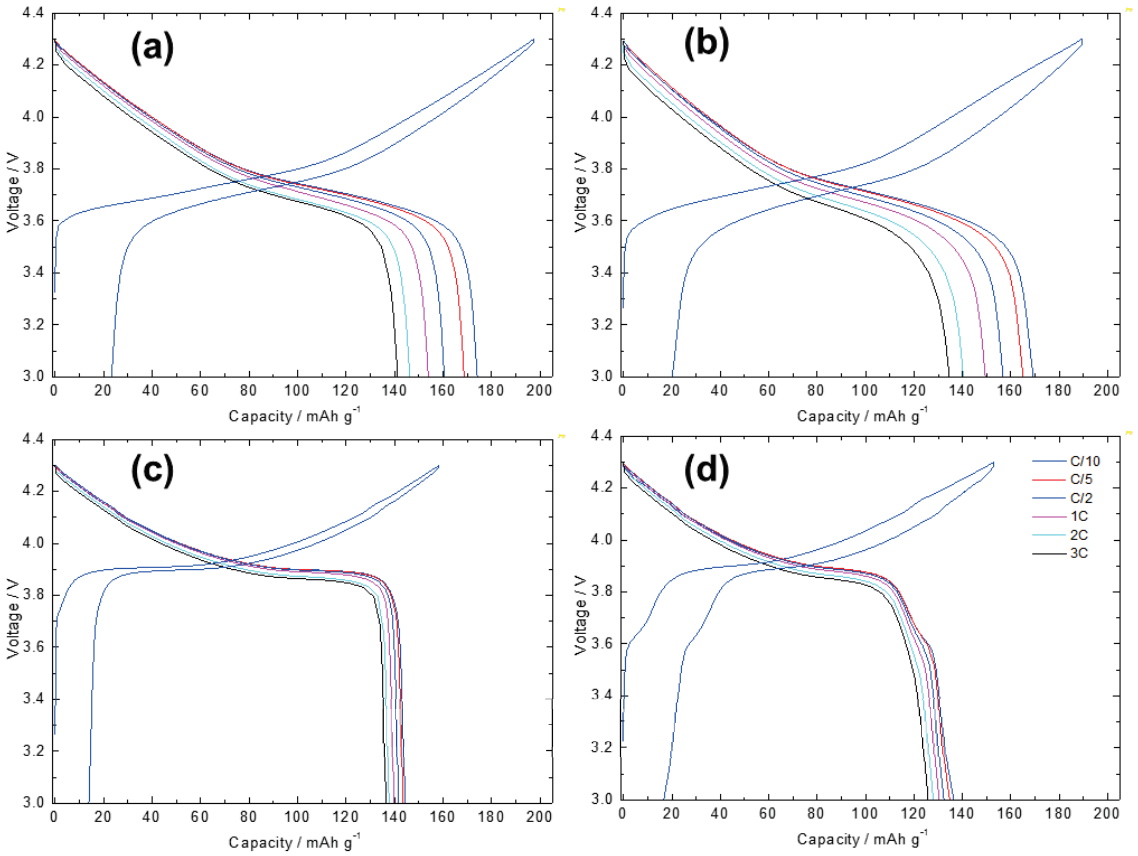

Fig. 4-14. Rate performance of (a) NMC-1, (b) NMC-2, (c) LCO-1, and (d) LCO-2 in the voltage range of 4.3 -3.0 V.

To understand structural change during charge/discharge of NMC-1 which has superior reversible capacity of ca. 175 mAh g^{-1} among the samples of Li_4MeWO_6 – NMC/LCO solid solution, *operando* XRD measurement is conducted. 003 peak shifts to

lower angle in charge up to 4.2 V corresponding to 0.7 Li extraction and then, shifts back to higher angle by charge to 4.6V. This tendency is consistent with Li extraction from conventional layered material such as LCO and NMC and understood that intra-layer distance increases due to electric repulsion between MO_2 at the first stage of Li extraction and then, shrinks by further Li extraction. During discharge, the peaks don't shift back to original position, implying structural change.

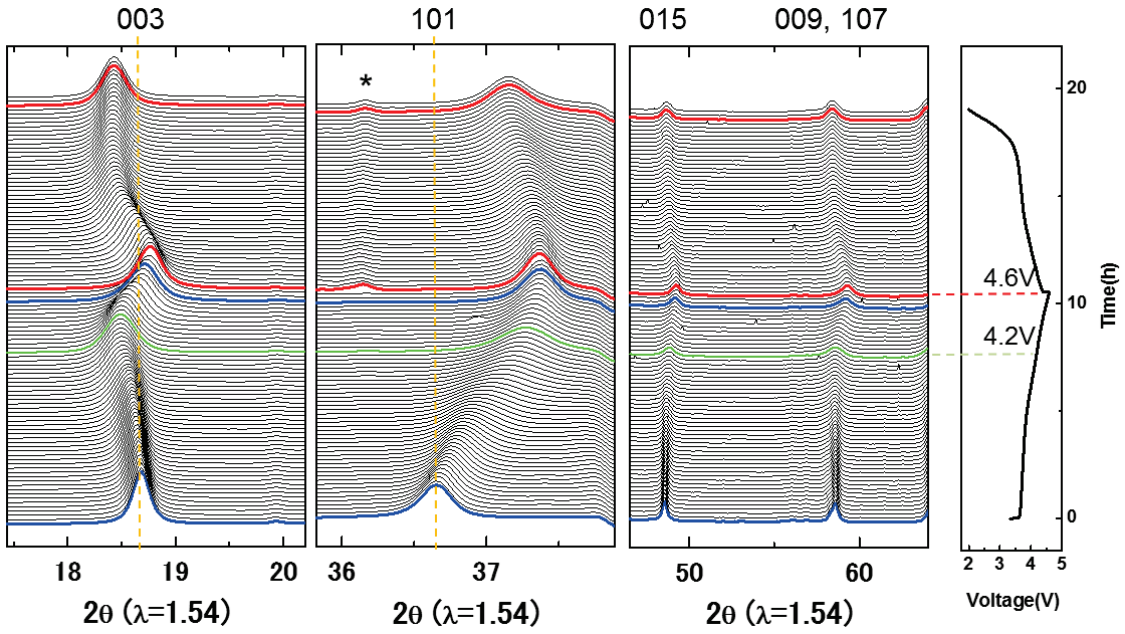

Fig. 4-15. *Operando* XRD patterns of NMC-1.

4.5 Inorganic additive and full cell evaluation

In this section, we have focused on the practical application and implemented the full cell application as a basis of collaborative research with Umicore. As we discussed above, tungsten containing compounds have a potential to improve Li diffusion, in other words, power performance of LIB cells in view of practical application. In general, practically-used layered oxides such as lithium cobalt oxide (LCO) and lithium nickel manganese cobalt oxide (NMC) are still required to be improved their power performance. Internal resistance is a key parameter to determine this power property. The lower the resistance is, the less energy the battery loses during high power usage. Thus, the growth of the internal resistance should be low enough during the battery's life. It is also expected that in the future the lithium battery market will be increasingly dominated by automotive applications. Life time of automotive batteries need to be more than 5 years. A long battery life is related to two properties: (a) small loss of capacity during storage and (b) high cycle stability.

To improve the power performance of LIB cells, many approaches have been tried to reduce the internal resistance of the cells, especially at the side of the positive electrode. One major approach is metal doping of positive electrode active materials. In particular, some patents disclosed doping with relatively heavy metals. US2007/0212607 discloses Zr and Nb doping for NMC to improve the DC resistance property of LIB full cells. In US2012/0276446, Mo, Ta and W doping of the same type of NMC materials is disclosed, which also reduces the DC resistance of the cells. These heavy metal elements can have a high valence state such as a tetra-, penta- or hexa-valent state, and can form many oxides with Li - having different lithium to metal ratios as discussed above. By doping these elements into positive electrode active materials, lithium heavy metal oxides

can be formed on the surface of the positive electrode materials and thus play a role in supporting Li diffusion and suppression of side reactions with the electrolyte, which may further reduce the internal resistance of the batteries. Another related approach is the addition of lithium heavy metal oxides, Li_4WO_5 to the slurry of the positive electrode, as is described in US2015/0021518. The slurry addition of a few mole% of lithium tungsten oxide reduces the initial DC resistance of NMC / carbon full cells.

In this section, we aim to further develop positive electrode systems containing layered lithium metal oxides as active material by electrode additive strategy and to analyze predominant internal resistance during battery cycling and storage in terms of a higher capacity and better stability.

4.5.1 Preparation of inorganic additive and initial full cell evaluation

As described in Section 4-2, several layered tungsten oxides, Li_4MeWO_6 (Me =Mg, Ni, Mn, Co) was obtained and we select 3 samples as new inorganic additives for positive electrode, Li_4NiWO_6 which shows the superior electrochemical properties as discussed in Section 4-4, Li_4MgWO_6 which is electrochemically inactive and insulating as well as Li_4WO_5, and Li_3NbO_4 as a counter example to understand the role of tungsten, which are hereinafter denoted by MW, NW and, Nb, respectively. Inorganic additives are prepared by conventional solid-state reaction as well as other tungsten containing compounds shown in this chapter. All samples are confirmed to be single phases and have no impurities by XRD as shown in Fig. 4-16a. After wet ball milling, their particle size is submicron, which is acceptable to distribute on micron NMC particles. (Fig. 4-16b)

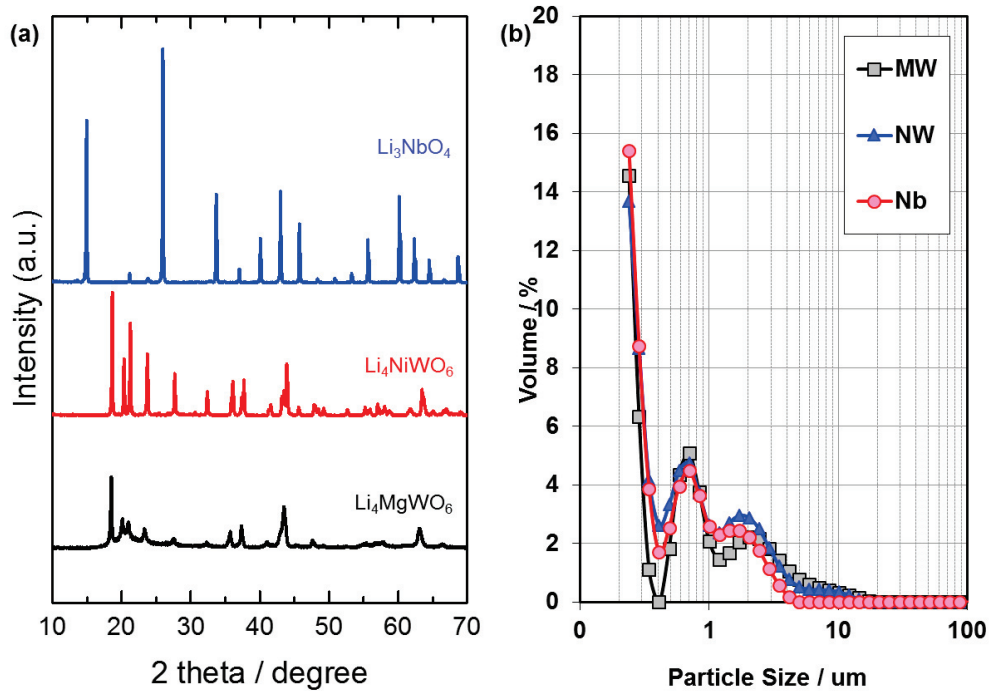

Fig. 4-16. (a) XRD patterns and (b) particle size distribution of inorganic additives, MW, NW, and Nb.

Then, here we describe the effect of the electrode additives on

- the capacity properties of a full cell during the formation step (f) (2-2-3, f)) and
- the DCR of fresh NMC-full cells (= full cells prepared after the formation step).

The full cells are labelled as follows:

- Full cell without addition of additives into the slurry of the positive electrode: Ref-cell;
- Full cell with addition of Li_4WO_5 in the slurry: W-cell, as is described in US2015/0021518;
- Full cell with addition of MW in the slurry: MW-cell;
- Full cell with addition of MW in the slurry: NW-cell;
- Full cell with addition of Nb in the slurry: Nb-cell.

Detailed experimental conditions are described in Chapter 2.

Table 4-1 shows the electrochemical properties of these cells when being prepared during the formation step. Compared with the Ref-cell, in which no additives were mixed in the slurry, all the cells with additives have a slightly lower capacity and energy density. But it is clear that the capacity and energy losses brought by the additives are not significant. The definition of other parameters are

- Coulombic Efficiency (%): ratio (in % for a charge-discharge cycle) between the energy removed from a battery during discharge compared with the energy used during charging. It is obtained from the ratio of discharge capacity in the first cycle to capacity capacity in the same cycle.
- Average Voltage (V): the average voltage during discharge
- Volumetric Energy Density (Wh/L): stored battery energy that is the product of voltage and discharge capacity in such voltage range per unit volume of battery.
- Gravimetric Energy Density (Wh/kg): stored battery energy that is the product of voltage and discharge capacity in such voltage range per unit mass of battery.

Table 4-1. Battery performance obtained from formation step for full cells with different additives of W, MW, NW, and Nb

Cell name	Capacity (mAh)	Specific Capacity (mAh/g)	Coulombic Efficiency (%)	Average Voltage (V)	Volumetric Energy Density (Wh/L)	Gravimetric Energy Density (Wh/kg)
Ref-cell	652	153	85.9	3.70	369	171
W-cell	628	148	85.1	3.70	350	166
MW-cell	634	150	85.3	3.70	350	167
NW-cell	634	150	85.4	3.70	359	168
Nb-cell	627	149	85.9	3.70	352	167

Fig. 4-17 shows the DC resistance results of fresh cells (after formation step as described in Section 2.2.2) at each state of charge (SOC) at a room temperature of 25°C, and at a low temperature of -10°C. In each graph, the DC resistance (expressed in "mOhm") vs. the state of charge (in percentage of full charge) are plotted. At 25°C, compared with the reference cell that has no additive in the positive electrode, the addition of Li_4WO_5, Li_4MgWO_6 and Li_4NiWO_6 reduces the DC resistance, while the addition of Li_3NbO_4 brings barely any benefit on reducing the resistance. In the low state of charge, the DC resistances at -10°C are quite similar for slurry-modified cells and are all lower compared to the reference cell. In the high state of charge, the effect on DC resistances at -10°C is less pronounced. The addition of Li_4WO_5 and Li_4MgWO_6 has the best overall results of the fresh cells. Accordingly, electrochemical tests on above fresh cells prove that the addition of lithium heavy metal oxide compounds into the positive electrode has no noticeable negative effect on capacity and energy density, and some additives like Li_4WO_5, Li_4NiWO_6 and Li_4MgWO_6 show promising DCR properties since 5 – 10% DCR improvement has been achieved compared with Ref-cell. In view of the intended use of the full cells, it is clear that for cells having comparable results before being intensively cycled, the results of cycle stability and DCR-evolution during cycling are more important, as is shown in the following section.

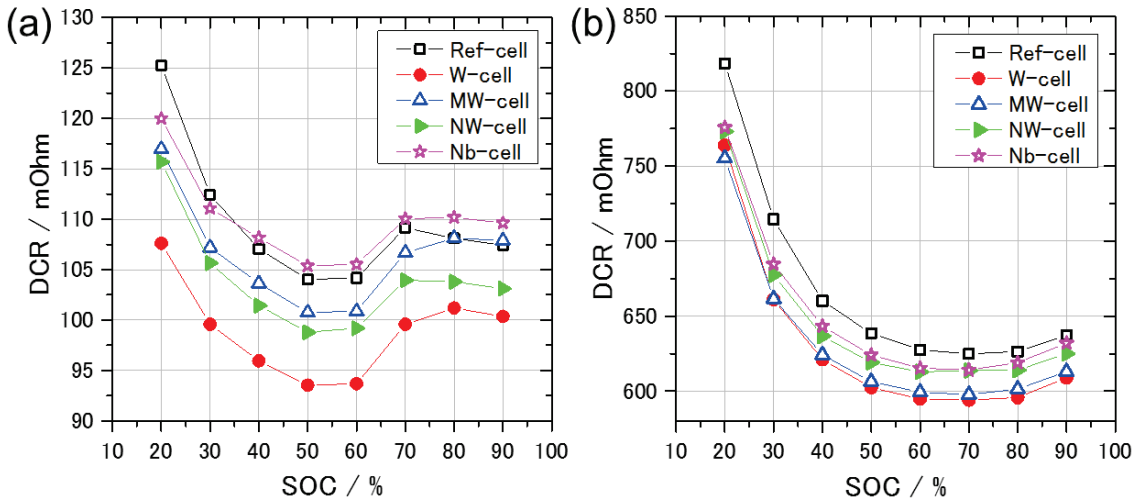

Fig. 4-17. DC resistance vs. state of charge plots of fresh full cells (a) at 25°C and (b) -10°C.

4.5.2 Cycle life test and DCR growth

This section presents the effect of lithium heavy metal oxide additives on full cells in the aspect of cycling stability and evolution of DC resistance during cycling. Figs. 4-18a, b give the cycle life of the full cells being cycled in the voltage range of 4.2 V to 2.7 V at 25°C and 45°C, respectively. In Fig. 4-18a, the cycle life of cells with modified electrodes is similar to the reference cell during 1400 cycles, and the benefit of the additives seems not obvious for cycle stability at room temperature. In Fig. 4-18b, however, compared to the prior art W-cell and the Ref-cell, the MW-, Nb-cell and NW-cell present a better cycling performance. So it can be concluded that the addition of lithium nickel tungsten oxide, lithium magnesium tungsten oxide and lithium niobium oxide brings an advantage to cycling stability, which is more pronounced than the addition of lithium tungsten oxide.

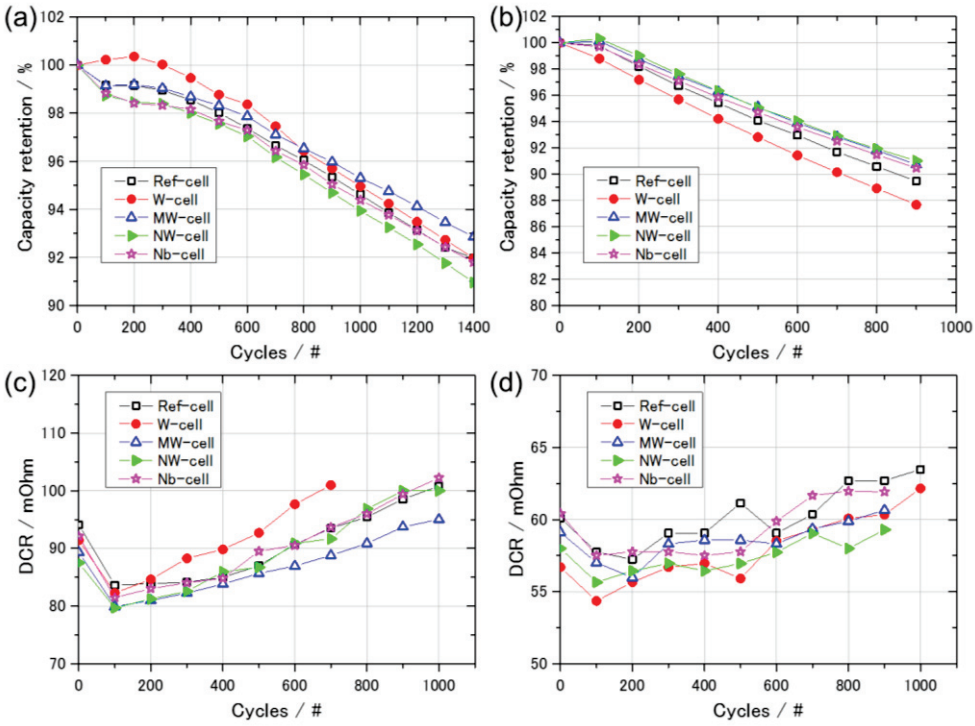

Fig. 4-18. Cycle life of full cells (a) at 25°C, (b) at 45°C and DCR during cycling (c) at 25°C, (d) at 45°C

Fig. 4-18c, d show the DC resistance measured every one hundred cycles during the cycling of full cells at 25°C and 45°C, respectively. The DC resistance of each cell increases during cycling. Compared to Ref-cell at 25°C, the Nb- and NW-cells have a similar performance, and the MW-cell has the smallest increase of DCR. The W-cell however has the worst DCR growth at room temperature. Thus, at room temperature, even though the W-cell has the smallest initial DCR (see Fig. 4-17), its DCR growth is the largest, which deteriorates the cycling performance. At higher temperature, the performance of DCR growth is quite similar for all cells. Thus, in the cycling tests of full cells, addition of Li_4MgWO_6, Li_4NiWO_6 and Li_3NbO_4 in the positive electrode leads to a much improved cyclability and good DC resistance. These additives are more effective and beneficial than Li_4WO_5.

4.5.3 Cell analysis after electrochemical cycling

In this section, we investigated if the electrode additives introduced in the slurry remain in the electrode after a cycling test of full cells. First, the MW-cell in Section 4.5.2 is disassembled after 2000 cycles, and the positive electrode is cut by ion beam milling. The cross-section morphology of the cycled positive electrode is analyzed with scanning electron microscopy. This measurement is conducted by a JEOL JSM 7100F scanning electron microscope (SEM) equipment under vacuum of 9.6×10^{-5} Pa at 25°C. The spectrum of the elements in the powders of the positive electrode is obtained by energy-dispersive X-ray spectroscopy (EDS) using SEM equipment. Fig. 4-19 gives the back scattering electron image of the positive electrode of the cycled MN-cell under magnification of 2500 times. The small white dots seem to be Li_4MgWO_6 particles and the big spherical particles are active NMC material. Four areas are selected in the EDS test (see Fig. 4-19), providing information on the elements found there. It is shown that Spectrum areas 1 and 3 barely have a trace of W, which indicates the additive does not diffuse into NMC particles and remains on the surface of the particles or in the pores between the particles, as demonstrated by the results of areas 2 and 4. The ratio of W to Mg is smaller than its initial value in the compound of Li_4MgWO_6, which is believed to be caused by selective dissolution of W into the electrolyte during cycling. The dissolution may be related to certain reactions that may be helpful to reduction of DCR growth. In accordance with SEM and EDS results, it can be confirmed that after a cycling test the electrode additives still exist in the positive electrode.

Secondly, the positive electrode is analyzed by X-ray diffraction by disassembling the cells after being cycled for 2000 times. Fig. 4-20 compares the XRD patterns of a fresh cell (pattern in the middle), the cycled cell (pattern at the top), and the

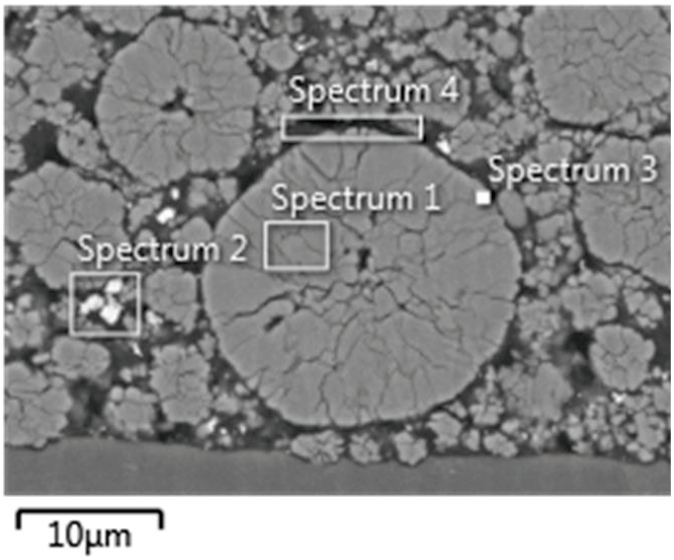

Spectrum Area	W/(Ni+Mn+Co) / mol %	W/Mg / mol %
#1	0.0	---
#2	10.3	75.8
#3	0.0	---
#4	0.1	75.0

Fig. 4-19. SEM image of positive electrode of MW-cell after 2000 cycles under magnification of 2500 times and the summary of Molar ratio of selected areas for a cycled MW-cell obtained by SEM/EDS.

only additive (pattern at the bottom) for each additive. In case of MW, because MW itself has low crystallinity and show low intensity of Bragg peaks, MW phase can't be detected even in XRD pattern of fresh electrode. On the other hand, NW and Nb themselves have adequately high crystallinity and their phases are found in the fresh cells. However, after 2000-times cycling, MW phase disappears and Nb phase remains as marked by arrows. In addition, as the lattice parameters of Li_3NbO_4 slightly increase during cycling, which could be caused by defects or residual stress - we also see the pattern shift slightly to the left. During cycling, Li_4NiWO_6 may lose the crystallinity or be decomposed. Thus, the XRD result of the Nb-cell confirms that the additive Li_3NbO_4 remains in the positive electrode after cycling.

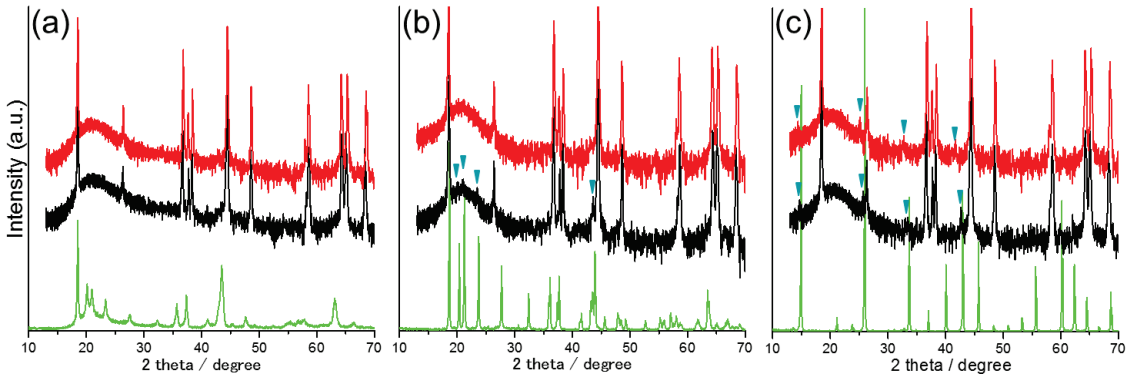

Fig. 4-20. XRD patterns of positive electrodes in fresh cell (middle pattern); in cycled cell (after 2000 cycles) (top), and only additice (bottom) for (a) MW, (b) NW, and (c) Nb-cell.

4.6 Conclusion

Li-excess layered compound Li_4MeWO_6 (Me=Ni, Mn, Co) and its solid solution with $LiMO_2$ are synthesized and their electrochemical properties are investigated. Large capacity exceeding theoretical capacity based on Ni(II/IV) couple is observed, indicating redox reaction of oxide ions. Li_4MeWO_6 (Me=Ni, Mg) was also examined as application to the additive of positive electrodes gave an improvement of power performance and cycle stability of large full cells. Since all components of full cells are interacting each other during electrochemical cycling, the improvement mechanism is probably complexed and will be investigated in future.

References

1. R. Hoffmann and R. Hoppe, *Z. Anorg. Allg. Chem.*, 1989, **1989**, 157.
2. N. Yabuuchi, M. Takeuchi, M. Nakayama, H. Shiiba, M. Ogawa, K. Nakayama, T. Ohta, D. Endo, T. Ozaki, T. Inamasu, K. Sato and S. Komaba, *Proc. Natl. Acad. Sci. U. S. A.*, 2015, **112**, 7650.
3. N. Yabuuchi, M. Takeuchi, S. Komaba, S. Ichikawa, T. Ozaki and T. Inamasu, *Chem Commun (Camb)*, 2016, **52**, 2051.
4. N. Yabuuchi, Y. Tahara, S. Komaba, S. Kitada and Y. Kajiya, *Chem. Mater.*, 2016, **28**, 416-419.
5. T. Matsuhara, Y. Tsuchiya, K. Yamanaka, K. Mitsuhara, T. Ohta and N. Yabuuchi, *Electrochemistry*, 2016, **84**, 797-801.
6. S. J. R. Prabakar, S. C. Han, S. P. Singh, D. K. Lee, K.-S. Sohn and M. Pyo, *J. Power Sources*, 2012, **209**, 57-64.
7. R. Kokado, K. Mori, M. Takagi and T. Hayashi, *Patetnt*, 2013, **WO2013/125426 A1**.
8. K. Shimokita and K. Kawai, *Patetnt* 2013, **US 2013/0277604 A1**.
9. P. Strobel and B. L. Andron, *J. Solid State Chem.*, 1988, **75**, 90.
10. A. D. Robertson and P. G. Bruce, *Chem Commun (Camb)*, 2002, 2790-2791.
11. N. Yabuuchi, K. Yoshii, S. T. Myung, I. Nakai and S. Komaba, *J Am Chem Soc*, 2011, **133**, 4404-4419.
12. M. Sathiya, K. Ramesha, G. Rousse, D. Foix, D. Gonbeau, K. Guruprakash, A. S. Prakash, M. L. Doublet and J. M. Tarascon, *Chem Commun (Camb)*, 2013, **49**, 11376-11378.

13. J. Bao, D. Wu, Q. Tang, Z. Ma and Z. Zhou, *Phys. Chem. Chem. Phys.*, 2014, **16**, 16145-16149.

14. Z. Lu and J. R. Dahn, *J. Electrochem. Soc*, 2002, **149**, A815.

15. D. Mohanty, S. Kalnaus, R. A. Meisner, K. J. Rhodes, J. Li, E. A. Payzant, D. L. Wood and C. Daniel, *J. Power Sources*, 2013, **229**, 239-248.

16. O. Dolotko, A. Senyshyn, M. J. Mühlbauer, K. Nikolowski and H. Ehrenberg, *J. Power Sources*, 2014, **255**, 197-203.

17. U. Jayarathne, P. Chandrasekaran, A. F. Greene, J. T. Mague, S. DeBeer, K. M. Lancaster, S. Sproules and J. P. Donahue, *Inorg Chem*, 2014, **53**, 8230-8241.

18. C. S. Johnson, J. S. Kim, C. Lefief, N. Li, J. T. Vaughey and M. M. Thackeray, *Electrochem. Comm.*, 2004, **6**, 1085-1091.

Chapter 5. Sodium and Manganese Stoichiometry of P2-Type $Na_{2/3}MnO_2$

5.1 Introduction

In Chapter 3 and 4, we have discussed the material development of Li-excess layered materials for LIBs as a purpose of high-capacity and/or high power application for LIBs. These have a chance to be applied for energy-density priority use such as portable electronics and electric vehicles. On the other hand, for application to large-format batteries, low cost is first priority and NIBs can be fit this direction. In addition to a great potential of NIBs for practical application, there are 2 more advantages to study on NIBs, 1) comparison of working mechanism with LIB system, 2) many compositions remained un-studied in the structural and physical field as well as electrochemistry as described already.

NIBs have been intensively studied for future application including grid-scale storages due to sodium availability across the world.[1] Among various positive electrode materials, layered sodium transition metal oxides (Na_xMO_2) based on abundant metals have attracted continuous attention,[2] and especially, Mn-based materials meet requirements for low cost battery systems without sacrificing energy density and safety.[3, 4] Besides their industrial benefit, Na_xMnO_2 stimulates scientific interests due to its unique phase variation. Phase diversity of Na_xMnO_2 usually depends on Na/Mn ratio,[5] and each phase has been discussed based on the criteria reported in 1980.[6] In accordance with this manner, the layered Na_xMnO_2 has several polymorphs, so-called P2- and O3-type classified by different MnO_2-slab stacking along *c*-axis. Their electrochemical Na extraction/insertion was firstly reported by Mendiboure *et al.* in 1985.[7] A valence state

of Mn also affects the polymorphism, and in particular, six-coordinated Mn(III) (t_{2g}^3-e_g^1) leads to distorted phase variation due to co-operative Jahn-Teller distortion (CJTD). In electrochemical discussion, since the Mn(III/IV) redox couple is thought to cause large and anisotropic volume change[2, 8, 9] and localization of cations and electrons due to a long range ordering of Na^+/vacancy and honeycomb structure of Mn(III/IV),[10, 11] Mn(III) ions have been regarded as "un-favorable" components which should be ruled out from targeted materials for battery application. Therefore, recent strategy has been based on the idea to keep average oxidation state of manganese close to +4 to avoid the Jahn-Teller effect of Mn(III) by substitution of other mono- or di-valent cations.[9, 12-14] However, we find no reports to fully understand and solve drawback of CJTD in layered Na_xMnO_2.

In this chapter, the study on P2-type $Na_{2/3}MnO_2$ polymorphs as basic Mn redox materials with/without CJTD will be described. By establishing successful preparation route for high-purity samples of the P2-$Na_{2/3}MnO_2$ polytypes, we discuss how the polymorphic characteristics bring difference in electrochemical and structural properties during (de)sodiation. We further demonstrate highly reversible redox of Mn(III/IV) couple involving CJTD in layered oxides.

5.2 Synthesis and structural characterization

5.2.1 Synthesis

The synthesis condition of $Na_{2/3}MnO_2$ polymorphs is summarized in Fig. 5-1. Stoichiometric mixtures of Na_2CO_3 (Kanto Chemical Co., Ltd.) and Mn_2O_3 powders were treated by ball-milling with acetone addition for 12 h at 600 rpm. The mixtures were dried, and then obtained powder was pressed into pellets. For the distorted $Na_{2/3}MnO_2$ sample, the pellet was heated in air at 1 °C min^{-1} up to 1050 °C and then, quenched by taking the reaction product out from the heated furnace and immediately transferred into an argon-filled glove box. To obtain the undistorted $Na_{2/3}MnO_2$ sample, the as-prepared distorted $Na_{2/3}MnO_2$ was used as the starting material and pressed into pellet. The pellets were heated up to 700 °C and slowly cooled to 500 °C, then quenched in the same way. The samples were cooled to room temperature in the glove box and were kept inside to avoid the contact with moisture and oxygen in air.

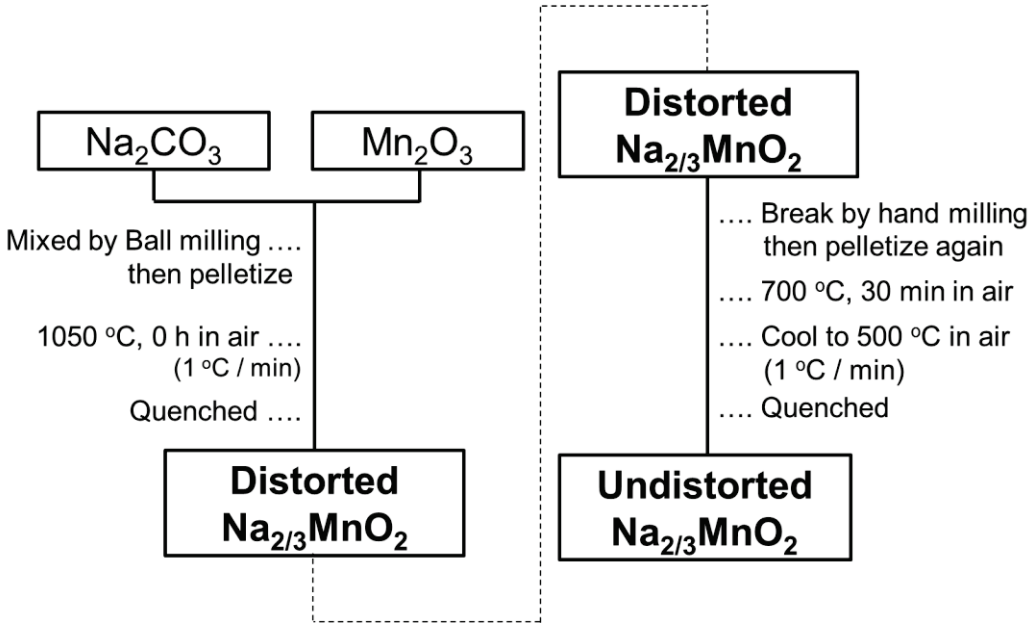

Fig. 5-1. Synthesis condition of $Na_{2/3}MnO_2$ polymorphs

5.2.2 Structural Characterization

Historically, the distorted polymorph with orthorhombic lattice is denoted by adding an additional prime symbol (P'2-Na_xMnO_2).[5, 15, 16] Crystallization of P2- and P'2-Na_xMnO_2 is highly dependent on synthesis condition such as heating process and Na/Mn ratio.[5, 9] P'2-Na_xMnO_2 is obtained by quenching from over 1000 ^oC, while synthesis of P2-Na_xMnO_2 requires slow cooling process after heating to ca. 1000 ^oC.[9, 15, 16] Because of uncontrollable Na loss during firing, P2/P'2 mixed phase[16] and/or monoclinic impurity phases[9, 15] always come out together in previous studies. During the cooling process, Mn(III) in P'2-Na_xMnO_2 tends to be Mn(IV) having no distortion, and simultaneously oxygen uptake occurs for charge compensation, which results in creating vacancy in Mn layer.[5, 16-18] Parant *et al*. first reported crystal structure, Jahn-Teller effect on lattice, sensitivity of the synthesis, and implication of Mn vacancy for the polymorphs in 1971.[5] Based on these knowledge, we stood for the idea that single phase of P2-Na_xMnO_2 can be only obtained from pure P'2-Na_xMnO_2 without Na loss, and we first optimized synthesis condition for pure P'2-$Na_{2/3}MnO_2$. Detailed synthesis condition and XRD patterns are shown in Fig. 5-2a, and hereinafter we term P2- and P'2-$Na_{2/3}MnO_2$ samples as *h*-NMO and *o*-NMO, respectively. The arrows in the inset indicate impurity peaks and an additional impurity peak appears for the sample synthesized with only 1wt% excess Na. Our optimization on synthesis for *o*-NMO shows that only 50 ^oC difference caused impurity which could be detected only by SXRD measurement.

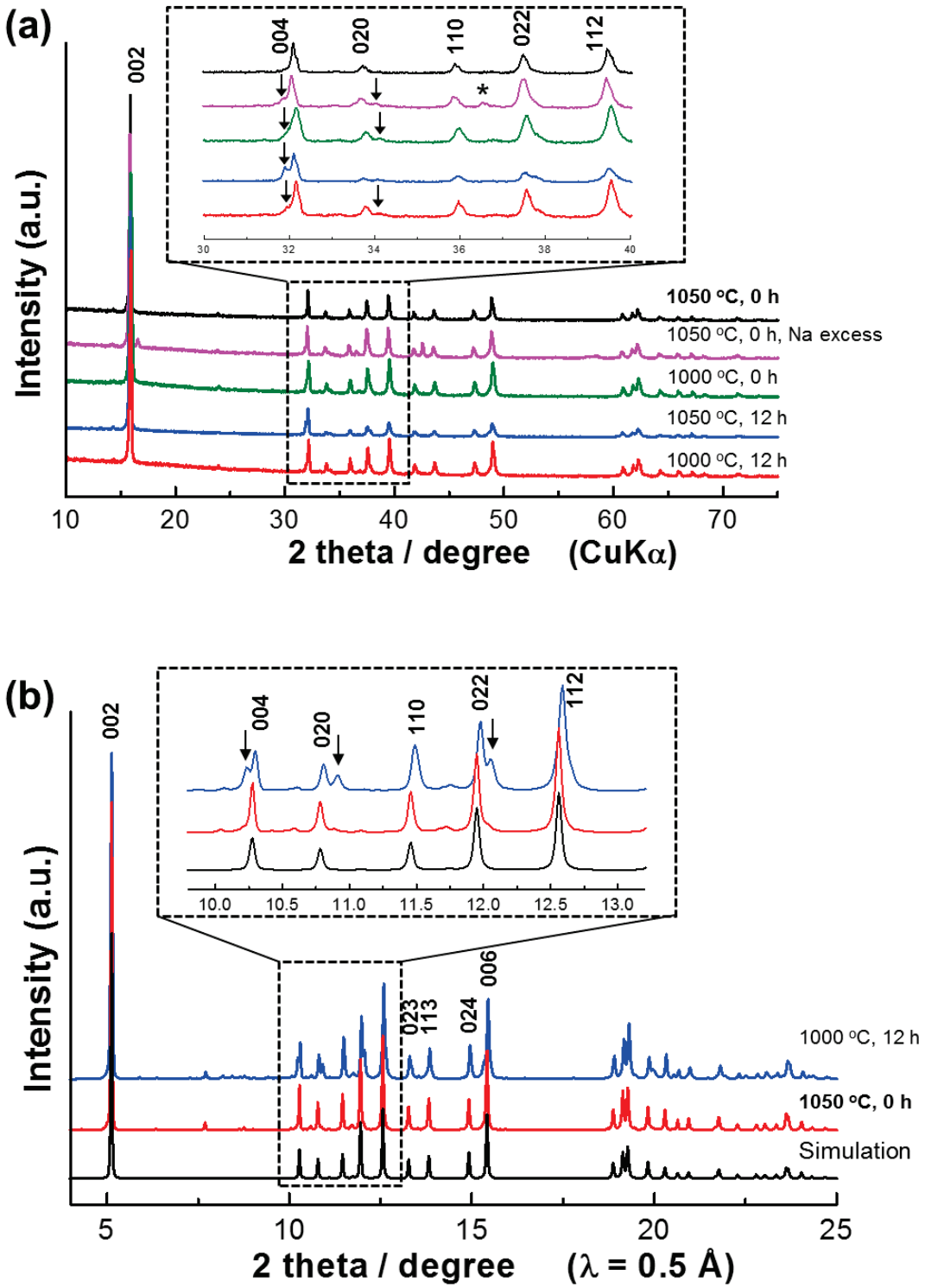

Fig. 5-2. (a) XRD and (b) SXRD patterns of *o*-NMO samples synthesized with different conditions.

As shown in Fig. 5-3a, heating up to 1050 °C followed by quench is the best synthesis condition to obtain pure *o*-NMO, and all the diffraction peaks, except a peak at 2θ = 7.8° indicated as ▼, can be indexed as P'2-type layered structure (S.G.*Cmcm*), whereas *h*-NMO was obtained by heating up *o*-NMO again to 700 °C followed by slow cooling to 500 °C and quench. Fig. 5-3b shows an SXRD pattern of *h*-NMO, and all the diffraction peaks can be indexed as P2-type structure (S.G. $P6_3/mmc$). As we expected, *h*-NMO was successfully obtained without impurity, and this is the first report to characterize structure of the pure P2-$Na_{2/3}MnO_2$ based on SXRD. Then, we conducted Rietveld analysis by using RIETAN-FP.[19] *R* factors for both samples become adequately low, and the lattice constant of *o*-NMO well agrees with the literatures (Table 5-1).[9, 16] Larger occupancy at Na_e than Na_f for *o*-NMO is observed, which is due to the fact that Na_e sites edge-sharing with MnO_6 octahedra are energetically more favorable than Na_f

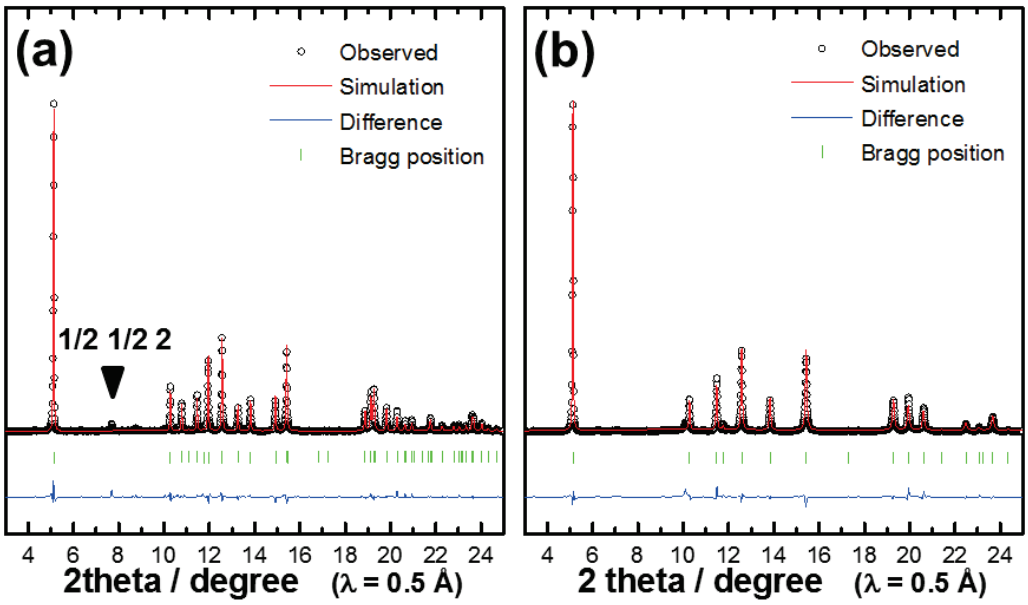

Fig. 5-3. SXRD patterns and fitting result by the Rietveld analysis on (a) *o*-NMO and (b) *h*-NMO

face-sharing with MnO_6 due to lower Na^{+}-$Mn^{(III/IV)}$ electrostatic repulsion. Compared with *o*-NMO, Na_f sites are more occupied and Na_e sites are less occupied for *h*-NMO, which agree with the appearance of Mn defect for *h*-NMO. The ratio of lattice constant of *o*-NMO is calculated to be $b_{ortho}/a_{ortho} = 1.87$, suggesting huge distortion due to longer *b* and shorter *a* axes compared to $b_{ortho}/a_{hexa} = \sqrt{3}$ for hexagonal lattice. Lattice parameter of a'_{ortho} is defined by using the parameter of distortion, δ to compare with a_{hexa}.and the degree of distortion, δ, is estimated to 8% for *o*-NMO. In Fig. 5-4, Anisotropic Mn-O bond length obtained by the refinement, in-plane arrangement of *o*-/*h*-NMO and the definition of δ are presented.

Table 5-1. Refined crystallographic parameters by Rietveld analysis for (a) *o*-NMO and (b) *h*-NMO. The fixed parameters are indicated by superscript "a." The isotropic displacement parameter, B, is refined after the refinement of other parameters as labeled superscript "b".

(a) *S.G., Cmcm*
a = 2.8389(1) Å, *b* = 5.3137(1) Å, *c* = 11.1503(2) Å

Atom	site	*x*	*y*	*z*	g	B
$Na_f(1)$	4*c*	0.0	-0.068(4)	1/4	0.182(4)	3.1(6) [b]
$Na_e(2)$	4*c*	0.0	0.312(1)	1/4	0.458(2)	1.4(2) [b]
Mn	4*a*	0.0	0.0	0.0	1.0 [a]	0.27(3) [b]
O	8*f*	0.0	0.6488(6)	0.0934(3)	1.0 [a]	0.72(8) [b]

R_{wp} = 13.0%, S = 1.44, R_B = 3.68% , R_F = 2.05%

(b) *S.G., P6₃/mmc*
a = 2.8827(1) Å, *c* = 11.1509(3) Å

Atom	site	*x*	*y*	*z*	g	B
$Na_f(1)$	2*b*	0.0	0.0	1/4	0.277(4)	5.6(4) [b]
$Na_e(2)$	2*c*	1/3	2/3	1/4	0.313(4)	4.3(3) [b]
Mn	2*a*	0.0	0.0	0.0	0.9 [a]	0.49(3) [b]
O	4*f*	1/3	2/3	0.5897(3)	1.0 [a]	1.1(1) [b]

R_{wp} = 11.8%, S = 1.38, R_B = 6.29% , R_F = 3.76%

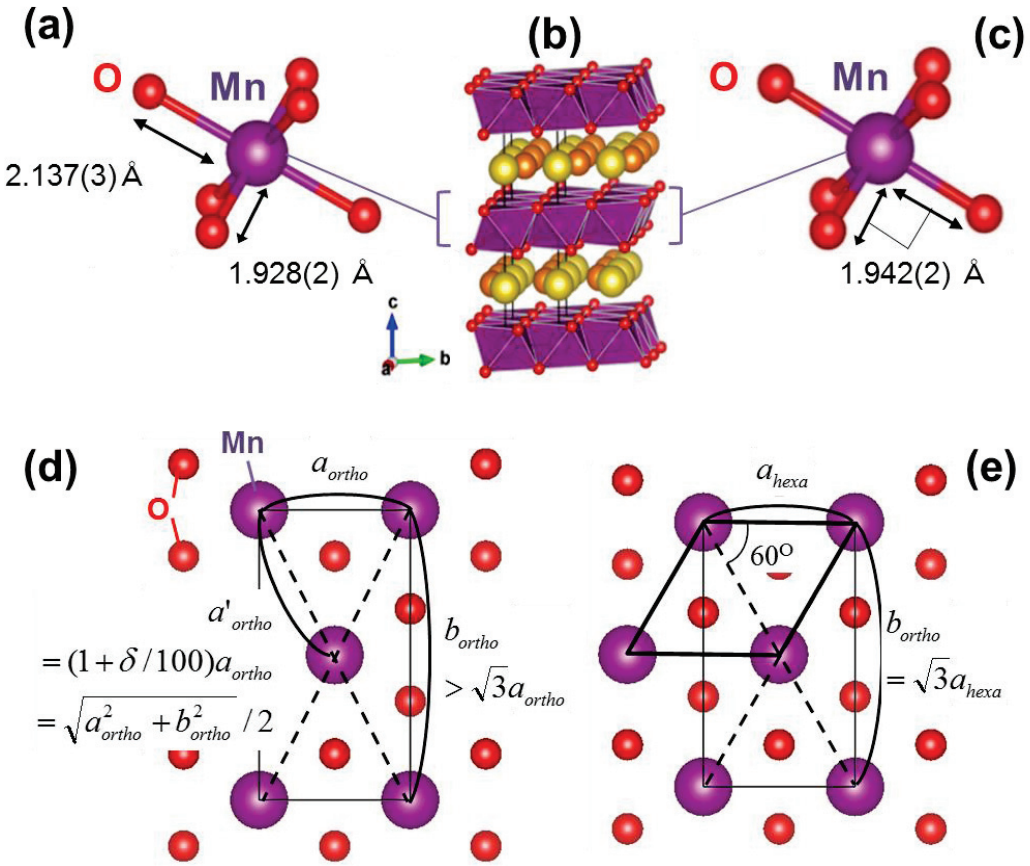

Fig. 5-4. Schematic illustration of (a) MnO_6 octahedra for *o*-NMO, (b) P2-type layered structure, and (c) MnO_6 octahedra for *h*-NMO. The arrangement of MnO_2 slab for (d) *o*-NMO and (e) *h*-NMO.

In addition to the structural analysis, ICP and iodometry measurement is conducted to determine the actual composition of the obtained samples. Table 5-2 shows that *o*-/*h*-NMO have the identical Na/Mn ratio from ICP analysis. By combining results of iodometry for average oxidation state of Mn, the chemical formula of *o*- and *h*-NMO were determined as $Na_{0.64}MnO_2$ and $Na_{0.59}Mn_{0.9}\square_{0.1}O_2$, respectively, in which vacancy of Mn site is expressed by □. Note that possible honeycomb-type charge ordering of Mn(III):Mn(IV) = 2:1 is thought to stabilize the *o*-NMO phase as the schematic

illustration is shown in Fig. 5-5a. In contrast, Mn vacancies of *h*-NMO is thought to be randomly distributed and charge distribution on Mn is also diffused. (Fig. 5-5b) Regarding the un-assigned peak at 2θ = 7.8° of *o*-NMO, a transmission electron microscope (TEM) image along [001] for *o*-NMO clearly indicates strong subspots of electron diffractions originating from an in-plane superstructure with $6a_{ortho}$*$4b_{ortho}$ units (Fig. 5-5c) which was not observed previously according to our knowledge. By using larger unit cell, the peak at 2θ = 7.8° can be assigned to "1/2 1/2 2" index. In Fig. 5-5f, streaky patterns along [100] of *h*-NMO support existence of stacking faults resulting from the Mn defect. Furthermore, possibilities of ordering of Mn vacancy along <310> for *h*-NMO (Fig. 5-5d) (similar to that of $Na_2Mn_3O_7$[20, 21]) and *c*-axial superstructure for *o*-NMO (Fig. 5-5e) are also proved. SEM and TEM images shown in Fig. 5-6 also confirm that average particle size is around 5 um and the morphology of the polymorphism is quite similar each other. SXRD, TEM, and electron diffraction results convinced the successful single-phase formation of $Na_{2/3}MnO_2$ polymorphs. Namely, *o*-NMO has remarkable CJTD without Mn vacancy though *h*-NMO has Mn vacancy without distortion.

Table 5-2. The summary of compositional analyses.

Sample	Oxidation state of Mn	Na/Mn ratio (Iodometry)	O/Mn ratio (ICP)	Composition
o-NMO	+ 3.37	0.64	2.00	$Na_{0.64}Mn^{+3}_{0.63}Mn^{+4}_{0.37}O_2$
h-NMO	+ 3.76	0.65	2.21	$Na_{0.59}Mn^{+3}_{0.16}Mn^{+4}_{0.74}\square_{0.10}O_2$

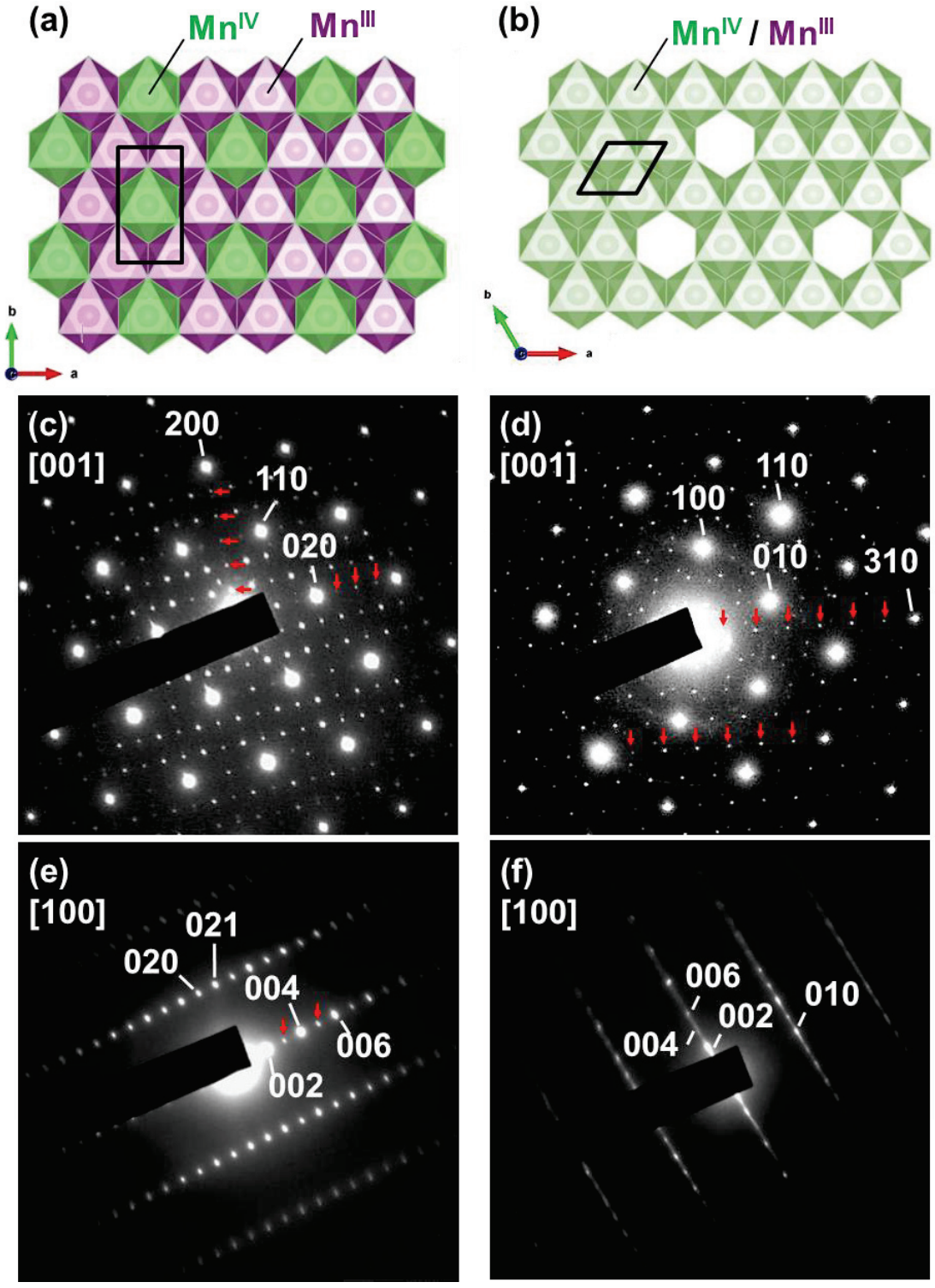

Fig. 5-5. Schematic illustration of MnO_2 layer of (a) *o*-NMO, (b) *h*-NMO and electron diffraction patterns along [001] for (c) *o*-NMO, (d) *h*-NMO, along [100] for (e) *o*-NMO, (f) *h*-NMO. The superstructure reflections are indicated by red arrows.

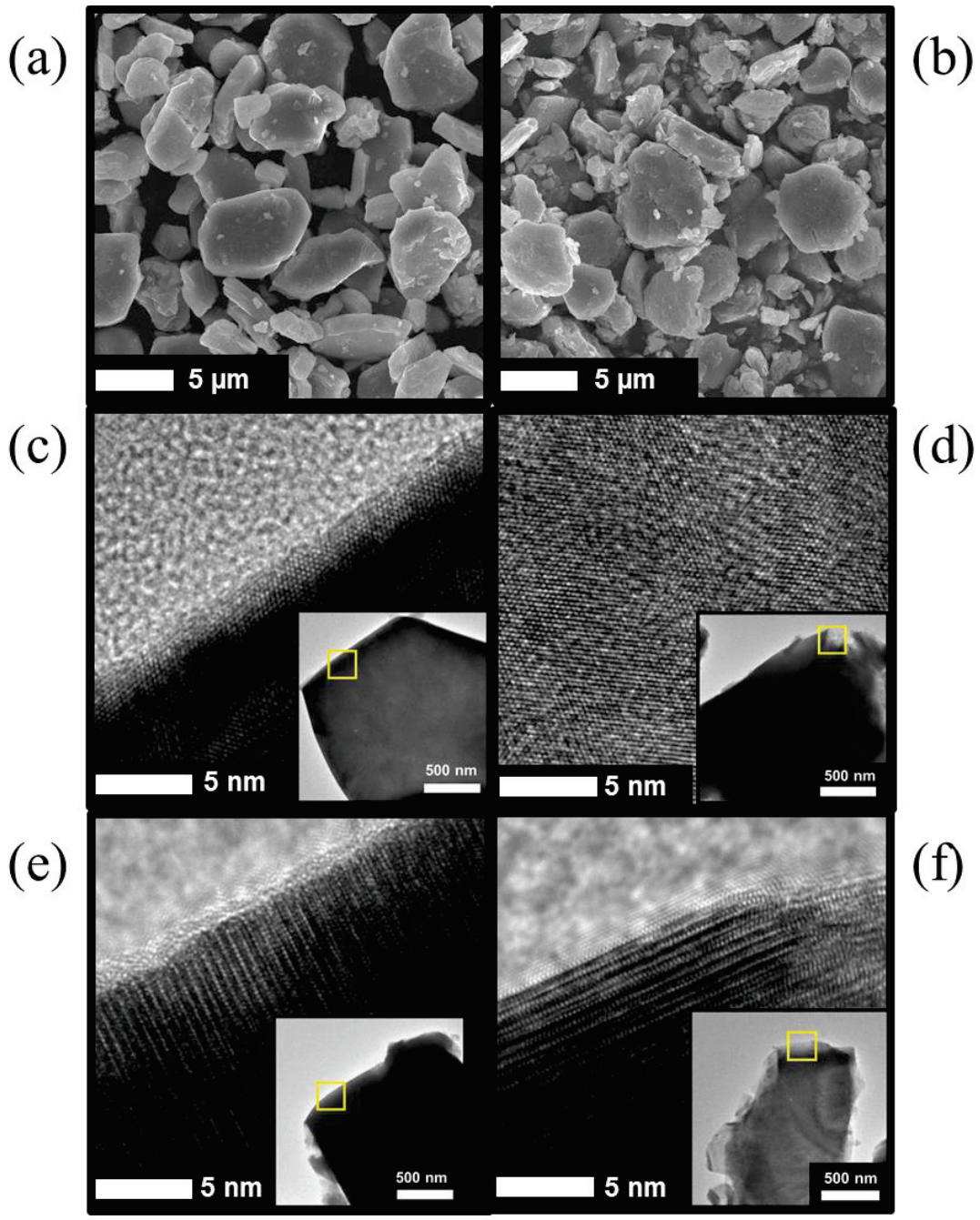

Fig. 5-6. SEM images of (a) *o*-NMO and (b) *h*-NMO and TEM images along [001] of (c) *o*-NMO and (d) *h*-NMO and along [100] of (e) *o*-NMO and (f) *h*-NMO. The observed area of TEM images in (c), (d), (e), and (f) corresponds to the area to observe electron diffraction patterns in Fig. 5-4.

5.3 Electrochemical characterization

5.3.1 Electrochemical properties

Their electrochemical properties of *o*- and *h*-NMO were further investigated in non-aqueous Na cells, and charge/discharge curves are represented in Fig. 5-7. *o*- and *h*-NMO show different first charge capacities of 142 and 94 mAh g^{-1}, corresponfding to 0.54 and 0.37 Na extraction, which are consistent with oxidation up to +4 from +3.37 and +3.76 of Mn (Table 5-2), respecFively. *o*-NMO delivers the larger reversible capacity of 216 mAh g^{-1} with average working voltage of about 2.74 V, demonstrating the higher energy density of ca. 590 Wh $(kg\text{-}oxide)^{-1}$ than 520 Wh $(kg\text{-}oxide)^{-1}$ for P2-$Na_xFe_{1/2}Mn_{1/2}O_2$.[2] On the other hand, although *h*-NMO has relatively smooth curves, its energy density is the lower energy of 490 Wh $(kg\text{-}oxide)^{-1}$ with initial reversible capacity of 198 mAh g^{-1}. Fig. 5-8 summarizes the energy density map of Na-ion cells with reported positive materials and hard-carbon anodes.[3, 13, 22, 23] For a hard carbon//*o*-NMO full cell, the calaculated energy density is more than 300 Wh kg^{-1}. Moreover, *o*-NMO shows excellent cycle stability, and >94% of initial discharge capacity is retained after 25 cycles (Fig. 5-9) in spite of the strong distortion and multiple-stepswise profiles indicating phase transitions. *dQ/dV* plots of *o*-NMO show highly reversible and stable profiles during cycles as showsn in Fig. 5-10a. For *h*-NMO, however, the capacity degradation is unavoidable unless limiting cut-off voltage (see Fig. 5-9). which is related with capacity decay. The intense peak between 2.0 and 2.2V is continuously broadened during cycles. The irreversible change of reduction peak below 2.2 V is seen in *dQ/dV* plots of *h*-NMO, suggesting structural change (Fig. 5-10a). Inferior rate property of *h*-NMO to *o*-NMO is evidenced (Fig. 5-10b) probably because the 10% Mn defects induce severe charge disorder in the $Mn_{0.9}O_2$ slab and deterioration of Na^+ duffusivity. Since particle size (~5

μm) and morphology of both samples are identical (Fig. 5-6), only explanation for these different electrochemical properites can be laid on crystal structure including CJTD, long-range ordering, and different Mn stoichiometry of these polymorphs.

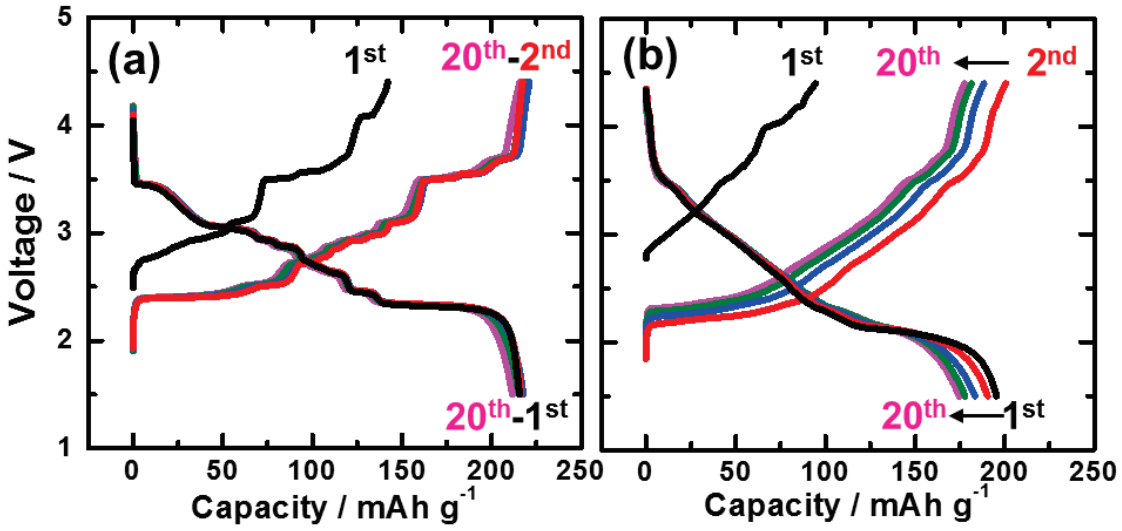

Fig. 5-7. Charge/discharge curves of (a) *o*-NMO and (b) *h*-NMO between 4.4-1.5V.

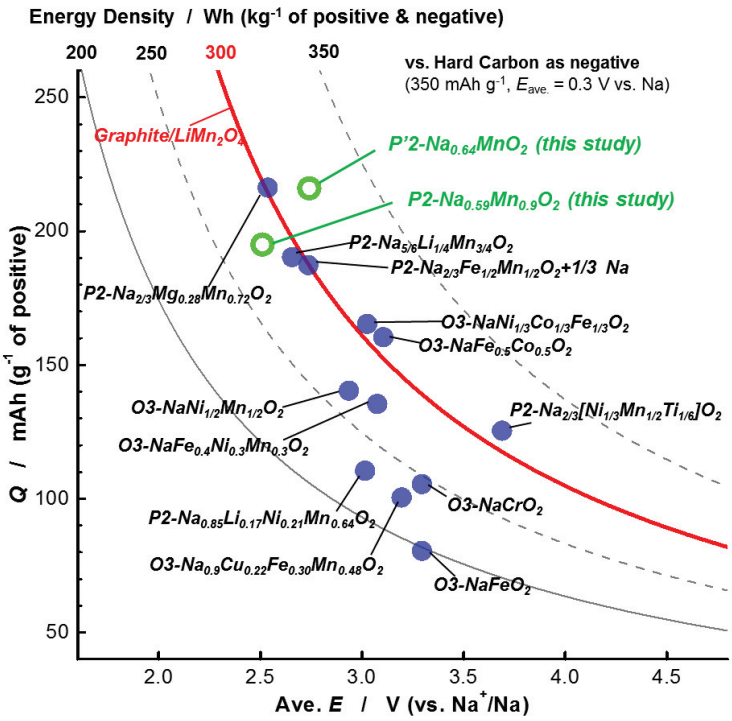

Fig. 5-8. Average voltage versus gravimetric capacity plots for reported positive materials with calculated energy density curves.[3, 13, 22, 23]

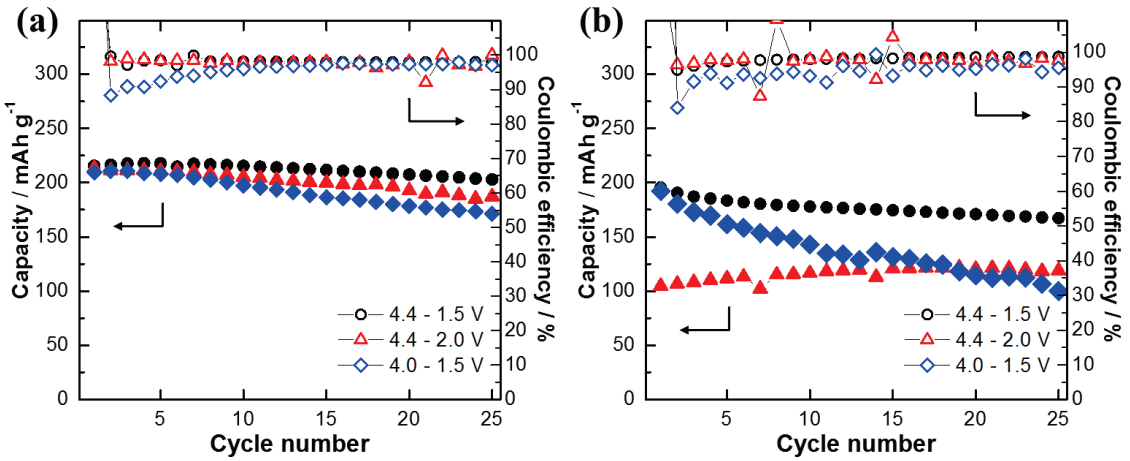

Fig. 5-9. Average voltage versus gravimetric capacity plots for reported positive materials with calculated energy density curves.

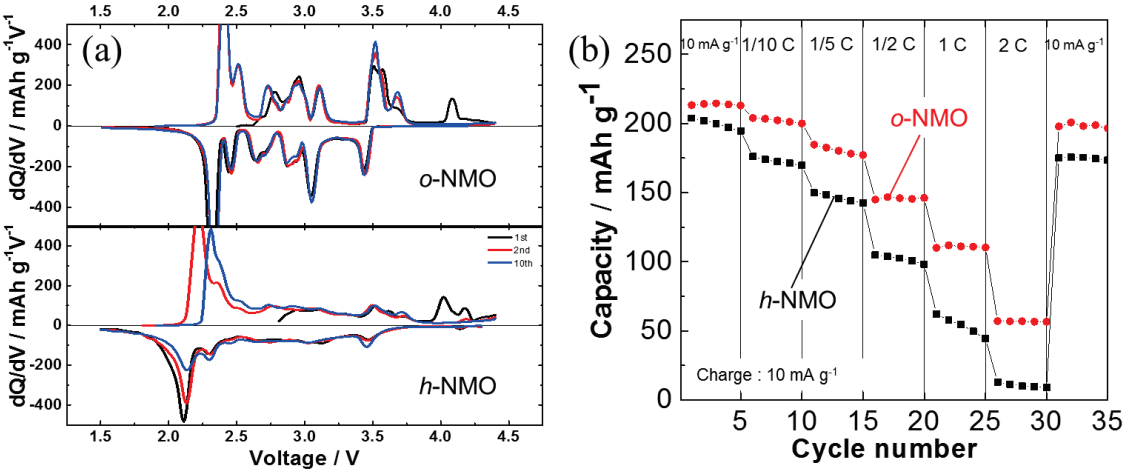

Fig. 5-10. (a) *dQ/dV* plot and (b) rate performance of *o*-NMO and *h*-NMO in Na cells. Current rate of 1C for *o*- and *h*-NMO is set to 262 mA g^{-1} and 254 mA g^{-1}, respectively, by considering their theoretical capacity based on Mn(III/IV) redox couple, 1.0 and 0.9 mol electrons for *o*-NMO and *h*-NMO. The constant charge rate of 10 mA g^{-1} was applied for all cycles of both cells of *o*- and *h*-NMO. The constant charge rate of 10 mA g^{-1} was applied for all cycles of both cells.

5.3.2 Reaction mechanism

Structural evolution during the initial galvanostatic cycle was further studied with operando XRD as shown in Fig. 5-11 for *o*-NMO and Fig. 5-13 for *h*-NMO. The P'2 phase (denoted as P'2-I in the figure) of *o*-NMO is maintained in $0.25 < x < 0.80$ in Na_xMnO_2, and changed into OP4 phase in $x < 0.3$ during charge. OP4-phase is also confirmed by *ex-situ* XRD (Fig. 5-12a).[2, 9] Furthermore, we simulate XRD patterns by introducing stacking faults of random O/P staking into the OP4-type structure by DIFFaX program and obtain better agreement with the experimental XRD pattern of the sample charged to 4.4 V. As shown in Fig. 5-12c, P2 and O2 structures are distinguished by the prismatic or octahedral environment for Na sites. OP4 structure with ideal stacking has ordered alternative stacking of P- and O-type Na layers. On the other hand, OP4 structure with stacking fault has random stacking of P- and O-type Na layers. The diffraction pattern of *o*-NMO charged to 4.4 V matches the simulated pattern of OP4 having stacking fault rather than ideal OP4 structure. Therefore, we concluded that the structure of *o*-NMO in $x < 0.3$ during charge is OP4 phase with stacking fault and this phase formation is derived from selective Na extraction from Na layer and the partial gliding of MnO_2.

During discharge, the OP4 phase reversibly transforms to P'2-I and finally to different P'2 phase (P'2-II) in $x > 0.64$. In addition, clear stepwise change in positon of 022 diffraction is observed in P'2-I phase, and the step intervals are consistent with the charge/discharge curves. Totally, 7 sub-phases, P'2-$l_{(1\text{-}7)}$ can be seen in $0.2 < x < 0.6$ as marked with white dashed lines in Fig. 5-11. Given CJTD effects along *b*-axis, complicated stepwise behavior of 022 line suggests interaction between Na/vacancy and Mn(III/IV) charge orderings via CJTD. Such interactive coupling has also been reported

in O'3-Na_xMnO_2,[24] and the detailed structural study of *o*-NMO is now under way and will be summarized in future.

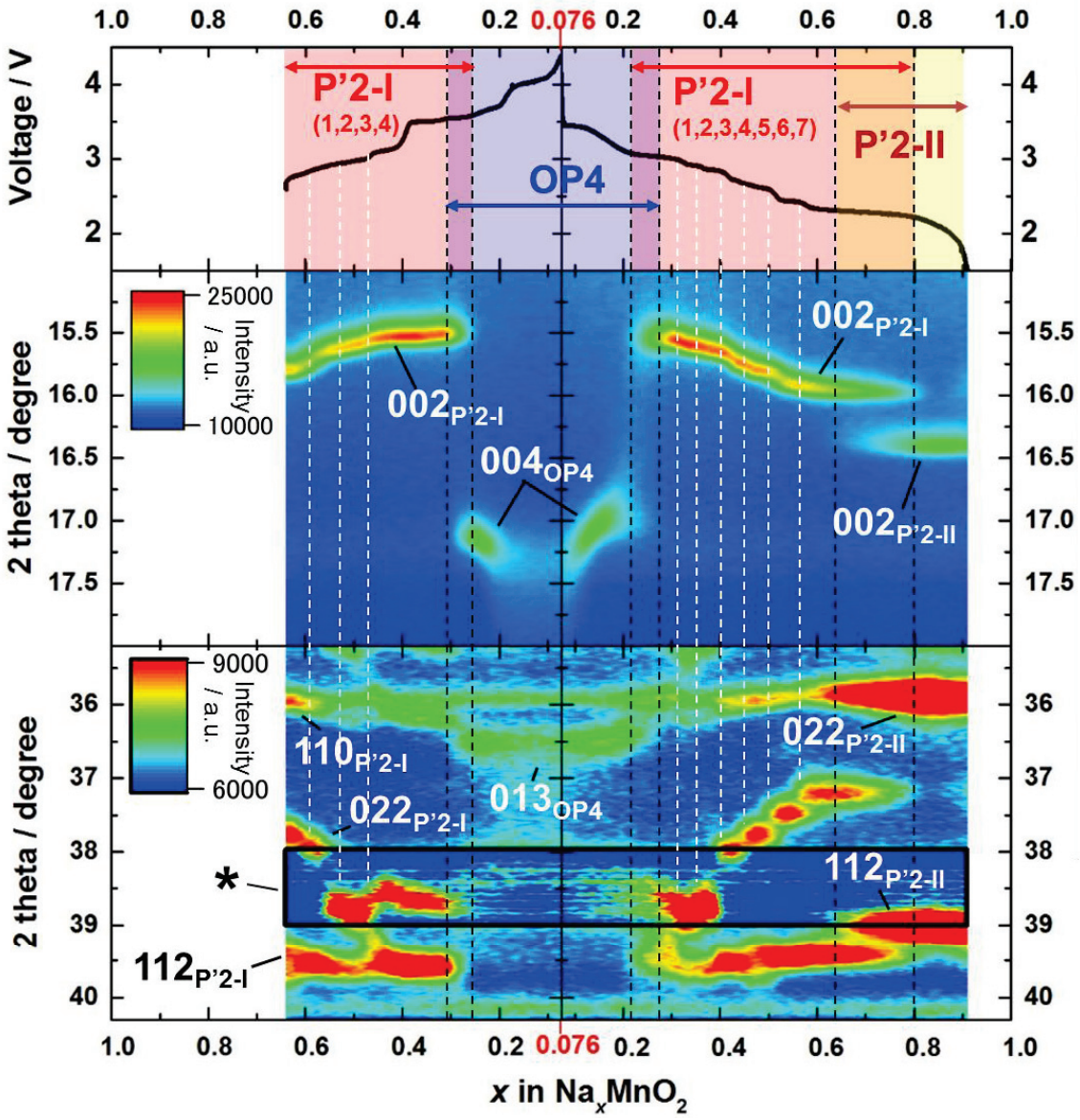

Fig. 5-11. The initial charge/discharge curves and phase evolution (top) and contour maps of operando XRD patterns for *o*-NMO. The diffraction intensity in the region marked "*" is treated by subtracting the background diffraction of Be window.

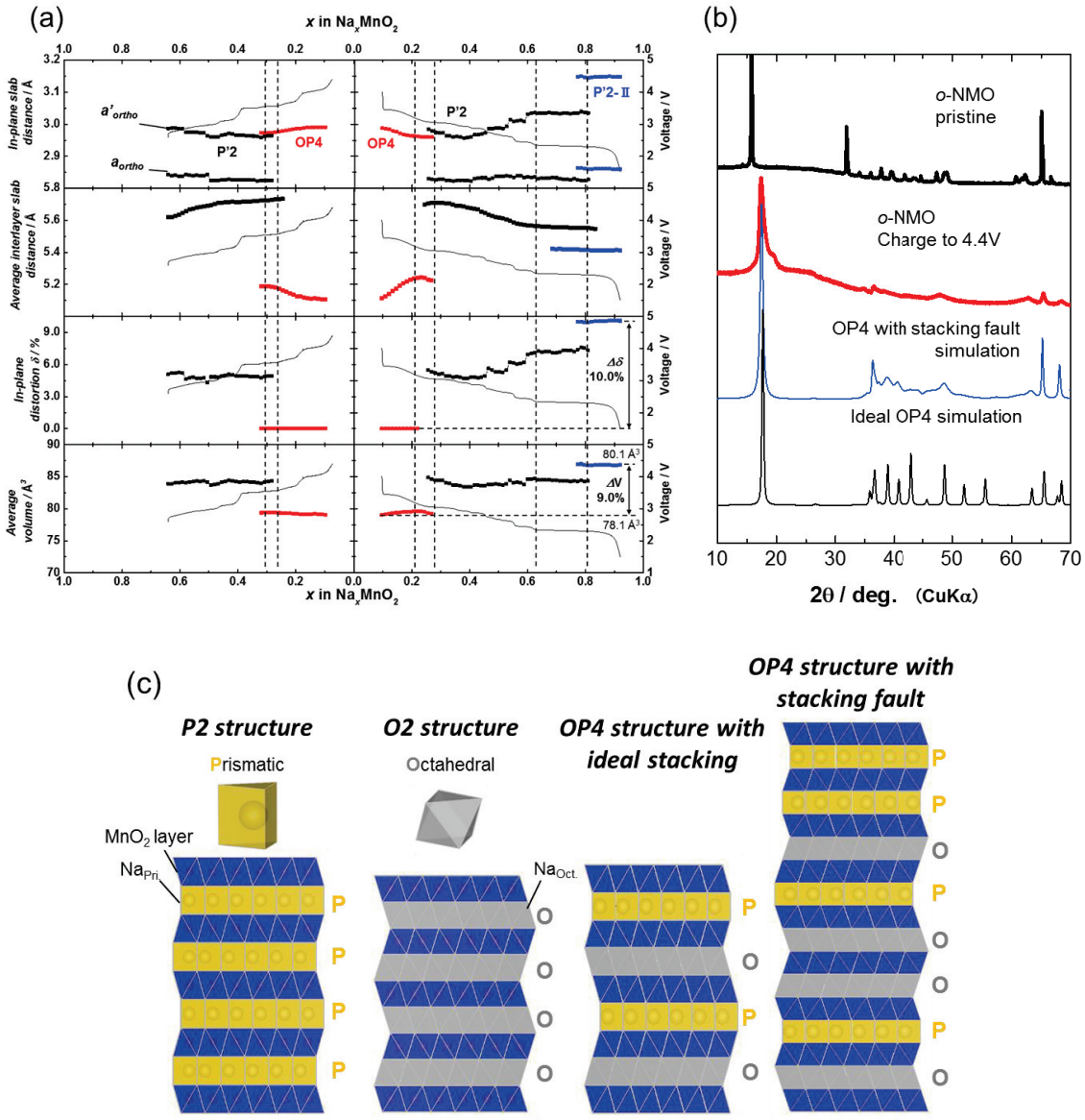

Fig. 5-12. (a) The change of MnO_2-slab distance, lattice distortion, and lattice volume during 1st cycle calculated from in-situ XRD patterns for *o*-NMO and (b) *ex-situ* XRD patterns of (a) *o*-NMO charged at 4.4 V compared to simulated OP4 ones with ideal stacking and stacking fault by DIFFaX program and (c) the crystal structures of P2, O2, and OP4 with ideal stacking and stacking fault.

Meanwhile, *h*-NMO shows moderate phase changes in Fig. 5-13. P'2-phase (P'2-lll) having distorted lattice, similar to P'2-ll phase of *o*-NMO, appears on discharge below 2.2 V ($x > 0.67$ in $Na_xMn_{0.9}O_2$) due to increase in Mn(III) ions, as is also evidenced by *ex-situ* XRD in Fig. 5-14b. The limited x range of distorted P'2 phase ($x > 0.67$) compared to *o*-NMO ($x > 0.22$) implies depression of co-operative lattice distortion by the Mn defects. The change of lattice parameters, degree of in-plane distortion, and lattice volume during the 1st cycle is summarized in Figs. 5-12a and 5-14a. The volume change is at most 9% for *o*-NMO and only 2.5% for *h*-NMO. In addition, the degree of in-plane distortion, δ, drastically changes from zero to 10% during first discharge for *o*-NMO. Despite of those severe changes, *o*-NMO demonstrates the superior cycle stability and highly reversible phase transitions. On the other hand, capacity degradation of *h*-NMO is mainly observed below 2.2 V, where P2 and P'2-lll bi-phasic region appears, as indicated in cyclability and *dQ/dV* plots (Figs. 5-9 and 5-10a). Thus, localized distortion with Mn defect and Jahn-Teller Mn(III) ions possibly induce irreversible structural change, leading to the faster capacity-decay. From these results, the highly reversible phase transitions and excellent electrochemical performance are believed to be due to positive effect of the "co-operative" distortion of *o*-NMO.

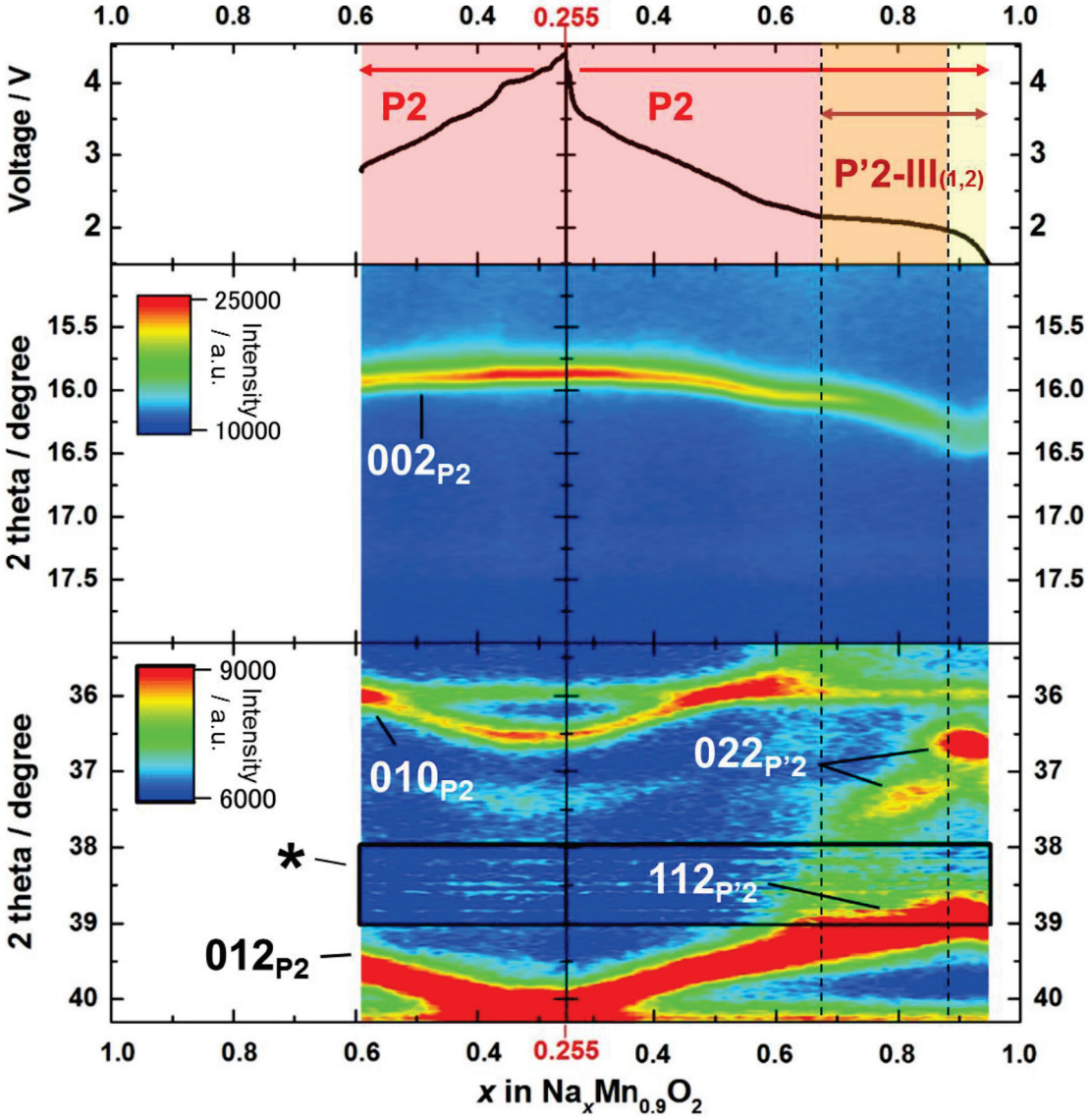

Fig. 5-13. The initial charge/discharge curves and phase evolution (top) and contour maps of operando XRD patterns for *h*-NMO. The diffraction intensity in the region marked "*" is treated by subtracting the background diffraction of Be window.

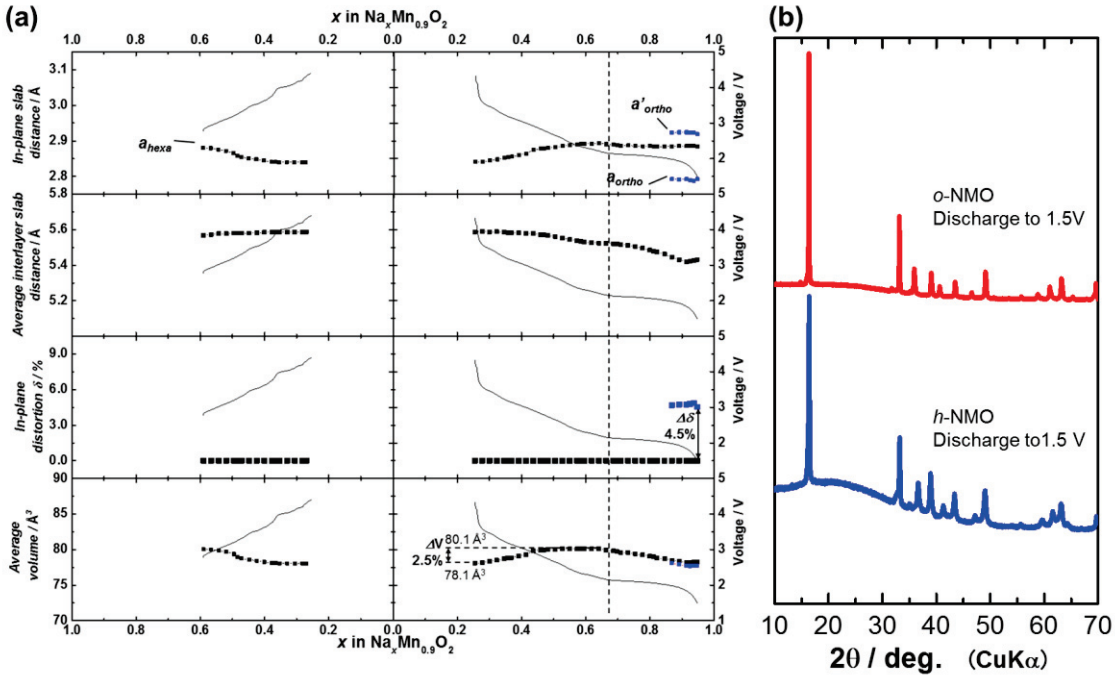

Fig. 5-14. (a) The change of MnO_2-slab distance, lattice distortion, and lattice volume during 1st cycle calculated from in-situ XRD patterns for *o*-NMO and (b) *ex-situ* XRD discharged electrodes for both *o*- and *h*-NMO to 1.5 V. Mn vacancy of *h*-NMO may attribute smaller distortion of P'2 phase (4.5%) than *o*-NMO (10%) and non-monotonous change of volume by Na extraction.

In summary, the precise single-phase preparation of P2 and P'2-$Na_{2/3}MnO_2$ is found and enables to demonstrate superior battery performance of *o*-NMO for highly energetic Na-ion battery. The Mn defect is a key factor leading to unfavorable effect on electrochemical property, and CJTD does not deteriorate reversible Na intercalation for *o*-NMO. We will further study and report their physical properties correlated with manganese and sodium stoichiometry and Jahn-Teller distortion.

5.4 Further investigation on crystal structure and electronic state

5.4.1 Structural transition from *o*-NMO to *h*-NMO

h-NMO is obtained from *h*-NMO by heat treatment above 500 °C as shown in Section 5.2.1. In this section, we focused on structural transition from *o*-NMO to *h*-NMO and investigated by temperature-controlled SXRD and thermal analyses by TG-DTA. Fig. 5-15 shows SXRD patterns of *o*-NMO at high temperature from RT to 700 °C. Heating up to 300 °C, *o*-NMO maintains orthorhombic lattice, however, diffraction peaks derived from P'2 structure (S.G. *Cmcm*) is suddenly decreased at 400 °C and finally, *o*-NMO thoroughly transforms undistorted P2 structure (S.G. $P6_3/mmc$) from P'2 structure. This is fully consistent with our synthesis optimization to obtain pure P2 phase in Section 5-2-2 and implies the scale of stabilization energy by Jahn-Teller distortion is around 500 °C (~ 70 meV). However, the influence of stoichiometry of Na and Mn on the transition remains unclear and will be discussed with thermal analyses later.

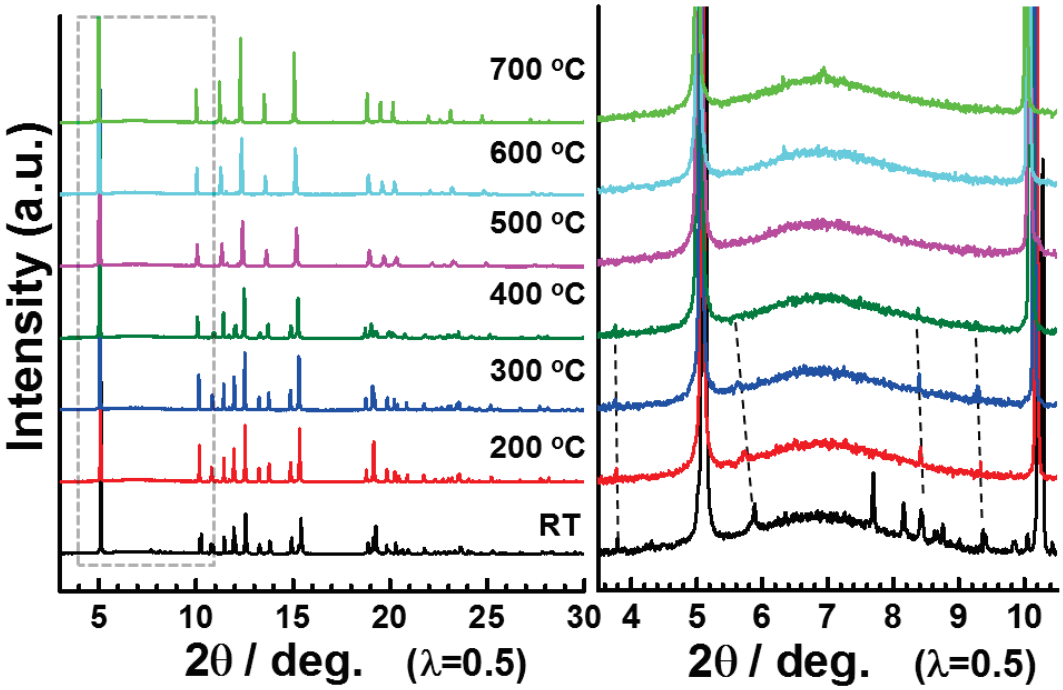

Fig. 5-15. High temperature SXRD for *o*-NMO from RT to 700 °C.

In addition to the structural transition from P'2 to P2 phase, high temperature SXRD reveals the disappearance of superstructure at high temperature. A part of diffraction peaks derived from superstructure, especially between 5 and 10°, disappear at 200 °C and almost all superlattice peaks disappear at 400 °C. These results support our assumption that the superstructure is originated from Na/vacancy ordering since mobility of Na^+ ions in lattice is increased at high temperature and thus, the ordering is expected to be broken.

Low temperature SXRD measurement is also examined in anticipation of finding additional superstructure or structural transition since P2-Na_xCoO_2 is known to show structural change from orthorhombic to monoclinic lattice at 290 K. [25] Fig. 5-16 shows SXRD patterns of *o*-NMO at low temperature from RT to -183 °C. Crystal structure is obviously unchanged and no additional peaks or structural transition is observed up to -183 °C, suggesting the structure at RT is stable enough to ignore the effect of thermal fluctuation on the phase formation including superstructure.

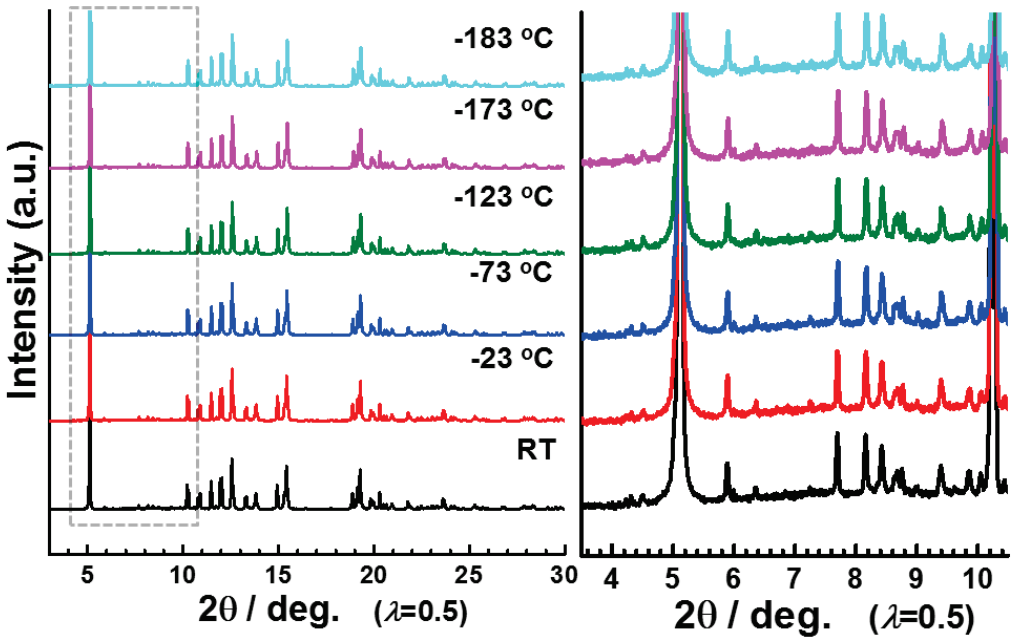

Fig. 5-16. Low temperature SXRD for *o*-NMO from RT to -183 °C.

Fig. 5-17 summarizes a change of lattice constant of *o*-NMO obtained from high and low temperature SXRD. The interlayer slab distance is proportionally increased by increasing surrounding temperature regardless of structural transition due to thermal expansion of the lattice. On the other hand, in-plane slab distance shows much little change with the temperature compared with the change of intra-plane slab. Such an anisotropic thermal expansion is often observed for layered materials such as Na_xCoO_2,[26] $NaCrO_2$,[27] and $LiNi_{1/2}Mn_{1/2}O_2$.[28] This anisotropy would be general for layered materials because weak Na(Li)-O bonds expand more than strong Me-O bonds with increasing temperature. In addition to the common anisotropy, the slight decrease of a'_{ortho} reflects decrease of Jahn-Teller distortion toward high temperature.

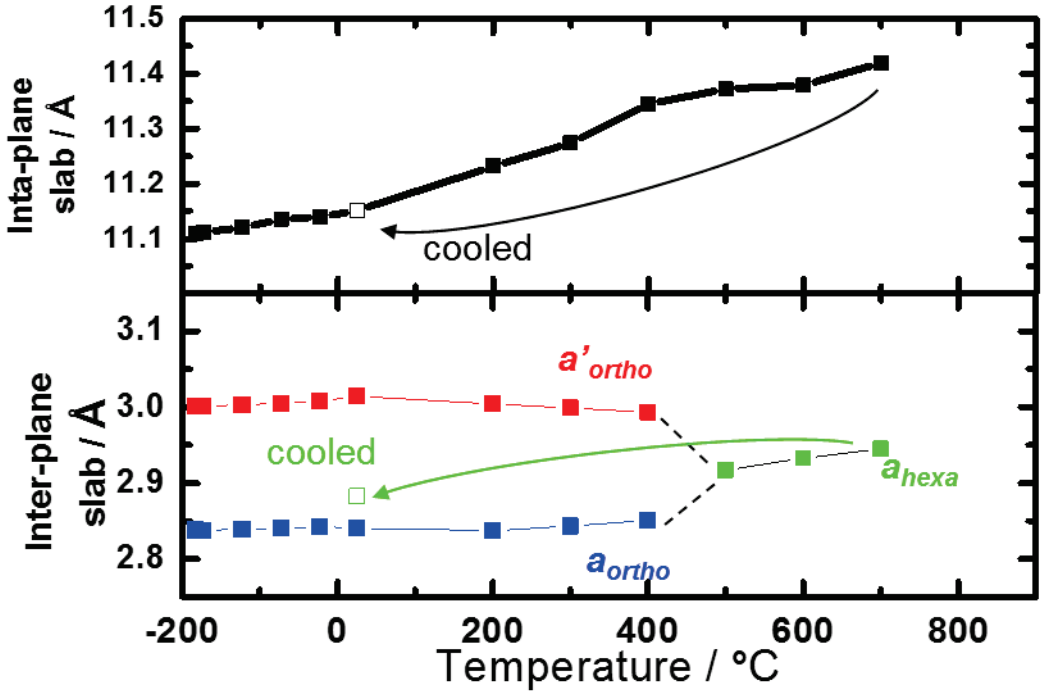

Fig. 5-17. Change of lattice constant of *o*-NMO obtained from SXRD patterns in Fig. 5-15 and 5-16.

To further understand the structural change from P'2 to P2 phase, thermal analysis is conducted. Fig. 5-18 shows TG and DTA profile for *o*-NMO in air and Ar. In section 5-2-2, we suggested Mn defect is induced by oxygen uptake which is a key factor to form P2 phase. Reaction with air is necessary for oxygen uptake as well as high temperature for rearrangement of Mn-O bonds. In fact, TG and DTA profile in Ar is highly symmetric during heating and cooling. Moreover, XRD pattern after TG-DTA measurement in Ar remains P'2 phase. On the other hand, TG and DTA profile in air shows relatively large change and asymmetric behavior on heating / cooling and XRD pattern after TG-DTA in air proves to be P2 phase. During cooling process in air, weight change turned from negative to positive and finally, 2.65% weight gain is observed. Since ICP and iodometry results suggest 10 molar % increase of oxygen (Table 5-2), weight gain from oxygen uptake is estimated about 3.2%, which is almost consistent with TG result. Here we have confirmed that P'2/P2 transition doesn't occur in heating in Ar and weight gain after heating in air is consistent with our compositional analysis.

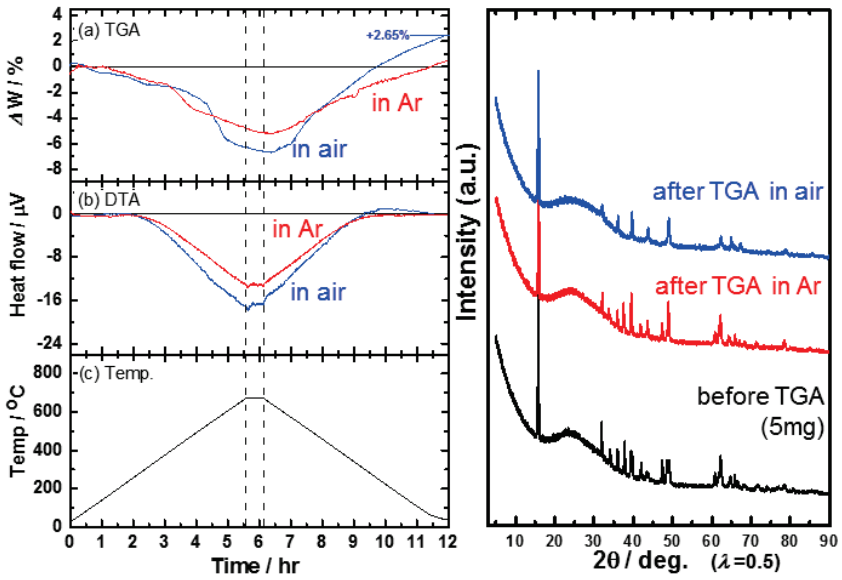

Fig. 5-18. TG-DTA measurement at different atmosphere, (a) TG, (b) DTA, and (c) heat profile for *o*-NMO.

5.4.2 Change of superstructure and electronic state during Na extraction of *o*-NMO

As-prepared *o*-NMO has obvious superstructure in SXRD and TEM/electron diffraction pattern (Figs. 5-3 and 5-5, respectively). In addition, during Na extraction / insertion, other superstructure is also implied as step-wise charge/discharge profiles (Fig. 5-7). In this section, we further investigate superstructure during Na extraction / insertion by *ex-situ* SXRD. *Ex-situ* SXRD patterns of *o*-NMO are measured for the electrodes at 2.97, 2.81. 2.57, 2.37, and 1.50 V corresponding to the steps of initial discharge curve as shown in Fig. 5-19. One important finding is the disappearance of superstructure peaks at fully discharged state to 1.50 V (x = 0.91 in Na_xMnO_2). Since most of all Na sites are occupied with sodium at 1.50 V, no Na/vacancy ordering is probably possible to form. Therefore, the disappearance of superstructure peaks at 1.50 V strongly proves that the superstructure peaks observed at other voltages originate from Na/vacancy ordering while Na/vacancy ordering is also expected to interact with charge ordering of Mn and long range modulation of the lattice as discussed in the *operando* XRD results. Different types of superstructure is observed at pristine, 2.97, 2.81, 2.57, and 2.37 V, however, it's very difficult to suggest what kinds of Na/vacancy ordering are formed at each state. Even though Na/vacancy ordering on hexagonal lattice for P2-Na_xCoO_2 is proposed by a first principle calculation,[29] no calculation is reported for P'2 structure so far and the case of *o*-NMO will be much more complicated due to the contribution of cooperative and local Jahn-Teller distortion.

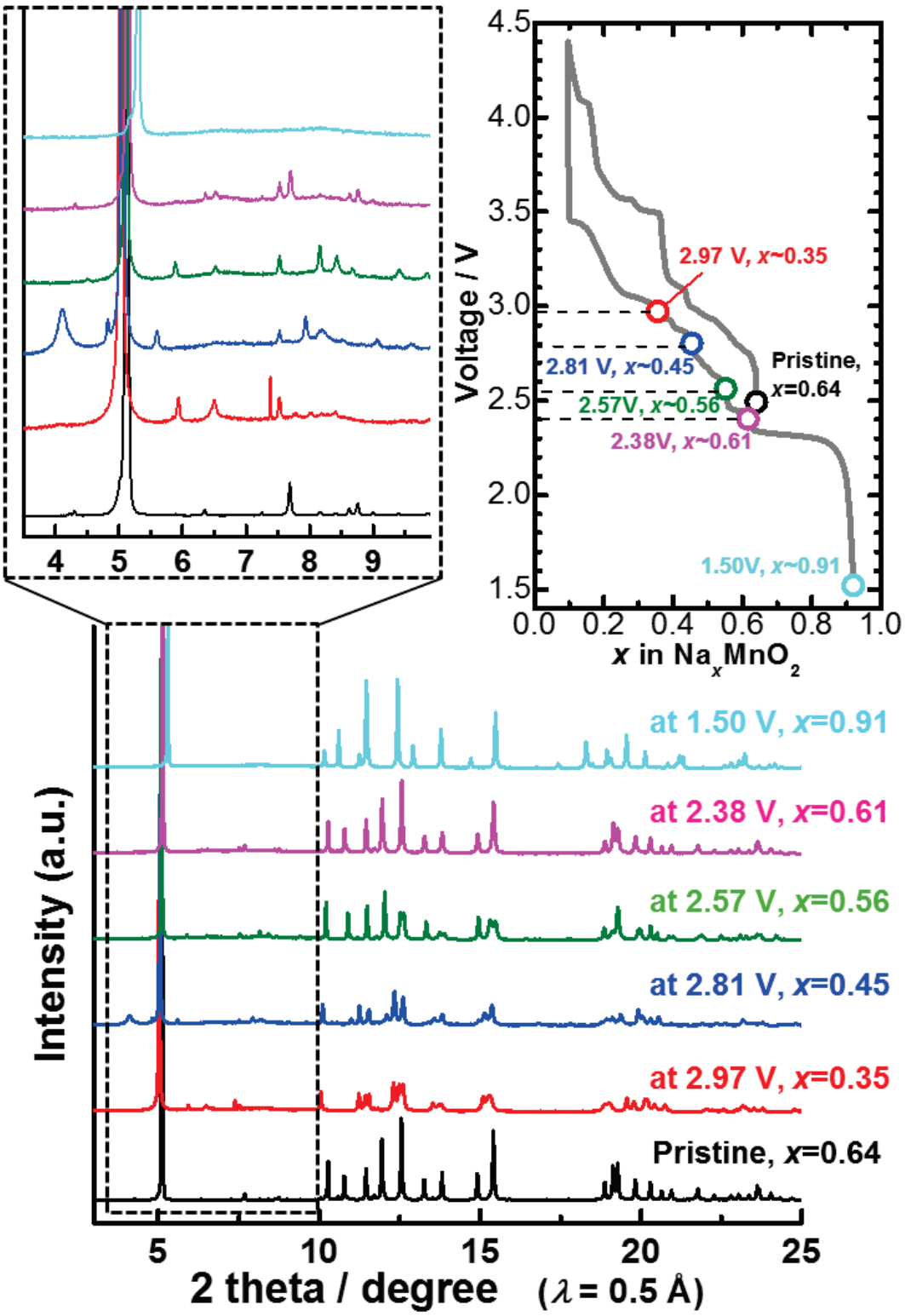

Fig. 5-19. *Ex-situ* SXRD patterns at different voltage for *o*-NMO.

To understand electronic state of Na_xMnO_2 polymorphs, magnetic measurement is also conducted for as-prepared and discharged *o*- / *h*- NMO samples. Fig. 5-20 shows temperature dependence of magnetic susceptibility of as-prepared *o*- / *h*- NMO. For both samples, the zero-field cooled (ZFC) curves have cusp-like peaks below 50 K and field cooled (FC) curves show little temperature dependence. This is a typical behavior of spin-glass state derived from geometric frustration of anti-ferromagnets having triangular lattice.[30, 31] Glass temperature, T_g can be defined as the peak top of ZFC curve[32] and *o*- / *h*- NMO have T_g at 13.3 and 17.8 k, respectively. Comparing the amplitude of magnetic order between both samples, *h*-NMO has 50 times larger net magnetism than *o*-NMO, which can be explained by magnetic interaction among Mn ions. All magnetic interaction, direct exchange of Mn(III/IV)-Mn(III/IV) and super-exchange of Mn(III/IV)-O^{2-}-Mn(III/IV) are anti-ferromagnetic, except Mn(IV)-O^{2-}-Mn(IV).[33]

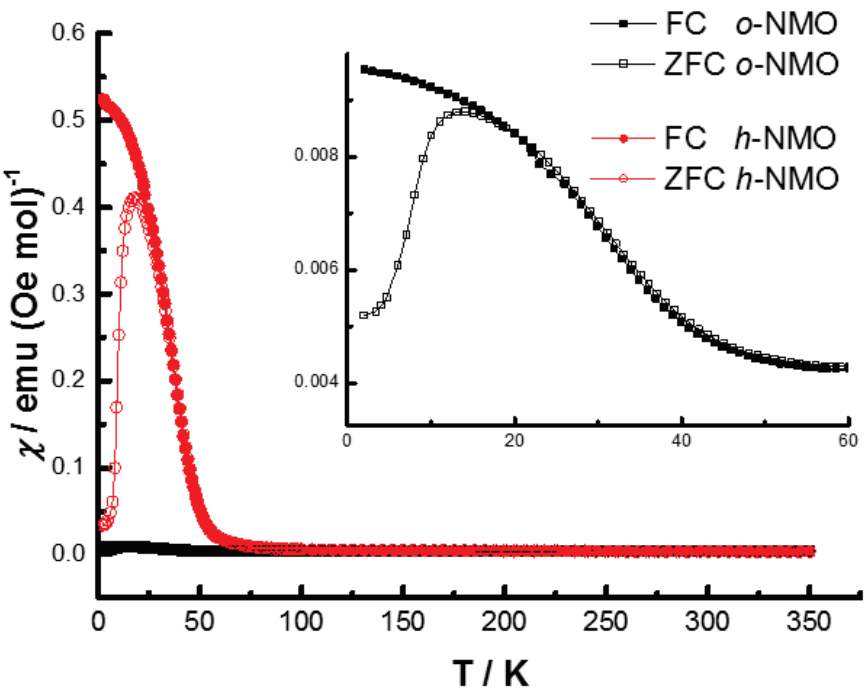

Fig. 5-20. Temperature dependence of magnetic susceptibility of as prepared *o*- / *h*- NMO. The applied magnetic field is fixed at 1000 Oe.

Therefore, this is a physical evidence that manganese in *h*-NMO is over-oxidized by oxygen uptake higher than *o*-NMO in agreement with the result of iodometry as a chemical approach. Fig. 5-21 shows magnetization vs. applied magnetic field measured at 5 K. *h*-NMO shows hysteresis curve. Such a strong ferromagnetic component of *h*-NMO implies clustering of Mn(IV) ions which may be related with distribution of Mn defect since Mn(IV) is likely to be located around zero-charged defect rather than Mn(III) ions.

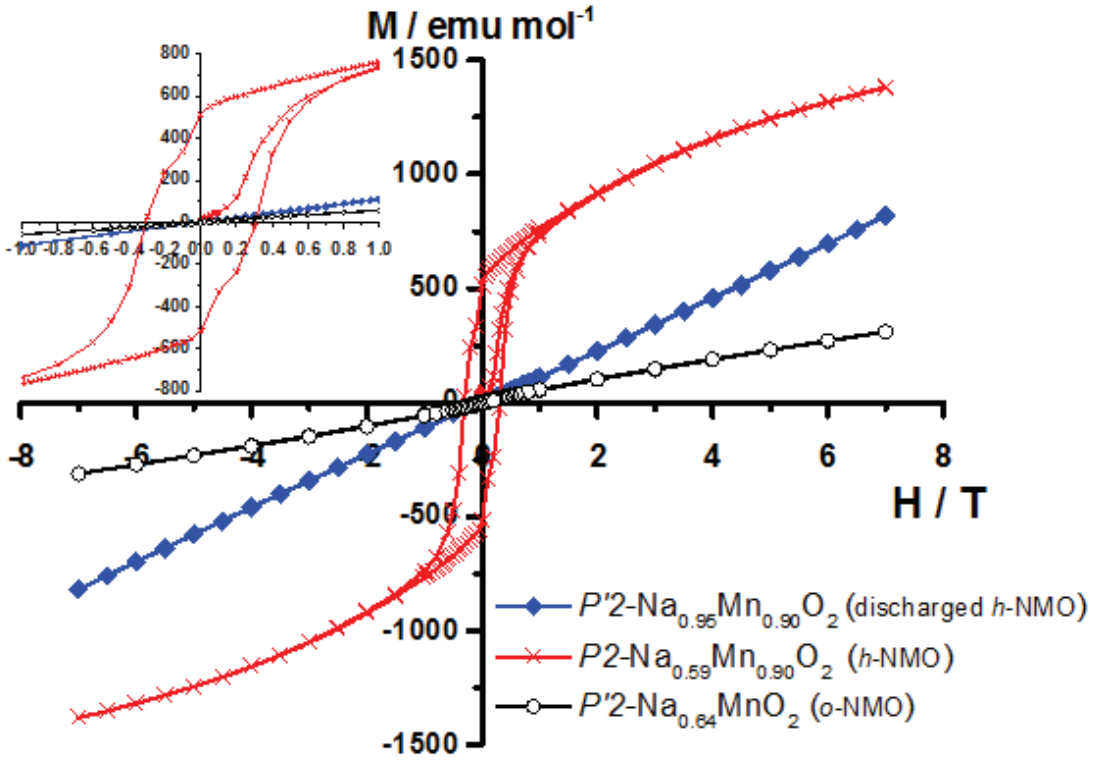

Fig. 5-21. Magnetization vs. applied magnetic field at 5 K.

Fig. 5-22 shows temperature dependence of magnetic susceptibility of the discharged *o*- / *h*- NMO samples to 1.5 V. Both samples have 2 anomalies around 50 K and 10 K. The cusp-like peak at 10 K can be assigned to glass (Neel) temperature since

energy scale of Mn-Mn interaction should be similar to as-prepared samples. The anomaly around 50 K is probably related with 2-dimentional Mn-Mn interaction reported in O'3-$NaMnO_2$[34] or charge ordering as analogy to P2-$NaCoO_2$,[35] but further investigation is needed to conclude it.

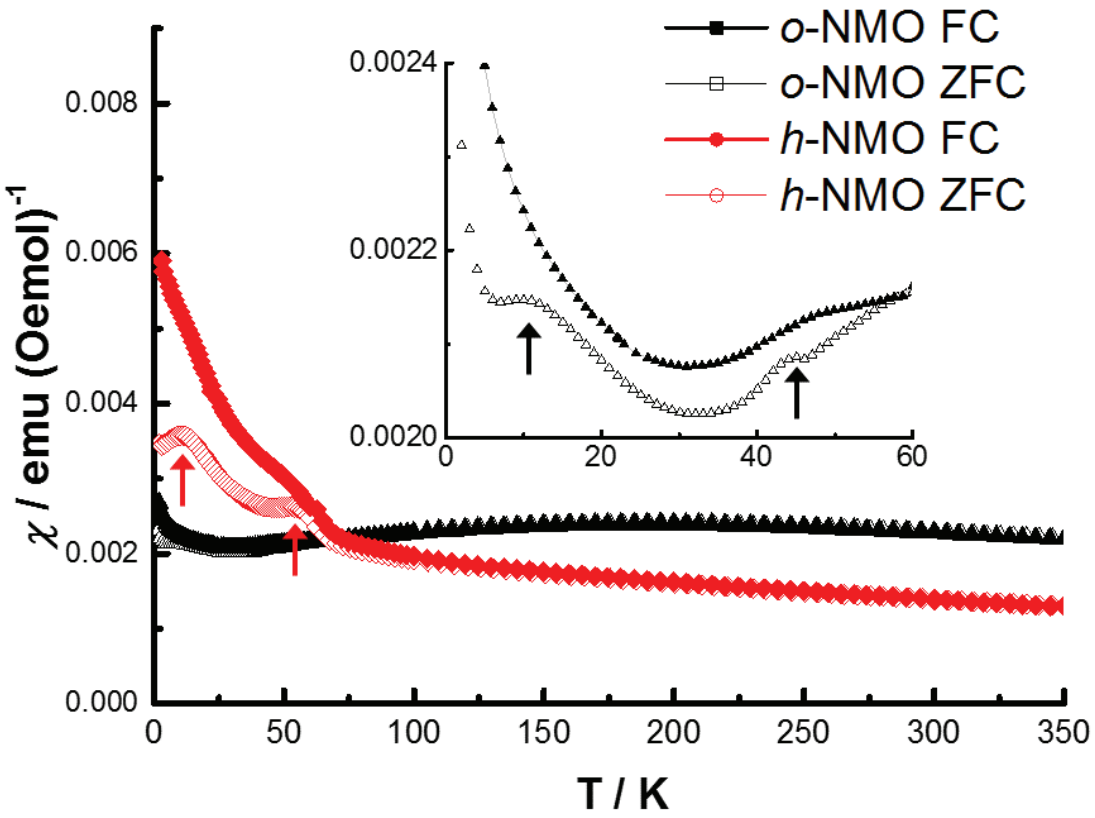

Fig. 5-22. Temperature dependence of magnetic susceptibility of *o*- / *h*- NMO discharged to 1.5 V. The applied magnetic field is fixed at 1000 Oe.

Interestingly, the discharged state of *h*-NMO to 1.5 V, P'2-$Na_{0.95}Mn^{3.39+}_{0.90}O_2$ is very similar to the as-prepared *o*-NMO, P'2-$Na_{0.95}Mn^{3.37+}O_2$. Both samples have same P'2 structure and similar oxidation state of manganese around 3.3+, and their difference is only Na concentration and the existence of Mn defect. Thus, comparison of magnetic properties between them may be useful to understand the effect of Mn defect on electronic

state. Table 5-3 summarizes magnetic properties for as-prepared and discharged samples including the results of Curie-wise fitting. While Fit 1 only considers Cuire-Wise para-magnetism and represents normal fitting, $\chi = C/(T-\theta_C)$, Fit 2 includes contribution of the temperature-independent para-magnetism arising from conduction electrons, χ_0 and represents $\chi = \chi_0 + C/(T-\theta_C)$. We optimized $\chi_0 \sim 0.0025$ emu (mol Oe)$^{-1}$, however, the data of electronic conductivity is needed for accurate estimation. Here, we used same value of χ_0 and *o*-NMO shows larger difference with theoretical value, suggesting larger electronic conductivity than that of *h*-NMO. Discharged *h*-NMO shows similar effective moment to *o*-NMO but Curie temperature θ_C is much different, implying less anti-ferromagnetic interaction. On the other hand, discharged *o*-NMO has anomalously low p_{eff} and θ_C. One possibility is low spin state of Mn(III), however, it's unlikely, considering largely distorted structure. (Fig. 5-14) Another possible explanation is that Curie-Wise fitting is not applicable due to 2-dimentional interaction restricted inter-plane Mn layer.

Table 5-3. The summary of magnetic properties and the result of Curie-Wise fitting

Sample	Mn^{x+}	p_{eff} / μ_B (Fit 1)	p_{eff} / μ_B (Fit 2)	p_{eff} / μ_B (Theo.)	T_g / K	θ_C
h-NMO	3.63	4.23	4.14	4.14	17.8	-392
o-NMO	3.37	5.06	4.70	4.55	13.3	-601
h-NMO (discharged)	3.39	5.18	4.61	4.53	10.5	-339
o-NMO (discharged)	3.06	2.89	2.40	4.82 (2.94 LS)	10.1	-1006

5.5 Conclusion

The precise single-phase preparation of P2 and P'2-$Na_{2/3}MnO_2$ enables to demonstrate superior battery performance of *o*-NMO and discuss the influence of CJTD and Mn defect on structural, electrochemical, and electronic properties. The Mn defect leads unfavorable effect on electrochemical property and induces ferromagnetic Mn(IV)-Mn(IV) interaction. CJTD does not deteriorate reversible Na intercalation for *o*-NMO and provides a variety of Na/vacancy ordering, which is a unique feature of o-NMO having orthorhombic lattice, during Na extraction. We believe the findings in this chapter give an insight to utilize the distorted layered materials for positive electrode materials and further investigation on physical properties will be an interesting platform to find an exotic electronic properties.

References

1. B. Dunn, H. Kamath and J. M. Tarascon, *Science*, 2011, **334**, 928-935.
2. N. Yabuuchi, M. Kajiyama, J. Iwatate, H. Nishikawa, S. Hitomi, R. Okuyama, R. Usui, Y. Yamada and S. Komaba, *Nat. Mater.*, 2012, **11**, 512-517.
3. N. Yabuuchi, K. Kubota, M. Dahbi and S. Komaba, *Chemical Reviews*, 2014, **114**, 11636-11682.
4. R. J. Clément, P. G. Bruce and C. P. Grey, *J. Electrochem. Soc.*, 2015, **162**, A2589-A2604.
5. J.-P. Parant, R. Olazcuaga, M. Devalette, C. Fouassier and P. Hagenmuller, *J. Solid State Chem.*, 1971, **3**, 1-11.
6. C. Delmas, C. Fouassier and P. Hagenmuller, *Physica B*, 1980, **99**, 81-85.
7. A. Mendiboure, C. Delmas and P. Hagenmuller, *J. Solid State Chem.*, 1985, **57**, 323-331.
8. A. Caballero, L. Hernán, J. Morales, L. Sánchez, J. Santos Peña and M. A. G. Aranda, *J. Mater. Chem.*, 2002, **12**, 1142-1147.
9. J. Billaud, G. Singh, A. R. Armstrong, E. Gonzalo, V. Roddatis, M. Armand, T. Rojo and P. G. Bruce, *Energy Environ. Sci.*, 2014, **7**, 1387.
10. Q. Huang, M. L. Foo, R. A. Pascal, J. W. Lynn, B. H. Toby, T. He, H. W. Zandbergen and R. J. Cava, *Phys. Rev. B*, 2004, **70**.
11. C. Didier, M. Guignard, J. Darriet and C. Delmas, *Inorg Chem*, 2012, **51**, 11007-11016.
12. N. Yabuuchi, R. Hara, M. Kajiyama, K. Kubota, T. Ishigaki, A. Hoshikawa and S. Komaba, *Adv. Energy Mater.*, 2014, **4**, 1301453.

13. N. Yabuuchi, R. Hara, K. Kubota, J. M. Paulsen, S. Kumakura and S. Komaba, *J. Mater. Chem. A*, 2014, **2**, 16851–16855.

14. D. Buchholz, C. Vaalma, L. G. Chagas and S. Passerini, *J. Power Sources*, 2015, **282**, 581-585.

15. J. M. Paulsen and J. R. Dahn, *Solid State Ionics*, 1999, **126**, 3-24.

16. R. Stoyanova, D. Carlier, M. Sendova-Vassileva, M. Yoncheva, E. Zhecheva, D. Nihtianova and C. Delmas, *J. Solid State Chem.*, 2010, **183**, 1372-1379.

17. L. Guenne, P. Deniard, P. Biensan, C. Siret and R. Brec, *J. Mater. Chem.*, 2000, **10**, 2201-2206.

18. C. Fouassier, C. Delmas and P. Hagenmuller, *Mater. Res. Bull.*, 1975, **10**, 443-449.

19. F. Izumi and K. Momma, *Solid State Phenom.*, 2007, **130**, 15-20.

20. F. M. Chang, M. Jansen and Z. Anorg, *Allg. Chem.*, 1985, **531**.

21. E. A. Raekelboom, A. L. Hector, J. Owen, G. Vitins and M. T. Weller, *Chem. Mater.*, 2001, **13**.

22. L. Mu, S. Xu, Y. Li, Y. S. Hu, H. Li, L. Chen and X. Huang, *Adv. Mater.*, 2015, **27**, 6928-6933.

23. H. Yamamoto, K. Kubota, M. Fukunishi, A. Watanabe, T. Kim and S. Komaba, *83th meeting of Electrochem. Soc. of Japan*, 2016.

24. X. Li, X. Ma, D. Su, L. Liu, R. Chisnell, S. P. Ong, H. Chen, A. Toumar, J. C. Idrobo, Y. Lei, J. Bai, F. Wang, J. W. Lynn, Y. S. Lee and G. Ceder, *Nat. Mater.*, 2014, **13**, 586-592.

25. M. Medarde, M. Mena, J. L. Gavilano, E. Pomjakushina, J. Sugiyama, K. Kamazawa, V. Y. Pomjakushin, D. Sheptyakov, B. Batlogg, H. R. Ott, M. Mansson and F. Juranyi, *Phys Rev Lett*, 2013, **110**, 266401.

26. C. A. M. dos Santos, J. J. Neumeier, Y.-K. Yu, R. K. Bollinger, R. Jin, D. Mandrus and B. C. Sales, *Phys. Rev. B*, 2006, **74**.

27. N. Yabuuchi, I. Ikeuchi, K. Kubota and S. Komaba, *ACS appl. mater. Interfaces*, 2016, **8**, 32292-32299.

28. N. Yabuuchi, Y.-T. Kim, H. H. Li and Y. Shao-Horn, *Chem. Mater.*, 2008, **20**, 4936.

29. Y. S. Meng, Y. Hinuma and G. Ceder, *J. Chem. Phys.*, 2008, **128**, 104708.

30. C. M. Julien, A. Ait-Salah, A. Mauger and F. Gendron, *Ionics*, 2006, **12**, 21-32.

31. A. P. Ramirez, *Annu. Rev. Mater. Sci.*, 1994, **24**, 453.

32. N. A. Chernova, G. M. Nolis, F. O. Omenya, H. Zhou, Z. Li and M. S. Whittingham, *J. Mater. Chem.*, 2011, **21**, 9865.

33. J. B. Goodenough, *Magnetism and the chemical bond*, Wiley, New York, 1964.

34. M. Giot, L. C. Chapon, J. Androulakis, M. A. Green, P. G. Radaelli and A. Lappas, *Phys Rev Lett*, 2007, **99**, 247211.

35. M. L. Foo, Y. Wang, S. Watauchi, H. W. Zandbergen, T. He, R. J. Cava and N. P. Ong, *Phys Rev Lett*, 2004, **92**.

Chapter 6. Cooperative Jahn-Teller Distortion and Electrochemical Property in Layered Na-Mn-O system

6.1 Introduction

In Chapter 5, the investigation of single-phase samples of P'2- and P2-$Na_{2/3}MnO_2$, exhibiting different stoichiometry, demonstrated the superior electrochemical performance of distorted P'2 sample.[1] Co-operative Jahn-Teller distortion (CJTD) derived from six-coordinated high spin Mn^{III} (t_{2g}^3-e_g^1) provides highly reversible phase transtions during Na extraction and obvious correlation between phase transitions and Na/vacancy ordering via charge ordering of manganse. These finidings stimulate quantitative understanding how CJTD affects electrochemical properties such as reversibility, kinetics of sodium diffusion, and long-cycle stability for layered materials and such studies are of great importance to realize high capacity performance of Mn^{III} based oxide materials for high energy density NIBs.

In this chapter, correlation between CJTD and electrochemical properties of P'2-$Na_{2/3}Mn_{0.9}Me_{0.1}O_2$ by changing the distoriton resulting from different concentration of Mn(III) ion by doping with different valance metals as a straightforward expansion of the studies in Chapter 5. In addition, we found a new material class, zigzag-layered Na(Mn, Cu)O_2 which has the largest Jahn-Teller distortion in layered Na-Mn-O system. It turned out that Cu doping is only the way to stabilize zigzag-layered phase. Consequently, we have a chance to discuss on correlation between Jahn-Teller distortion and electrochemical properties in whole layered Na-Mn-O system.

6.2 Correlation between CJTD and electrochemical property in P'2-$Na_{2/3}Mn_{0.9}Me_{0.1}O_2$

Although layered oxides of Na_xMnO_2 ($x = 1 – 2/3$) have been intensively studied as positive electrode materials of NIBs because of abundance of Mn among 3d transition metals, studies on (electro-)chemical and physical properties of P2-$Na_{2/3}MnO_2$ suffered from difficulty in its single phase synthesis, low energy density, and poor cycle stability.[2-4] In consequence, the current trend of study on P2-$Na_{2/3}MnO_2$ materials for NIB is metal substitution for Mn, such as electrochemically active metals, Fe^{III}, $Ni^{II,III}$, Co^{III}, and Cu^{II} [5-11] and inactive cations, Li^{I}, Mg^{II} and Zn^{II}.[3, 4, 12-14] In Chapter 5, however, we have demonstrated that excellent electrochemical properties of P'2-$Na_{2/3}MnO_2$ based on redox couple of Mn(III/IV) with large CJTD. Here, we focus on doping effect on electrochemical properties with maintaining P'2 structure and redox couple of Mn(III/IV).

In this study, we demonstrate the systematic synthesis of differently distorted P'2-$Na_{2/3}MnO_2$ samples by partial replacement of Mn with different metal elements and compared their electrochemical properties. The distortion is highly correlated with average oxidation state of manganese varied by divalent metals (Mg^{II}, Ni^{II}, Cu^{II}, Zn^{II}), trivalent metal (Co^{III}) and tetravalent metal (Ti^{IV}). The effect of metal-substitution and lattice distortion on electrochemical properties are discussed, and Cu-doping successfully improves both cycle and rate performance.

6.2.1 Synthesis

P'2-$Na_{2/3}Mn_{0.9}Me_{0.1}O_2$ samples are synthesized by a solid-state reaction and the detailed synthesis method is Fig. 6-1. Stoichiometric mixtures of Na_2CO_3 (Kanto Chemical Co., Ltd.), Mn_2O_3, and dopant precursor, $(MgCO_3)_4Mg(OH)_2 \cdot 5H_2O$, TiO_2, Co_3O_4, $Ni(OH)_2$, Cu_2O and ZnO powders were treated by ball-milling with acetone addition for 12 h at 600 rpm. The mixtures were dried, and thus obtained powder was pressed into pellets. The pellet except Zn-NMO was heated in air at 1 °C min^{-1} up to 1050 °C (900 °C for Zn-NMO) and then, quenched by taking the reaction product out from the heated furnace and immediately transferred into an argon-filled glove box. The samples were cooled to room temperature in the glove box and were kept inside to avoid the contact with moisture and oxygen in air.

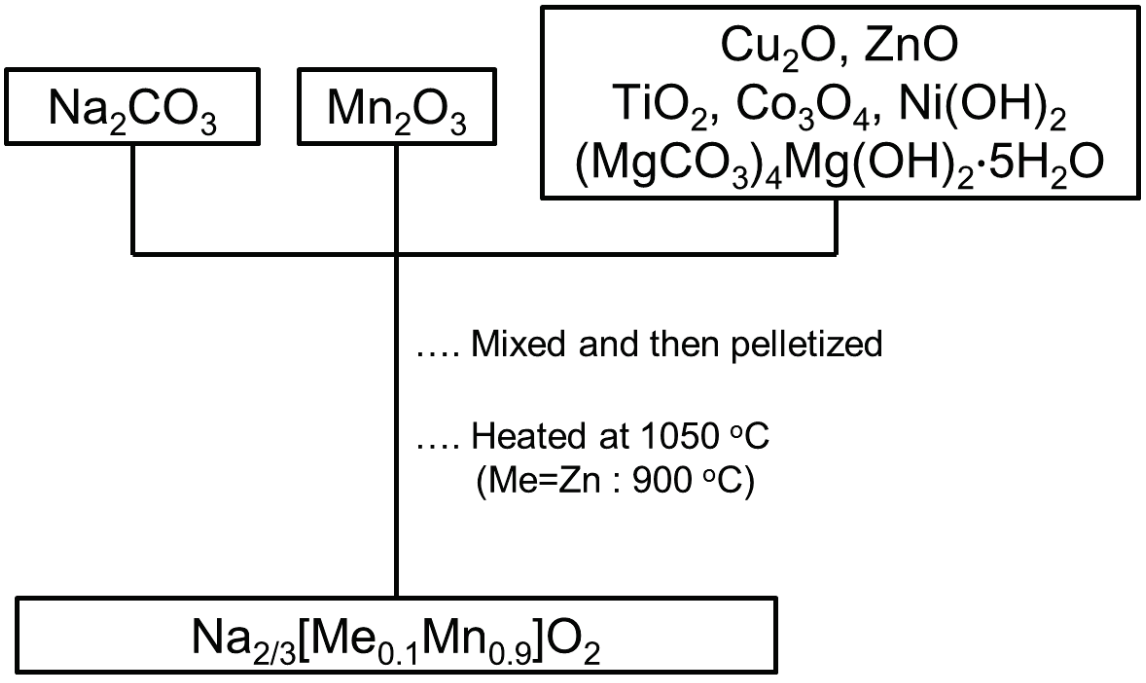

Fig. 6-1. Synthesis condition of P'2-$Na_{2/3}Mn_{0.9}Me_{0.1}O_2$ samples.

6.2.2 Structural and physical characterization

P'2-$Na_{2/3}Mn_{0.9}Me_{0.1}O_2$ samples are synthesized by a solid-state reaction. Fig. 6-2 shows XRD patterns of synthesized P'2-$Na_{2/3}MnO_2$ and $Na_{2/3}Mn_{0.9}Me_{0.1}O_2$ (Me = Mg, Ti, Co, Ni, Cu, Zn) samples which are hereinafter denoted by Mn-NMO (non-doped P'2-$Na_{2/3}MnO_2$), Mg-NMO, Ti-NMO, Co-NMO, Ni-NMO, Cu-NMO, and Zn-NMO, respectively. All diffraction peaks in the patterns can be indexed as a P'2-type layered structure (S.G. *Cmcm*) without any crystalline impurity. SXRD also proves the single phase for Cu- and Zn-NMOs (see Fig. 6-3).

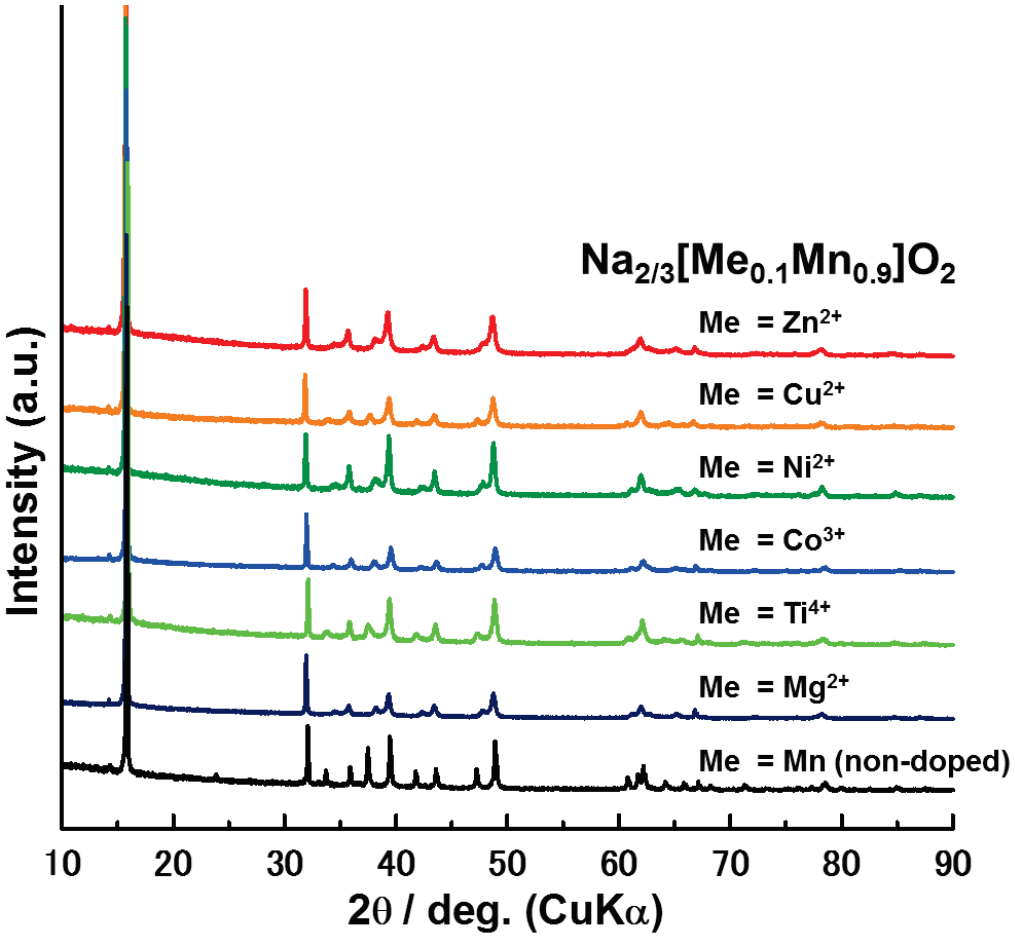

Fig. 6-2. XRD patterns for $Na_{2/3}Mn_{0.9}Me_{0.1}O_2$.

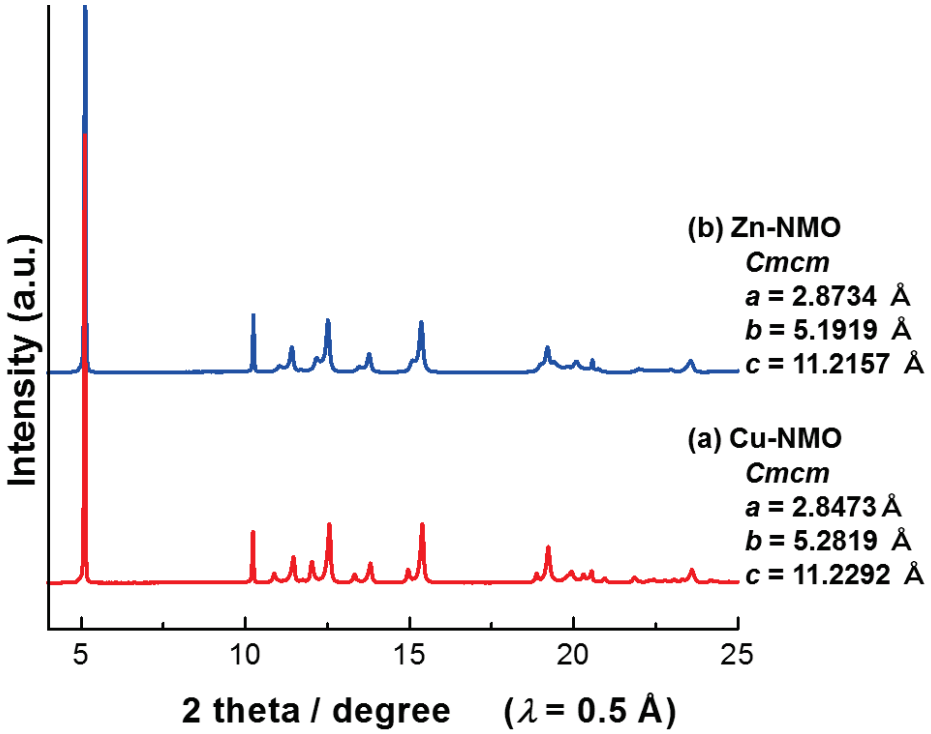

Fig. 6-3. Synchrotron XRD patterns of (a) Cu-NMO and (b) Zn-NMO.

A schematic illustration of P'2-type crystal structure and in-plane arrangement of orthorhombic lattice is shown in Fig. 6-4a. If the $b_{ortho.}/a_{ortho.}$ ratio equals $\sqrt{3}$, hexagonal setting is proper to express the crystal structure. When CJTD induces distorted orthorhombic lattice by *b*-axial elongation and/or *a*-axial shrinkage, the degree of an in-plane distortion is defined as "δ" in $b_{ortho.}/a_{ortho.} = (1+\delta)\sqrt{3}$ to express how the orthorhombic lattice is distorted from hexagonal one.[1] Indeed, the $b_{ortho.}/a_{ortho.}$ ratio for Mn-NMO becomes 1.87, namely, distortion degree , δ = ca. 8%. The partial substitution for manganese significantly affects the distortion. Lattice parameter and the defined distortion of the obtained samples are summarized in Table 6-1. Although minor contribution of ionic radii of dopants to the distortion is observed in Fig. 6-4b, the interesting dependency of distortion degree on concentration of Mn^{III} is found in Fig. 6-4c. Relation between δ and the molar ratio of Mn^{III} to total metal amount, $Mn^{III}/(Mn +$

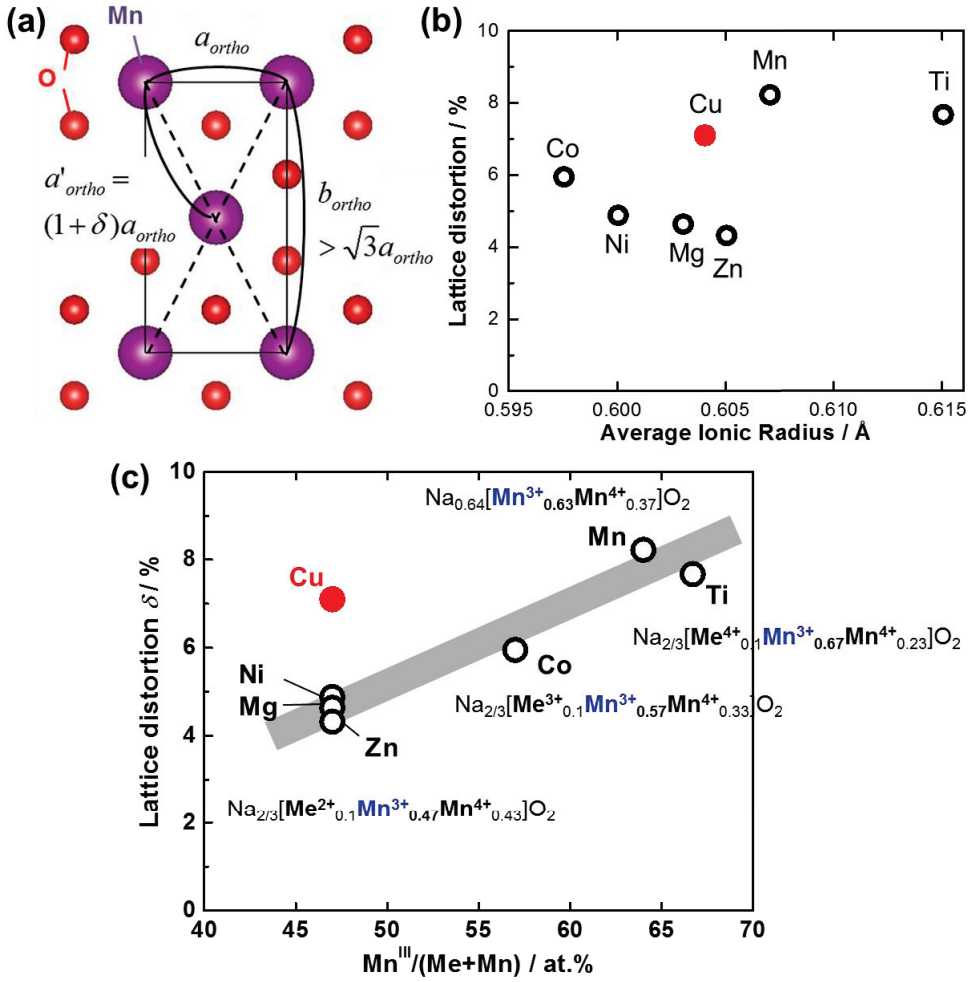

Fig. 6-4. (a) Schematic illustration of P'2 structure, (b) comparison with average ionic radius and lattice distortion and (c) lattice distortion vs. Mn^{III}.

Table 6-1. Summary of dopant, lattice constant, and defined distortion

Sample ID	Dopant	Composition	*a* / Å	*b* / Å	*c* / Å	Degree of distortion / δ
Mn-NMO	---	$Na_{2/3}MnO_2$	2.8349	5.3140	11.1506	8.22%
Mg-NMO	Mg^{2+}	$Na_{2/3}Mg_{0.1}Mn_{0.9}O_2$	2.8664	5.1949	11.2101	4.64%
Ti-NMO	Ti^{4+}	$Na_{2/3}Ti_{0.1}Mn_{0.9}O_2$	2.8455	5.3067	11.1485	7.67%
Co-NMO	Co^{3+}	$Na_{2/3}Co_{0.1}Mn_{0.9}O_2$	2.8408	5.2131	11.1965	5.95%
Ni-NMO	Ni^{2+}	$Na_{2/3}Ni_{0.1}Mn_{0.9}O_2$	2.8622	5.1995	11.2233	4.88%
Cu-NMO	Cu^{2+}	$Na_{2/3}Cu_{0.1}Mn_{0.9}O_2$	2.8473	5.2819	11.2292	7.10%
Zn-NMO	Zn^{2+}	$Na_{2/3}Zn_{0.1}Mn_{0.9}O_2$	2.8734	5.1919	11.2157	4.32%

Me) is plotted by reasonably assuming the valence such as Mg^{II}, Ni^{II}, Cu^{II}, Zn^{II}, Co^{III}, and Ti^{IV} coexistent with Mn^{III} and Mn^{IV}. Linear relation between δ and $Mn^{III}/(Mn+Me)$ except Cu-NMO proves that Mn^{III} is a key factor leading CJTD. Compared to Ni^{II}, Mg^{II}, and Zn^{II}, Cu^{II} doping results in significant distortion, which is because of extra Jahn-Teller distortion caused by six-coordinated Cu^{II} (t_{2g}^6-e_g^3). Consequently, we have successfully obtained P'2-$Na_{2/3}Mn_{0.9}Me_{0.1}O_2$ samples having different distortion.

6.2.3 Electrochemical properties

Their electrochemical properties are investigated in non-aqueous Na cells and initial charge/discharge curves are compared in Fig. 6-6. Galvanostatic charge/discharge cut-off voltages are set to 4.4/1.5 V at a current rate of 10 mA g^{-1}. Since SEM images shown in Fig. 6-6 indicate that morphology of every sample is platelet with a similar particle size of ~5 μm, their electrochemical properties should not be influenced by the particle morphology. All samples show high reversible capacity beyond 200 mAh g^{-1} corresponding to reversible insertion of 0.8 mole Na per formula. The P'2-$Na_{2/3}Mn_{0.9}Ni_{0.1}O_2$ delivers the reversible capacity of 227 mAh g^{-1}. Mn-NMO shows multiple stepwise curves on charge/discharge. These steps are derived from two major structural changes and several phase transitions originating from Na/vacancy and Mn charge orderings.[1] All metal-doped samples, however, have smooth charge/discharge curves, which are generally beneficial for practical applications. Metal substitution for manganese induces charge-disorder into transition metal layer[15] and thus, suppresses phase transition related to long-range ordering of both Na/vacancy and $Mn^{III/IV}$ charge. Consequently, the structural change during sodium extraction is remarkably influenced by the metal substitution.

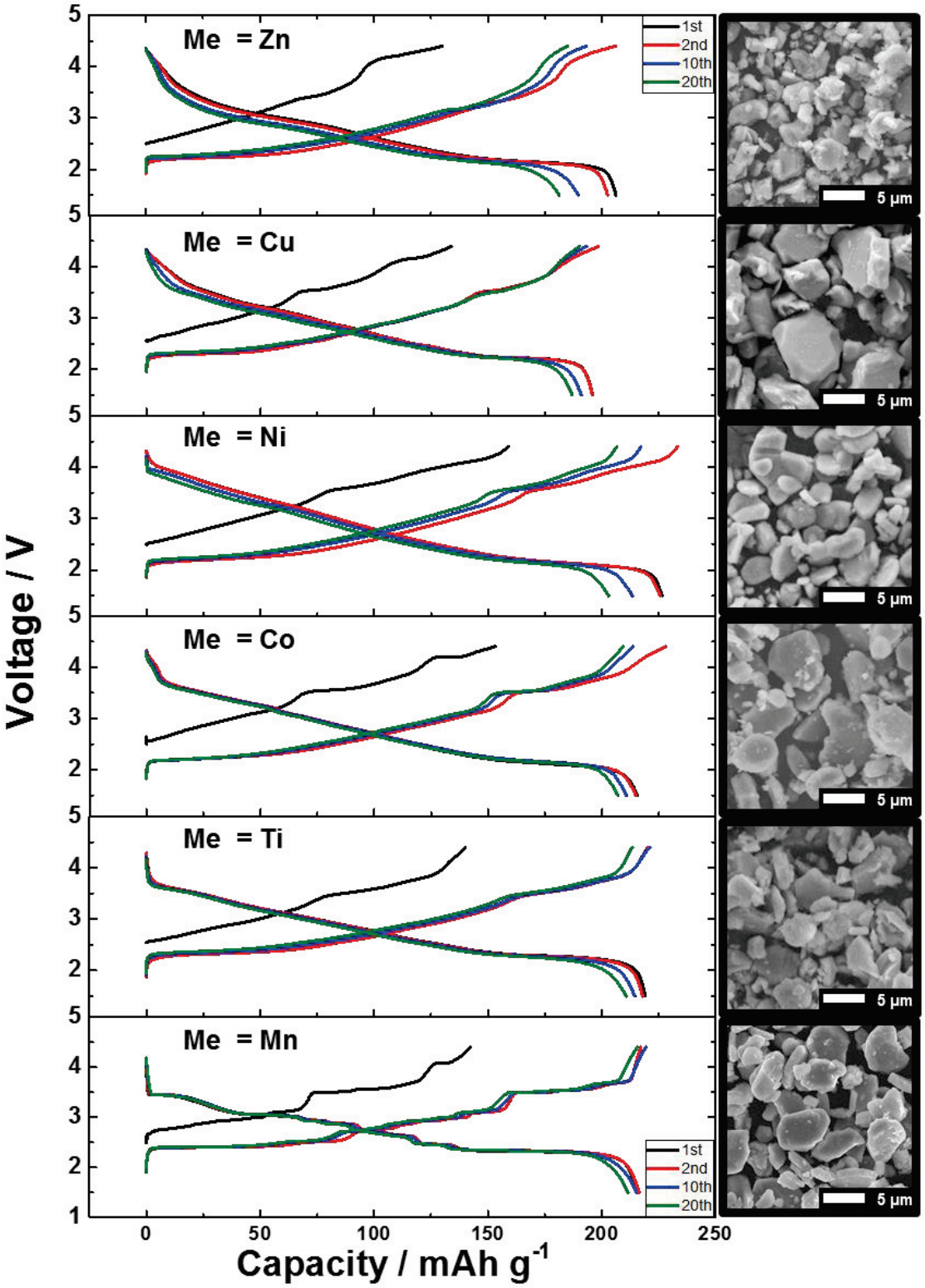

Fig. 6-6. Charge/discharge curves and SEM images for $Na_{2/3}Mn_{0.9}Me_{0.1}O_2$.

To further investigate the influence of metal substitution on the electrochemical reactions, *dQ/dV* plots, rate and cycle performances are compared among the doped samples. *dQ/dV* plots of 1st discharge and 2nd charge are shown in Fig. 6-7. For Mn-NMO, the largest peak at 2.3 V upon discharge is assigned to the two-phase reaction of

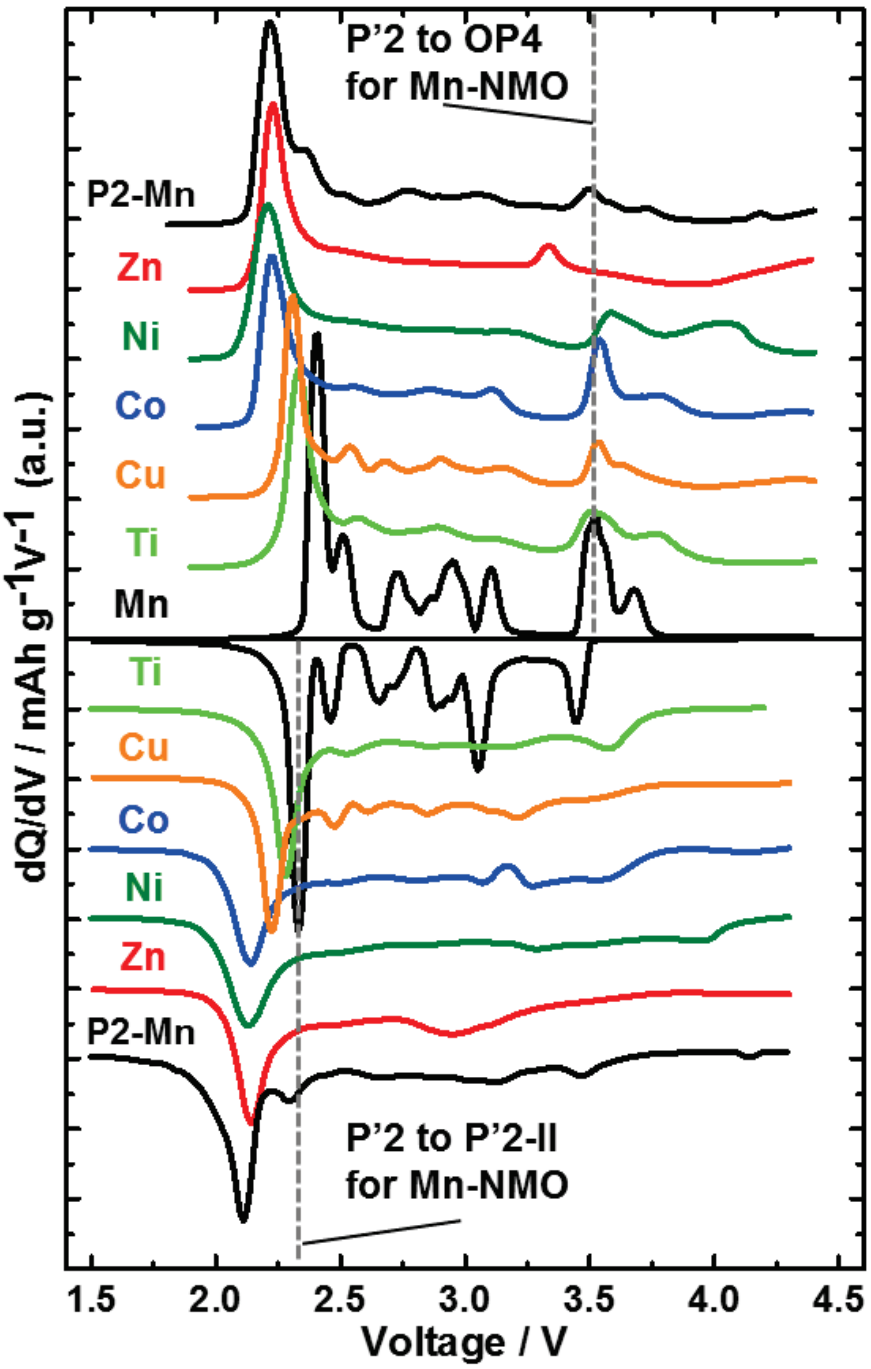

Fig. 6-7. *dQ/dV* plot of 1st discharge (bottom) and 2nd charge (top).

P'2 and another P'2 (P'2-II) phases.[1] All doped samples show the similar largest peaks at around 2.3 V, indicating the same two-phase reactions are observed. Fig. 6-8 shows the relation between *dQ/dV* peak voltage vs. distortion degree. Clearly, the plot proves that the less distorted material shows lower potential of the two-phase reaction. Note that this trend is not consistent with oxidation state of Mn because of obvious difference among divalent dopant samples, Ni-, Cu-, and Zn-NMO. This result shows correlation between CJTD and electrochemical reactions in $Na_{2/3}Mn_{0.9}Me_{0.1}O_2$. During extensive fifty cycles, the correlation is confirmed to be maintained without any apparent irreversible phase change. Fig. 6-8 compares discharge-rate capability for $Na_{2/3}Mn_{0.9}Me_{0.1}O_2$ samples. Mn-NMO shows inferior rate property, especially above 1C rate, and those of Ti- and Co-NMO are even worse than Mn-NMO. On the other hand, Mg-, Ni-, and Zn-NMOs, classified in a less distorted group, exhibit better rate performance. Interestingly, capacity retention test gave us opposite tendency, i.e. Ti- and

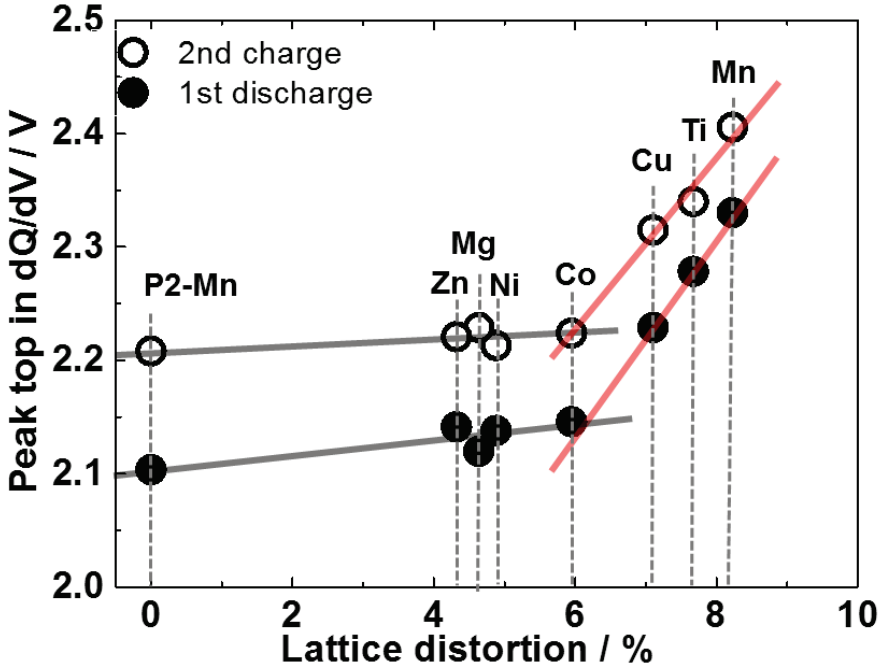

Fig. 6-8. The largest peak top in *dQ/dV* plot.

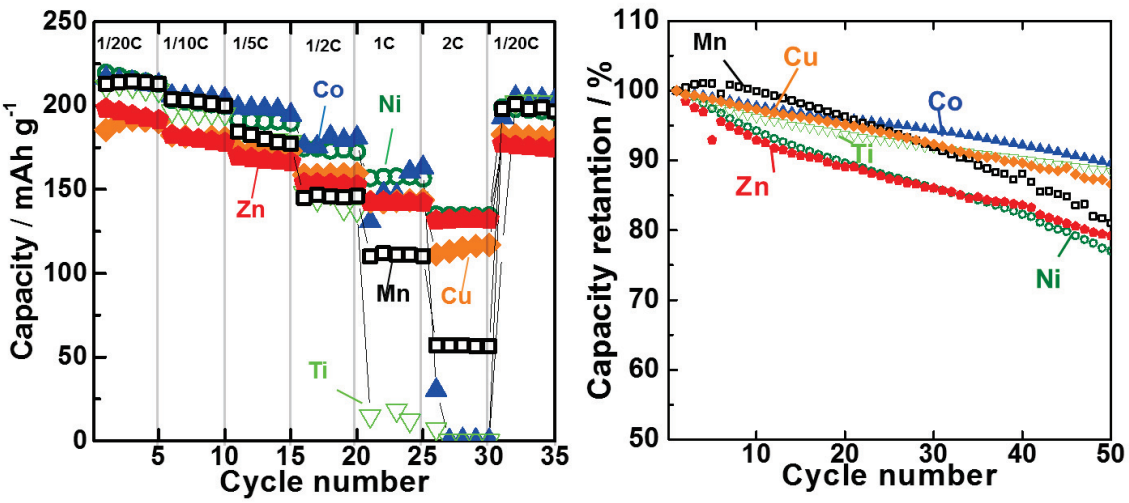

Fig. 6-9. (a) Rate properties and (b) cycle stability of $Na_{2/3}Mn_{0.9}Me_{0.1}O_2$.

Co-NMOs are better than Mg-, Ni-, and Zn-NMOs in terms of cycle stability (see Fig. 6-10). Electrochemical properties of the samples are summarized in Table 6-2. Fig. 6-10 summarizes the relationship between capacity maintenance as $Q_{3C}/Q_{0.05C}$ ratio and capacity retention at 50th cycle for $Na_{2/3}Mn_{0.9}Me_{0.1}O_2$ samples. Basically the linear relationship appears, indicating trade-off relationship between cycle stability and rate

Table 6-2. Summary of electrode performances of $Na_{2/3}Mn_{0.9}Me_{0.1}O_2$.

Sample ID	Dopant	Composition	1st discharge capacity / mAhg^{-1}	Capacity retention after 25 cycles	Capacity retention after 50 cycles	Rate 2C/0.05C
Mn-NMO	---	$Na_{2/3}MnO_2$	211.6	94.2 %	80.7%	21.8 %
Mg-NMO	Mg^{2+}	$Na_{2/3}Mg_{0.1}Mn_{0.9}O_2$	204.4	88.9 %	(78%)	67.4 %
Ti-NMO	Ti^{4+}	$Na_{2/3}Ti_{0.1}Mn_{0.9}O_2$	211.3	92.7%	88.6%	0.3 %
Co-NMO	Co^{3+}	$Na_{2/3}Co_{0.1}Mn_{0.9}O_2$	216.5	95.4%	89.7%	0.1 %
Ni-NMO	Ni^{2+}	$Na_{2/3}Ni_{0.1}Mn_{0.9}O_2$	219.6	87.8 %	76.7 %	61.2 %
Cu-NMO	Cu^{2+}	$Na_{2/3}Cu_{0.1}Mn_{0.9}O_2$	194.4	95.1 %	86.6%	59.7 %
Zn-NMO	Zn^{2+}	$Na_{2/3}Zn_{0.1}Mn_{0.9}O_2$	206.3	85.5 %	79.2%	68.0 %

capability. However, Cu-NMO exhibits exceptional property among them as only Cu-NMO achieves both good cycle stability and high rate property. Such an exceptional electrochemical behavior of Cu-NMO is possibly related with exceptionally high CJTD of Cu-NMO as described in Fig. 6-4b. Further distortion induced by Jahn-Teller Cu^{II} ions may enhance Jahn–Teller assisted Na conduction in the oxide[16] and suppress steep volume change and/or irreversible structural change during Na extraction process.

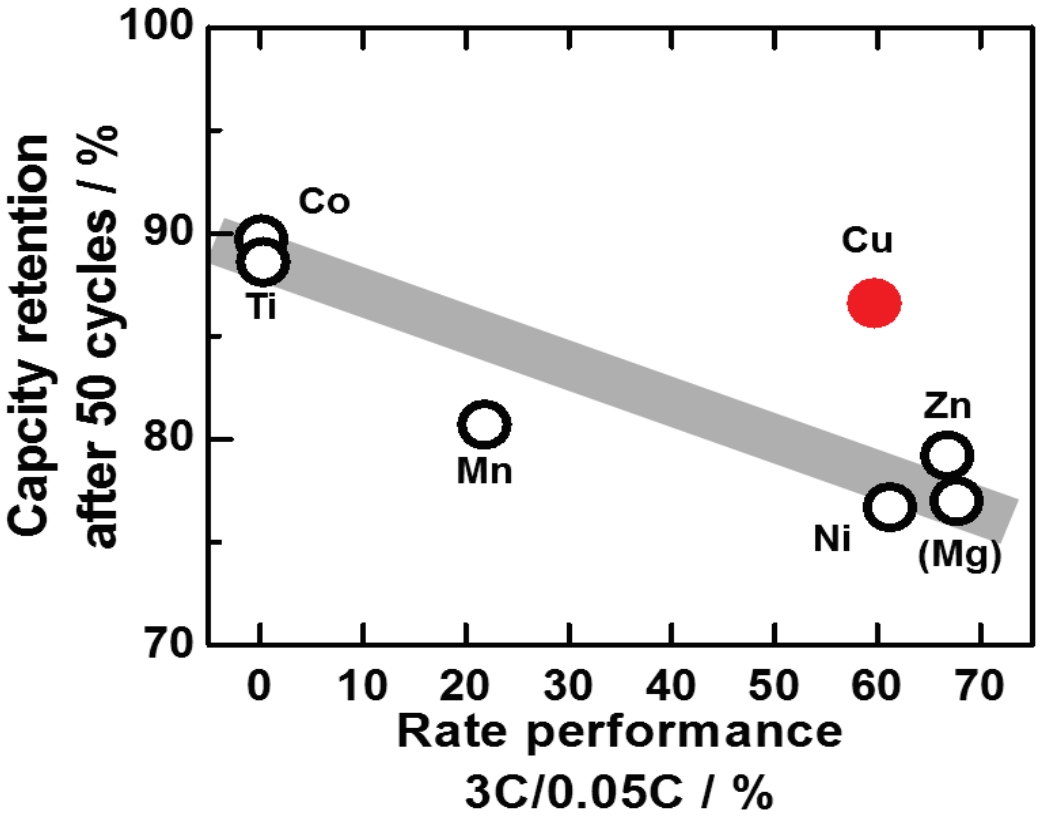

Fig. 6-10. Capacity retention vs. rate capability plots for $Na_{2/3}Mn_{0.9}Me_{0.1}O_2$. "P2-Mn" represents undistorted P2-$Na_{2/3}MnO_2$ containing Mn defect. (the same sample as *h*-NMO in Chapter 4).

6.2.4 Reaction mechanism

Electronic state of transition metals and structural evolution during Na extraction/insertion are examined to understand exceptional behavior of electrode performance for Cu-NMO. Fig. 6-11 shows XANES spectra of Mn K-edge of pristine, fully charged, and fully discharged electrodes. Mn K-edge shifts to higher energy by charge and then shift back to lower energy by discharge, and than that of the pristine state. Cu K-edge spectra shown in Fig. 6-11, however, hardly change or even slightly shifts to opposite direction, i.e. toward lower and higher energy upon charge and discharge, respectively, in contrast to $Cu^{II/III}$ redox reaction observed in P2-$Na_{2/3}Cu_{1/3}Mn_{2/3}O_2$.[10] Therefore, we conclude that $Mn^{III/IV}$ redox couple is responsible for electrochemical activity for Cu-NMO. Cu^{II} is electrochemically inactive and the electronic state of copper is slightly changed via oxide ions bonding with neighbor Mn.

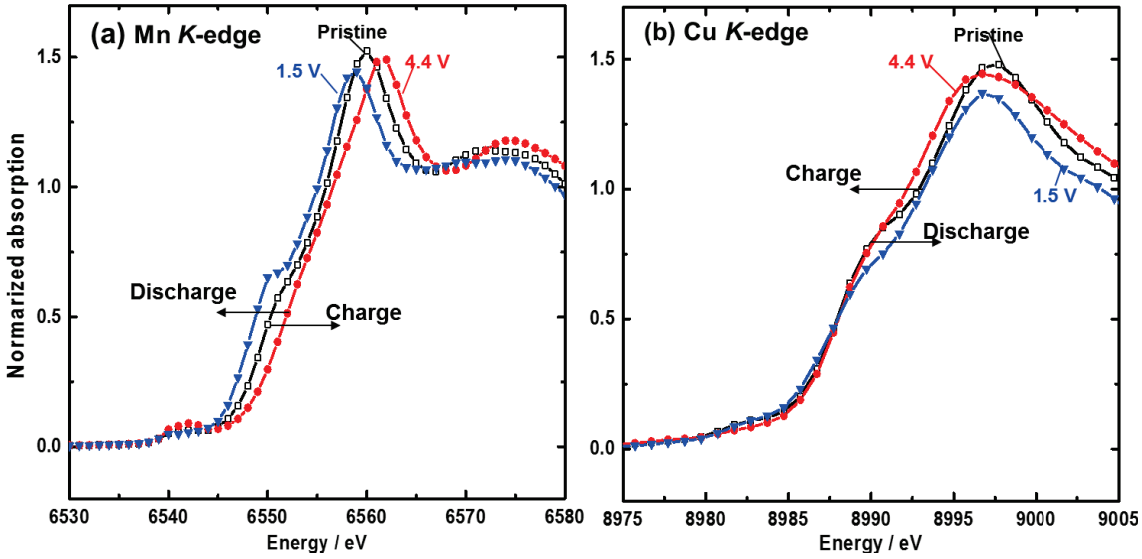

Fig. 6-11. XANES spectra of (a) Mn K-edge and (b) Cu K-edge for $Na_{2/3}Mn_{0.9}Cu_{0.1}O_2$.

Fig. 6-12 shows the contour maps of *operando* XRD patterns for Mn-NMO and Cu-NMO during initial charge and discharge. For Mn-NMO, P'2 structure fully transforms into OP4 structure at $x < 0.25$ in Na_xMO_2, which is also seen in *dQ/dV* plot (Fig. 6-7) at 3.5 V upon charge. On the other hand, Cu-NMO shows that P'2 structure is being kept until charge to $x \sim 0.16$ in Na_xMO_2 (4.4 V) and another phase, probably P2-O2 intergrowth phase appears as a single-phasic reaction. The existence of electrochemically inactive Cu^{II}, which is well integrated in the lattice resulting in the large distortion, stabilizes P'2 structure and suppresses capacity degradation during cycling. *Ex-situ* XRD patterns are consistent with the *operando* XRD results. (Fig. 6-13) In summary, electrochemically inactive and Jahn-Teller active feature of Cu^{II} ions enables to achieve superior rate and cycle properties to P'2-$Na_{2/3}MnO_2$. Detailed analyses of stoichiometry, supper structure, phase transtion, magnetic properties, and so on are under investigation for the P'2-$Na_{2/3}Mn_{0.9}Me_{0.1}O_2$ system.

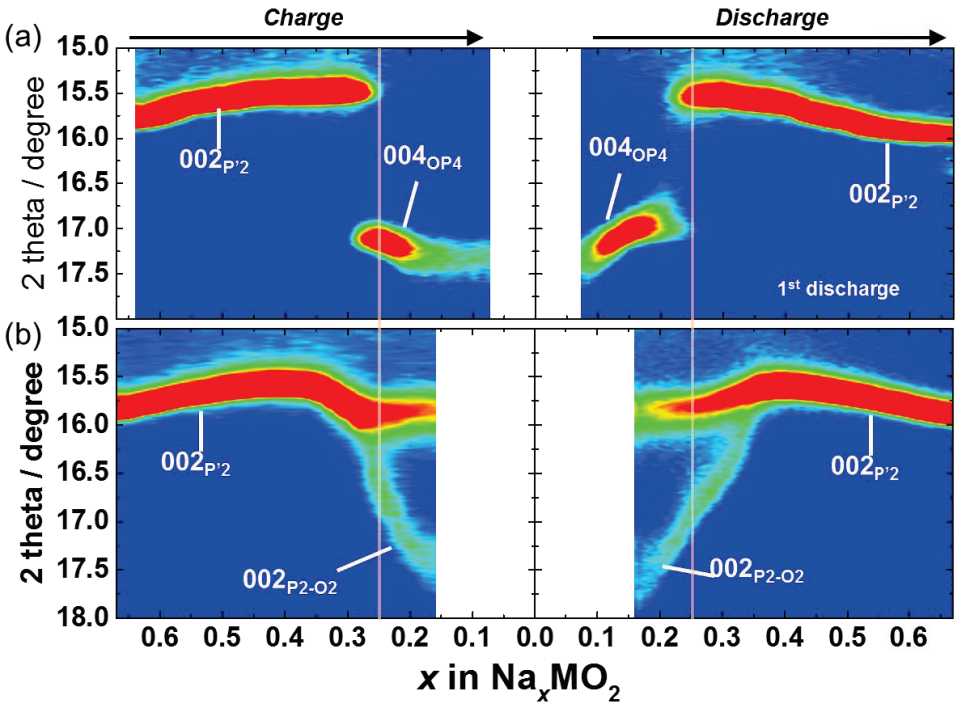

Fig. 6-12. *Operando* XRD of (c) Mn-NMO and (d) Cu-NMO in the initial cycle.

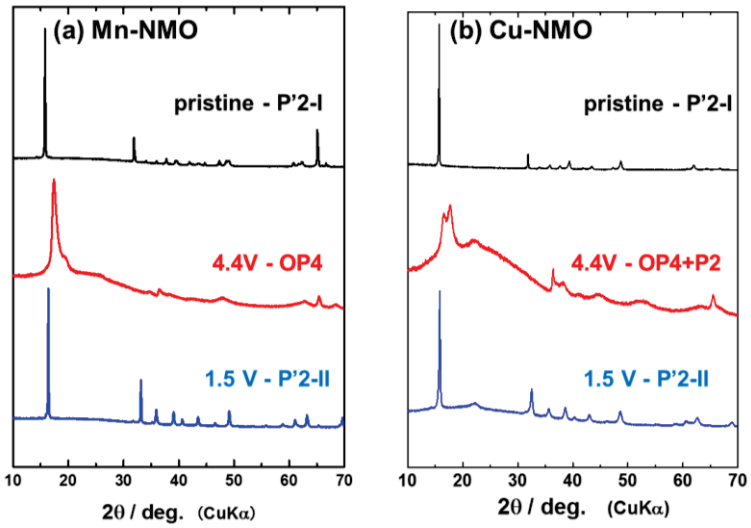

Fig. 6-13. *Ex-situ* XRD of (a) Mn-NMO and (b) Cu-NMO at 4.4 V and 1.5 V.

6.2.5 Summary

In this study, single phases of P'2-$Na_{2/3}Mn_{0.9}Me_{0.1}O_2$ are successfully obtained for a variety of dopants, Me = Mg, Ti, Co, Ni, Cu, and Zn. CJTD of P'2-$Na_{2/3}Mn_{0.9}Me_{0.1}O_2$ is systematically changed by the amount of Mn^{III} ions via di-/tri-/tetra-valent metal dopants. Because of Jahn-Teller active Cu^{II}, P'2-$Na_{2/3}Mn_{0.9}Cu_{0.1}O_2$ possesses anomalous distortion compared to other samples with divalent-metal dopants. We emphasize that CJTD is not always disadvantageous for sodium insertion materials. The distortion is found to be one of the key factors to understand good electrochemical properties of P'2-$Na_{2/3}Mn_{0.9}Me_{0.1}O_2$. Namely, P'2-$Na_{2/3}Mn_{0.9}Cu_{0.1}O_2$ demonstrates both of good cycle life and rate capability as the copper doping would provide better structural stability of the framework oxide against Na extraction/insertion and significant CJTD, which should further enhance superior sodium diffusion. We will study the effect of cooperative distortion by Jahn-Teller effect on the phase stability of Mn(III)-based oxides to design high-performance sodium insertion materials for higher energy density NIBs.

6.3 Synthesis and electrochemical property of zigzag-layered Na(Mn,Cu)O_2

We have discussed the importance of Jahn-Teller distortion to understand electrochemical properties of P'2 structure in Section 6-2. By further investigation of synthesis, we have successfully obtained the new phase, zigzag-layered Na(Mn,Cu)O_2 which is so-called β-phase since this structure is found as high-temperature phase compared with low-temperature phase of α- (O'3-)$NaMnO_2$.[17] Non-doped β-$NaMnO_2$ was firstly reported in 1971,[17 18] however, single phase has never been reported so far.[19, 20] The reason of difficulty to obtain pure β-$NaMnO_2$ was assumed stacking fault[20, 21] or multiple twins[19] with α-phase due to the little gap of formation energy between α and β phases.[22] Here, we found that Cu doping dramatically stabilized β-phase and thus, pure β-Na(Mn,Cu)O_2 has been obtained. Interestingly, β phase can be regarded as the most Jahn-Teller distorted structure in layered Na-Mn-O system as summarized in Fig. 6-14, therefore, its electrochemical investigation gives us new understanding of correlation with Jahn-Teller distortion.

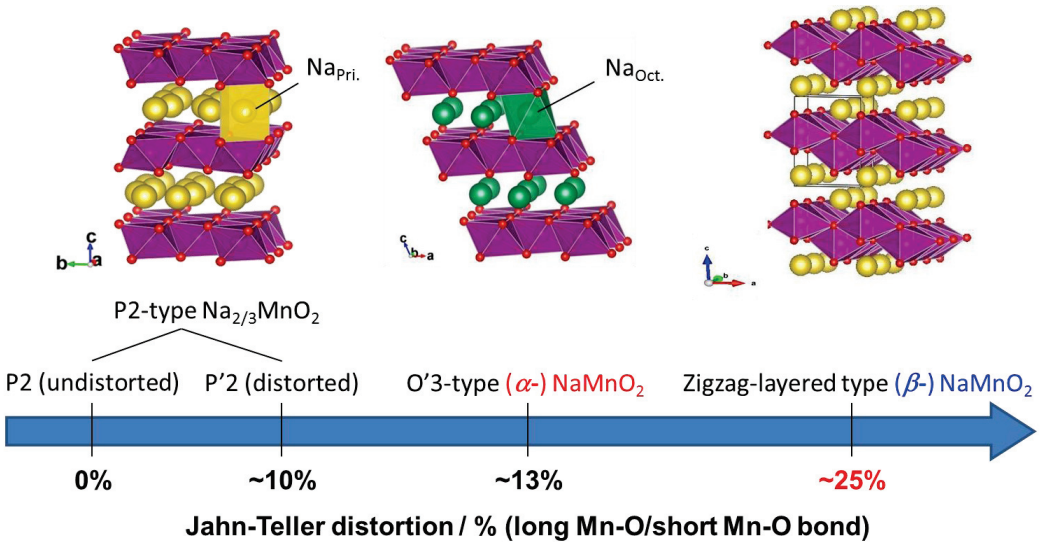

Fig. 6-14. Jahn-Teller distortion in layered Na-Mn-O polymorphs.

6.3.1 Synthesis

$Na(Mn,Me)O_2$ samples are synthesized by a solid-state reaction and the detailed synthesis method is Fig. 6-15. Stoichiometric mixtures of Na_2CO_3 (Kanto Chemical Co., Ltd.), Mn_2O_3, and dopant precursor, TiO_2, $Ni(OH)_2$,Cu_2O and ZnO powders were treated by ball-milling with acetone addition for 12 h at 600 rpm. The mixtures were dried, and thus obtained powder was pressed into pellets. The pellet was heated in air at 1 °C min-1 up to 1050 °C and then, quenched by taking the reaction product out from the heated furnace and immediately transferred into an argon-filled glove box. The samples were cooled to room temperature in the glove box were kept inside to avoid the contact with moisture and oxygen in air.

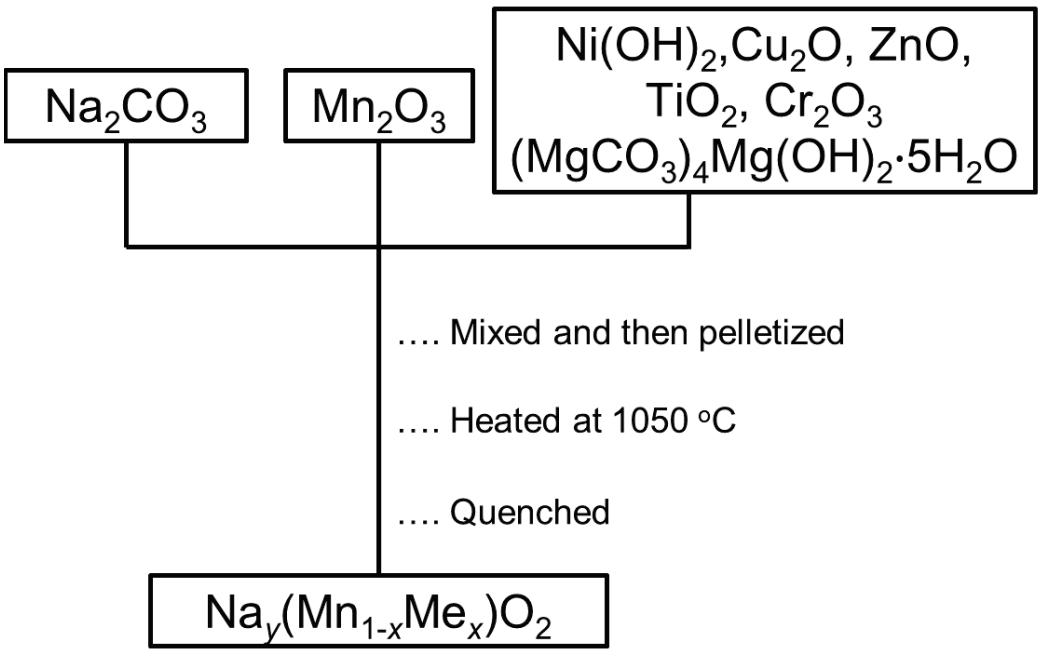

Fig. 6-15. Synthesis condition of $Na(Mn,Me)O_2$ samples.

6.3.2 Structural and electrochemical property of zigzag-layered $Na_yMn_{0.9}Cu_{0.1}O_2$

β-Na(Mn,Cu)O_2 samples with different Na/Me ratio are synthesized by a solid-state reaction. Fig. 6-16 shows X-ray diffraction (XRD) patterns of synthesized β-$Na_yMn_{0.9}Cu_{0.1}O_2$ samples. When Na/Me ratio is at 2/3, P'2 phase is obtaibed as well as the sample repoeted in Section 6-2. At y = 7/9 and 8/9, a mixed sample of P'2 and β-phase is found and at stoichiometric point of y = 1, nearly pure phase of β structure is obtained. This is the closest to pure β structure among previous works to the best of our knowledge. Billaud et al. reported non-doped β-$NaMnO_2$, however, obvious disappearance of 011 diffraction peaks as shown in Fig. 6-17c suggests severe stacking fault and/or multiple twins with α phase.[20]

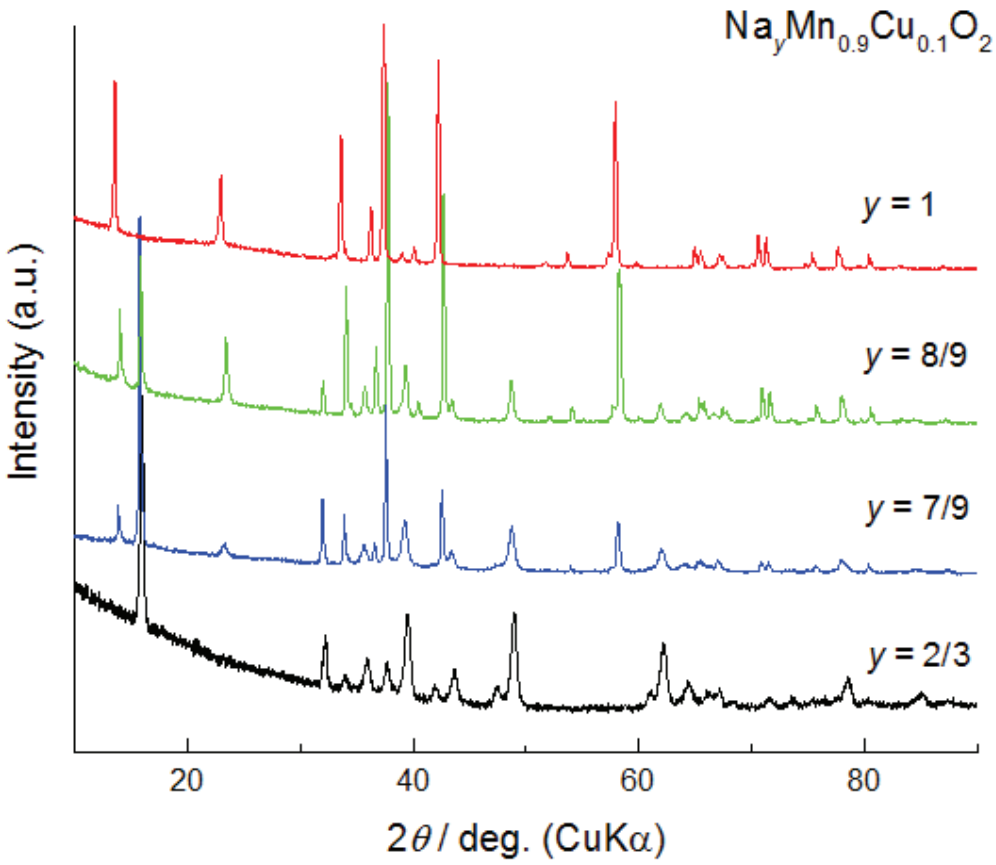

Fig. 6-16. Synthesis condition of β-Na(Mn, Cu)O_2 samples.

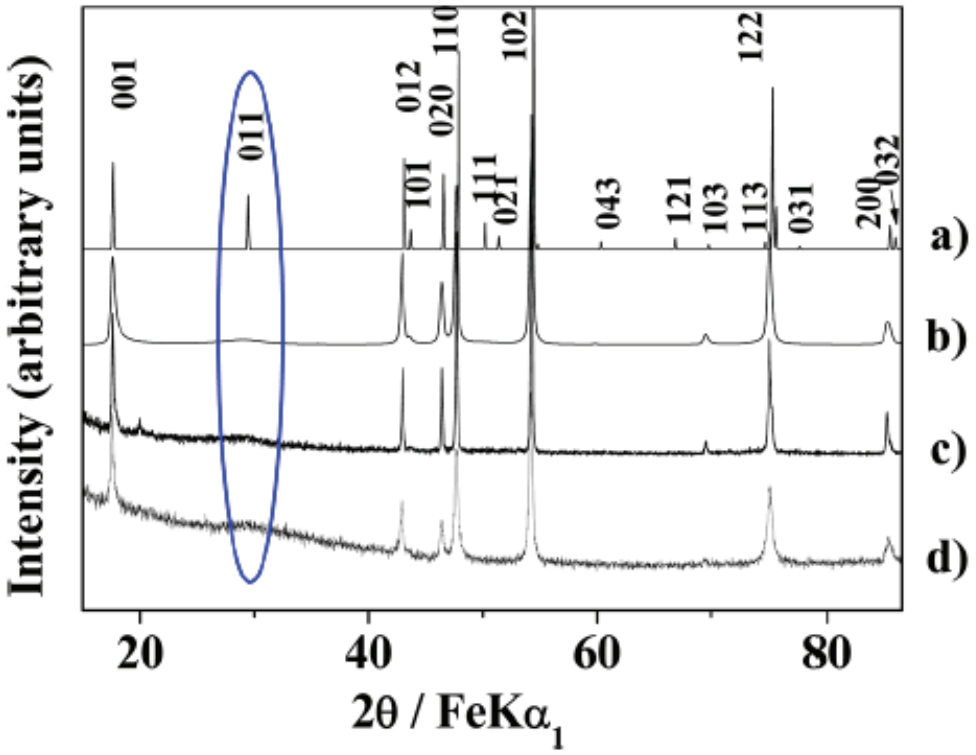

Fig. 6-17. XRD patterns of (a) the ideal β-$NaMnO_2$ structure, (b) simulated with 25% stacking faults, (c) as-prepared β $NaMnO_2$ and (d) after 5 cycles. Highlighted with the blue circle is the major difference between the ideal and experimental data with the 011 peak greatly broadened.[20]

Fig. 6-18 shows initial charge and discharge curves of as-prepared samples. The $NaMn_{0.9}Cu_{0.1}O_2$ sample shows reversible capacity of 170 mAh g^{-1} and 2 plateaux at 3.4 and 2.6 V on discharge and $Na_{8/9}Mn_{0.9}Cu_{0.1}O_2$ shows nearly a mixed behavior between P'2- and β-phase, which is consistent with XRD patterns. Therefore, the plateau at 3.4 V is probably the unique feature derived from β-phase. In addition to an interest in crystal structure of β-$Na(Mn,Cu)O_2$, electrochemical and physical properties are of great interest

because this material group is totally new. Therefore, we have tried further investigation in the following section.

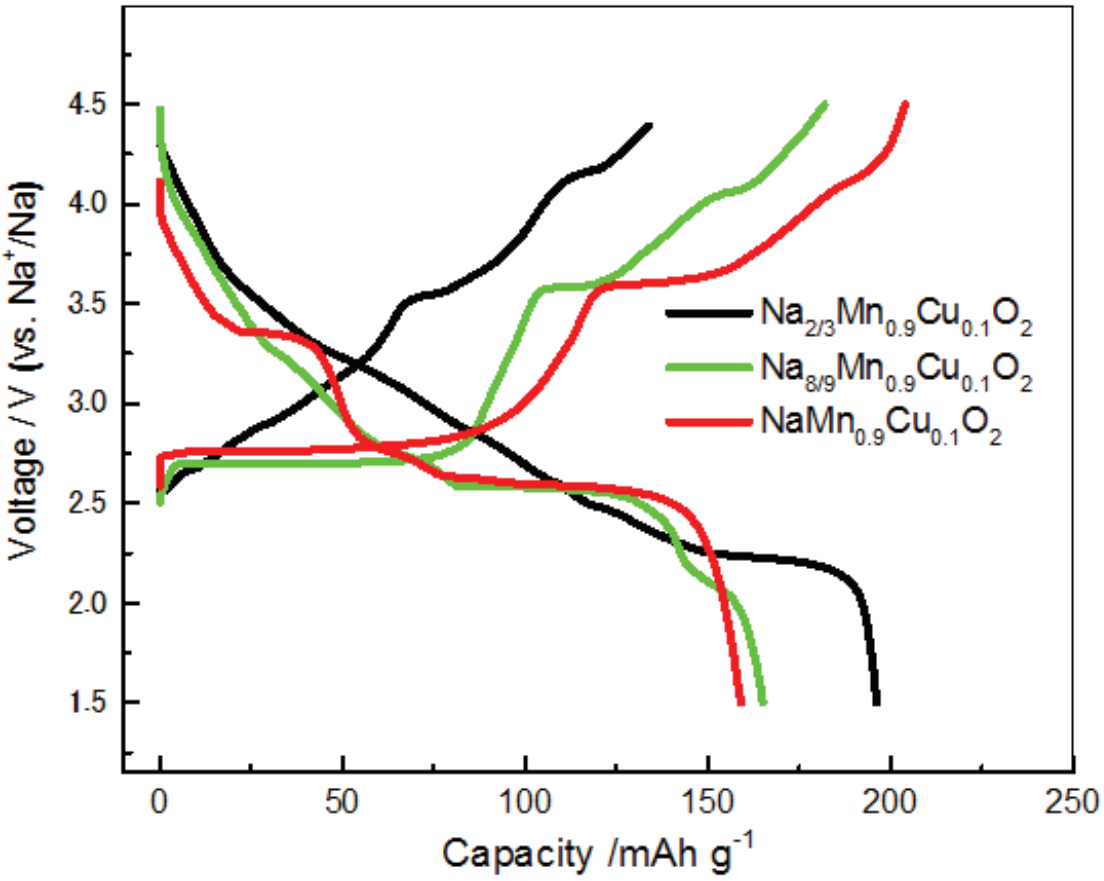

Fig. 6-18. Initial charge and discharge curves of β-$Na(Mn,Cu)O_2$ samples.

6.3.3 Doping effect on stabilization of zigzag layered phase

In the last section, we show Cu doping stabilizes β-phase at the ratio of Na/Me=1. In this section, we have conducted other doping to understand doping effect on stabilization of β-phase. Fig. 6-19 shows XRD patterns of $NaMn_{0.9}Me_{0.1}O_2$ (Me = Mg, Ti, Cr, Ni, Cu, and Zn) by preparing the same firing condition. Among all doped samples, only Cu and Ti doped samples has pure β- and α- phase, respectively. Other samples

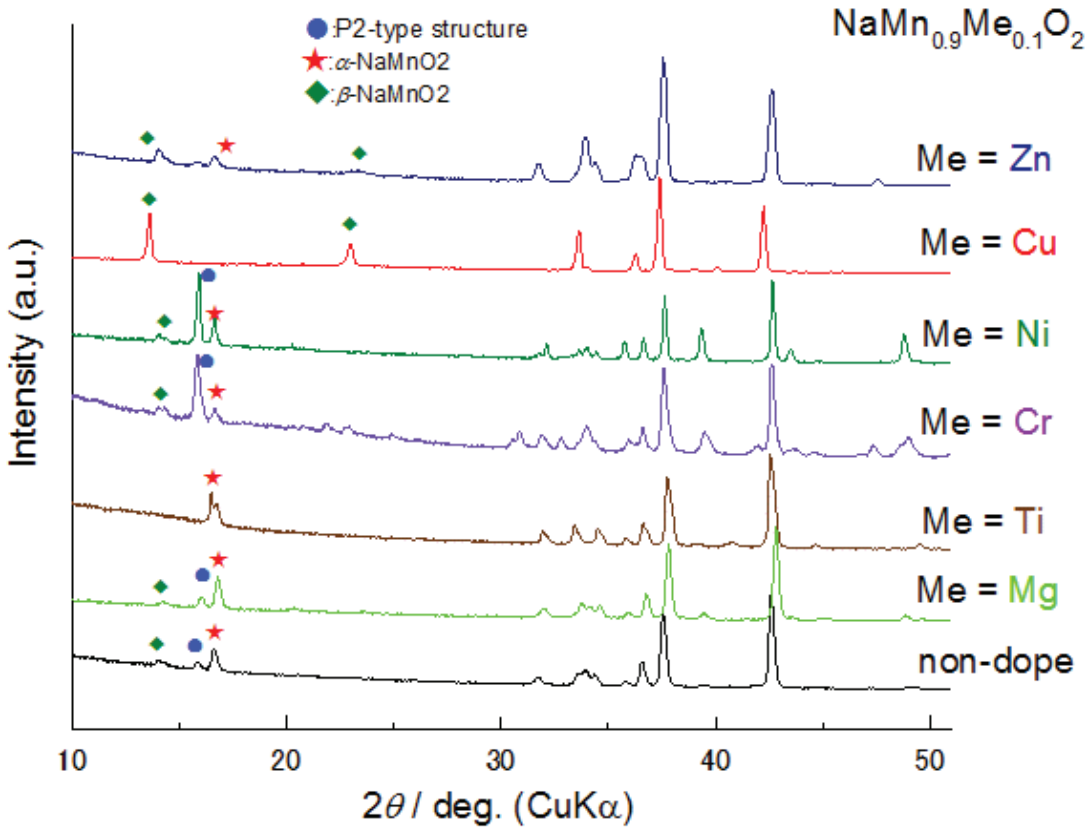

Fig. 6-19. XRD patterns of $NaMn_{0.9}Me_{0.1}O_2$ (Me = Mg, Ti, Cr, Ni, Cu, and Zn)

have mixed phases. This results indicate significant effect of doping and the different tendency of phase formation for each dopant. For example, Ni and Cr doping tends to form P2 phase and Mg and Ti doping tends to form α- phase. In zigzag-layered $LiMnO_2$, change of formation energy by metal doping was estimated by DFT calculation.[22] Combining such a calculation is also applicable to this system and will be done in future. The unique effect of Cu doping on stabilizing β-phase should be related with Jahn-Teller activity of Cu ions and the largest distortion of β-phase among layered Na-Mn-O system.

6.3.4 Dependence of Cu doping on formation of zigzag-layered phase

In this section, $NaMn_{1-x}Cu_xO_2$ samples with different doping amount of copper are synthesized and their electrochemical properties are investigated. Fig. 6-20 shows XRD patterns and SEM images of $NaMn_{1-x}Cu_xO_2$ samples (x=0.05, 0.10, 0.125). All samples have stick-like particles. 101 diffraction peak is increasing by increase of Cu amount, indicating Cu doping stabilizes β-phase and/or suppresses staking fault and x = 0.125 is nearly the maximum in the current synthesis condition since x = 0.15 has CuO impurity (not shown). Therefore, we have concluded that x = 0.125 is the limit to avoid formation of impurity phases in the closest to the targeted β phase. To further understand the crystal structure of $NaMn_{1-x}Cu_xO_2$ samples, SXRD and TEM / electron diffraction

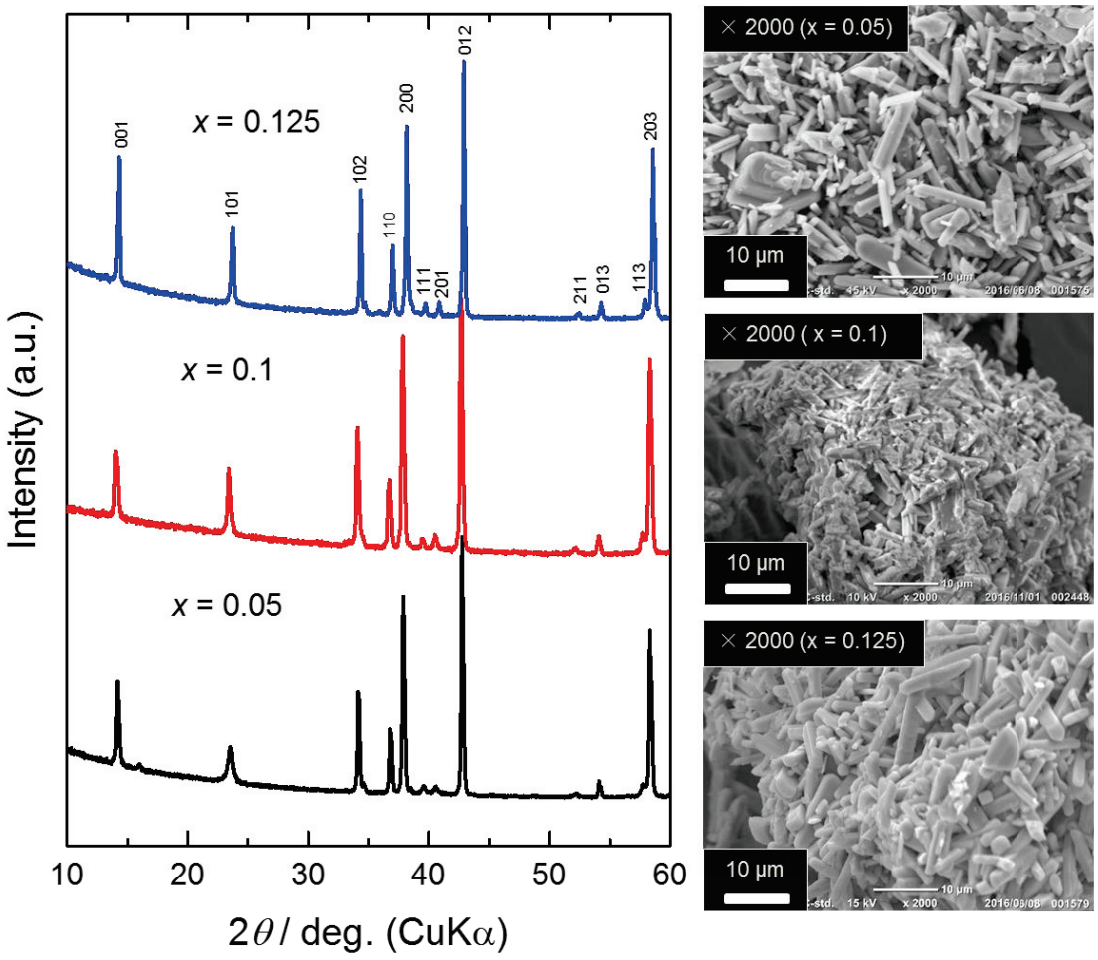

Fig. 6-20. XRD patterns and SEM images of $NaMn_{1-x}Cu_xO_2$ samples.

measurement is conducted for x = 0.05 and 0.125 as shown in Fig. 6-21. No impurity peaks are observed except the peaks labeled with green arrows. We have confirmed that these peaks reversibly disappear at low temperature below 200 K obtained by low temperature SXRD (Fig. 6-22a) and thus, these peaks are not from impurity and probably derived from long range ordering.

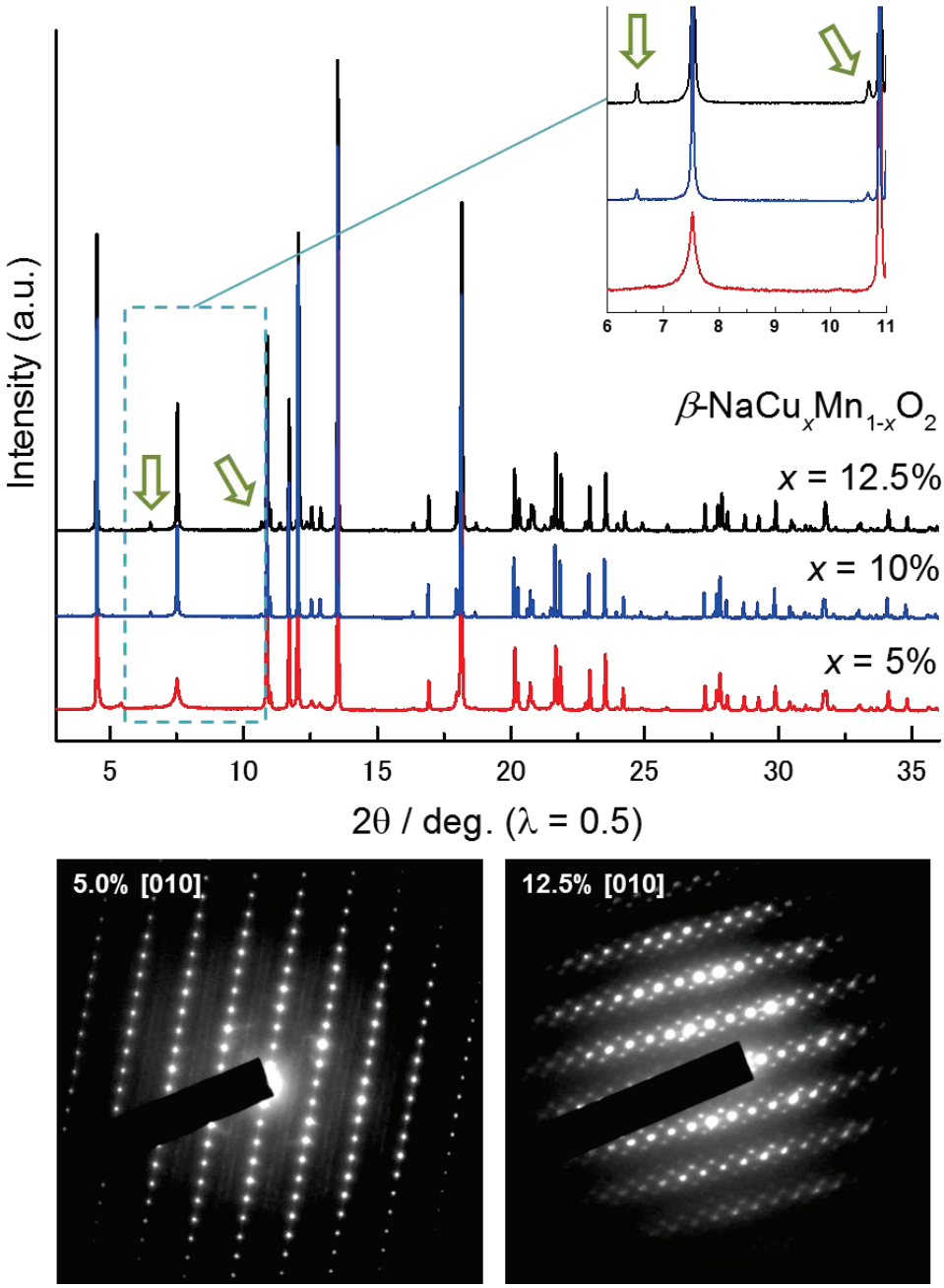

Fig. 6-21. SXRD and electron diffraction patterns of $NaMn_{1-x}Cu_xO_2$ samples.

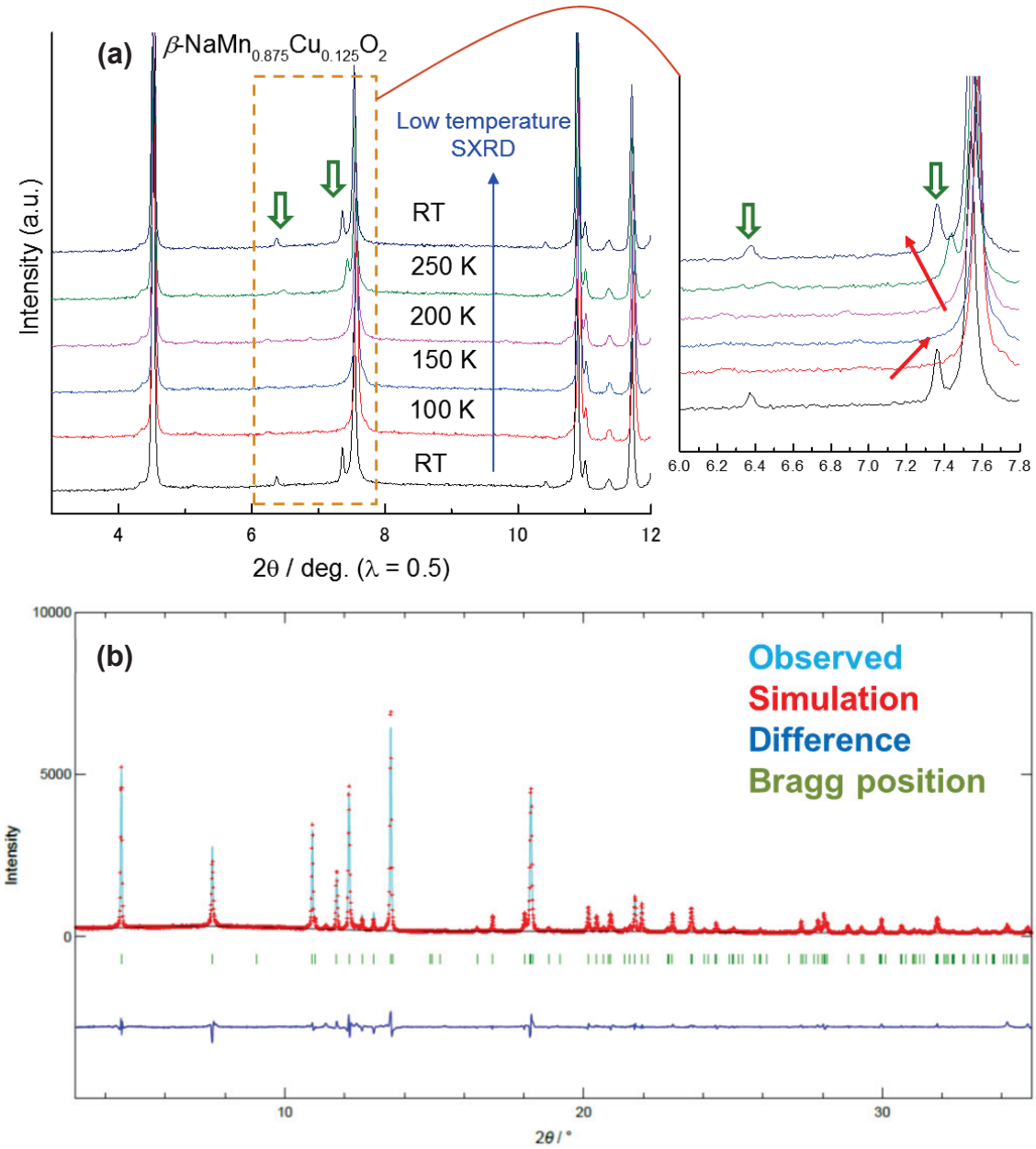

Fig. 6-22. (a) Low temperature SXRD of β–$NaMn_{0.875}Cu_{0.125}O_2$ and (b) Rietveld analysis for SXRD pattern at 100 K.

Since the LT SXRD result shows that all diffraction peaks of β–$NaMn_{0.875}Cu_{0.125}O_2$ below 200K can be assigned to β–phase (S.G. *Pmnm*), Rietveld analysis is conducted for β–$NaMn_{0.875}Cu_{0.125}O_2$ at 100 K. The observed, fitting and difference curves are shown in

Fig. 6-22b. *R* factors are adequately low and summarized in Table 6-3 with refined structural parameters. Here, we conclude that we have obtained single *β*–phase for *β*–$NaMn_{0.875}Cu_{0.125}O_2$ without stacking fault and this is the first report of successful Rietveld refinement for *β*– $NaMnO_2$ or $Na(Mn,Cu)O_2$. The fact, that the additional peaks reversibly appear above 250 K despite of single *β*–phase at low temperature, strongly proves that the structure at RT contains superstructure or long-range modulation. In fact, electron diffraction images along [100] of the 12.5% sample (Fig. 6-21) shows obvious satellite peaks while the 5% sample doesn't have such satellite peaks. This long range modulation should be related with formation of pure *β* phase without stacking fault and further structural analysis is under way.

Table 6-3. Refined crystallographic parameters by Rietveld analysis for the SXRD pattern of *β*–$NaMn_{0.875}Cu_{0.125}O_2$ at 100 K. The fixed parameters are indicated by superscript "a." The isotropic displacement parameter, B, is refined after the refinement of other parameters as labeled superscript "b". B(Na) indicated by superscript "c" converged nearly zero when it's refined and thus, it is fixed at 0.30.

S.G. Pmnm a = 4.7163(3) Å , *b* = 2.8531(5) Å , *c* = 6.3099(1) Å

Atom	site	*x*	*y*	*z*	g	B
Mn	2a	0.25[a]	0.25[a]	0.6252(2)	0.875[a]	0.294(1)[b]
Cu	2a	0.25[a]	0.25[a]	= *z* (Mn)	0.125[a]	= B(Mn)
Na	2a	0.25[a]	0.25[a]	0.1328(3)	1.00[a]	0.30[c]
O (1)	2b	0.75[a]	0.25[a]	0. 1707(2)	1.00[a]	0.478(4)[b]
O (2)	2b	0.75[a]	0.25[a]	0. 5796(1)	1.00[a]	0.478(4)[b]

R_{wp} = 8.41%, *S* = 1.37, R_B = 2.52% , R_F = 2.35%

6.3.5 Electrochemical property and structural change of zigzag-layered $Na(Mn,Cu)O_2$

Fig. 6-23 shows initial charge and discharge curves and cycle stability of $NaMn_{1-x}Cu_xO_2$ samples. $NaMn_{0.95}Cu_{0.05}O_2$ shows 175 mAh g^{-1} of reversible capacity with insufficient cycle stability, and $NaMn_{0.875}Cu_{0.125}O_2$ shows stable electrochemical cycling with reversible capacity around 150 mAh g^{-1}. Firstly, a decrease of initial reversible capacity by increase of Cu amount is because of electrochemically inactive Cu ions substituted for manganese. Secondly, large and unstable electrochemical activity reminds us (O'3-) α-$NaMnO_2$ which shows 185 mAh g^{-1} of initial reversible capacity in a voltage range of 2.0 and 3.8 V with rapid capacity degradation.[23] The fraction of α-domain integrated in β-lattice, which induced stacking fault, probably causes insufficient cycle stability. The long plateau at 2.7 V on discharge is observed for all samples as well as P'2 samples, implying two-phase reaction between the high and less distorted phases. The redox potential of this plateau will be compared in the following section. The plateau at 3.4 V on discharge is found for x = 0.10 and 0.125 despite of no plateau for x = 0.05 above 3.0 V. This is consistent with an intensity of 101 peak and thus, the reaction at 3.4 V may be related with β-phase.

Structural evolution of $NaMn_{0.875}Cu_{0.125}O_2$ and $NaMn_{0.95}Cu_{0.05}O_2$ during initial charge and discharge is perused by *operando* XRD measurement and shown in Fig. 6-24. At first, by rough comparison with $NaMn_{0.875}Cu_{0.125}O_2$ and $NaMn_{0.95}Cu_{0.05}O_2$, structural change of $NaMn_{0.875}Cu_{0.125}O_2$ is much more complex during Na extraction than that of $NaMn_{0.95}Cu_{0.05}O_2$. One reason is the complex behavior of 101, 111, and 201 peaks which are not clear for $NaMn_{0.95}Cu_{0.05}O_2$ due to stacking fault. While major structural change

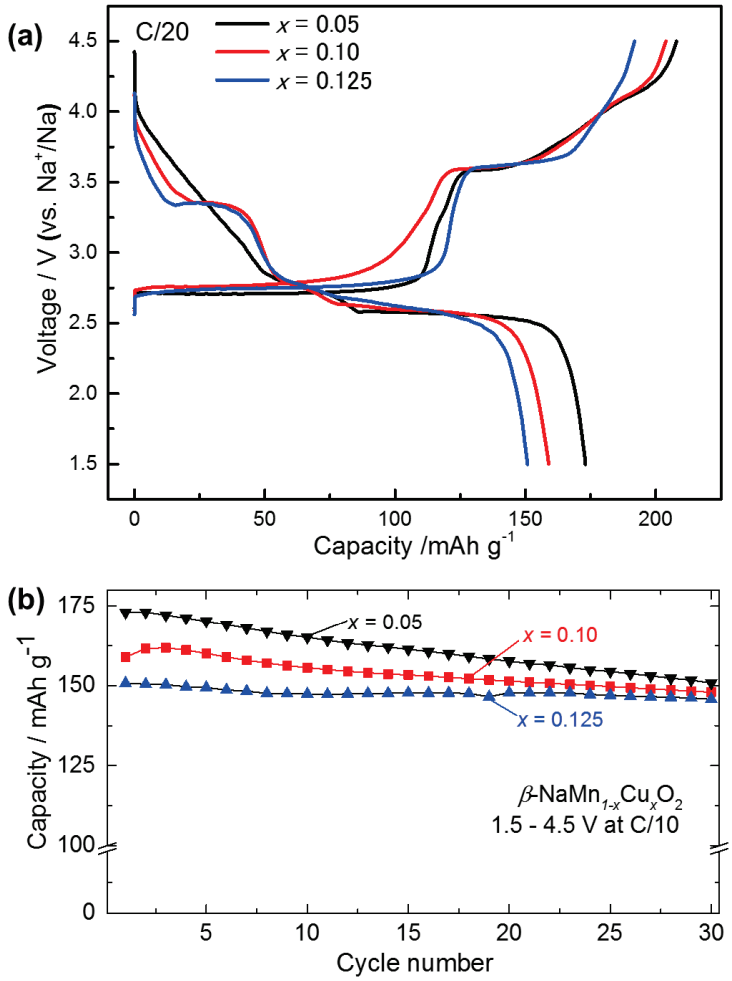

Fig. 6-23. (a) Initial charge and discharge curves and (b) cycle stability

of β–$NaMn_{1-x}Cu_xO_2$ samples. such as the change of lattice constant of the samples is similar each other, the appearance of new peaks for $NaMn_{0.875}Cu_{0.125}O_2$, as indicated by white arrows, in x < 0.4 of Na_xMO_2 suggests structural transition to the structure with lower symmetry. Phase transition is also significantly different and $NaMn_{0.875}Cu_{0.125}O_2$ shows more obvious two-phasic transitions, especially on discharge. As well as P2-Na_xMnO_2, P'2-Na_xMnO_2, and P'2-$Na_xMn_{0.9}Cu_{0.1}O_2$, the plateau around 2.7 V in $x > 0.7$ of $Na_xMn_{0.875}Cu_{0.125}O_2$ is derived from two-phase reaction between largely distorted and less distorted phases. Even though further structural investigation is needed to fully

understand the structural change, pure synthesis of β–phase stabilized by Cu doping reveals rich phase transitions during Na extraction which is hidden by stacking fault in non-doped and Cu 5% doped β–$NaMnO_2$.

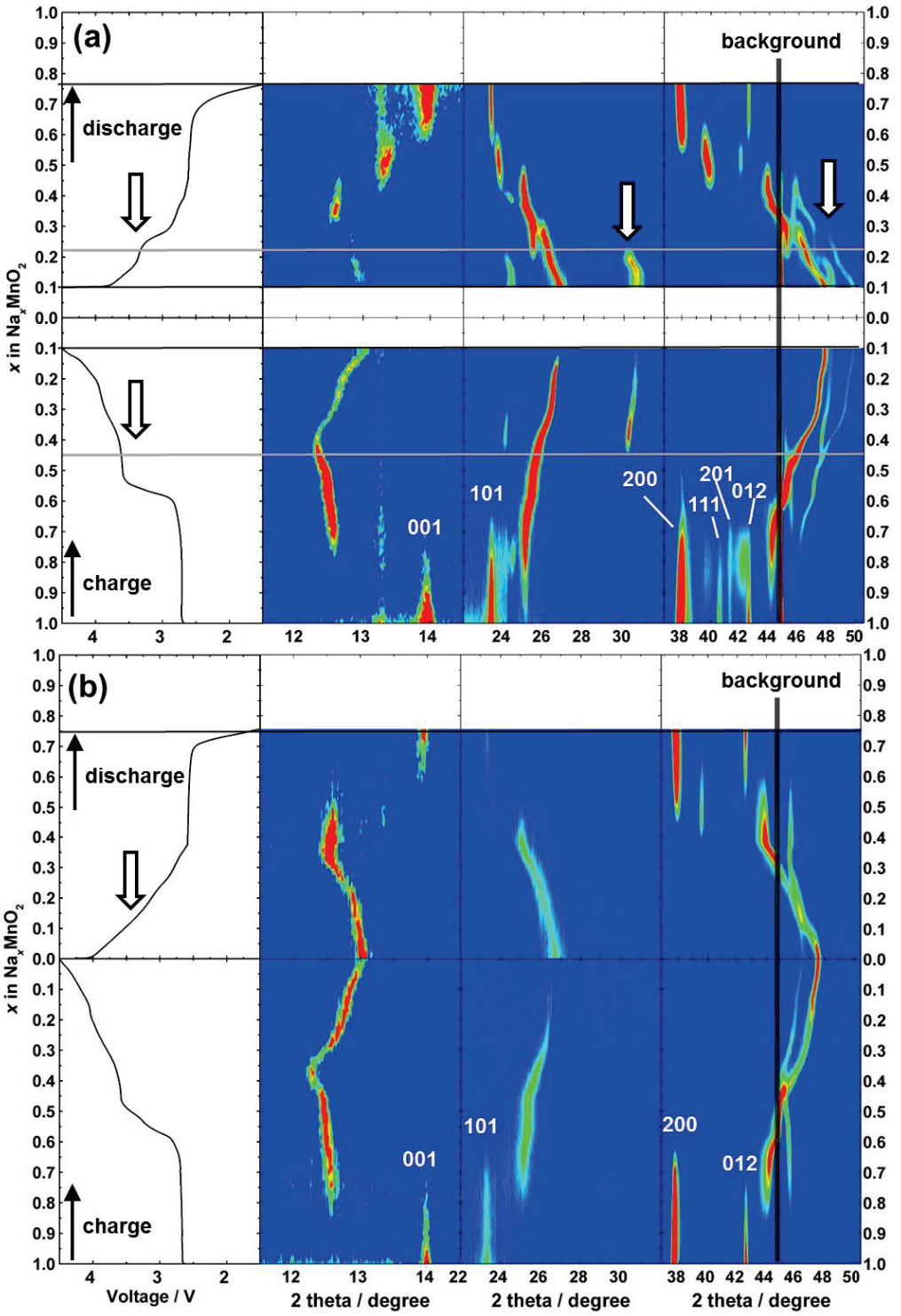

Fig. 6-24. (a) *Operando* XRD patterns for (a) x= 0.125 and (b) x= 0.05 of $NaMn_{1-x}Cu_xO_2$.

6.3.6 Summary

In this chapter, single phase products of β-$NaMn_{1-x}Cu_xO_2$ are successfully obtained. β-structure had never been obtained for un-doped β-$NaMnO_2$, and Cu doping plays a significant role to stabilize β-structure to avoid formation of impurity. Since other divalent dopant doesn't stabilize the β-phase, Jahn-Teller activity is highly related to phase formation of β-structure. $NaMn_{0.875}Cu_{0.125}O_2$.has the closest to the β-structure and reversible capacity of 150 mAh g^{-1}. By *operando* XRD measurement, interesting structural evolution of $NaMn_{0.875}Cu_{0.125}O_2$ is observed, which is unseen previously because of insufficient purity of β-phase due to stacking fault.

Here, we have a chance to summarize whole system of layered Na-Mn-O by combining P2-Na_xMnO_2 and P'2-Na_xMnO_2 in Chapter 5, P'2-$Na_xMn_{0.9}Me_{0.1}O_2$, in Section 6-2, and β-$NaMn_{1-x}Cu_xO_2$ in Section 6-3 and α-(O'3-)$NaMnO_2$ reported by our group.[24] Fig. 6-25 shows the relation between *dQ/dV* peak voltage vs. distortion degree in layered Na-Mn-O system. The lattice distortion is estimated by the ratio of larger and shorter Mn-O bond length and the discharged state are used for P2- and P'2-Na_xMnO_2 electrodes. There is a very clear correlation that largely distorted materilas have higher reaction potential regardless of the detailed layered type and composition. In other words, lattice distortion of $x > 0.9$ of Na_xMO_2 generaly rules the potential of two-phase reaction with less distorted phase in whole Na-Mn-O system. The correlation with the redox potential and CJTD regardless of the layered-type implies this redox potential is a direct probe of stabilization energy of Jah-Teller effect in electronic state of manganese.

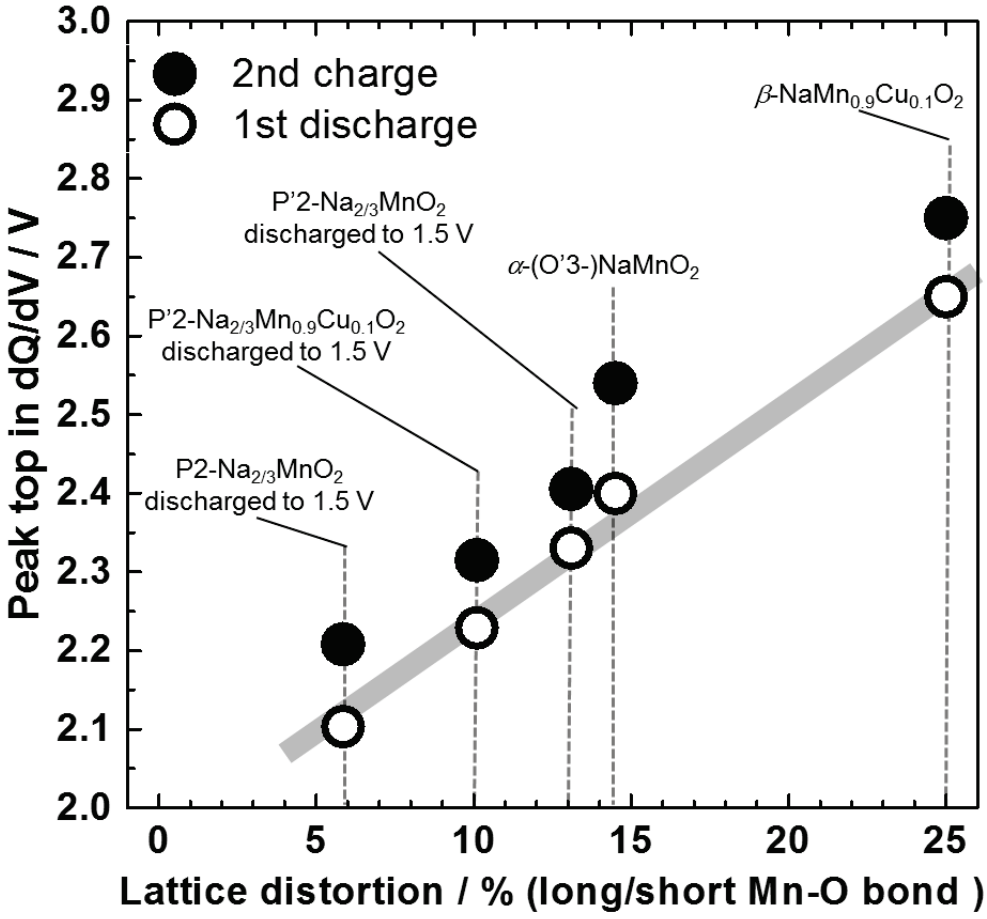

Fig. 6-25. The relation between *dQ/dV* peak voltage vs. distortion degree in layered Na-Mn-O system.

6.4 Conclusion

To understand the correlation between cooperative Jahn-Teller distortion and electrochemical property in Na-Mn-O system, P'2-$Na_{2/3}Mn_{0.9}Me_{0.1}O_2$ and β-$NaMn_{1-x}Cu_xO_2$ are synthesized and their electrochemical properties and structural evolution during charge and discharge are investigated. By combining the result in Chapter 5 and the previous work,[24] the redox potential of Mn(III/IV) couple is compared in whole layered Na-Mn-O system and reveals the obvious correlation with CJTD.

References

1. S. Kumakura, Y. Tahara, K. Kubota, K. Chihara and S. Komaba, *Angew. Chem. Int. Ed.*, 2016, **55**, 12760-12763.
2. A. Caballero, L. Hernán, J. Morales, L. Sánchez, J. Santos Peña and M. A. G. Aranda, *J. Mater. Chem.*, 2002, **12**, 1142-1147.
3. N. Yabuuchi, R. Hara, M. Kajiyama, K. Kubota, T. Ishigaki, A. Hoshikawa and S. Komaba, *Adv. Energy Mater.*, 2014, **4**, 1301453.
4. J. Billaud, G. Singh, A. R. Armstrong, E. Gonzalo, V. Roddatis, M. Armand, T. Rojo and P. G. Bruce, *Energy Environ. Sci.*, 2014, **7**, 1387.
5. N. Yabuuchi, M. Kajiyama, J. Iwatate, H. Nishikawa, S. Hitomi, R. Okuyama, R. Usui, Y. Yamada and S. Komaba, *Nat. Mater.*, 2012, **11**, 512-517.
6. Z. Lu and J. R. Dahn, *J. Electrochem. Soc.*, 2001, **148**, A1225.
7. H. Yoshida, N. Yabuuchi, K. Kubota, I. Ikeuchi, A. Garsuch, M. Schulz-Dobrick and S. Komaba, *Chem Commun (Camb)*, 2014, **50**, 3677-3680.
8. N. Yabuuchi, R. Hara, K. Kubota, J. M. Paulsen, S. Kumakura and S. Komaba, *J. Mater. Chem. A*, 2014, **2**, 16851–16855.
9. S.-Y. Xu, X.-Y. Wu, Y.-M. Li, Y.-S. Hu and L.-Q. Chen, *Chinese Physics B*, 2014, **23**, 118202.
10. C. W. Mason, F. Lange, K. Saravanan, F. Lin and D. Nordlund, *ECS Electrochem. Lett.*, 2015, **4**, A41-A44.
11. Y. Li, Z. Yang, S. Xu, L. Mu, L. Gu, Y.-S. Hu, H. Li and L. Chen, *Adv. Science*, 2015, **2**, 1500031.
12. D. Buchholz, C. Vaalma, L. G. Chagas and S. Passerini, *J. Power Sources*, 2015, **282**, 581-585.

13. K. Hemalatha, M. Jayakumar, P. Bera and A. S. Prakash, *J. Mater. Chem. A*, 2015, **3**, 20908-20912.

14. X. Wu, J. Guo, D. Wang, G. Zhong, M. J. McDonald and Y. Yang, *J. Power Sources*, 2015, **281**, 18-26.

15. Y. Wang, R. Xiao, Y. S. Hu, M. Avdeev and L. Chen, *NatCommun*, 2015, **6**, 6954.

16. X. Li, Y. Wang, D. Wu, L. Liu, S.-H. Bo and G. Ceder, *Chem. Mater.*, 2016, **28**, 6575-6583.

17. J.-P. Parant, R. Olazcuaga, M. Devalette, C. Fouassier and P. Hagenmuller, *J. Solid State Chem.*, 1971, **3**, 1-11.

18. R. Hoppe, G. Brachtel and M. Jansen, *Z. Anorg. Allg. Chem.*, 1975, **417**, 1.

19. A. M. Abakumov, A. A. Tsirlin, I. Bakaimi, G. Van Tendeloo and A. Lappas, *Chem. Mater.*, 2014, **26**, 3306-3315.

20. J. Billaud, R. J. Clement, A. R. Armstrong, J. Canales-Vazquez, P. Rozier, C. P. Grey and P. G. Bruce, *J. Am. Chem. Soc.*, 2014, **136**, 17243-17248.

21. R. J. Clément, D. S. Middlemiss, I. D. Seymour, A. J. Ilott and C. P. Grey, *Chem. Mater.*, 2016, **28**, 8228-8239.

22. S. K. Mishra and G. Ceder, *Phys. Rev. B*, 1999, **59**, 6120.

23. X. Ma, H. Chen and G. Ceder, *J. Electrochem. Soc*, 2011, **158**, A1307.

24. M. Miyazaki, *Master thesis, Tokyo University of Science*, March, 2016.

Chapter 7. Conclusions and Future Works

In this thesis, for the purpose of application to positive electrodes of Li-ion and Na-ion batteries, several types of layered transition metal oxides are investigated via the detailed synthesis, electrochemical testing, and investigation on structural change during change and discharge. For the positive electrode materials of LIBs, we have designed the layered materials to improve reversible capacity and power performance. For the positive electrode materials of NIBs, to realize NIB cells consisting of earth abundant elements for large-format battery application, we have investigated on the electrochemical reactions of Mn based layered materials.

Positive electrode materials for LIBs

In Chapter 3 and 4, large reversible capacity after transformation from layered to disordered cubic structure for Li_2MoO_3 / carbon composite and redox reaction of oxide ions for Li_4NiWO_6 are found. These finding will be useful for material design of high capacity positive electrodes for LIBs. For example, originally disordered materials can be a promising candidate if they contain excess Li. In addition, Li_4MgWO_6 is useful as an additive for positive electrode to improve DCR of LIBs. This can be a very simple and powerful method to easily improve power performance of large full cells. Therefore, understanding the improvement mechanism is necessary in future

Positive electrode materials for NIBs

In Chapter 5 and 6, Mn(III/IV) redox reaction involving Jahn-Teller distortion is thoroughly investigated in layered Na-Mn-O system. Started from $Na_{2/3}MnO_2$ polymorphs, P2 and P'2 $Na_{2/3}MnO_2$ in Chapter 5, the concept is expanded into doped P'2 $Na_{2/3}Mn_{0.9}Me_{0.1}O_2$ and zigzag-layered (β-) $NaMn_{0.9}Me_{0.1}O_2$ step-by-step in Chapter 6.

As a result, electrochemical properties and relation between redox potential and Jahn-Teller distortion are examined in the whole system of layered Na-Mn-O materials with a wide range of distortion from 0 to 25%. Jahn-Teller distortion doesn't provide negative effect on electrochemical properties and even a chance of the positive effect on diffusion of Na ions and structural stability is demonstrated for $Na_{2/3}Mn_{0.9}Me_{0.1}O_2$. Jahn-Teller distortion plays a fundamental role in phase formation of Na-Mn-O system and their electrochemical reactions

Future prospects

Recently, due to the rapid growth of battery market, researches of layered transition metal oxides are sometimes only focusing on their electrochemical properties. However, layered transition metal oxides in general are a very important class that have a high impact not only on battery application but also on fundamental chemical and physical properties such as transport, thermoelectric, magnetic, and superconducting properties and so on. These all properties are derived from the same origin, electronic state of the materials. In addition, electrochemical approach is a very powerful way to modify the electronic state and to see the meta-stable phase which is not possible to be obtained by a direct synthesis. Therefore, deep understanding of electrochemical properties and reaction mechanism of layered transition metal oxides will also provide an impact on progress of solid state chemistry and material science of battery materials. The author believes that interaction with such fields will be very useful for further development of positive electrode materials.

List of Publications

1 Shinichi Kumakura, Yotaro Shirao, Kei Kubota, and Shinichi Komaba

"Preparation and electrochemical properties of Li_2MoO_3/C composites for rechargeable Li-ion batteries"

Phys. Chem. Chem. Phys., 18, 28556 (2016). (Chapter 3)

2 Shinichi Kumakura, Yoshiyuki Tahara, Kei Kubota, Kuniko Chihara and Shinichi Komaba

"Sodium and Manganese Stoichiometry of P2-Type $Na_{2/3}MnO_2$"

Angew. Chem. Int. Ed., 55, 12760 (2016). (Chapter 5)

3 Shinichi Kumakura, Yoshiyuki Tahara, Syuhei Sato, Kei Kubota, and Shinichi Komaba

"Correlation with Jahn-Teller distortion and Electrochemical property in the Doped P'2-$Na_{2/3}MnO_2$ System"

Submitted. (Chapter 6)

Other Achievements

Publications

1 Naoaki Yabuuchi, Ryo Hara, Kei Kubota, Jens Paulsen, Shinichi Kumakura, and Shinichi Komaba

"A new electrode material for rechargeable sodium batteries: P2-type $Na_{2/3}[Mg_{0.28}Mn_{0.72}]O_2$ with anomalously high reversible capacity"

J. Mater. Chem. A, 2, 16851 (2014). (Chapter 1)

Patents

1. Patent application (WO2016/170454) (Chapter 4)

2. Patent application (WO2016/188877) (Chapter 6)

3. Patent application (EU, not opened) (Chapter 4)

Presentations

1. **S. Kumakura**, Y. Tahara, K. Kubota, N. Yabuuchi, J. Paulsen, K. Yamanaka, M. Ogawa, T. Ohta, and S. Komaba

"Electrode Reaction Mechanism of P2-Na2/3(Mg, Mn)O2 for Na-ion Battery",

Oral presentation at 82th meeting of Electrochemical Society of Japan

2. Y. Shirao, **S. Kumakura**, K. Kubota, and S. Komaba

"Carbon composite effect and electrode reaction mechanism of Li_2MoO_3"

Oral presentation at 82th meeting of Electrochemical Society of Japan

3. Y. Tahara, K. Kubota, **S. Kumakura**, K. Gotoh, and S. Komaba

   "Polymorphism and non-stoichiometry of P2-type $Na_{2/3}MnO_2$"

   Oral presentation at 82th meeting of Electrochemical Society of Japan

4. Y. Shirao, **S. Kumakura**, K. Kubota, and S. Komaba

   "Carbon composite Li_2MoO_3 as positive electrode materialsfor Li-ion batteries"

   Oral presentation at EMCMRE-3

5. Y. Tahara, K. Kubota, **S. Kumakura**, and S. Komaba

   "P2-type Na2/3MnO2 polymorphs as positive electrode materials for Na ion batteries"

   Oral presentation at EMCMRE-3

6. Y. Tahara, K. Kubota, **S. Kumakura**, and S. Komab

   "Synthesis and electrochemical properties of Orthorhombic layered sodium manganese oxides"

   Oral presentation at the 56th Battery Symposium in Japan

7. S. Suzuki, **S. Kumakura**, Y. Shirao, Y. Tahara, K. Kubota, and S. Komaba

   "Cation disordering and electrochemical properties of Li-rich oxide $Li_{3+x}Ni_{2-2x}Cr_xNbO_6$"

   Oral presentation at 83th meeting of Electrochemical Society of Japan

8. **S. Kumakura**, Y. Tahara, K. Kubota, and S. Komaba

   "Study on crystal polymorphism and electrochemical properties of P2-type $Na_{2/3}MnO_2$",

   Poster presentation at 2nd International Conference on Sodium Batteries

9. **S. Kumakura**, K. Kubota and S. Komaba

   "Li_4MeWO_6 (Me=Ni, Mn, Co) as Positive Electrode Materials for Li-Ion Batteries",

   Oral presentation at 228th meeting of the Electrochemical Society

10. **S. Kumakura**, Y. Tahara, K. Kubota, and S. Komaba

    "Structural evolution of P2-type $Na_{2/3}MnO_2$ polymorphs by Na extraction/insertion",

    Poster presentation at 67th meeting of International Society of Electrochemistry

    Awarded as ISE Best Poster Award

Acknowledgements

This work was done under the direction of Professor Dr. Shinichi Komaba, Department of Applied Chemistry, Tokyo University of Science (TUS), in the Japanese academic years of 2014-2016. I would like to express my deepest gratitude to Prof. Dr. Shinichi Komaba, who has given me many opportunities to gain valuable experiences throughout the work. I have been enormously stimulated and encouraged by him and his professional attitude, communication skill and so on. I would also like to express my sincere gratitude to Assistant Prof. Dr. Kei Kubota, TUS, who has given me the kind support and the valuable insight. I also thank Ms. Chihara who gave me the great support and fruitful discussions.

This work was also supported by Umicore as a collaborative research with Komaba laboratory. I am eternally grateful for Dr. Jens Paulsen and Dr. Saburo Hori who gave me a great chance to start this adult doctoral course. I believe they bet my potential so that I will give my best to contribute research activity in Umicore to pay back something.

I would like to thank many students in Komaba lab studying with me, Mr. Yotaro Shirao, Mr. Yoshiyuki Tahara, Mr. Shinya Suzuki, Mr. Syuhei Sato, and Mr. Norikazu Yoshinaga. They all are so kind and gave me so much support. In addition, I'm really impressed by their diligence. I would really appreciate again for what every member in Komaba laboratory has done for me.

My sincere thanks also go to my family. I would like to thank my parents who gave me their support and trust. Last but not least, I am deeply grateful to my wife, Chiaki, for her encouragement.